



**HAL**  
open science

# Dynamics driven by emerging vertical drafts in stratified turbulent flows

Fabio Feraco

► **To cite this version:**

Fabio Feraco. Dynamics driven by emerging vertical drafts in stratified turbulent flows. Other. Université de Lyon; Università degli studi della Calabria, 2022. English. NNT : 2022LYSEC010 . tel-03720707

**HAL Id: tel-03720707**

**<https://theses.hal.science/tel-03720707v1>**

Submitted on 12 Jul 2022

**HAL** is a multi-disciplinary open access archive for the deposit and dissemination of scientific research documents, whether they are published or not. The documents may come from teaching and research institutions in France or abroad, or from public or private research centers.

L'archive ouverte pluridisciplinaire **HAL**, est destinée au dépôt et à la diffusion de documents scientifiques de niveau recherche, publiés ou non, émanant des établissements d'enseignement et de recherche français ou étrangers, des laboratoires publics ou privés.



N°d'ordre NNT : 2022LYSEC010

**THESE de DOCTORAT DE L'UNIVERSITE DE LYON  
opérée au sein de l'École centrale de Lyon**

Ecole Doctorale N° 162  
**Mécanique Énergétique Génie Civil Acoustique**

Spécialité de doctorat :  
**Mécanique des fluides**

Soutenue publiquement le 11/03/2022, par :

**Fabio Feraco**

---

**Dynamics driven by emerging vertical  
drafts in stratified turbulent flows**

---

Devant le jury composé de :

Lanotte Alessandra	Senior Scientist, Professor (CNR; Italie)	Rapporteuse
Liu Hanli	Senior Scientist, Professor (NCAR-CU; États-Unis)	Rapporteur
Folini Doris	Senior scientist, Lecturer (ETH; Suisse)	Examinatrice
Bourgoin Mickaël	Directeur de Recherche (ENS, CNRS; France)	Président du jury
Moisy Frédéric	Professeur (Université Paris-Saclay; France)	Examineur
Bertoglio Jean-Pierre	Directeur de Recherche (ECL, CNRS; France)	Directeur de thèse
Marino Raffaele	Chargé de Recherche (CNRS; France)	Co-directeur de thèse
Primavera Leonardo	Professor (UNICAL; Italie)	Co-directeur de thèse



## *Abstract*

Intermittency is a characteristic feature of turbulent flows. Typically observed as the localized enhancement of small-scale field fluctuations, it is at the origin of the bursty behavior of the energy dissipation in fluids. However, the intermittent character of the velocity and of the temperature fields has been reported in many observations in geophysical flows also in the large scales.

The purpose of this thesis is precisely to characterize the emergence of large-scale intermittent vertical velocity drafts and temperature bursts in stratified turbulent flows of geophysical interest, as detected in the atmosphere and the oceans. In particular, using direct numerical simulations (DNSs) of the Boussinesq equations (with or without rotation), I explore the parameter space with the aim of investigating dynamics and energetics in stratified flows in which the interplay of internal waves and turbulent motions produces powerful enhancements of the vertical velocity and temperature at large-scale. This phenomenon, resulting from a resonant mechanism that I describe through a simple one-dimensional model, feeds back on the energy transport and dissipation property of the flow, influencing mixing. The large-scale intermittency detected in stratified flows has been investigated here by means of high order statistics of the prognostic fields, and in particular through the kurtoses of the vertical velocity and temperature, which are found to have a non-monotonic behavior with the Froude number, that is, the control parameter of the turbulent system viewed as a superposition of waves and nonlinear eddies.

The Eulerian fields are used to characterize the distribution of the energy across the scales and the exchanges between kinetic and potential energies within the resonant regime. Lagrangian tracers have also been released in DNSs to investigate their dispersion in stratified turbulent flows developing extreme vertical drafts. The first radar observation of an extreme event in the vertical velocity field in the mesosphere and lower thermosphere, interpreted here as a “super-bore”, is finally presented together with a study of the diffusion of a passive scalar in a turbulent flow, preliminary to future characterizations of the passive scalar diffusion in a stratified environment in the resonant regime identified as before in terms of the Froude number.



## *Résumé*

L’intermittence est un trait caractéristique des écoulements turbulents. Généralement observée comme l’intensification localisée des fluctuations de champ à petite échelle, elle est à l’origine du comportement en rafale de la dissipation et du taux de transfert d’énergie. Toutefois, le caractère intermittent des champs de vitesse et de température a été également documenté dans de nombreuses observations d’écoulements géophysiques à grande échelle.

L’objectif de cette thèse est précisément de caractériser l’émergence de vents verticaux intermittents et de rafales de température, dans des turbulences stratifiées des écoulements d’intérêt géophysique, comme ceux qui sont détectés dans l’atmosphère et les océans. En particulier, en utilisant des simulations numériques directes (DNSs) des équations de Boussinesq (avec ou sans rotation), j’ai exploré l’espace des paramètres dans le but d’étudier la dynamique et l’énergétique des écoulements stratifiés dans lesquels l’interaction des ondes internes et des mouvements turbulents produit des puissantes intensifications de la vitesse verticale et de la température à grande échelle. Ce phénomène est le résultat d’un mécanisme résonant que je décris à travers un modèle simple à une dimension; il se répercute sur la propriété de transport et de dissipation d’énergie de l’écoulement, influençant le mélange. L’intermittence à grande échelle détectée dans les écoulements stratifiés a été étudiée ici en utilisant de statistiques d’ordre élevé des champs pronostiques, et en particulier à travers les coefficients d’aplatissement de la vitesse verticale et de la température, qui ont un comportement non monotone avec le nombre de Froude, c’est-à-dire, le paramètre de contrôle du système turbulent considéré comme une superposition d’ondes et de tourbillons non linéaires.

Les champs Eulériens sont utilisés pour caractériser la distribution de l’énergie à travers les échelles et les échanges entre énergie cinétique et énergie potentielle dans le régime résonant. Les traceurs Lagrangiens ont aussi été distribués dans les DNS pour étudier leur dispersion dans des écoulements turbulents stratifiés, développant des courants ascendants extrêmes. Finalement, la première observation radar d’un événement extrême dans le champ de vitesse verticale dans la mésosphère et la thermosphère inférieure (MLT), interprété ici comme un “super-bore”, est présentée avec une étude de la diffusion d’un scalaire passif dans un écoulement turbulent, préalable à de futures caractérisations de la diffusion scalaire passive en milieu stratifié dans le régime résonant, identifié comme avant en termes de nombre de Froude.



# Contents

<b>1</b>	<b>Introduction</b>	<b>1</b>
1.1	The Navier-Stokes equations . . . . .	4
1.2	The Boussinesq approximation . . . . .	5
1.3	The Lagrangian approach . . . . .	5
1.4	Turbulence and its properties . . . . .	6
1.5	Statistical description . . . . .	8
1.5.1	The probability density function . . . . .	8
1.5.2	The moments of a random variable . . . . .	8
1.5.3	The normal distribution . . . . .	9
1.5.4	Random functions . . . . .	10
1.6	Homogeneous and isotropic turbulence . . . . .	10
1.7	The K41 theory . . . . .	11
1.8	Stratified turbulence . . . . .	13
1.9	Rotating turbulence . . . . .	14
1.10	Intermittency in turbulence . . . . .	15
1.11	Large-scale intermittency . . . . .	17
1.12	Methodology . . . . .	17
1.12.1	Direct numerical simulations . . . . .	18
1.12.2	Radar observations . . . . .	20
1.12.3	Wind tunnel experiment . . . . .	22
<b>2</b>	<b>Mixing and transport in stratified flows with and without rotation</b>	<b>25</b>
2.1	Emergence of vertical drafts in stratified flows . . . . .	29
2.1.1	A model for the vertical drafts . . . . .	33
2.1.2	Vertical drafts, overturning and mixing . . . . .	35
2.2	Lagrangian particle dispersion in stratified flows with rotation . . . . .	38
<b>3</b>	<b>Observation of vertical drafts in the Earth's upper atmosphere</b>	<b>71</b>
3.1	Evidence of extreme vertical wind velocities in the mesosphere and lower thermosphere . . . . .	72
3.2	The role of horizontal shears in the statistics of vertical drafts . . . . .	73
<b>4</b>	<b>Enhancement of small-scale intermittency and dissipation in stratified flows</b>	<b>87</b>
4.1	The link between large- and small-scale intermittency . . . . .	87
4.2	Modulation of local energy dissipation by vertical drafts . . . . .	89
<b>5</b>	<b>Modeling of the probability density function of a passive scalar concentration in a turbulent flow: a preliminary study</b>	<b>117</b>
5.1	Evolution of the PDF of the passive scalar concentration and mixing phases . . . . .	117
5.2	Validation of a model distribution in DNSs and wind tunnel experiments	119





# List of Abbreviations

<i>CAT</i>	<b>C</b> lear <b>A</b> ir <b>T</b> urbulence
<i>DNS</i>	<b>D</b> irect <b>N</b> umerical <b>S</b> imulation
<i>FFT</i>	<b>F</b> ast <b>F</b> ourier <b>T</b> ransform
<i>FID</i>	<b>F</b> lame <b>I</b> onization <b>D</b> etector
<i>GFD</i>	<b>G</b> eophysical <b>F</b> luid <b>D</b> ynamics
<i>HIT</i>	<b>H</b> omogeneous and <b>I</b> sotropic <b>T</b> urbulence
<i>MLT</i>	<b>M</b> esosphere and <b>L</b> ower <b>T</b> ermosphere
<i>MAARSY</i>	<b>M</b> iddle <b>A</b> tmosphere <b>A</b> lomar <b>R</b> adar <b>S</b> ystem
<i>MMARIA</i>	<b>M</b> ultistatic and <b>M</b> ultifrequency <b>A</b> gile <b>R</b> adar for <b>I</b> nvestigations of the <b>A</b> tmosphere
<i>PBL</i>	<b>P</b> lanetary <b>B</b> oundary <b>L</b> ayer
<i>PDF</i>	<b>P</b> robability <b>D</b> ensity <b>F</b> unction
<i>PMSE</i>	<b>P</b> olar <b>M</b> esospheric <b>S</b> ummer <b>E</b> choes
<i>PSD</i>	<b>P</b> ower <b>S</b> pectral <b>D</b> ensity
<i>SMR</i>	<b>S</b> pecular <b>M</b> eteor <b>R</b> adar
<i>SNR</i>	<b>S</b> ignal-to- <b>N</b> oise <b>R</b> atio
<i>VHF</i>	<b>V</b> ery <b>H</b> igh <b>F</b> requency
<i>VSHW</i>	<b>V</b> ertically <b>S</b> heared <b>H</b> orizontal <b>W</b> ind



## Chapter 1

# Introduction

The main purpose of this thesis is to characterize properties and physical characteristics of stratified turbulence in geophysical flows, by means of a combined approach that makes use of numerical simulations, theoretical modeling and observations. In particular, numerical experiments have been performed through the integration of the Navier-Stokes equations in the Boussinesq approximation, a framework suitable for the investigation of geophysical turbulence in presence of gravity waves. Theoretical models were also developed to interpret the outcome of the simulations and observations of the stratified upper atmosphere have been utilized to confirm the existence of extreme phenomena developing in stratified flows, here characterized for the first time in a systematic and rigorous manner. Finally a preliminary investigation of the transport of a passive scalar in homogeneous and isotropic turbulent flows was developed in preparation to future (numerical and laboratory) experiments aiming at characterizing the dynamics of scalars in stratified flows developing extreme velocity fluctuations.

Turbulence is ubiquitous in nature. It plays a major role in determining the properties of fluids, being responsible of phenomena such as of the weakening of the flow rate in a pipeline, the enhancement mixing as well as of the opposite effect, namely the trapping of tracers under some specific conditions. However, turbulence also influences the properties of complex fluids, like liquid crystals, or the superfluids (e.g. the so called Bose-Einstein Condensates), many geophysical and astrophysical contexts (atmosphere, oceans, Earth's interior, Solar and Stellar atmospheres, the Solar Wind, the interstellar medium, and many others).

The main features of turbulence are rather well known for homogeneous and isotropic flows, thanks to the seminal works of Richardson [61] and, subsequently, Obukov [52] and Kolmogorov [33]. The first postulated that the transfer of energy in turbulent motions happens because large-scale, energy-containing, “eddies” interact among them due to the nonlinearities of the fluid, by producing smaller eddies, to which part of the energy is transferred. This process goes on until a considerable amount of energy is transferred from the largest eddies to the ones for which the dissipative phenomena become important, thus determining a continuous process of “cascade” of energy from the largest scales, at which the energy itself is injected, to the scales where it can be efficiently dissipated. The mathematical nature of this energy transfer was explained separately in 1941 by Obukhov (through closure arguments) and Kolmogorov, in its celebrated 1941 theory (K41). In the latter, Kolmogorov established that, under the hypothesis of incompressibility, homogeneity and isotropy of the flow, along with the assumption that the energy flux  $\Pi_\ell$  across the different scales  $\ell$  happens at a constant rate, some theoretical scaling relations regarding the way in which energy is distributed among the different scales in the form:

$$E(k) \sim \varepsilon^{2/3} k^{-5/3} \quad (1.1)$$

where  $E(k)$  is the energy on a wave-vector  $k = 2\pi/\ell$  and  $\varepsilon$  the rate of energy dissipation (that is the energy flux  $\Pi_\ell$  for a vanishing viscosity). Therefore, the energy cascade in incompressible, homogeneous and isotropic, turbulence happens by injecting energy to the flow at larger scales; such energy is afterwards transferred to smaller and smaller scales (according to Richardson's phenomenology) following Kolmogorov's law (1.1), and subsequently dissipated at a scale at which the viscosity of the fluid is effective:

$$\eta = \left( \frac{\nu^3}{\varepsilon} \right)^{1/4},$$

$\nu$  being the kinematic viscosity of the flow (ratio between the dynamic viscosity and the constant density of the fluid). The quantity  $\eta$  is called the Kolmogorov length scale, or dissipation scale.

Kolmogorov's fifth-third law (1.1) basically implies a "self-similarity" in the distribution of the energy across the different scales involved in the turbulent cascade. This means that, when magnifying the plot of a turbulent signal (for instance a component of the velocity field at a given point as a function of time) at different scales, one should always find a structure of the signal which resembles itself independently of the magnifying scale. However, such a behaviour is not actually found in all situations. For instance, Batchelor and Townsend (1949) observed that when deriving a turbulent signal, it became more and more "bursty" with increasing order of differentiation. Such phenomenon, later called "intermittency", indicates that the energy transfer and dissipation at smaller scales is indeed not continuous, but it happens in bursts, alternating with quiet periods, in which no dissipation occurs.

Turbulence and intermittency play a fundamental role in Geophysical Fluid Dynamics (GFD), which is the subject of the present thesis work. Both the atmosphere and the oceans are fluids in which the viscosity is so small that they can be considered in a fully developed turbulent state. However, a basic difference with respect to homogeneous, isotropic, turbulent (HIT) fluids is that in the case of the atmosphere and oceans the presence of the gravity induces a stratification in density, pressure and temperature, namely there is an anisotropy direction. Moreover, Earth's rotation produces a further source of both inhomogeneity and anisotropy, which make the problem harder to treat starting from the known Kolmogorov's theory obtained in the HIT case. At the same time, this phenomenology introduces a huge amount of richness to the dynamics of such flows.

An important difference between turbulence and intermittency in the HIT case and in the GFD case lies in the fact that observations indicate that intermittency, in the atmosphere and oceans, can take place not only at the dissipative scales but also at large scales [12, 39]. This result has been confirmed in the numerical simulations carried out during this thesis work. In fact, I found that large excursions (hereinafter called "drafts") in the vertical component of the velocity and in the temperature fields are observed in the numerical simulations of the Navier-Stokes turbulence in Boussinesq approximation, for a range of parameters (Froude number, ratio between the inertial and gravity characteristic scales) of geophysical interest. The presence of such drafts and their dynamics have been subsequently confirmed by the direct observation of an event with similar characteristics in the mesosphere of the Earth [10].

The outline of the thesis is the following. In the rest of this introductory chapter, I describe in detail the equations that are numerically solved, that is the incompressible Navier-Stokes equation in the Boussinesq approximation, along with the equations that describe the evolution of temperature. Then, I give a more in-depth description of the phenomenology of homogeneous, isotropic, turbulence and intermittency, along

with the basic statistical tools that are used to describe those phenomena, essentially in terms of Probability Density Functions (PDFs) and moments at various orders. After that, I provide some details on anisotropic turbulence and the definition of the governing parameter of stratification and rotation. Finally, I briefly describe the different tools used in the present investigation of stratified turbulence: the Geophysical High Order Suite for Turbulence (GHOST) code, through which the numerical simulations have been carried out very efficiently, the ground-based observational tools that have been used to detect an event in the Mesosphere and Lower Thermosphere (MLT) with characteristics similar to the large-scale drafts I found in the numerical simulations and finally the wind tunnel through which the laboratory measurements have been obtained, that have been subsequently compared with the results of the numerical experiments performed to characterize the transport of a passive scalar.

Each chapter, from the second on, is structured with an introduction, in which the different science cases the journal articles deal with are presented, the main motivations for our study are discussed and the main results briefly summarized with the help of plots and figures. Then the articles concerning those specific issues are proposed in the manuscript, to present all the results in detail.

In the second chapter, I present two articles dealing with the study of mixing and dissipation for both a purely stratified fluid and flows in presence of both rotation and stratification. In the first article, the evidence for the existence of large-scale intermittency in stratified fluids is presented, in a range of Froude numbers of geophysical interest, and a connection between the presence of the drafts and the mixing and dissipative properties of the fluid is provided [16]. Most important is that a simple reduced model, capable of reproducing the dynamics of the observed dependency of the drafts on the competition between turbulence and gravity waves is derived from the Navier-Stokes equations. This work was conceived during the preparation of the research project used to apply for the fellowship that supported me throughout the entire duration of my PhD program. In the second article, the effects of rotation, along with the presence of dissipation, are considered. In both articles, the investigations are carried out in terms of both the Eulerian velocity and temperature fields and a Lagrangian description, based on the motion of Lagrangian particles in the flow (also simulated with GHOST). Therefore, a detailed study of the diffusive properties of such Lagrangian tracers is performed [7].

In the third chapter, I present an observation, made through ground-based instruments, of an extreme vertical draft in the MLT [10]. This observation shares many different characteristics, discussed in details in the chapter, with the intense vertical drafts in the velocity field observed in the numerical simulations. Moreover, I propose a possible connection between the appearance of the drafts and the presence of vertical shears in the horizontal velocity field.

In the fourth chapter, I show that a link exists between the small-scale intermittency, typical of the HIT case, and the large-scale intermittency, characterized by the drafts discussed in chapter one. An important finding of this chapter will be that the kurtosis of the small-scale velocity field as a function of the Froude number follows a very similar behaviour (albeit with smaller values) to that of the large-scale vertical velocity and temperature. Moreover, I will show as large-scale drafts enhance the small-scale intermittency [15].

In the fifth chapter, I compare some measurements of the diffusion of a passive scalar, taken in a wind tunnel, with the numerical simulation of the same quantity in a HIT case [53]. I will show how the laboratory measurements not only agree very well with the numerical results in terms of the standard deviations of the concentration of the passive scalar, but also that both results evidence as the gamma distribution is a

suitable model to describe the evolution in time of the PDFs of the concentration. This work was conducted in preparation for an extensive investigation of the dispersion of passive scalar in a stratified environment to be carried out in the near future.

Finally, in the last chapter, I draw some conclusions about the findings obtained in the different articles.

## 1.1 The Navier-Stokes equations

The motion of a viscous, hence real, newtonian fluid is described through the Navier-Stokes equations. They are based on Newton's second law and relate the fluid acceleration to the surface and body forces experienced by the fluid. Surface forces are usually of molecular origin and are described by a stress tensor. Body forces, instead, for neutral fluids, can be for instance gravity, the centrifugal force and the Coriolis force. The Navier-Stokes equations can be written as:

$$\partial_t \mathbf{u} + \mathbf{u} \cdot \nabla \mathbf{u} = \frac{1}{\rho} \nabla \cdot \overset{\leftrightarrow}{P} + \frac{\mathbf{F}}{\rho} \quad (1.2)$$

where  $\mathbf{u}$  is velocity field,  $\rho$  is the mass density of the flow,  $\overset{\leftrightarrow}{P}$  is the stress tensor and  $\mathbf{F}$  contains the body forces. The stress tensor  $\overset{\leftrightarrow}{P}$  quantifies the stress acting in the  $x_j$  direction on the unit area surface normal to  $x_i$ . In the general case it has the form:

$$P_{ij} = -p\delta_{ij} + p_{ij} \quad (1.3)$$

where  $p$  is the isotropic pressure at  $x_i$  when there is no strain.

$$p_{ij} = \mu \left( \frac{\partial u_i}{\partial x_j} + \frac{\partial u_j}{\partial x_i} \right) + \frac{2}{3} \mu \frac{\partial u_k}{\partial x_k} \delta_{ij}, \quad (1.4)$$

is the viscous stress tensor,  $\mu$  being the coefficient of viscosity.

Eqs. 1.2 are usually coupled with the continuity equation for the mass:

$$\partial_t \rho + \nabla \cdot (\rho \mathbf{u}) = 0, \quad (1.5)$$

and with an equation for the energy:

$$\rho \partial_t (c_V \theta) + \rho (\mathbf{u} \cdot \nabla) (c_V \theta) = \kappa \nabla^2 \theta - p \nabla \cdot \mathbf{u} + \Phi \quad (1.6)$$

where  $\theta$  is the temperature,  $c_V$  is the specific heat at constant volume,  $\kappa$  is the coefficient of heat conduction and  $\Phi$  represents the energy dissipated due to viscosity. However these equations do not form a closed system, and it is at this point that an approximation is needed. One possible way to close the system is through an equation of state. In the specific case of convective fluids, a reasonable equation of state is given by:

$$\rho = \rho_0 [1 - \alpha(\theta - \theta_0)] \quad (1.7)$$

where  $\alpha$  is the coefficient of volume expansion and  $\theta_0$  is the temperature at  $\rho = \rho_0$ . Eq. 1.7 describes the changes in density due to temperature and derives from the first Gay-Lussac's law.

For incompressible flows (i.e. assuming that  $\rho$  is a constant), the continuity equation (Eq. 1.5) reduces to:

$$\nabla \cdot \mathbf{u} = 0 \quad (1.8)$$

and  $p_{ij}$  assumes the simpler form:

$$p_{ij} = \mu \left( \frac{\partial u_i}{\partial x_j} + \frac{\partial u_j}{\partial x_i} \right). \quad (1.9)$$

Substituting  $p_{ij}$  in Eqs. 1.2 leads to:

$$\partial_t \mathbf{u} + (\mathbf{u} \cdot \nabla) \mathbf{u} - \nu \nabla^2 \mathbf{u} = -\frac{1}{\rho} \nabla p + \frac{\mathbf{F}}{\rho} \quad (1.10)$$

where  $\nu = \frac{\mu}{\rho}$  is the kinematic viscosity of the flow. An incompressible flow can then be described by the system:

$$\begin{cases} \partial_t \mathbf{u} + (\mathbf{u} \cdot \nabla) \mathbf{u} - \nu \nabla^2 \mathbf{u} = -\frac{1}{\rho} \nabla p + \frac{\mathbf{F}}{\rho} \\ \rho \partial_t (c_V \theta) + \rho (\mathbf{u} \cdot \nabla) (c_V \theta) = \kappa \nabla^2 \theta + \Phi \\ \rho = \rho_0 [1 - \alpha (\theta - \theta_0)] \\ \nabla \cdot \mathbf{u} = 0. \end{cases} \quad (1.11)$$

## 1.2 The Boussinesq approximation

In the Boussinesq approximation, it is assumed that variations of density are small. Thus, in the inertial terms, and in the continuity equation, the density  $\rho$  can be considered constant. However, even weak density variations are relevant in buoyancy, and so the variations of density in the buoyancy term  $\rho g$  are not negligible. The dynamics of a stably stratified incompressible fluid subjected to a stable background mass density stratification due to gravity can then be described by the Boussinesq equations, which are obtained from the equations in 1.11 as described in [9]:

$$\partial_t \mathbf{u} + (\mathbf{u} \cdot \nabla) \mathbf{u} = -\frac{1}{\rho_0} \nabla p + \left( 1 + \frac{\delta \rho}{\rho_0} \right) \mathbf{F} + \nu \nabla^2 \mathbf{u} \quad (1.12)$$

$$\partial_t \theta + \mathbf{u} \cdot \nabla \theta = \kappa \nabla^2 \theta \quad (1.13)$$

$$\delta \rho = -\rho_0 \alpha (\theta - \theta_0) \quad (1.14)$$

$$\nabla \cdot \mathbf{u} = 0. \quad (1.15)$$

## 1.3 The Lagrangian approach

Two different points of view can be used in fluid theory to investigate the behaviour and the properties of flows: the Eulerian approach and the Lagrangian approach. The Navier-Stokes equations, presented in the previous section, are derived in the Eulerian approach, where the observer focuses on the specific volume occupied by the fluid at a given instant of time and describes how dynamical quantities (i.e. velocity, pressure, etc.) change pointwise due to the transit of different infinitesimally small regions of fluid, known as fluid parcels. At a given time, these quantities can change because different parcels of fluid transit by the same point. In the Lagrangian approach, instead, the observer “follows” a single fluid parcel or Lagrangian particle, which is considered pointlike and massless, as it moves in the flow with the local fluid velocity. Within this approach, the velocity field is no longer described as a pointwise quantity evolving in time, but can be mapped and characterized by means of Lagrangian particles exploring the domain flow, namely by their velocity and acceleration. The position of each Lagrangian particle at every  $t$  defines its trajectory which is described by the



equations:

$$\begin{cases} \partial_t \mathbf{X}(\mathbf{X}_0, t) = \mathbf{u}(\mathbf{X}(\mathbf{X}_0, t), t) \\ \mathbf{X}(\mathbf{X}_0, t_0) = \mathbf{X}_0 \end{cases} \quad (1.16)$$

where  $\mathbf{X}_0$  is the position of the particle at  $t = t_0$ , often called Lagrangian coordinate or material coordinate, and  $\mathbf{u}(\mathbf{x}, t)$  is the Eulerian velocity field. For a given  $\mathbf{u}(\mathbf{x}, t)$ , Eq. 1.16 can be integrated backward and forward in time to obtain the position of the Lagrangian particle at every  $t$ . This approach is useful, for instance, when studying how a polluting agent disperses in the air. The Lagrangian velocity field  $\tilde{\mathbf{u}}(\mathbf{x}, t)$  is related to the Eulerian one by:

$$\tilde{\mathbf{u}}(\mathbf{X}_0, t) = \mathbf{u}(\mathbf{X}(\mathbf{X}_0, t), t) \quad (1.17)$$

For a fixed value of  $\mathbf{X}_0$ , every  $\mathbf{X}(\mathbf{X}_0, t)$  defines the trajectory of a given Lagrangian particle in the  $x - t$  space. This approach will be used later to characterize particle dispersion in presence of stratification and rotation.

## 1.4 Turbulence and its properties

Most of the flows in nature are turbulent. A typical way in which turbulent flows originate is when instabilities start growing in a laminar, unstable, flow. These instabilities are related to the interactions of the viscous term and the non-linear term in the Navier-Stokes equations (Eqs. 1.10) and they start growing at high Reynolds numbers. The Reynolds number, defined as  $Re = \frac{UL}{\nu}$ , where  $U$  is the characteristic velocity of the flow,  $L$  its characteristic length scale and  $\nu$  its kinematic viscosity, is a dimensionless number that describes how turbulent is the fluid [60]. It can be obtained by computing the ratio of the non-linear term and the viscous term in the Navier-Stokes equations (Eqs. 1.10). As such, if the viscous term prevails over the non-linear one, viscous effects dominate the flow which will then remain laminar, not developing turbulence. On the other hand, if the non-linear term prevails over the viscous one then the instabilities in the flow will grow and it will become turbulent. At low  $Re$  the flow is laminar. At high  $Re$  the flow becomes irregular and chaotic due to the instabilities (Fig. 1.1).

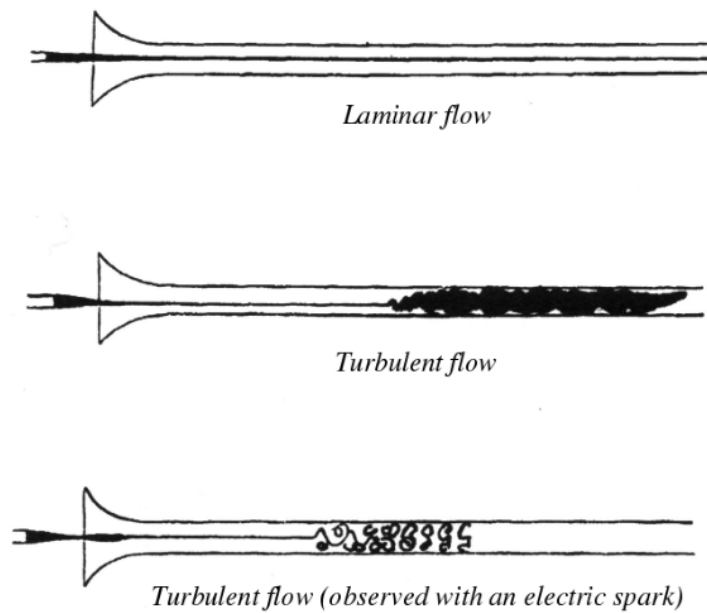


FIGURE 1.1: *Original sketches made by O. Reynolds during his studies on turbulence. Image taken from wikipedia.org*

Turbulent flows have different characteristics than laminar. The most significant one is the apparent randomness of these flows. In turbulent flows quantities like velocity, density, pressure and temperature fluctuates in time and space. This means, for instance, that when these quantities are measured in turbulent flows experiments, they will not always have the same values, even under the same set of conditions. This property of turbulent flows is of utter importance, as Navier-Stokes equations are deterministic and should be able to describe exactly all the properties of the flow. Actually, a solution of the Navier-Stokes equation for turbulent flows has not been derived yet, These equations do not allow to properly predict the state of the system. A possible way to deal with the apparent randomness of turbulent flows is through the use of statistics, as discussed in the next section. Another important property is the capability of turbulent flows to transport and mix fluid in a more efficient way than the laminar ones. Turbulence increases momentum, heat and mass transfer.

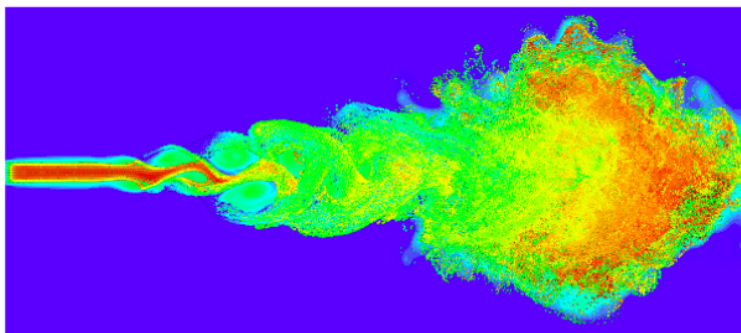


FIGURE 1.2: *Development of turbulent flow in a jet. Image taken from mriquestions.com*

## 1.5 Statistical description

### 1.5.1 The probability density function

As already said in section 1.4, one of the main properties of turbulent flows is that quantities like velocity, density, pressure and temperature are randomly fluctuating at every point in space. But, despite the randomness of these variables, under the same initial conditions, while their values may be different with every measurement, their statistical properties are not. Due to this, instead of focusing on the single value assumed by these quantities, what is considered is their probability density function (PDF). The probability density function of a random variable  $x \in D$ , where  $D$  is the (continuous) set of possible values that the variable  $x$  can assume, is defined as:

$$P(x) = \frac{dF(x)}{dx} \quad (1.18)$$

where  $F(X)$  represents the ‘‘cumulative probability’’, namely the probability that the variable  $x$  has to assume values smaller than  $X$ . The cumulative probability must respect the conditions:

- $F(X \notin D) = 0$ , that is the probability of an event not belonging to the domain  $D$  is vanishing;
- the cumulative probability function is always increasing, that means that it is always:  $P(x) \geq 0$ ;

- $$\int_D P(x)dx = 1 \quad (1.19)$$

that is, the probability is normalized to 1.

This means that the cumulative probability function is a non-decreasing function always assuming values between 0 and 1. The probability density function of a given random variable tells how much is the probability to obtain, for that variable, a value between  $x$  and  $x + dx$ .

### 1.5.2 The moments of a random variable

For a random variable  $x$ , its mean value (or expectation value) is given by:

$$\mu_x = \langle x \rangle = \int_D xP(x)dx \quad (1.20)$$

If  $\langle u \rangle$  is equal to 0 the variable  $x$  is said to be ‘‘centered’’.

$\langle u \rangle$  is also known as the first moment of the random variable  $x$ .

In general, the moment of  $n$ -th order for the random centered variable  $x$  is defined as:

$$\langle u^n \rangle = \int_D x^n P(x)dx \quad n \in N \quad (1.21)$$

If the random variable  $x$  is centered, its second moment, defined as:

$$\sigma_x^2 = \langle x^2 \rangle = \int_D x^2 P(x)dx, \quad (1.22)$$

is known as “variance” of  $x$ . The variance is a measure of dispersion of the possible values of the random variable around the expected value. The square root of the variance,  $\sigma_u$ , is called standard deviation.

The third moment of a centered random variable:

$$S_u = \int_D x^3 P(x) dx \quad (1.23)$$

is known as the skewness. The skewness is a measure of the asymmetry of the probability distribution of the random variable with respect to its mean. A negative value of the skewness indicates that the tail on the left side of the PDF is longer or fatter than the right side. Conversely, a positive value of the skewness indicates that the tail on the right side is longer or fatter than the left side (Fig. 1.3).

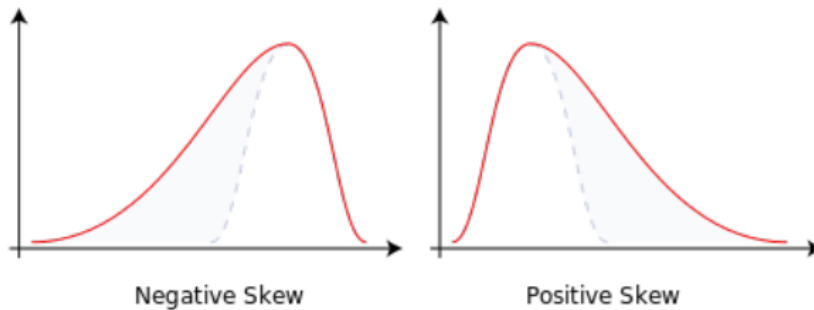


FIGURE 1.3: An example of a distribution with a negative skewness (left) and with a positive skewness (right). Image taken from wikipedia.

The fourth moment for a centered random variable:

$$F_x = \int_D x^4 P(x) dx \quad (1.24)$$

is known as the kurtosis or flatness. Like the skewness, the value of the kurtosis gives information on the shape of a PDF. Since kurtosis is the average of the standardized data (i.e. the data divided by its standard deviation) raised to the fourth power, the contribution to the kurtosis of any standardized values less than  $1\sigma$  is negligible. Values higher than  $1\sigma$ , instead, contribute in a more significant way to the kurtosis. Thus, a higher value of the kurtosis means that the tails of the PDF extend more than those of a PDF with a lower kurtosis.

In this work, the quantity referred to as kurtosis is the fourth order moment of a given variable normalized by its standard deviation:

$$K_x = \frac{F_x}{(\sigma_x^2)^2} = \frac{\int_D x^4 P(x) dx}{[\int_D x^2 P(x) dx]^2} \quad (1.25)$$

### 1.5.3 The normal distribution

The normal distribution, also called Gaussian distribution, is a particular probability density function. The form of a Gaussian distribution for a variable  $x$  is the following:

$$f(x, \mu, \sigma) = \frac{1}{\sqrt{2\pi\sigma^2}} e^{-\frac{(x-\mu)^2}{2\sigma^2}} \quad (1.26)$$

where  $\mu$  is the mean value of  $x$  and  $\sigma$  its standard deviation. The case where  $\mu = 0$  and  $\sigma = 1$  is called standard normal distribution. In this case, the Gaussian distribution becomes:

$$f(x, \mu, \sigma) = \frac{1}{\sqrt{2\pi}} e^{-\frac{x^2}{2}} \quad (1.27)$$

Fig. 1.4 shows the shape assumed by a Gaussian distribution for different values of  $\mu$  and  $\sigma$  (do note that the  $y$  axis is in log scale).

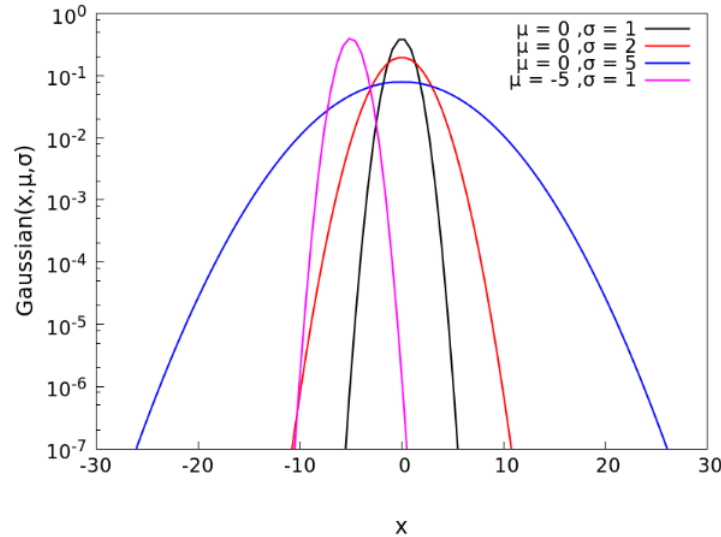


FIGURE 1.4: Examples of Gaussian distributions of the random variable  $x$  with different values of  $\mu$  and  $\sigma$ .

The Gaussian distribution is also characterized by having a value of the skewness  $S_x = 0$ , along with all its moments of odd order due to parity, and a value of the kurtosis  $K_x = 3$ . The main reason behind the importance of the Gaussian distribution is the central limit theorem. The central limit theorem states that as the sample size  $N$  of a random variable becomes large then the sampling distribution of the means becomes approximately a Gaussian, regardless of the distribution of the original variable, centered around the mean  $\mu$  of the original variable. In addition to this, the standard deviation of the distribution of the means goes with  $\sigma$  as  $\frac{\sigma}{\sqrt{N}}$ .

#### 1.5.4 Random functions

Extending the concept of random variables, a random function is a function, which depends on one or more arbitrary arguments, whose values are defined in terms of a certain experiment and may vary with the outcome of this experiment according to a given probability distribution. It can be seen as a collection of random variables. A probability density function and all the statistical quantities defined in section 1.5.2 can still be defined on random functions.

## 1.6 Homogeneous and isotropic turbulence

An approximation used in many fluid models is to consider the velocity field  $\mathbf{u}(\mathbf{x}, t)$  statistically homogeneous and isotropic. Due to homogeneity, the statistical quantities that characterize the field, are invariant under translations of the reference frame. Due to isotropy, the statistics of  $\mathbf{u}(\mathbf{x}, t)$  is invariant under rotations or reflections.

Turbulence developing in a flow which is both statistically homogeneous and isotropic is called “homogeneous and isotropic turbulence” (HIT).

## 1.7 The K41 theory

One of the first models to describe turbulence was proposed by L. F. Richardson in 1922 [62]. According to his theory, turbulence is made up of eddies which exist at different scales. These eddies were not defined rigorously but indicated a region of turbulent motion with a characteristic length scale  $\ell$ . Each eddy at length scale  $\ell$  has a velocity,  $u(\ell)$ , and a time scale,  $\tau(\ell) = \frac{\ell}{u(\ell)}$ , that depend on the length scale. The eddies with a characteristic length scale  $\ell_0$  comparable to the characteristic length scale of the flow are the largest and were considered unstable by Richardson. Due to their instability, they break up in eddies of a smaller characteristic length scale. This process transfers energy from one scale to the smaller one. The smaller eddies produced in this way break up again and the transfer of energy continues. This process is known as “turbulent cascade” because energy is continuously transferred from the large scale to the small scales as the eddies break up. This energy cascade continues until the local Reynolds number of the eddies becomes small enough (Fig. 1.5).

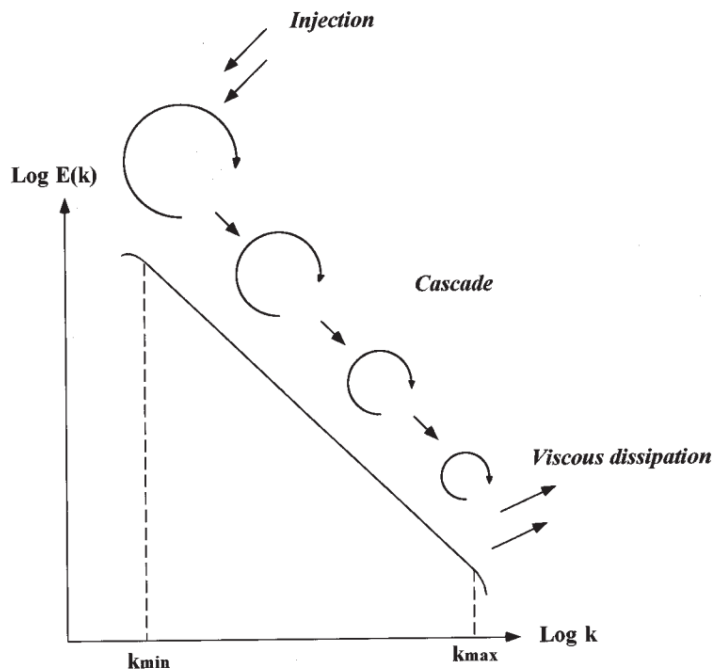


FIGURE 1.5: Schematic representation of the turbulent cascade. Taken from [70].

When this happens, the viscous term of the Navier-Stokes Eqs. 1.10 starts to prevail over the non-linear one, which is responsible for the energy transfer from large to small scales. Since the time scale of the largest eddies is  $\tau_0 = \frac{\ell_0}{u_0}$  and their energy is of order  $u_0^2$ , then the dissipation rate  $\varepsilon$  obtained from this model is of order  $\varepsilon = \frac{u_0^3}{\ell_0}$ . From this model, however, it is not clear what is the scale of the smallest eddies, and, as such, at which scale dissipation occurs, and how  $u(\ell)$  and  $\tau(\ell)$  scale with  $\ell$ .

These questions found a possible answer in the model proposed in 1941 by A. N. Kolmogorov, known today as “Kolmogorov theory” or “K41 theory” [33]. Kolmogorov formulated three hypotheses to build his model, which is a more refined version of the

Richardson's one. One of his hypotheses, known as the "local isotropy hypothesis", states that if  $Re$  is large enough the flow is statistically isotropic at small scales ( $\ell \ll \ell_0$ ). This means that the turbulent flow, which may be anisotropic at large scales, becomes more and more isotropic at smaller scales. The other hypothesis, known as Kolmogorov's first similarity hypothesis, states that if  $Re$  is large enough the statistics at small scale depends only on the viscosity  $\nu$  and on the dissipation  $\varepsilon$ . From these two quantities a length scale, a time scale and a characteristic velocity can be formed. They are  $\eta = (\frac{\nu^3}{\varepsilon})^{\frac{1}{4}}$ ,  $\tau_\eta = (\frac{\nu}{\varepsilon})^{\frac{1}{2}}$  and  $u_\eta = (\nu\varepsilon)^{\frac{1}{4}}$  respectively and are known as the Kolmogorov scales. At that scale, the Reynolds number, built with the length and velocity of the eddies, is equal to 1:

$$Re = \frac{u(\eta)\eta}{\nu} = \frac{(\nu\varepsilon)^{\frac{1}{4}}(\frac{\nu^3}{\varepsilon})^{\frac{1}{4}}}{\nu} = 1 \quad (1.28)$$

From Eqs. 1.28 it is clear that this scale is the one of the smallest eddies, at which dissipation occurs. This happens because  $Re$  is small enough so that dissipative effects start to become more important than the non-linear ones. From the definition of the Kolmogorov scales,  $\eta$ ,  $\tau_\eta$  and  $u_\eta$ , the ratio of the smallest scale to the largest one can be determined:

$$\begin{cases} \frac{\eta}{\ell_0} \sim \left(\frac{\nu^3}{\varepsilon}\right)^{\frac{1}{4}} \frac{1}{\ell_0} \sim \left(\frac{\nu^3 \ell_0}{u_0^3}\right)^{\frac{1}{4}} \frac{1}{\ell_0} \sim \left(\frac{\nu}{u_0 \ell_0}\right)^{\frac{3}{4}} \sim Re^{-\frac{3}{4}} \\ \frac{\tau_\eta}{t_0} \sim \left(\frac{\nu}{\varepsilon}\right)^{\frac{1}{2}} \frac{1}{t_0} \sim \left(\frac{\nu \ell_0}{u_0^3}\right)^{\frac{1}{2}} \frac{1}{t_0} \sim \left(\frac{\nu}{u_0^2 \ell_0}\right)^2 \sim Re^{-\frac{1}{2}} \\ \frac{u_\eta}{u_0} \sim \frac{(\nu\varepsilon)^{\frac{1}{4}}}{u_0} \sim \left(\frac{\nu}{u_0 \ell_0}\right)^{\frac{1}{4}} \sim Re^{-\frac{1}{4}} \end{cases} \quad (1.29)$$

From the Eqs. 1.29 it follows that, at sufficiently high  $Re$ , the time scale and the velocity of the smallest eddies are small compared to the characteristic ones of the flow or to those of the largest eddies. If the separation of the scale is this large, it must exist a scale  $\ell$  much larger than  $\eta$  but, at the same time, much smaller than  $\ell_0$ , such that:

$$\eta \ll \ell \ll \ell_0 \quad (1.30)$$

Then, due to  $\ell \gg \eta$ , at this scale  $Re$  should still be high enough and dissipative effects can be neglected. The properties of the flow do not depend on  $\nu$  at this scale. From this consideration and from the first similarity hypothesis it comes the second similarity hypothesis which states that if  $Re$  is large enough then it exists a scale  $\ell$ , where  $\eta \ll \ell \ll \ell_0$ , such that at this scale the properties of the flow do not depend on  $\nu$  but are only determined by  $\varepsilon$ . All the values of  $\ell$  that satisfy this property are part of what is known as the inertial subrange. In this subrange all the properties of the flow are determined only by  $\varepsilon$ , as both dissipation and energy injection are negligible. This subrange is therefore delimited by  $\ell_{EI}$ , at which energy injection becomes relevant, and by  $\ell_{DI}$ , at which dissipation is not negligible anymore. If the rate at which energy is transferred,  $T$ , in the inertial subrange is considered this will be given by:

$$T \sim \frac{u^2(\ell)}{\tau(\ell)} \sim (\varepsilon\ell)^{\frac{2}{3}} \left(\frac{\varepsilon}{\ell^2}\right)^{\frac{1}{3}} = \varepsilon \quad (1.31)$$

which means that through the whole inertial subrange the rate at which energy is transferred is constant and is equal to  $\varepsilon$ . From the hypotheses in this model it also follows that the distribution of the energy in the inertial range gives a spectrum that follows a  $-\frac{5}{3}$  power law. Another consequence of the Kolmogorov's hypotheses is that in the inertial subrange, structure functions follow a power-law with a constant

exponent  $\zeta_p$  for any order  $p$  considered:

$$S_p(\ell) = \langle \delta u^p(\ell) \rangle \propto \ell^{\zeta_p} \quad (1.32)$$

where  $\delta u$ :

$$\langle \delta u^p(\ell) \rangle = \langle [u(x + \ell) - u(x)]^p \rangle. \quad (1.33)$$

Structure functions quantify the correlations of velocity in different measuring points.

## 1.8 Stratified turbulence

The term “stratified turbulence” was coined by the meteorologist D. K. Lilly for fully three-dimensional turbulence in which turbulent motion in the vertical is constrained by gravity. A question central to research in this flow regime is how much of classical turbulence theory applies to stratified turbulence. In predicting weather, for instance, the classical turbulence models are not always applicable. This happens because, due to the stratification, the dynamics is different compared to the homogeneous and isotropic case. Indeed, stratified flows support the propagation of waves known as “internal gravity waves” which coexist with turbulence. The frequency at which these waves propagate has an upper limit,  $N$ , known as the Brunt-Väisälä frequency, which depends on the gravity acceleration  $g$ , the density gradient  $\frac{\partial \rho(z)}{\partial z}$  and the average density  $\rho_0$ :

$$N = \sqrt{-\frac{g}{\rho_0} \frac{\partial \rho(z)}{\partial z}}. \quad (1.34)$$

Thus, turbulence has to compete with waves in transferring energy across the scales. In stratified flows gravity contrasts vertical motions of turbulent eddies larger than a given size called the Ozmidov length, defined as the square root of the ratio between the dissipation rate of turbulent kinetic energy  $\varepsilon$  and the third power of the Brunt-Väisälä frequency  $N$ :

$$\ell_{Oz} = \sqrt{\frac{\varepsilon V}{N^3}} \quad (1.35)$$

At scales smaller than  $\ell_{Oz}$ , stratification effects become almost negligible.

Several mechanisms can cause turbulence in stratified flows, such as Kelvin-Helmholtz instabilities. These can occur when there is a velocity shear, or where there is a velocity difference across the interface between two fluids. An important parameter is the gradient Richardson number  $Ri$  defined by:

$$Ri = N \left( N - \frac{\partial \theta}{\partial z} \right) \left( \frac{\partial u_{\perp}}{\partial z} \right)^{-2} \quad (1.36)$$

where  $N$  is the Brunt-Väisälä frequency,  $\theta$  is the potential temperature (expressed in units of velocity),  $\frac{\partial \theta}{\partial z}$  is the imposed temperature stratification of the flow and  $u_{\perp}$  the perpendicular velocity with respect to the gravity. The Richardson number measures both the gravitational stability of the stratification and the dynamical competition with the mean shear. When  $Ri < 0$ , if the Reynolds number  $Re$  is high enough, convective turbulence arises in the flow. When  $0 \leq Ri \leq \sim 1$  at high  $Re$  the flow will be a type shear turbulence. On the other hand, if  $Ri \gg 1$  turbulence is different from both these regimes and is referred to as “stratified turbulence”.

Another relevant quantity in stratified flows is the Froude number  $Fr$ . The Froude number is a dimensionless parameter used to quantify how strong is the influence of gravity on the flow. The lower the value of  $Fr$ , the stronger is the level of stratification



of the flow. It is defined as:

$$Fr = \frac{U}{\sqrt{gL}} \quad (1.37)$$

where  $U$  is the characteristic velocity of the flow,  $L$  its characteristic length and  $g$  is the gravitational acceleration.

The buoyancy Reynolds number  $R_B = Re Fr^2$  measures the relative strength of buoyancy to dissipation and is commonly used to identify regimes where waves ( $R_B < 10$ ) or turbulence ( $R_B > 10^2$ ) dominate [5]. An alternative definition of the buoyancy Reynolds number is also given by  $R_{IB} = \frac{\varepsilon_V}{\nu N^2}$ , where  $\varepsilon_V$  is the mean dissipation rate of turbulent kinetic energy and  $\nu$  is the kinematic viscosity. This definition of the buoyancy Reynolds is linked to the previous one through  $\beta = \frac{\varepsilon_V L}{U^3}$ . In fully developed turbulence,  $\beta$  is expected to be constant [29]. However, it has been shown that  $\beta$  depends on the strength of stratification [56].

## 1.9 Rotating turbulence

Another effect that can introduce anisotropy in a flow is rotation. Similarly to purely stratified turbulence, the anisotropy stemming from rotation allows for the propagation of waves, which, in this case, are known as inertial waves. These waves propagate with the Coriolis frequency:  $f = 2\Omega \cos\phi$ , where  $\Omega$  is the rotation rate of the flow and  $\phi$  is the angle between the axis of rotation and the direction of the wave.

The governing parameter of rotation, the Rossby number  $Ro$ , can be defined as:

$$Ro = \frac{U}{\Omega L}, \quad (1.38)$$

where  $U$  and  $L$  are the characteristic velocity and length scale of the flow. The lower  $Ro$  the stronger the effect of rotation.

Even in this case, a scale after which the effects of rotation are negligible and isotropy is recovered exists. This scale is known as the Zeman scale:

$$\ell_\Omega = \sqrt{\frac{\varepsilon}{(2\Omega)^3}}. \quad (1.39)$$

If both rotation and stratification are present the dynamics of the flow becomes significantly more complex, due to the many different governing parameters and scales of the flow. In this case, the Navier-Stokes equations, under the Boussinesq approximation and assuming a constant solid body rotation rate  $\Omega$  with respect to the  $z$  axis, become:

$$\partial_t \mathbf{u} + (\mathbf{u} \cdot \nabla) \mathbf{u} = -\frac{1}{\rho_0} \nabla p - f \hat{z} \times \mathbf{u} + \left(1 + \frac{\delta\rho}{\rho_0}\right) \mathbf{F} + \nu \nabla^2 \mathbf{u} \quad (1.40)$$

$$\partial_t \theta + \mathbf{u} \cdot \nabla \theta = \kappa \nabla^2 \theta \quad (1.41)$$

$$\delta\rho = -\rho_0 \alpha (\theta - \theta_0) \quad (1.42)$$

$$\nabla \cdot \mathbf{u} = 0. \quad (1.43)$$

An important parameter when both rotation and stratification are present in the flow is the ratio of  $Fr$  to  $Ro$ . This ratio provides a measure of the relative strength of stratification to rotation. Typical values of  $Fr/Ro$  observed are of order 10 in the ocean [21, 49] and of order 100 in the stratosphere.

## 1.10 Intermittency in turbulence

Self similarity of the velocity field in the inertial range is one of the focal points of the K41 theory. Although the Navier-Stokes equations (Eqs. 1.2) are deterministic, the strong sensitivity to initial conditions and the non-linear amplification of noise allow us to consider values of the velocity in a flow (as a function of space or time) as a fluctuating signal, which varies largely in different realizations of the same experiment. Portions of this signal have different local properties, however they are characterized by similar statistical features that can be used to describe the dynamics of turbulence in fluids. In this section the velocity field of a turbulent flow is considered as a random function and the definition of self-similar and intermittent function will be given as well. A random function is called self-similar if the signal obtained by delimiting it in a window has the same statistical properties as the function in the entire domain (Fig. 1.6, left panel). On the contrary, if the statistical properties of a signal depend on where the window is located or on its size then the function is said to be “intermittent”. An intermittent function displays activity only in a fraction of its temporal domain. Intermittency can be quantified for a stationary random function  $x(t)$  by applying a

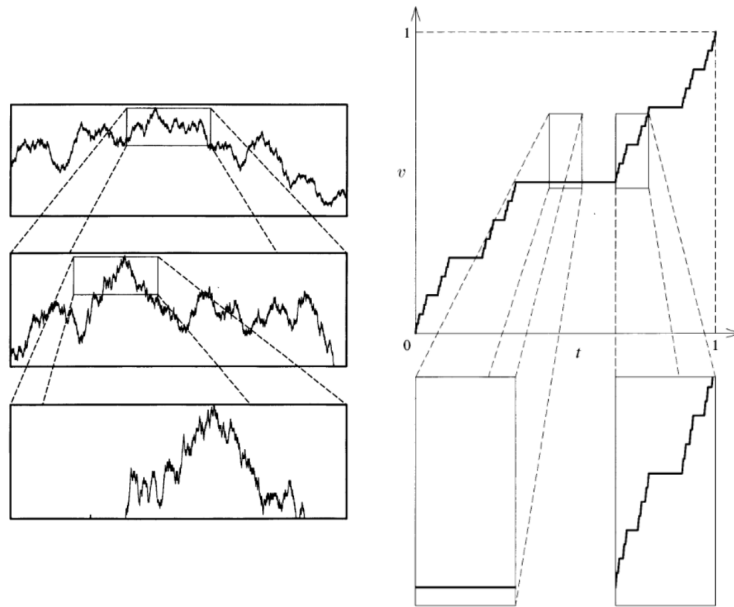


FIGURE 1.6: *Brownian motion curve, enlarged twice, showing self similarity (left panel) and the “Devil’s staircase”, an example of an intermittent function (right panel).* [19]

high pass filter on the signal at a fixed frequency  $\Omega$  and computing non-dimensional ratio of the moments of the random signal obtained,  $u_{>\Omega}(t)$ . Odd order moments are, however, not appropriate since they may vanish because of cancellations due to the symmetry of signal probability density function (PDF). A parameter that can be used to quantify intermittency is the kurtosis of the filtered signal as a function of  $\Omega$ :

$$K_x(t)(\Omega) = \frac{\langle x_{>\Omega}^4(t) \rangle}{[\langle x_{>\Omega}^2(t) \rangle]^2} \quad (1.44)$$

If  $K_u(t)(\Omega)$  grows without bound with the frequency  $\Omega$  then the random function  $x(t)$  is said to be intermittent. For a self-similar signal, which corresponds to a Gaussian

distribution,  $K_x(t)(\Omega)$  does not depend on  $\Omega$ , thus it is not intermittent. In particular, as already stated, the kurtosis of a Gaussian function is always equal to 3.

At large scales, according to the K41 theory, homogeneous and isotropic turbulence is expected to be self-similar. However, when applying a high pass filter to the velocity field of a turbulent flow, if the frequency  $\Omega$  is high enough so that its corresponding length scale is comparable to the Kolmogorov scale  $\eta$ , then turbulence shows traces of an intermittent behaviour. The studies of small-scale intermittency in turbulence originated from Landau's "footnote objection" to the K41 theory who pointed out the dependence of the large-scale energy dissipation over the averaged values of that at small scales. Small-scale intermittency in isotropic and homogeneous turbulence was later discovered by Batchelor and Townsend in 1949 by applying successive derivatives to a turbulent signal [2]. They showed that the signal obtained from turbulence is bursty and intermittent and that the smaller the scale considered the more intermittent the signal. The fact that intermittency was found in the proximity of the dissipative scale did not imply that the K41 theory claim of self similarity was not valid. However the presence of intermittency in the inertial range was questioned in the following years. During the 1980s, several experimental measurements on the fluctuations of the energy dissipation were carried out in order to verify the presence of intermittency in the inertial range, which could have indeed invalidated the K41 theory. Based on the K41 theory, in the inertial range, structure functions follow a power law behaviour and linear relations must be found for the scaling exponent:

$$S_p(\ell) = \langle \delta u^p(\ell) \rangle \propto \ell^{\zeta_p} \quad (1.45)$$

where  $\zeta_p$ , the exponents of the structure functions, scale with  $p$  as:

$$\zeta_p = \frac{p}{3} \quad (1.46)$$

The experiments performed at the time confirmed that in the inertial range structure functions are actually power laws and the scaling obtained for the values of  $\zeta_p$  up to  $p = 18$  was compared to the one expected by the K41 theory. The comparison between the expected value of the K41 theory and the value estimated from the experiments done in that period are shown in Fig. 1.7.

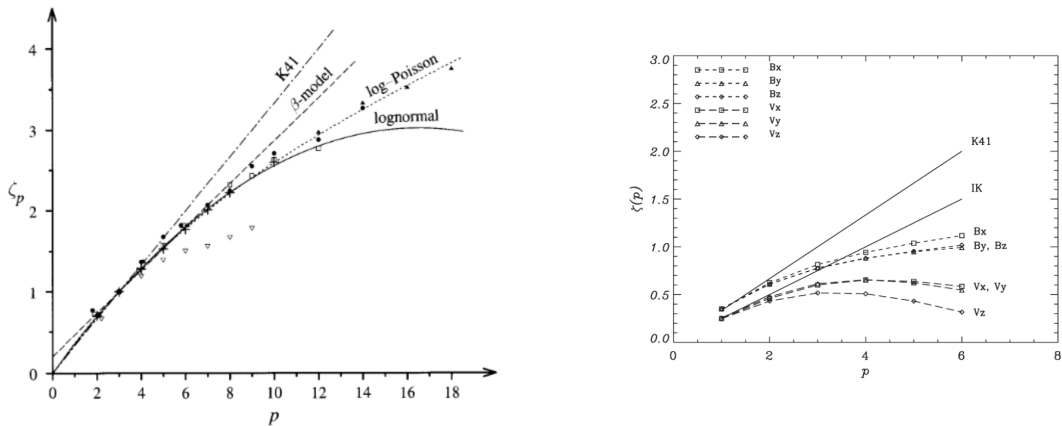


FIGURE 1.7: Left: Scaling exponents  $\zeta_p$  for the  $p^{\text{th}}$  order as a function of  $p$  for the structure functions obtained from the K41 theory, other models and from experiments in homogeneous and isotropic turbulence Right: Scaling exponents of the magnetic field and solar wind velocity components  $B_x$ ,  $B_y$ ,  $B_z$ ,  $V_x$ ,  $V_y$ , and  $V_z$  obtained in the solar wind, taken from [68].

Fig. 1.7 (left panel) shows that there is a discrepancy between the K41 theory and experimental results. This discrepancy is commonly attributed to the presence of intermittency at small scales, which is not taken into account in the K41 theory. These evidences suggested that due to intermittency, not only the dissipation but also the energy transfer rate  $\varepsilon$  in the inertial range must indeed fluctuate and it is not constant as stated in the K41 theory. Later on, the departure of  $\zeta_p$  from the linear scaling expected by the Kolmogorov theory was observed in a large variety of turbulent flows and also in turbulent plasmas. This is the case, for instance, of the solar wind (Fig. 1.7, right panel) [68].

In order to reconcile the theory with the experiments, a new model for turbulence that included intermittency was thus needed. In 1962, Kolmogorov proposed then a refined version of his K41 theory, known as K62 theory [32], that included the influence of small-scale intermittency. In the K62 theory, Kolmogorov stated that the statistical properties of the flow in the range  $r$  such that  $\eta r \ll \ell_0$  is independent of  $\nu$  and does not depend on the mean value of  $\varepsilon$  but on its local average (over the distance  $r$ )  $\varepsilon_r$ . The K62 theory became then the starting point for the future models about fully developed turbulence. The first analytical explanation for the small-scale intermittency was made by Kraichnan in 1967 [34], who has shown that in turbulent flows the intermittent events contain the majority of the energy in the small scales.

## 1.11 Large-scale intermittency

In homogeneous and isotropic turbulent (HIT) flows, intermittency is observed in the small scales, at high Reynolds numbers. In the stratified geophysical flows, as the Earth's atmosphere and the oceans, on the other hand, intermittency is not only present at the small scales, as diagnosed through the PDFs of the velocity gradient, but also at scales comparable to that of the mean flow [12, 40, 39]. In these flows internal gravity waves and turbulence coexist and this results in a scenario that is even more complex than for the HIT case [25, 45, 64, 82]. The influence of intermittency at large scales in stratified turbulent flows is crucial for the development of weather and climate models, as intermittency is usually considered to be at the origin of the extreme events. Despite their low probability of occurrence, the extreme events are those that have more impact on these systems. Several works have highlighted the presence of large-scale intermittency in geophysical flows. For example, in the work by Mahrt [39], data collected by research aircrafts equipped with fast response instrumentation under a variety of atmospheric conditions were analyzed. The data show the presence of two different types of intermittency: the classical intermittency, which occurs at small-scale, and a large-scale intermittency, occurring at scales comparable to that of the mean flow. The estimated value for the kurtosis of the velocity field was, in some cases, exceeding 20.

In the work by D'Asaro et al. [12], vertical velocity measurements obtained by means of Lagrangian floats deployed in the Oregon continental shelf (the submerged portion of a continent) displayed large-scale intermittency. As it can be seen from Fig. 1.8, the PDF of the vertical velocity is non-Gaussian with a calculated kurtosis of 19 [12].

## 1.12 Methodology

This section is devoted to the description of the different tools that have been employed during the PhD research work for the study of the dynamics of stratified turbulent

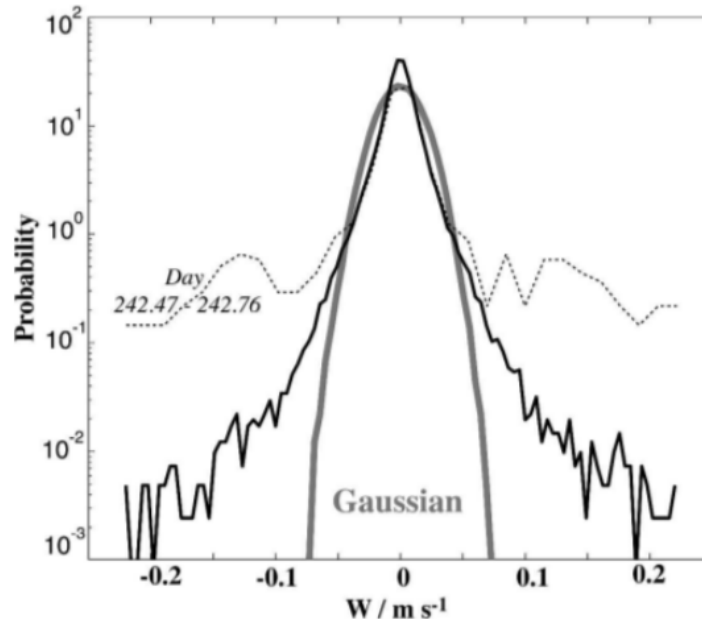


FIGURE 1.8: *PDF of the vertical velocity obtained by means of Lagrangian floats deployed in the Oregon continental shelf. Taken from [12].*

flows. Indeed, one of the strength of this work is that it provides several investigations performed using a variety of different tools.

First, I present the numerical framework used to carry out numerical simulations and to analyze and visualize their output. This is the main tool of investigation of this work. Then, I provide information on ground-based instruments used to investigate Earth’s atmosphere: radars. The type of radars used to collect data in the atmosphere are described, along with the physical principles used. Finally, the experimental setup which allowed to retrieve measurements of passive scalar concentration is described.

### 1.12.1 Direct numerical simulations

We present here the numerical framework used to produce the runs analyzed throughout the present manuscript. The code used to carry out the numerical simulations is the Geophysical High-Order Suite for Turbulence (GHOST) [47]. GHOST is a hybrid MPI/OpenMP pseudo-spectral code written mostly in Fortran 90/95 which supports GPU acceleration via the NVIDIA-CUDA programming model [66].

Pseudo-spectral codes have the advantage of resolving all the scales of the systems with almost no numerical dissipation. This approach with numerical simulations where all the scales are resolved is known as Direct Numerical Simulations (DNS). Thus, the main feature of DNSs is that the small scales are not parametrized. This can be really useful in the context of research on turbulent flows, where one wants to characterize all the small-scale effects arising from non-linear turbulent interactions. Another important feature of DNSs is the possibility to investigate the properties of the field in every point of the simulation domain, which, in the case of the runs presented in this manuscript, is a cubic grid with a resolution of  $512^3$  points. This is one of the main advantages of DNSs over experiments. The novelty of the GHOST code resides in its domain decomposition which involves a two-level parallelization scheme by means of Message Passing Interface (MPI) and Open Multi-Processing (OpenMP), hence consisting in a hybrid MPI/OpenMP scheme. MPI and OpenMP are a set of message-passing standards which allow multiple processors to communicate and share

data between them. Parallelizing codes using MPI or OpenMP is a necessity when dealing with a lot of data and allows to perform tasks such as numerical simulations in way less time than using a serialized version of the same code. The domain decomposition employed by GHOST allows to efficiently parallelize Fast Fourier Transforms (FFTs) in different directions of the domain in distributed memory environments [47]. For a cubic domain containing  $N^3$  gridpoints in the physical space, using the hybrid MPI/OpenMP decomposition implemented in GHOST, one of the three directions is distributed among the processors, hence the domain is first decomposed in slabs of size  $N^2 \times M$ , where  $M = N/N_{MPI}$ , with  $N_{MPI}$  being the number of MPI tasks. For instance, the sketch in Fig. 1.9 (left panel) shows how the vertical direction  $z$  is divided in slabs. The FFT along the directions  $x$  and  $y$  can therefore be computed easily in parallel for each slab, namely for each processor. The result of such 2D FFT operation is a parallelepiped of dimensions  $(N/2+1) \times N \times M$ . This happens because, due to the fact that the generic field is real, in the spectral space only  $(N/2+1)$  Fourier harmonics are saved, since the negative wavevectors are the complex conjugates of the positive harmonics. Then, when one has to compute the FFT in the  $z$  direction, since the information concerning the field is distributed on the different processors, GHOST transposes each of these parallelepipeds in such a way to have this time the  $z$  direction entirely on each single processor and the  $x$  direction, having now a dimension equal to  $(N/2+1)$ , is shared among the processors. Thus, after transposing, the computational domain on each processor will have a dimension  $P \times N \times N$ , where now  $P = (N/2+1)/N_{MPI}$ , and all the FFTs along the  $z$  direction can be again computed in parallel.

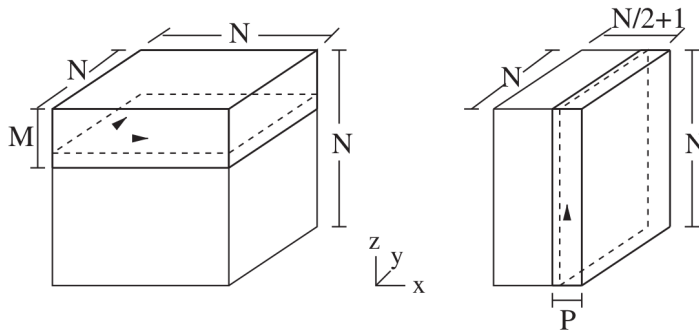


FIGURE 1.9: *Underlying 1D (slab) domain decomposition for pseudo-spectral method (left). Each compute core works on a slab of size  $N \times N \times M$ , where  $M = N/N_{MPI}$ . The FFT is done by first doing the FFTs locally in each slab, in the directions specified by the arrows, yielding partially transformed data of size  $(N/2 + 1) \times N \times M$ . Then, an all-to-all communication is done to transpose the data globally (right), so that the remaining 1D FFT can be done in the direction specified by the arrow. The data for this step is stored in a cube of size  $P \times N \times N$ , with each core computing the FFT locally in a slab of size  $P = (N/2 + 1)/N_{MPI}$ .*

Time integration is done through a second- or fourth-order Runge-Kutta scheme. The Fourth order Runge-Kutta scheme can provide more accurate results in exchange of a larger consumption of CPU time and larger use of RAM memory.

GHOST is a powerful tool that can solve several systems of Partial Differential Equations (PDEs), including, but not limiting to: compressible and incompressible hydrodynamic equations, stratified flows using the Boussinesq approximation with and without rotation, passive scalars, integration of lagrangian or test particles. Since it is

not limited to neutral fluids equations it can also be used to investigate plasma or superconductors, since it can also solve compressible and incompressible magnetohydrodynamic (MHD) equations, the Gross-Pitaevskii Equation and the Ginzburg-Landau equations.

The post-processing of the output of GHOST was performed using codes written in Fortran90 appropriately developed for this thesis work. These consist in both serial and parallelized codes which can compute statistics and derivatives, that will be used for the post-processing of the fields generated by GHOST. Still frame (two- and three-dimensional) renderings and animations of the fields presented in this manuscript were made using VAPOR (the Visualization and Analysis Platform for Ocean, Atmosphere, and Solar Researchers) [80]. These visualizations were made in order to investigate the characteristics and morphology of turbulent structures that develop in the domain of the DNSs and their evolution. Finally, all the other figures shown in this manuscript have been produced using GNUPLOT and Python.

### 1.12.2 Radar observations

We introduce now the tools used for the detection of wind velocity in the MLT, a region of the Earth's upper atmosphere.

Earth's atmosphere is divided into several layers, identified by their characteristics and altitudes. A diagram displaying them is shown in Fig. 1.10. The MLT is the region found between 80 – 120 km of altitude.

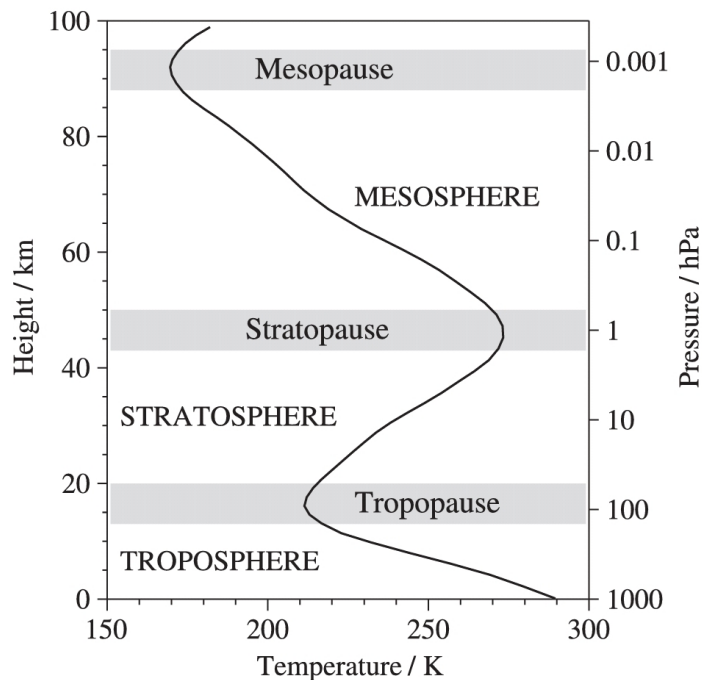


FIGURE 1.10: *Evolution of temperature and pressure in the Earth's atmosphere as a function of the altitude.*

In situ measurements are difficult to obtain in the MLT region since it is too high for meteorological balloons, and too low for satellites to fly through. Ground-based instruments, on the other hand, provide a reliable way to continuously observe the MLT region. Lidars, different radars and optical imagers are some of the instruments used

to study this region. Even though significant improvements have occurred in observing MLT using various radars, kilometer-scale dynamics have scarcely been measured. However, in the past decades significant progress has been made which allowed to provide reliable local observations over small volumes of the mesosphere using radars. This is the case of Mesosphere-Stratosphere-Troposphere (MST) radars, which can detect backscattered signals from 2 km up to 100 km of altitude, covering the mesosphere, stratosphere and troposphere regions of the Earth's atmosphere. In Chap. 3 we will show results based on measurements made using the Middle Atmosphere Alomar Radar System (MAARSY). MAARSY is a powerful Very-High-Frequency (VHF) radar, an array of 433 antennas operating at 53.5 MHz located on the Andøya island, in northern Norway, installed by the Leibniz Institute of Atmospheric Physics in Kühlungsborn, Germany (IAP) to the aim of investigating the dynamics of the polar mesosphere [36]. VHF radars can provide direct measurements of the MLT regions using tracers. A particular type of natural tracers can be found at polar latitudes in the mesosphere. During summer the polar mesosphere is one of the coldest regions on Earth, reaching minimum temperatures of  $\sim 130$  K. The extremely low temperatures of the polar mesosphere allow the formation of ice particles which, in turn, accumulate into ice clouds. These clouds can generate measurable signatures in the form of strong radar echoes known as Polar Mesospheric Summer Echoes (PMSE) which are caused by inhomogeneities in the electron number density [59]. The signal coming from PSME, which act as natural tracers, can then be tracked by VHF radars in order to estimate wind velocity. MAARSY uses PMSE as a suitable tracer to monitor the dynamic structure of the mesospheric region [69]. A sketch of the antennas configuration of MAARSY is shown in Fig. 1.11.

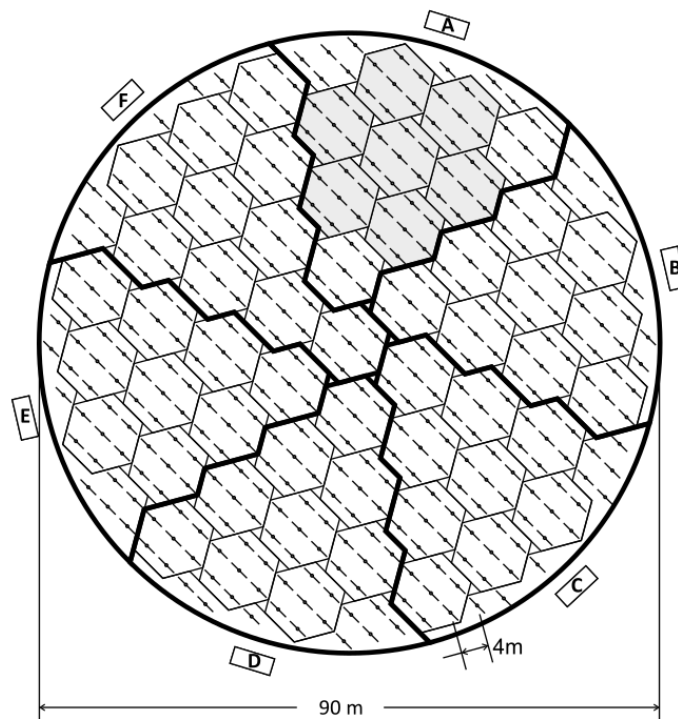


FIGURE 1.11: Sketch of MAARSY. The antenna array is divided in 61 subarrays, 55 identical hexagons consisting of 7 antennas each and 6 asymmetric groups consisting of 8 antennas located at the perimeter of the array. The equipment buildings are indicated with the letters A-F. Taken from [36].



Another tool that has been extensively used in the last decades to investigate the dynamics of the mesosphere are Specular Meteor Radars (SMRs). SMRs exploit meteoroids to provide estimates of wind velocity by using one transmitting antenna and a receiving array. Meteoroids are rocky or metallic bodies up to 1 m wide which frequently get caught by Earth's gravity. It is estimated that  $\sim 25$  million meteoroids enter Earth's atmosphere daily. As they enter Earth's atmosphere they start heating due to friction, leaving a ionized trail of air molecules behind them in the process. These ionized trails drift with the neutral wind and this properties of them can be exploited to estimate the radial velocity of the wind. By combining the measurements coming from several meteoroids in the same region, the line of sight wind velocity can be estimated [26]. Moreover, the higher the meteor count the more accurate will be the estimated velocity. It is for this reason that a novel approach to SMRs, which involves the detection of meteor trails from different sites, has been recently developed, the Multistatic and Multifrequency Agile Radar for Investigations of the Atmosphere (MMARIA) [72]. This approach, in fact, employs one transmitting antenna but multiple receiving arrays. It has been shown that this configuration not only improves the quality of the measurements by increasing the number of trails detected but also increases the illuminated volume and allow to compute derivatives of velocity. SMRs have also been installed in Andøya [11] and have been used to estimate horizontal wind velocity gradients which will be relevant for the results shown in Chap. 3. Fig. 1.12 shows a diagram with the SMRs setup.

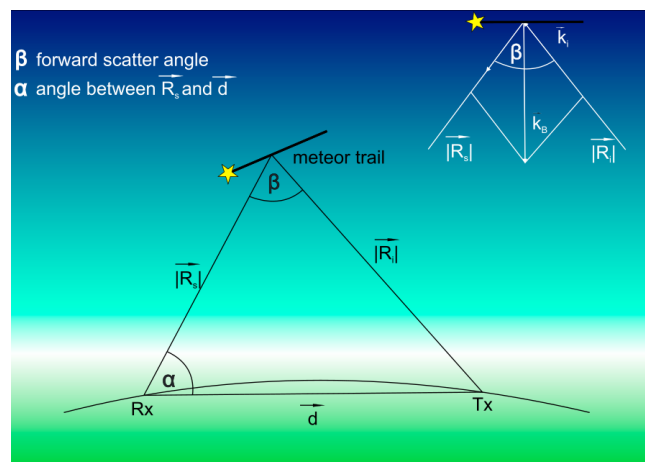


FIGURE 1.12: Schematic diagram showing the Specular Meteor Radars setup. The plasma trail of a meteoroid is simultaneously detected from two stations and used to compute the radial velocity of the wind. Tx marks the position of the transmitting antenna, Rx marks the position of the receiving array Taken from [72].

### 1.12.3 Wind tunnel experiment

In the last part of this section I describe the experimental setup that was used to obtain the measurements of passive scalar concentration presented in Chap. 5. These measurements were taken in the atmospheric wind tunnel of the Laboratoire de Mécanique des Fluides et d'Acoustique at the École Centrale de Lyon in France. A sketch of the wind tunnel is shown in Fig. 1.13. It is a closed return wind tunnel (also known as Prandtl or Göttingen tunnel), where the air exiting the test section is fed back at the beginning of it by a fan. Guide vanes found at each of the corners of the tunnel help the flow in taking the sharp turns. The test section of the tunnel measures 14 m long, 2.5 m high and 3.7 m wide. The speed of the flow can go from 0.5 to 10 m/s. The

contraction before the test tunnel speeds up the flow and is used to increase the mean velocity of the flow. The grid at the entrance of the test section is used to generate an approximately homogeneous turbulence. The spires (Irwin type) at the beginning of the test section serve the purpose of accelerating the stream-wise development of the larger scale eddies. The cubes placed on the floor of the test section assure the production of turbulence.

The configuration we used for the results presented in Chap. 5 allowed for a Reynolds number  $Re$  of order  $10^5$  and the flow speed was set to 5 m/s.

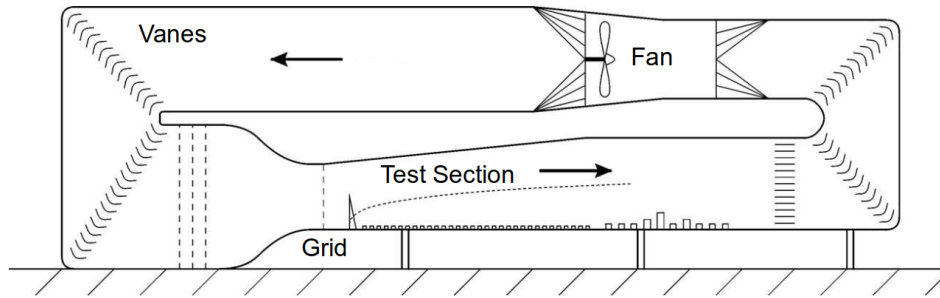


FIGURE 1.13: Sketch of the wind tunnel installed in the *Laboratoire de Mécanique des Fluides et d'Acoustique* at the *École Centrale de Lyon*, France.

In the test section of this wind tunnel, measurements of hydrocarbons concentration in the air were performed using a Flame Ionization Detector (FID). The FID is used to detect the amount of ions produced by the combustion of hydrocarbons. The concentration of hydrocarbons can be estimated from the number of ions produced. These ions, in fact, induce a current to an electrode which is proportional to the concentration of the hydrocarbons [14]. Air containing hydrocarbons is then aspirated by a tube. The FID used for the measurements shown in Chap. 5 is a HFR400 Fast FID, produced by Cambustion LTD, which allowed for a sampling frequency of 1000 Hz. The hydrocarbon that acted as the passive scalar is ethane, chosen as a tracer since it is neutrally buoyant in air due to their similar density. Ethane is continuously released in the wind tunnel from a point source. Measurement stations of the concentration were placed in the test section at different distances from the source. Since ethane recirculates in the wind tunnel, the background concentration accumulates in the test section and increases with time. In order to take into account this fact, the background concentration is measured before and after acquiring any of the concentration time series. Assuming that the background concentration evolves linearly with time, concentration estimates are ultimately obtained by subtracting the background concentration to the measured values. Vertical profiles of the concentration at different distances from the source are obtained. However, for the comparison with the DNSs that will be shown in Chap. 5, only the measurements taken at the centreline of the wind tunnel are considered. This is done in order to minimize as much as possible the effects of the boundaries.



## Chapter 2

# Mixing and transport in stratified flows with and without rotation

The occurrence of large-scale intermittency in stratified turbulence is a well known phenomenon which has been investigated mainly through observations in oceans and in the atmosphere [12, 39]. However, due to the difficulty of investigating multi-scale turbulent flows, with a large number of degrees of freedom and several governing parameters (i.e.  $Re$ ,  $Fr$ ,  $Ro$  etc.), many of its aspects are not yet fully understood. It is not easy to carry on both experiments or numerical simulations at very high Reynolds numbers  $Re$  and in most cases the values of this parameter are from 10 to 1000 times smaller than those observed in geophysical flows. Nevertheless, DNSs can nowadays reproduce with very high accuracy many important features of turbulent flows observed in nature. Only recently, the issue of the large-scale intermittency was tackled by means of DNSs by Rorai et al. [65]. In order to explain the intense and sporadic bursts of turbulent activity occurring in the nocturnal Planetary Boundary Layer (PBL), caused by the non-linear amplification of waves [1, 77], large-scale intermittency was investigated in [65] from a numerical point of view. The PBL is the lowest part of the atmosphere and it is strongly influenced by the presence of the Earth's surface. Shortly after sunrise, surface heating causes convection to develop. At the sunset, surface cooling creates a stable (nocturnal) boundary layer. The nocturnal PBL is thus a stable and well-ordered flow in which instabilities decay rapidly. In spite of that, the nocturnal PBL does also develop intense and sporadic bursts of turbulent activity that disappear slowly in time [17, 76, 78]. The processes behind these bursts were not clearly understood and poorly modeled. Thus, the problem was analyzed in order to provide a better understanding of this phenomenon, which may lead to a more accurate parametrization in climate models. In [65] an attempt was carried out through decaying DNS of purely stratified flows at very high resolution on grids of  $2048^3$  points. Two cases with a different degree of stratification, set by the Brunt-Väisälä frequency, namely  $N = 4$ , which corresponds to a Froude number of  $Fr \approx 0.1$ , and  $N = 12$ , corresponding instead to a  $Fr \approx 0.03$ , were analyzed. In both the simulations the Reynolds number is of the order  $Re \sim 10^4$ . The intuition would suggest that as stratification increases, the flow is expected to become more stable and predictable. However, the opposite happens. It was indeed found that the stronger events likely occur when the flow is more stable, although a study on the characterization of these events was not performed, which is indeed one of the main subject of this research work. The extreme events, diagnosed through the analysis of the PDFs of the prognostic fields, do not only occur in the velocity and temperature gradients, as it happens due to the well known phenomenon of small-scale (or internal) intermittency, but also in the fields themselves. Fig. 2.1 from [65] shows the results obtained for the PDF of the vertical velocity field  $w$ , the temperature fluctuations  $\theta$  and their gradients. The normalized distributions of all these quantities are clearly non Gaussian.

The velocity and the temperature fluctuations are therefore found to be intermittent, with heavy tails for the PDFs for the fields and their gradients, and with the flow with a stronger stratification having the highest probability to develop extreme events. A

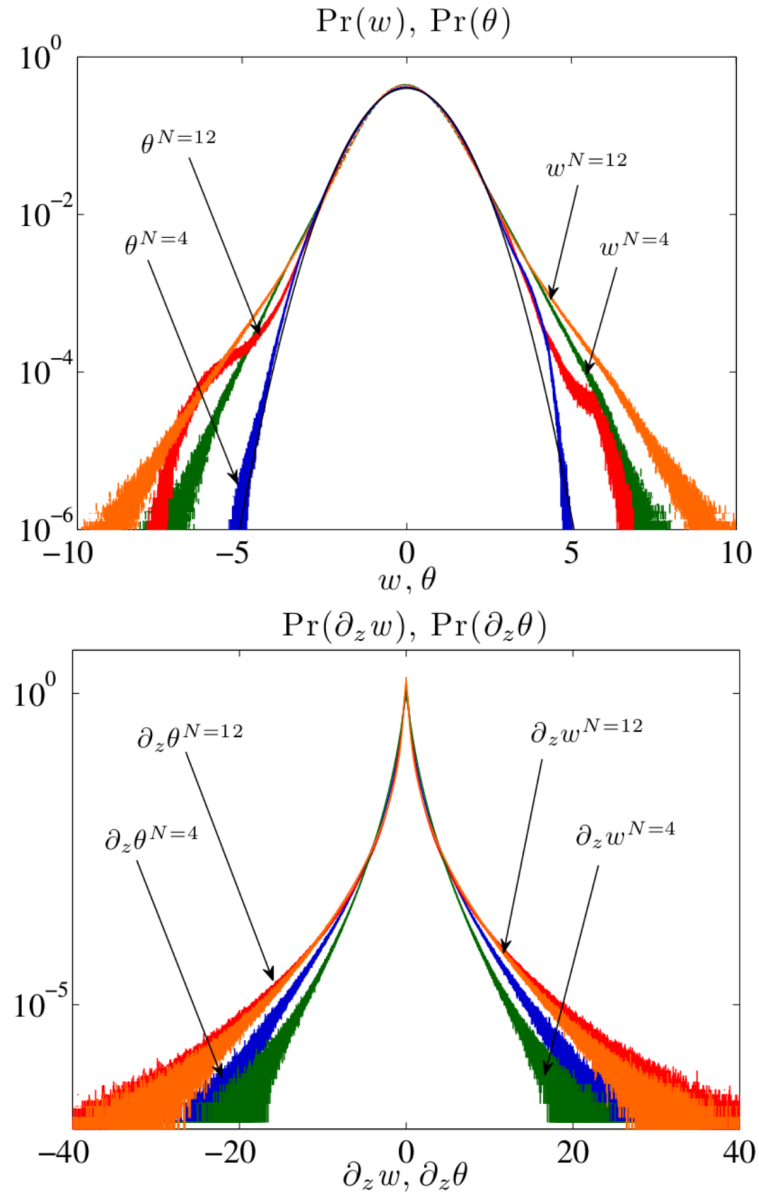


FIGURE 2.1: PDF of the vertical velocity  $w$  and temperature fluctuations  $\theta$  for the fields (top panel) and their gradients (bottom panel) found in [65].

model that could reproduce the dynamics of the observed large-scale bursts was derived in [65] based on the model previously developed by Vieillefosse [81]. In order to derive this model, the Boussinesq equations (Eqs. 1.13, 1.14) were first reduced to the one-dimensional case, considering only the  $z$  component. They then considered a system with no dependence on the horizontal directions, thus, the fields  $w$  and  $\theta$  will depend only on  $z$ . The above is valid assuming that the vertical component of the velocity field and the vertical gradients dominate the dynamics of the system and the contribution of the horizontal components and horizontal gradients can be neglected.

By neglecting the dissipation and pressure terms of Eqs. 1.13,1.14, one obtains:

$$\partial_t w + (w \cdot \nabla) w = -N\theta \quad (2.1)$$

$$\partial_t \theta + w(\cdot \nabla) \theta = Nw. \quad (2.2)$$

Taking the  $z$ -derivatives of Eqs. 2.1, 2.2, one obtains:

$$\partial_z(\partial_t w) + \partial_z(w\partial_z w) = \partial_z(-N\theta) \quad (2.3)$$

$$\partial_z(\partial_t \theta) + \partial_z(w\partial_z \theta) = \partial_z(Nw). \quad (2.4)$$

Since  $w$  and  $\theta$  depend only on  $z$ , Eqs. 2.3, 2.4 can be rewritten as:

$$\partial_t(\partial_z w) + w\partial_z^2 w + (\partial_z w)^2 = -N\partial_z \theta \quad (2.5)$$

$$\partial_t(\partial_z \theta) + w\partial_z^2 \theta + (\partial_z w)(\partial_z \theta) = N\partial_z w. \quad (2.6)$$

By keeping into account that the total derivative with respect to  $t$  of  $\partial_z w$  and  $\partial_z \theta$  Eqs. 2.5, 2.6 are equal to:

$$d_t(\partial_z w) = \partial_t(\partial_z w) + w\partial_z^2 w \quad (2.7)$$

$$d_t(\partial_z \theta) = \partial_t(\partial_z \theta) + w\partial_z^2 \theta, \quad (2.8)$$

then by substituting (2.7, 2.8) in Eqs. 2.5, 2.6 one obtains:

$$d_t(\partial_z w) = -N\partial_z \theta - (\partial_z w)^2 \quad (2.9)$$

$$d_t(\partial_z \theta) = N\partial_z w - (\partial_z w)(\partial_z \theta). \quad (2.10)$$

By assuming that fields are smooth on an arbitrary scale  $\ell$ :

$$\delta w = \langle w(\mathbf{x} + \ell \hat{z}) - w(\mathbf{x}) \rangle \approx \ell \partial_z w \quad (2.11)$$

$$\delta \theta = \langle \theta(\mathbf{x} + \ell \hat{z}) - \theta(\mathbf{x}) \rangle \approx \ell \partial_z \theta. \quad (2.12)$$

This allows to convert spatial derivatives to increments in Eqs. (2.9, 2.10), which brings to:

$$d_t \delta w = -\frac{\delta w^2}{\ell} - N\delta \theta \quad (2.13)$$

$$d_t \delta \theta = -\frac{\delta w \delta \theta}{\ell} + N\delta w. \quad (2.14)$$

For a fixed value of  $\ell$ , if  $N$  is high enough waves prevail over turbulence and in Eqs. 2.13, 2.14 the terms  $\frac{\delta w^2}{\ell}$  and  $\frac{\delta w \delta \theta}{\ell}$  can be neglected, obtaining:

$$d_t \delta w = -N\delta \theta \quad (2.15)$$

$$d_t \delta \theta = N\delta w. \quad (2.16)$$

On the other hand, for a fixed value of  $\ell$ , if  $N$  is small, turbulence prevails on waves and in Eqs. 2.13, 2.14 the terms that can be neglected are  $N\delta \theta$  and  $N\delta w$ , which brings to:

$$d_t \delta w = -\frac{\delta w^2}{\ell} \quad (2.17)$$

$$d_t \delta \theta = -\frac{\delta w \delta \theta}{\ell}. \quad (2.18)$$

Eqs. 2.13, 2.14 can be seen as a crude one-dimensional approximation of Lagrangian trajectories in a stratified flow and are known as the “restricted Euler dynamics”. They have been used to study intermittent structures in a variety of turbulent flows [44, 74]. For a fixed value of  $\ell$ , if  $N$  is high enough, waves prevail over turbulence and the terms  $-\frac{\delta w^2}{\ell}$  and  $-\frac{\delta w \delta \theta}{\ell}$  in Eqs. 2.13, 2.14 can be neglected. On the other hand, if  $N$  is small, turbulence prevails on waves and the terms that can be neglected in Eqs. 2.13, 2.14 are  $-N\delta\theta$  and  $+N\delta w$ . For intermediate values of  $N$ , instead, all the terms in equations Eqs. 2.13, 2.14 have to be considered, thus both turbulence and waves will be present in the system. With an initial condition given by  $\delta w(t=0) > 0$ , if no stratification is present ( $N=0$ )  $\delta w(t)$  goes to 0. By gradually increasing the value of  $N$ , a region in which the model diverges ( $\delta w(t)$  goes to  $-\infty$ ) is found. Here, waves are non-linearly amplified. In this region the higher the value of  $N$  the faster the model diverges. If  $N$  is further increased the model stops diverging and  $\delta w(t)$  assumes an oscillating behaviour. These different scenarios can be seen in Fig. 2.2, in which the time evolution of  $\delta w$  for different values of  $N$  is shown. In agreement with the results

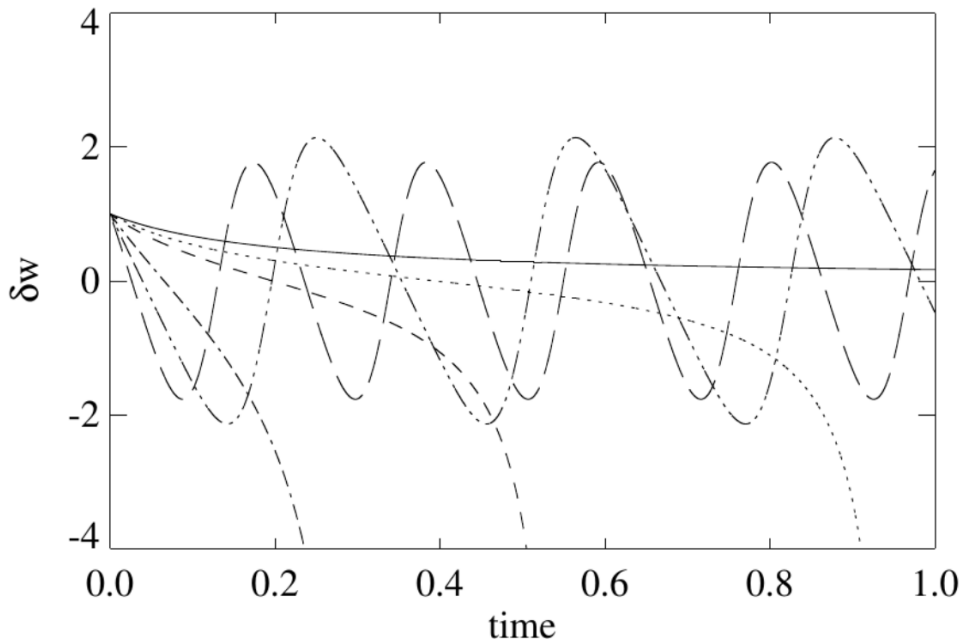


FIGURE 2.2: Evolution in time of vertical velocity variations  $\delta w$  in the model of Eqs. 2.13, 2.14 for  $\ell = 0.2$  and  $N = 0$  (no stratification, solid line), and for  $N = 2$  (dotted), 4 (dashed), 12 (dash-dotted), 20 (dash-triple-dotted), and 30 (long dashed line). Taken from [65]

obtained from the DNS in [65], the model shows that in stably stratified turbulence, the stronger bursts occur when the flow is expected to be moderately or strongly stratified, within a certain range of values of the Brunt-Väisälä frequency. The model also shows that propagating gravity waves are non-linearly amplified, resulting in their breaking and the generation of turbulence when the linear and nonlinear effects are balanced. A phenomenological interpretation of the presence of intermittency at large scale in purely stratified flows was also proposed in [65]. They show indeed how these flows are prone to develop strong Kelvin-Helmholtz instabilities, which in turn are likely to be responsible for the bursts characterized by large values of the fields and their gradients. These bursts are actually seen in the PDFs of the fields and in their gradients as extreme events. The intermittent bursts in the nocturnal PBL can thus be interpreted as the coupling between vertical velocity and temperature fluctuations in

the flow. The large-scale intermittent behaviour of  $w$  is interpreted through this model as a resonance phenomenon between gravity waves and turbulence. The interplay between the two amplifies the formation of vertical negative velocity gradients and generates the extreme vertical drafts.

In this chapter I present two articles ([16] and [7]) which provide a quantitative characterization of large-scale intermittency in stratified flows and its effects on their mixing properties, with and without rotation. This investigation has been performed through an extended parametric study of DNSs produced using GHOST (see section 1.12.1). The level of intermittency in the flows will be quantified through high order statistics of Lagrangian and Eulerian velocity and of the temperature field and will be used to infer the conditions under which large scale intermittency is observed to be stronger. The effects of large-scale intermittency are then evaluated by investigating the mixing properties of the flow and particle dispersion.

## 2.1 Emergence of vertical drafts in stratified flows

In homogeneous and isotropic turbulence, the PDF of the velocity field computed at a scale  $\ell$  such that  $\ell \sim \ell_0$ , where  $\ell_0$  is the integral scale, is approximately a Gaussian. However, as the scale  $\ell$  becomes smaller, the PDF of the field increments has the tendency to develop exponential wings. When the  $\ell$  considered is comparable to the Kolmogorov length scale  $\eta$  the PDF takes the form of a 'stretched' exponential, with a significant probability to develop extreme events in the flow. This effect is the consequence of the presence of intermittency at the small scales, that has been introduced in Chap. 1.

This behaviour is illustrated in Fig. 2.3 for a HIT simulation we produced as a reference case for our parametric study. Here, the PDF of the  $z$ -component of the velocity field  $w$  has been computed at different scales, ranging from  $\ell \sim 120\eta$ , which, in our case, is comparable to the scale of the mean flow, to  $\ell \sim 1.3\eta$ .

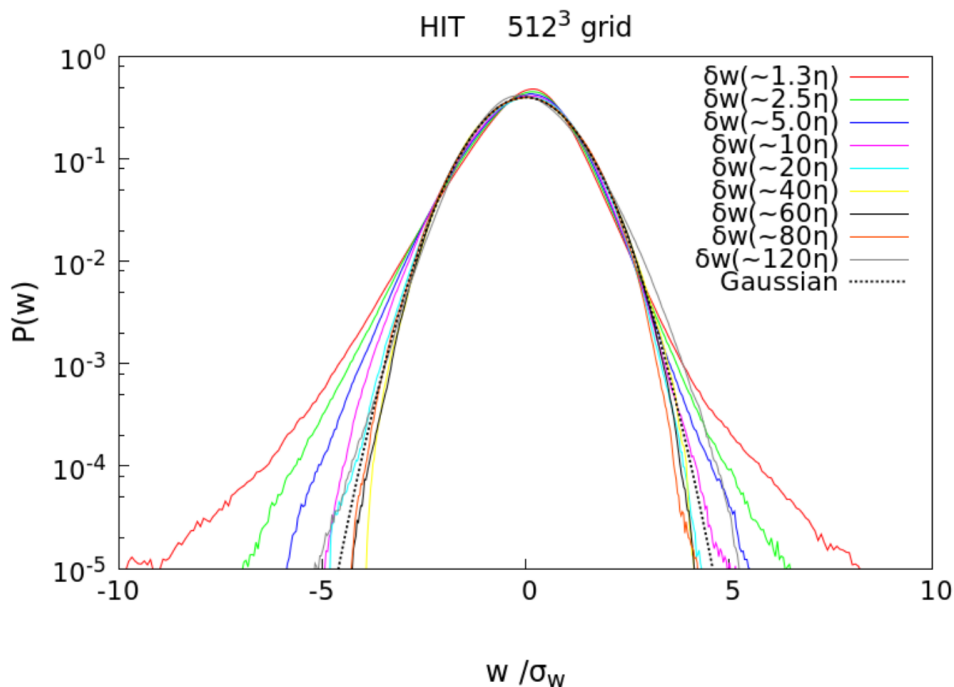


FIGURE 2.3: PDFs of the Eulerian vertical velocity at different scales in the homogeneous and isotropic case compared to a Gaussian (black dotted line).



A relevant quantity that allows to properly quantify intermittency is the kurtosis, introduced in Chap. 1. The kurtosis of the PDF of the signal fluctuations built on a scale  $\ell \sim \ell_0$  will have a value close to 3 and the distribution of the signal will be approximately Gaussian. A departure from this value of the kurtosis will instead be observed as the fluctuations of the signal are built at smaller scales.

As the kurtosis gets higher the flow becomes more intermittent. Conversely, a kurtosis close to 3 means that the PDF of the signal investigated should be compatible with a Gaussian. The increase of the value of kurtosis due to a higher probability of extreme events will be used in this work to identify the presence of intermittency.

The data obtained from the DNSs performed consist in the velocities of Lagrangian particles released in the flow, Eulerian velocity and temperature field.

The more particles there are in the simulation box, the more accurately they will be able to map the velocity field, thus increasing the quality of the statistics. For this work  $\sim 1.5$  million particles have been injected in the flow after it reaches a fully developed turbulent state. The Eulerian velocity and temperature consist in the values of each field at a given time and each grid point.

Several runs with different levels of stratification, obtained by modifying the value of  $Fr$  have been generated using GHOST (see 1.12.1).

Data obtained from a homogeneous and isotropic turbulence run were also analyzed and used as a reference case in our investigation.

Fig. 2.4 shows the PDFs of the three components of the Lagrangian velocities,  $\tilde{u}$ ,  $\tilde{v}$  and  $\tilde{w}$ . These are compatible with a Gaussian distribution, added in Fig. 2.4 as a reference (dotted line), in agreement with the known evidence that at large scales the velocity field fluctuations in homogeneous and isotropic turbulence follow a Gaussian distribution.

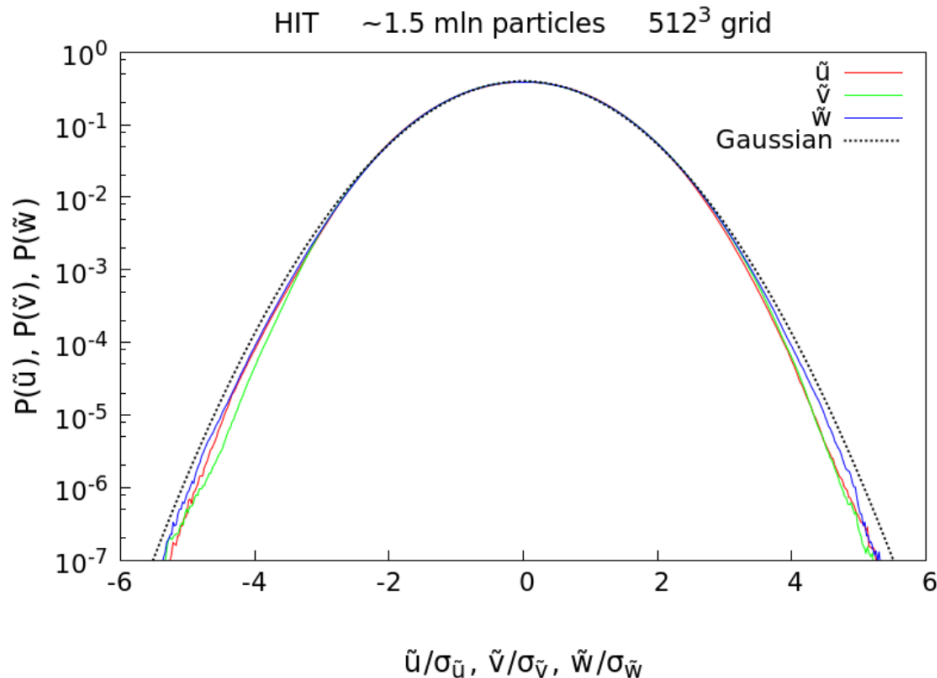


FIGURE 2.4: PDFs of the three components of the Lagrangian velocity in the homogeneous and isotropic case compared to a Gaussian (black).

The Eulerian velocity field at large scales shows similar statistics.

However, the shape of the PDF of the velocity at smaller scales is different. Fig. 2.3 shows that the smaller the scale observed the further the tails of the PDF are larger.

This evidence was discussed in the previous chapter and it is due to the presence of intermittency in the dissipation range.

We now use the kurtosis to characterize large-scale intermittency in purely stratified turbulent flows. From the trajectories of the particles integrated with GHOST we obtain the three components of the Lagrangian velocity,  $\tilde{u}$ ,  $\tilde{v}$  and  $\tilde{w}$ . Unlike the HIT case, when analyzing the stratified runs, separating the vertical components from the horizontal ones is necessary. Since we are now dealing with an anisotropic framework, when stratification is non-negligible, we expect to find different results for  $\tilde{w}$  compared to the two horizontal components  $\tilde{u}$  and  $\tilde{v}$  due to the increased anisotropy in the  $z$  direction. After turbulence is fully developed (meaning, the runs have reached the peak of dissipation), we inject the particles in the flow and collect the data of the velocity field.

The trajectories of some particles in the case with  $Fr = 0.076$  are shown in Fig. 2.5 as a reference.

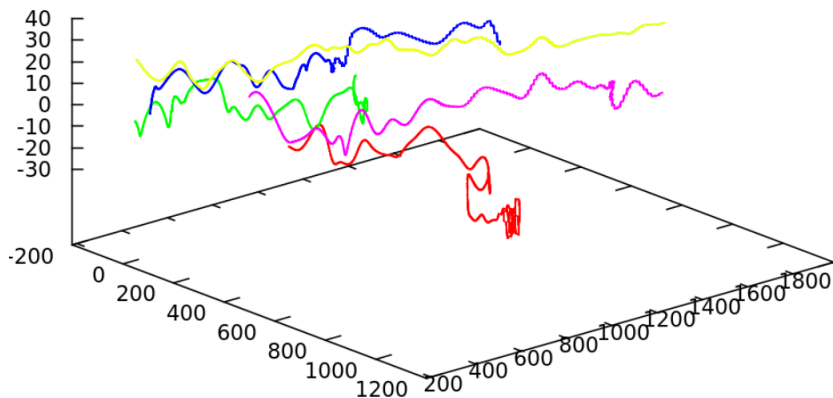


FIGURE 2.5: Trajectories of four Lagrangian particles in the purely stratified case with  $Fr = 0.076$ . The axes report values in terms of grid points.

Due to stratification, it can be observed in Fig 2.5 that particles oscillate and the frequency of their oscillation is determined by the Brunt-Väisälä frequency,  $N$  (see Chap. 1), characteristic of the gravity waves developing in the flow.

The PDFs for the stratified case with  $Fr = 0.076$  computed from the particles velocities are shown in Fig. 2.6.

Unlike the HIT case (Fig. 2.4), the distribution of the  $z$ -component of the Lagrangian velocity,  $\tilde{w}$  does not follow a Gaussian distribution. Its tails are heavier than the tails of a Gaussian meaning that the  $\tilde{w}$  has more probability to develop extreme events compared to  $\tilde{u}$  and  $\tilde{v}$ , whose PDFs are instead compatible with sub-Gaussian distributions. Thus, while  $\tilde{u}$  and  $\tilde{v}$  are clearly not intermittent, the distribution of  $\tilde{w}$  reveals the presence of intermittency with an evaluated kurtosis  $K_{\tilde{w}} = 10.44$ . Moreover, this intermittency occurs in the large scale velocity field itself, thus it is different from the classical "internal" intermittency, developing at small scales in homogeneous and isotropic turbulence (Fig. 2.3).

The intermittency observed here is compatible with the one seen in [65] (Fig. 2.1). All in all 17 runs have been analyzed whose parameters have values falling in the following ranges:  $2900 \lesssim Re \lesssim 3800$ ;  $0.15 < Fr < 0.93$ ;  $0.9 < R_B < 2560$ .

In each case analyzed, the PDFs of  $\tilde{u}$  and  $\tilde{v}$  were always sub-Gaussian distributions, with a low probability to develop extreme events. The Lagrangian statistics of  $\tilde{u}$  and  $\tilde{v}$  show no evidence of large-scale intermittency in all the runs analyzed in this study.

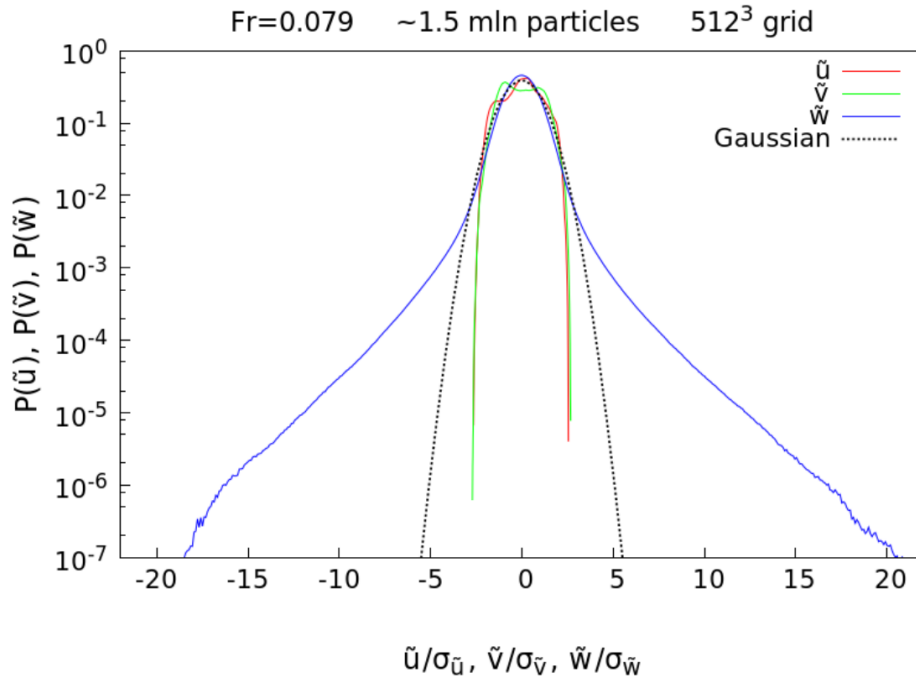


FIGURE 2.6: PDFs of the three components of the Lagrangian velocity,  $\tilde{u}$ ,  $\tilde{v}$  and  $\tilde{w}$ , in the purely stratified case with  $Fr = 0.076$  compared to a Gaussian (black).

On the other hand, the distribution of  $\tilde{w}$  displays a strong departure from a Gaussian for a sharp range of  $Fr$ . In Fig. 2.7 the PDFs of  $\tilde{w}$  computed for different values of  $Fr$  are shown.

When considering the Eulerian approach, instead of a single PDF for  $\tilde{w}$ , for every run, the number of PDFs becomes equal to the total number of time steps. By doing so it is possible to check at which time steps there is a higher probability to develop extreme events 2.8.

The Eulerian PDFs of  $w$  with wider tails are the ones containing the strongest events that also appear in the Lagrangian velocity. From the comparison between the Lagrangian and the Eulerian PDFs we note that the former is equivalent to an average over time and space of the Eulerian statistics of the whole simulation box at every time step (Fig. 2.8).

In Fig. 2.8, the Lagrangian PDF of  $\tilde{w}$  for the case with  $Fr = 0.076$  is shown along with all the PDFs of the  $z$ -component of the Eulerian field  $w$ , computed on the simulation box for each of the time steps we outputted the matrix containing the fields  $u$ ,  $v$  and  $w$ . The extreme events emerging in the PDF of  $\tilde{w}$  and their origin will now be investigated through the PDF of  $w$ , the vertical component of the velocity in the Eulerian framework. Fig. 2.8 shows that the PDF of  $\tilde{w}$  can be obtained from the envelope of the PDFs of  $w$  for all the outputted Eulerian fields. It is also evident from Fig. 2.8 that the PDFs of  $w$  are intermittent in time, as the tails are larger at certain time steps, when the flow is more active. Thus, the probability of occurrence of extreme events and all the statistical properties of the PDF of  $w$  change depending on the time step considered, which, in other words, means that the flow is not stationary. Thus, the statistical quantities that characterize the fields do actually depend on the time step considered. For instance, the value of the kurtosis is different at different time steps.

In order to quantify the link between the strength of stratification and intermittency,

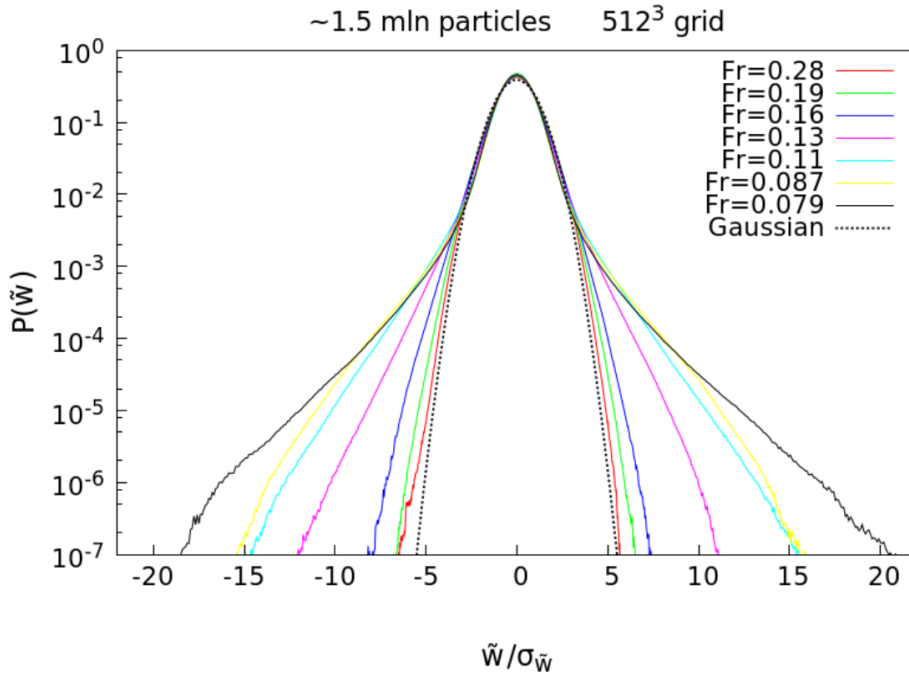


FIGURE 2.7: PDF of the  $z$ -component of the Lagrangian velocity,  $\tilde{w}$ , in the purely stratified case for different values of  $Fr$ .

we estimated the kurtosis of  $u$ ,  $v$ ,  $w$  and  $\theta$  from the Eulerian statistics for every run of this study and plotted it as a function of the Froude number  $Fr$  in Fig. 2.9.

We observe that the behaviour of  $K_w$  as a function of  $Fr$  is non-monotonic and identifies three different regimes. In the regime with weaker stratification ( $0.28 < Fr < 0.19$ ) the PDF of  $w$  is still very close to a Gaussian, having only a relatively small probability to develop extreme events (i.e. events that deviate more than  $3\sigma$  from the mean value of  $\tilde{w}$ ) and an evaluated  $K_w$  close to 3. A second regime is observed from  $Fr = 0.16$  to  $Fr = 0.076$ , where the distribution of  $w$  deviates more from a Gaussian as the stratification gets stronger. The evaluated  $K_w$  for these cases is always higher than 3, going from 3.87 up to 10.44, which is the value obtained for  $Fr = 0.076$  and the highest value across all the different runs. After this point, increasing the stratification does not produce an increase of the value of  $K_w$ . The latter is the third regime observed and goes from  $Fr = 0.076$  to  $Fr = 0.032$ , which corresponds to the cases with the strongest stratification analyzed. Here, if the stratification is further increased,  $K_w$  rapidly decreases going to 3.17 for the case with  $Fr = 0.032$ . These regimes can also be identified using the buoyancy Reynolds number  $R_B$ , which provides a measure of the relative strength of waves with respect to turbulence. The three observed regimes are indicated with different symbols in Fig. 2.9.

From Fig. 2.9 we observe that the temperature  $\theta$  displays the same type of large scale intermittency of  $w$ .

On the other hand, the PDFs of  $u$  and  $v$  are sub Gaussian with negligible probability to develop extreme events.

### 2.1.1 A model for the vertical drafts

We now examine our results from the point of view of the one-dimensional model shown at the beginning of this chapter. If viscous damping and a forcing  $f$  are taken into account in the model, Eqs. 2.13, 2.14 become:

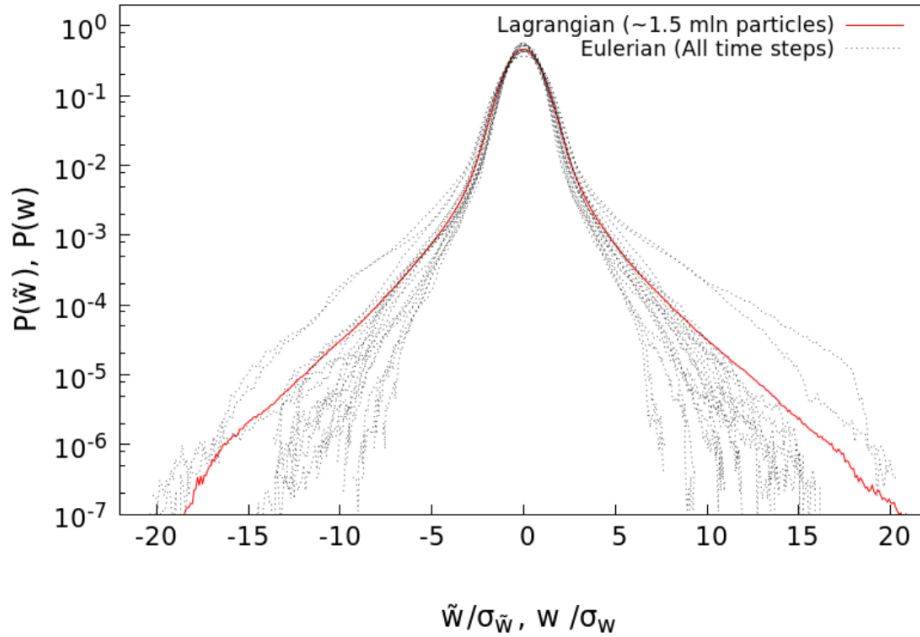


FIGURE 2.8: Comparison between the Lagrangian PDF of the  $z$  component of the velocity,  $\tilde{w}$  (red), and the Eulerian PDFs for every time steps of  $w$  (dotted lines) in the purely stratified case with  $Fr = 0.076$ .

$$\begin{cases} d_t \delta w = -\frac{\delta w^2}{\ell} - N \delta \theta - \nu \frac{\delta w}{\ell^2} + f \\ d_t \delta \theta = -\frac{\delta w \delta \theta}{\ell} + N \delta w - \kappa \frac{\delta \theta}{\ell^2} \end{cases} \quad (2.19)$$

where  $\kappa$  is taken equal to  $\nu$  and the forcing  $f$  is considered in order to avoid damping. The chosen form for the random superposition of (gravity) waves  $f = f_0 \sum \sin(\frac{Nt}{2i} + \varphi_i)$ , where  $\varphi_i$  is a random phase different for every Fourier mode. The flat (white) spectrum up to the Brunt-Väisälä frequency considered is compatible with the Garrett-Munk spectrum, observed in oceans [22]. The amplitude of  $f$  is fixed in order to obtain finite amplitude solutions. Assuming the extreme events are the result of local shear instabilities or overturning, we take the free parameter  $\ell$  proportional to the Ozmidov length scale (see Eq. 1.35 in Chap. 1),  $\ell = \alpha \ell_{oz}$ . We note that this particular choice of  $\ell$  leads to a strong dependence of the outcome on the Froude number since:

$$\ell_{oz} = \sqrt{\frac{\varepsilon V}{N^3}} = L(\beta Fr^3)^{1/2}. \quad (2.20)$$

By integrating Eqs. 2.19 numerically and considering an ensemble of 20 realizations for each run we obtain the temporal evolution of  $\delta w$  and  $\delta \theta$  shown in Fig. 2.10.

From the signals of  $\delta w(t)$  and  $\delta \theta(t)$  we can estimate the value of the kurtosis of  $w$  and  $\theta$  as a function of  $Fr$  (shown in Fig. 2.11), for all the sets of parameters stemming from each DNS run of this study.

The comparison between  $K_w(Fr)$  obtained from the model with the values coming from the DNS, found in the left panel of Fig. 2.11, show a qualitatively good agreement: the one-dimensional model is able to recover the peak in  $K_w$  and the non-monotonic behaviour of the kurtosis as is observed in the DNS. From the model's point of view the increase of the value of the kurtosis is related to the growing amplitude at which  $\delta w$  oscillates in time. However, the amplitude of  $\delta w$  grows only within a specific range

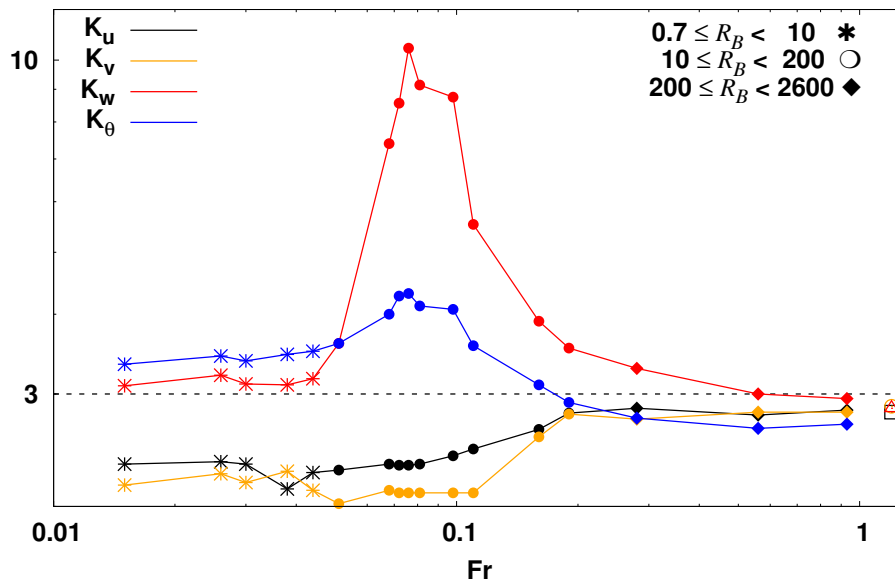


FIGURE 2.9: Kurtosis of  $u$ ,  $v$ ,  $w$  and  $\theta$  as a function of the Froude number  $Fr$ . The different symbols identify ranges in terms of the buoyancy Reynolds number  $R_B$ . Empty symbols placed at  $Fr \gg 1$  represent the values of the HIT run. The dashed black line marks the Gaussian reference value 3.

of values of  $Fr$ . If  $Fr$  is outside this range, the amplitude at which  $\delta w$  oscillates will be constant and no increase in the value of the kurtosis will occur.

The peak of the kurtosis is found in correspondence with the value of  $Fr$  for which both the scale of the non-linear amplification and of the waves are comparable. This results in a behaviour similar to a resonance. The  $Fr$  which causes the amplitude of  $\delta w$  to grow faster (Fig. 2.10) is the one for which the kurtosis will reach its maximum value.

Moreover, in the region to the left of the peak, due to the low value of  $Fr$ , the linearization is faster. For this reason the kurtosis decreases more rapidly on that side. In the region to the right of the peak, instead, the effects of non-linearity, which are the cause of the amplification of  $\delta w$ , are larger. This is likely the reason for the asymmetry in the curve of  $K_w(Fr)$ .

In the right panel of Fig. 2.11 we show the results obtained for  $K_\theta(Fr)$ . In this case the overall behaviour is again well reproduced but the model predicts values much larger than the one estimated from the DNS, especially at intermediate  $Fr$ , due to the faster growth of negative gradients in  $\delta\theta$ . This could be attributed to the one-dimensional model not being able to completely capture the dynamics of a three-dimensional turbulent and stratified flow.

### 2.1.2 Vertical drafts, overturning and mixing

To investigate the tendency of turbulent stratified flows to develop local overturning we computed the pointwise gradient Richardson number  $Ri$  (see Eq. 1.36 in Chap. 1), which provides a measure of the stability of a flow. The critical value  $Ri_c = 0.25$  is commonly used to identify the most unstable regions and to determine how likely it is for a flow to develop shear instabilities [3, 46, 27]. If  $Ri > Ri_c$  is satisfied everywhere then the flow is stable, otherwise local overturning may take place in the regions where  $Ri < Ri_c$ . This overturning originates from large negative vertical gradients of  $\theta$  (i.e. when a denser fluid parcel is on top of a less dense one) which

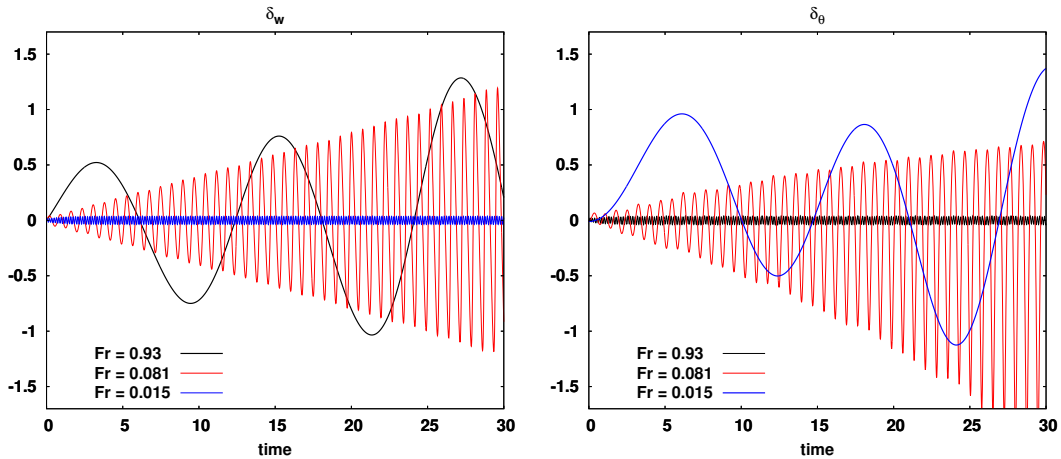


FIGURE 2.10: Evolution in time of  $\delta_w$  (left) and  $\delta\theta$  (right) obtained from an ensemble of 20 realizations of Eqs. 2.19.

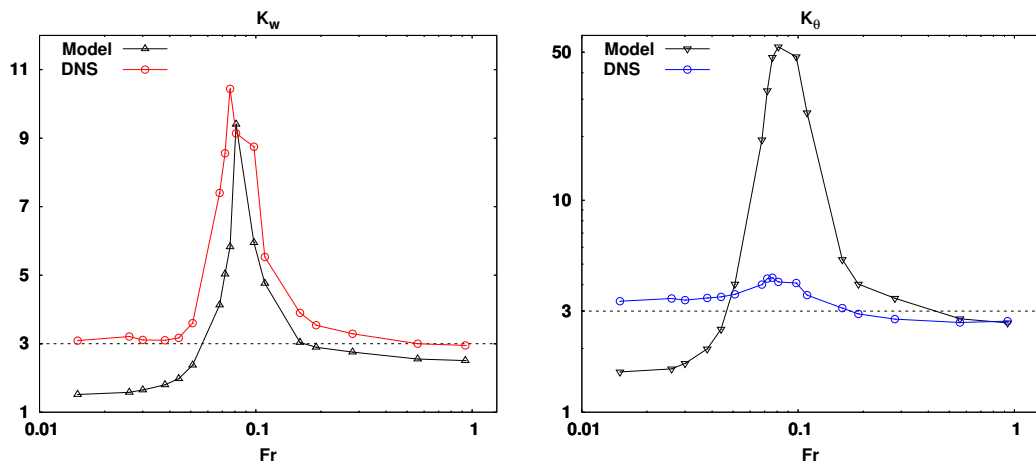


FIGURE 2.11: Comparison between the kurtosis of  $w$  (left) and  $\theta$  (right) obtained from the one-dimensional model (black lines) and from the DNS (red and blue lines) as a function of the Froude number  $Fr$ . The dashed black line marks the Gaussian reference value 3.

can overcome the background stratification, producing instabilities in the flow and developing local convection. The unstable regions, associated with  $Ri \lesssim 0$ , have been visualized through three-dimensional renderings of  $Ri$  in the simulation domain produced using VAPOR. Comparing these with visualizations of the vertical velocity field  $w$  where extreme events are highlighted shows that the most unstable regions of the flow, associated to a negative  $Ri$ , correspond to the same regions where extreme vertical drafts develop. Thus we were able to identify a qualitative correlation between vertical drafts and unstable overturning regions. We proceed in characterizing mixing by computing the mixing efficiency, which quantifies how efficient is the conversion of turbulent kinetic energy into background potential energy. One possibility to do that is to define the mixing efficiency as the ratio of the potential energy dissipation rate  $\varepsilon_P = \kappa(|\nabla\theta|^2)$  to the kinetic energy dissipation rate [38, 57, 67]:

$$\hat{\Gamma} = \varepsilon_P / \varepsilon_V. \quad (2.21)$$

With this definition, only the irreversible conversion of available potential into background potential energy, quantified by  $\varepsilon_P$ , is accounted for the mixing efficiency. The

variation of  $\hat{\Gamma}$  as a function of  $Fr$  is shown in Fig. 2.12. As previously observed from the behaviour of  $K_w$  and from the model, we identify three different regimes based on the value of  $Fr$ . For the runs with intermediate stratification we find that  $\hat{\Gamma}$  increases almost linearly with the Froude number, displaying a variation of one order of magnitude between  $Fr \sim 0.07$  and  $Fr \sim 0.2$ . This range of  $Fr$  is compatible to the one where extreme events develop in the flow. Thus it is likely that extreme vertical drafts, which are also at the origin of large-scale overturning, enhance mixing efficiency. For stronger stratification ( $Fr \lesssim 0.07$ ) we observe a saturation of  $\hat{\Gamma}$  around  $\hat{\Gamma}_0 \sim 0.1$ , compatible with the proxy value of the mixing efficiency commonly used in the oceanographic community ( $\sim 0.2$ ) [54]. For weaker stratification ( $Fr > 0.3$ ), we observe a decrease in the value of  $\hat{\Gamma}$ , consistently with what was found in [38]. The maximum value of  $\hat{\Gamma}$  estimated is found for  $R_B \sim 200$ , consistently with [43]. Another way to estimate the efficiency of the mixing is to evaluate the ratio of volume-averaged kinetic to potential energies  $E_V/E_P$  and the volume-averaged horizontal kinetic to potential energies  $E_{V\perp}/E_P$ . These quantities provide a measure of the partition of energy between kinetic and potential modes at all scales. They are shown as a function of the Froude number  $Fr$  in the inset of Fig. 2.12 (bottom). Both  $E_V/E_P$  and  $E_{V\perp}/E_P$  have a peak around  $Fr \sim 0.07$ , the value for which  $K_w$  assumes its maximum value. Again, this suggests that vertical drafts enhance mixing, as they generate large-scale overturning by increasing the mean kinetic energy of the flow, leading to the observed peaks in  $E_V/E_P$  and  $E_{V\perp}/E_P$ . It is also interesting to notice that for  $Fr \lesssim 0.2$  we have that  $E_V/E_P \approx E_{V\perp}/E_P$ , which can be interpreted as  $E_V \approx E_{V\perp}$ : almost all of the kinetic energy  $E_V$  is due to the energy from the horizontal components of the velocity field,  $u$  and  $v$ . This is likely due to a more efficient generation of horizontal winds at low  $Fr$ , that makes the horizontal kinetic energy  $E_{V\perp}$  dominating the ratio.

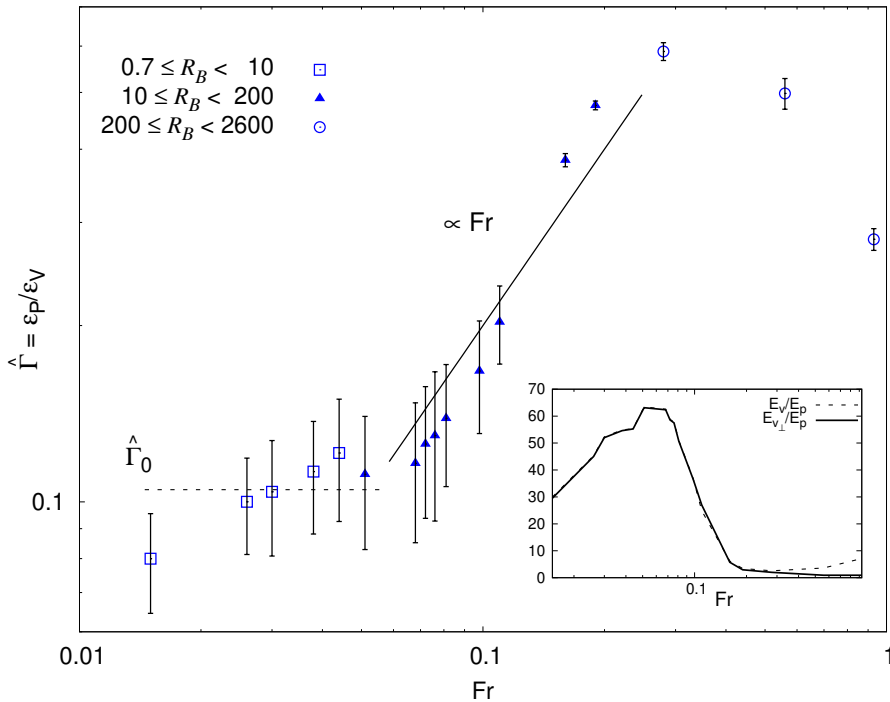


FIGURE 2.12: Irreversible mixing efficiency parameter  $\hat{\Gamma}$ , with  $E_V/E_P$  and  $E_{V\perp}/E_P$  in the inset, as a function of  $Fr$  in log-log scale;  $\hat{\Gamma}_0$  is the estimated saturation value obtained in the limit of small Froude numbers.



## 2.2 Lagrangian particle dispersion in stratified flows with rotation

To extend our characterization of mixing in anisotropic turbulence we investigated the Lagrangian velocity and acceleration statistics as well as particle dispersion in rotating and stratified turbulent flows [7]. We vary this time both the Froude number  $Fr$  and the Rossby number  $Ro$  while keeping fixed the ratio  $N/f = 5$  (see Chap. 1). Along with the value of  $Fr$  and  $Ro$ , the buoyancy Reynolds number  $R_{IB} = \beta R_B$  (see Chap. 1) is also used to identify the different runs. Lower values of  $R_{IB}$  indicate that waves are stronger and dominate over turbulence in the flow. As previously done for the purely stratified runs, we inject  $\sim 1.5$  million of Lagrangian particles when turbulence is fully developed and use them to collect velocity and acceleration statistics. The shape of the time-averaged energy spectra for each run are used to confirm they reached a turbulent state. We observe a slope close to  $-5/3$  in the energy spectra of runs with  $R_{IB} > 1$  (weak rotation and stratification) while runs with  $R_{IB} < 1$  display a steeper slope, closer to a Bulgiano-Obukhov scaling (see Chap. 1) [4, 51]. The different behaviours of the spectra also emerge when identifying the runs using the quantity  $\xi^u = [\langle u_{\perp}^2 \rangle / \langle u_{\parallel}^2 \rangle]^{1/2}$ , which provides a measure of the anisotropy of the flow. A value of  $\xi^u$  close to 1 indicates that the flow is almost isotropic,  $\xi^u = 1$  being an isotropic flow. As expected, we find values of  $\xi^u$  larger than 1 for the runs where rotation and stratification are stronger ( $R_{IB} < 1$ ). This anisotropy ratio can also be extended to the acceleration:  $\xi^a = [\langle a_{\perp}^2 \rangle / \langle a_{\parallel}^2 \rangle]^{1/2}$ . In this case, for the strongly rotating and stratified runs we find smaller values compared to  $\xi^u$ , suggesting that the effects of anisotropy on the small scales is less impactful. In order to gauge the effects of anisotropy in the flow we investigate the Lagrangian velocity and acceleration statistics. Consistently with what was done in the purely stratified runs, we compute the PDFs and kurtoses of the horizontal and vertical components of the Lagrangian velocity. The results obtained allow to identify two distinct regimes based on the value of  $R_{IB}$  or on the anisotropy  $\xi$ . Runs with high anisotropy ( $R_{IB} < 1$ ) display broader tails compared to the others in the PDFs of the vertical velocity. We also find high values of the kurtosis, much higher than the Gaussian reference value of 3, for the vertical velocity when  $R_{IB} < 1$ . The high kurtosis of the vertical velocity and the non-Gaussian PDFs confirm the presence of large-scale extreme events in the flow even in the case of rotating and stratified turbulent flows. On the other hand, for all the runs analyzed, the PDFs of the horizontal velocity is closer to a Gaussian, with its kurtosis being close to 3. Again, this result is consistent with the results obtained in purely stratified flows.

The PDFs of the Lagrangian acceleration also show a dependence on the anisotropy, although its effects are less significant when compared to the vertical velocity. We note that all the PDFs of the Lagrangian acceleration components have tails broader than a Gaussian. In this case, when  $R_{IB} < 1$ , we observe that the PDF of the horizontal acceleration rapidly decays compared to the runs with  $R_{IB} > 1$ . For all the runs we find that the kurtosis of both the horizontal and the vertical acceleration is rather high and far from the Gaussian reference value of 3.

Finally, we characterize single-particle dispersion and analyze its behaviour as a function of the anisotropy of the flow. We define dispersion as the mean-square displacement of a particle from its initial position [48] and consider horizontal and vertical dispersion separately. Fig. 2.13 shows the evolution with time of the mean-square displacement for horizontal (left panel) and vertical (right panel) directions. We first note that in the runs with rotation and stratification, vertical dispersion is inhibited compared to the horizontal dispersion of the same run. The difference between the

two is quantified in Fig. 2.13, where it can be seen that particles travel longer distances in the horizontal direction. It is also clear from Fig. 2.13 (right) that as  $R_{IB}$  decreases, hence when  $Fr$  decreases, particles travel smaller distance in the vertical direction in the same time. This effect is strongly emphasized at larger times and is due to vertical motion being inhibited when stratification is present. We also observe from Fig. 2.13 that the scaling of both horizontal and vertical dispersion is the same for all the runs at small times. Independently of the parameters of the run, all of them show a  $t^2$  scaling. A transition to a diffusive regime is observed in the vertical direction for the runs with  $R_{IB} > 1$  at later times. Runs with  $R_{IB} < 1$  do not reach this regime, as their evolution is slower than a linear scaling. They show, however, a slow approach to a diffusive regime which could have been probably reached by integrating the trajectories for longer times.

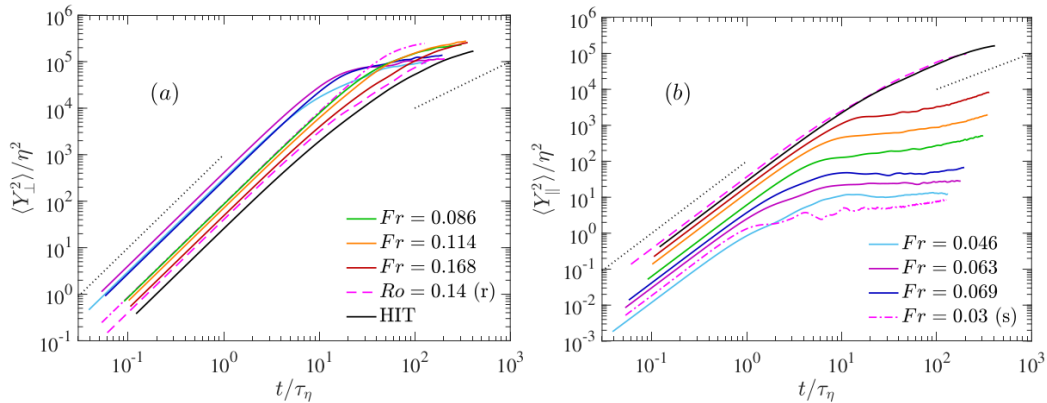


FIGURE 2.13: Mean square displacement as a function of time in the (a) perpendicular (horizontal) direction and (b) parallel (vertical) direction. All quantities are normalized by Kolmogorov scales. The dashed lines represent slopes 2 and 1 at short and long times respectively. [7]

We note from this analysis that extreme events seems to not play a role in the single-particles dispersion. We must consider, however, that the extreme vertical drafts are quite rare in the flow since they reside in the tails of the PDFs. Thus, at a given time, it is reasonable to assume that the majority of the particles is not crossing one of these extreme events. If we consider that, in order to compute the dispersion we average over all the particles then the effect of the extreme events may be suppressed. This might impact the evolution of the dispersion and could be the reason why we cannot appreciate a significant contribution of the extreme events to dispersion. Indeed, we observe that the relative distance between two close particles in a stratified run grows rapidly when they encounter extreme events. Fig. 2.14 shows the trajectories of two close particles and their final positions (indicated by the full dots) in a purely stratified flow with  $Fr = 0.076$ . Conversely, particles which do not encounter extreme events tend to remain close to each other. Thus, we leave for future works a characterization of two-particles statistics in order to quantify the effect of vertical drafts on the particles dispersion.

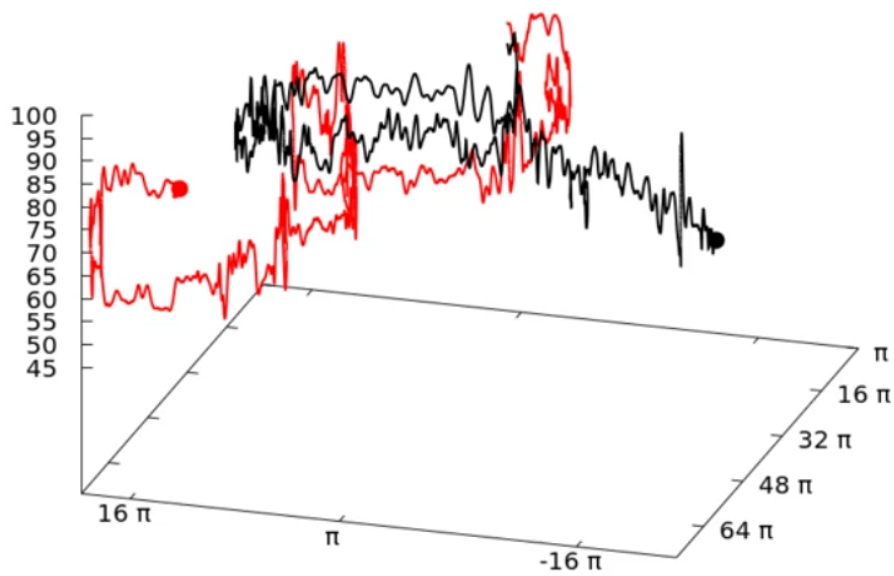


FIGURE 2.14: Trajectories of a pair of Lagrangian particles in the purely stratified run with  $Fr = 0.076$ . The two particles are close at  $t = 0$  but their trajectories rapidly diverges as they encounter vertical drafts. The final positions of the particles are indicated by the full dots.

# Vertical drafts and mixing in stratified turbulence: sharp transition with Froude number

F. Feraco<sup>1,2</sup>, R. Marino<sup>1</sup>, A. Pumir<sup>3</sup>, L. Primavera<sup>2</sup>, P.D. Mininni<sup>4</sup>, A. Pouquet<sup>5,6</sup> and D. Rosenberg<sup>7</sup>

<sup>1</sup>*Laboratoire de Mécanique des Fluides et d'Acoustique,*

*CNRS, École Centrale de Lyon,*

*Université Claude Bernard Lyon 1,*

*INSA de Lyon, F-69134 Écully, France.*

<sup>2</sup>*Dipartimento di Fisica, Università della Calabria, Italy.*

<sup>3</sup>*École Normale Supérieure de Lyon, Lyon France.*

<sup>4</sup>*Departamento de Física,*

*Facultad de Ciencias Exactas y Naturales,*

*Universidad de Buenos Aires, and IFIBA,*

*CONICET, Buenos Aires 1428, Argentina.*

<sup>5</sup>*Laboratory for Atmospheric and Space Physics,*

*University of Colorado, Boulder, CO 80309, USA.*

<sup>6</sup>*National Center for Atmospheric Research,*

*P.O. Box 3000, Boulder, CO 80307, USA.*

<sup>7</sup>*1401 Bradley Drive, Boulder CO 80305, USA.*

We investigate the large-scale intermittency of vertical velocity and temperature, and the mixing properties of stably stratified turbulent flows using both Lagrangian and Eulerian fields from direct numerical simulations, in a parameter space relevant for the atmosphere and the oceans. Over a range of Froude numbers of geophysical interest ( $\approx 0.05 - 0.3$ ) we observe very large fluctuations of the vertical components of the velocity and the potential temperature, localized in space and time, with a sharp transition leading to non-Gaussian wings of the probability distribution functions. This behavior is captured by a simple model representing the competition between gravity waves on a fast time-scale and nonlinear steepening on a slower time-scale. The existence of a resonant regime characterized by enhanced large-scale intermittency, as understood within the framework of the proposed model, is then linked to the emergence of structures in the velocity and potential temperature fields, localized overturning and mixing. Finally, in the same regime we observe a linear scaling of the mixing efficiency with the Froude number and an increase of its value of roughly one order of magnitude.

## I. INTRODUCTION

Intermittency is a hallmark of fully developed turbulence in fluids. Contrary to the predictions of the Kolmogorov's original theory [1], both experiments and numerical simulations show that dissipation exhibits intense (intermittent) fluctuations, localized in space and time, giving rise to a characteristic behavior of quiescence interrupted by local bursts of high amplitude [2, 3]. This phenomenon, known as small-scale intermittency, is widely observed in the atmosphere [4], where it can explain the formation of rain droplets [5, 6], and in the ocean in the form of highly concentrated and sporadic dissipation [7, 8]. Small-scale intermittency is often characterized by the strong deviations from Gaussian statistics of the probability distribution functions (PDF) of velocity and temperature gradients. Intermittency, however, is not only present at the smallest scales. In transitional pipe flows [9], in the problem of mixing of a passive scalar by a turbulent flow [10], in the solar wind [11], and for stratified flows as in the Earth's atmosphere [12] and in the oceans, non-stationary energetic bursts at scales comparable to that of the mean flow are also observed [8, 13–15]. The origin of this large-scale intermittency in stratified turbulence and the mechanisms by which it may affect overturning and mixing in geophysical flows are still un-

clear. In the present letter we characterize the vertical drafts occurring at a large scale, using direct numerical simulations (DNS) of stably stratified Boussinesq flows, varying the buoyancy frequency. The large scale intermittent behavior is studied here by direct integration of the Boussinesq equations, without any parametrization of the smaller scales and with periodic boundaries, contrary to what was done in previous work. In particular, we relate the wings of the PDFs of the vertical component of Lagrangian and Eulerian velocities and of the potential temperature, to large-scale bursts, which result from the interplay of gravity waves and turbulent motions in a range of Froude numbers relevant to geophysical flows. This is explained with the help of a simple one-dimensional (1D) model, which captures the extreme events [15] and the sharp transition observed in our simulations between Gaussian and non-Gaussian PDFs. Finally we provide clear evidence of the connection between local overturning events and mixing in stratified flows – characterized through the gradient Richardson number [16], the mixing efficiency and the ratio of kinetic to potential energy – with the emergence of large-scale intermittency and structures.

## II. EQUATIONS, PARAMETERS, AND RUNS

The Boussinesq approximation assumes that the variations of density are small and depend linearly on temperature; they are neglected, except in the expression of the buoyancy force. The incompressible velocity field  $\mathbf{u}$  ( $\nabla \cdot \mathbf{u} = 0$ ) and temperature, expressed in suitable units satisfy:

$$\begin{aligned} \partial_t \mathbf{u} + (\mathbf{u} \cdot \nabla) \mathbf{u} &= -\nabla p - N\theta \hat{z} + \mathbf{F} + \nu \nabla^2 \mathbf{u} & (1) \\ \partial_t \theta + \mathbf{u} \cdot \nabla \theta &= Nw + \kappa \nabla^2 \theta & (2) \end{aligned}$$

where  $\theta$  is a temperature fluctuation relative to the mean  $\bar{\theta}$ ,  $\nu$  is the kinematic viscosity, and  $\kappa = \nu$  is the thermal diffusivity. The velocity field is written as  $\mathbf{u} = (\mathbf{u}_\perp, w)$  and the flows in this study are subject to a random isotropic mechanical forcing  $\mathbf{F}$  (as also described in [17]), applied in a wavenumber shell:  $k_F = 2\pi/L_f \in [2, 3]$ , the size of the periodic three-dimensional computational box being  $L_0 = 2\pi$ . Finally,  $N = [-g\partial_z \bar{\theta}/\theta_0]^{1/2}$  is the Brunt-Väisälä frequency. We define the Reynolds and Froude numbers, the dimensionless parameters of the problem:  $Re = UL/\nu$ ,  $Fr = U/LN$ , where  $U, L$  are respectively the characteristic velocity and the integral scale of the fluid. The buoyancy Reynolds number,  $R_B \equiv Re Fr^2 = (\ell_{Oz}/\eta)^{4/3}$ , where  $\ell_{Oz} \equiv (\varepsilon_V/N^3)^{1/2}$  and  $\eta \equiv (\varepsilon_V/\nu^3)^{-1/4}$  are the Ozmidov and Kolmogorov dissipation lengths, and  $\varepsilon_V \equiv \nu \langle (\nabla \mathbf{u})^2 \rangle$  is the kinetic energy dissipation rate.  $R_B$  measures the relative strength of buoyancy and dissipation: for  $R_B = 1$ , the Ozmidov scale at which dispersive and nonlinear effects balance is at the Kolmogorov scale. To solve these equations numerically we use the Geophysical High-Order Suite for Turbulence (GHOST) code, a versatile pseudo-spectral framework parallelized with a hybrid MPI/OpenMP method [18]. All computations are performed on isotropic grids of  $512^3$  points, altogether for of the order of  $40 \tau$ , where  $\tau = L/U$  is the turn-over time. Together with the Eulerian velocity and temperature field, we determined also the trajectories of tracer particles in the flow, whose positions  $\mathbf{X}(\mathbf{X}_0, t)$  satisfy  $\partial_t \mathbf{X}(\mathbf{X}_0, t) = \mathbf{u}(\mathbf{X}(\mathbf{X}_0, t), t)$  (with  $\mathbf{X}(\mathbf{X}_0, 0) = \mathbf{X}_0$ ). We followed  $n \approx 1.5 \cdot 10^6$  particle trajectories, initially uniformly distributed in space. They are injected randomly after turbulence becomes fully developed, *i.e.*, after the dissipation in the flow has reached its maximum (see Fig. 2), and their trajectories are determined for a duration of 6 to 10 turnover times. Lagrangian temporal statistics are always collected throughout the entire time of integration. To characterize the statistical distribution of a fluctuating variable, we introduce the dimensionless fourth-order moment (kurtosis), defined as:

$$K_\alpha = \langle \alpha^4 \rangle / \langle \alpha^2 \rangle^2 \quad (3)$$

where  $\alpha$  is the generic field and averages can be taken over the entire box, horizontal planes, time, or over ensembles of particles as specified below. The Gaussian reference

value of the kurtosis is equal to 3. The Reynolds number varies roughly by 35% throughout the parametric study, from  $\approx 2600$  to  $\approx 3900$ . All the runs have been initialized with zero potential temperature and a random velocity field with energy distributed on spherical shells centered on the wavenumber  $k_0 = 2\pi/L_0$  in the range  $k_0 = [2, 3]$ .

## III. LARGE SCALE INTERMITTENCY IN STRATIFIED FLOWS

As a result of the stratification, the Lagrangian particles mostly wander around in horizontal planes, with sharp vertical excursions which leave a signature in the PDFs of  $w$  and  $\tilde{w}$ , respectively the vertical component of the Eulerian velocity field and the vertical velocities of the Lagrangian particles. Figure 1 gives both the instantaneous PDFs of  $w$ , each corresponding to a dotted curve (computed every 1000 time-steps of the DNS, within the domain of integration of the particles), and PDFs of the Lagrangian particles velocity  $\tilde{w}$  (solid red curves), for three different Froude numbers. In all plots, the Lagrangian PDFs appear, up to statistical errors, as the time average of the instantaneous Eulerian PDFs. In the case shown in the middle panel ( $Fr = 0.076$ ), the wings for high values of  $w$  and  $\tilde{w}$  are significantly broader than the Gaussian wings, with a kurtosis of the Lagrangian particles velocity  $K_{\tilde{w}} \approx 10.44$ . This is the signature of the occurrence of extreme events at some time in the evolution of the flow, in some regions of the spatial domain. The departures from the Gaussian behavior are very weak for the cases with smaller and larger Froude number displayed in the lateral panels ( $Fr = 0.03$  and  $Fr = 0.28$ , respectively left and right), with the kurtosis becoming  $K_{\tilde{w}} \approx 3$  for the smallest and highest  $Fr$  considered in this parametric exploration (see Table I). Fig. 1 also shows the PDFs of the horizontal Lagrangian components of the velocity field  $\tilde{u}_\perp$  (solid blue line) that is markedly below the Gaussian distribution, in all 17 runs. For some of the stratified flows under study, the instantaneous PDFs of the Eulerian vertical velocity  $w$  vary strongly over time, as it is for run 9 in Fig. 1 (dotted lines, middle panel). This time-dependence leads to strong fluctuations of the corresponding Eulerian PDFs' kurtosis,  $K_w$ , shown in Fig. 2 ( $Fr = 0.076$ ). The kurtosis of the Lagrangian PDFs,  $K_{\tilde{w}}$ , resulting from global spatio-temporal statistics of  $1.5 \cdot 10^6$  particles' vertical velocities (over the entire integration time) is plotted in Fig. 5 against the Froude number for the runs in Table I. It is noteworthy that the curve  $K_{\tilde{w}}(Fr)$  is characterized by a non-monotonic behavior, showing a rapid increase and then decrease of the Lagrangian kurtosis in a sharp range between  $Fr \approx 0.05$  and  $\approx 0.3$ , with a peak centered around  $Fr \approx 0.076$ . The kurtosis of temperature fluctuations (not shown) also deviates from 3 in the same range of parameters. This result provides clear evidence that stably stratified turbulent flows are characterized by large scale intermittency and strong vertical drafts in a well de-

Id	1	2	3	4	5	6	7	8	9	10	11	12	13	14	15	16	17
$Re$ ( $\times 10^3$ )	3.8	3.8	3.8	3.8	3.8	3.8	3.9	3.8	<b>3.8</b>	3.8	3.7	3.6	3.0	2.6	2.6	2.8	2.9
$Fr$	.015	.026	.030	.038	.044	.051	.068	.072	<b>.076</b>	.081	.098	.11	.16	.19	.28	.56	.93
$K_{\tilde{w}}$	3.11	3.17	3.07	3.06	3.17	3.41	7.40	9.50	<b>10.44</b>	9.39	8.86	5.63	3.87	3.53	3.30	2.95	3.00
$\ell_{Oz}$	.07	.014	.018	.024	.029	.037	.056	.061	<b>.067</b>	.076	.11	.14	.39	.65	1.25	3.66	8.00
$R_B$	.9	2.5	3.4	5.6	7.3	10.2	17.7	19.7	<b>22.1</b>	25.2	35.9	47.5	75.2	90.9	201	895	2560

TABLE I: Table of the runs. Reynolds, Froude and buoyancy Reynolds numbers are respectively  $Re$ ,  $Fr$  and  $R_B$ ;  $\ell_{Oz}$  is the Ozmidov scale;  $K_{\tilde{w}}$  is the kurtosis of the Lagrangian PDFs computed over the entire integration interval of the particles. Run 9 (boldface) has the highest  $K_{\tilde{w}}$  and is used as a reference case for the visualizations in Figures 3 and 4.

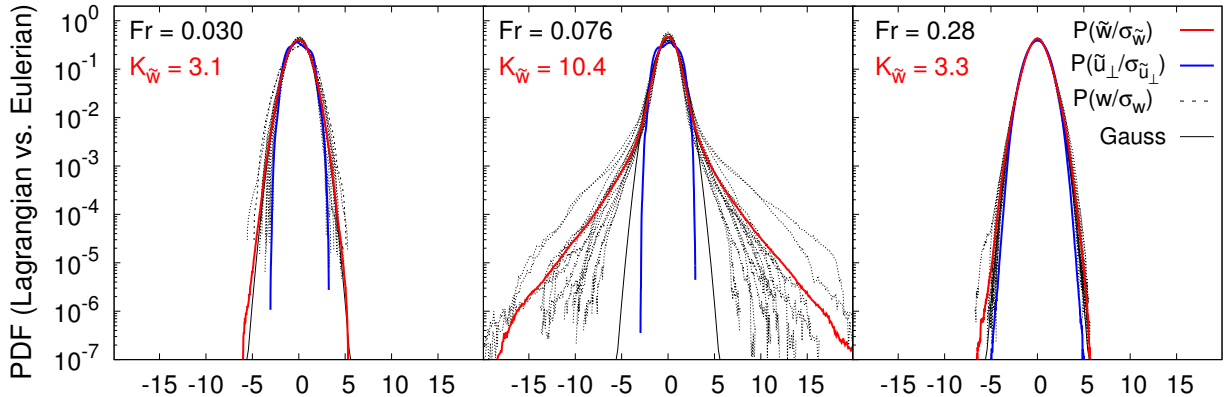


FIG. 1: PDFs of the Lagrangian vertical velocity  $\tilde{w}$  (solid line, red), Lagrangian horizontal velocity  $\tilde{u}_\perp$  (solid line, blue) and instantaneous Eulerian vertical velocity  $w$  at several times (all dashed lines, black), for runs 3 (left), 9 (middle) and 15 (right). All quantities are normalized by their dispersion. A Gaussian PDF is indicated as reference in each panel (solid line, black).

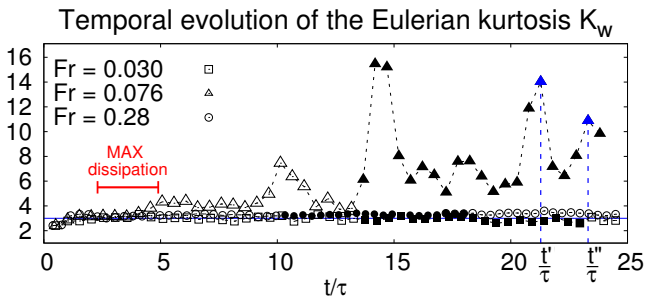


FIG. 2: Kurtosis of the Eulerian vertical velocity ( $w$ ) as a function of time for runs 3, 9 and 15. Each point is the statistical moment (eq. 3) of the corresponding instantaneous PDFs showed in Fig.1 (dashed lines). Solid symbols identify the periods of integration of the Lagrangian particles, injected systematically after the peak of the dissipation, here indicated with a red segment for the runs displayed. Points in blue identify the relative maxima at which the Eulerian fields of run 9 ( $Fr = 0.076$ ) are rendered in Figures 3 and 4.

finer regime of stratification. It is also worth to point out that for all the runs outside the range  $0.05 < Fr < 0.3$  no large-scale intermittency is detected from Lagrangian and Eulerian statistics and the kurtosis of the instantaneous Eulerian PDFs does not fluctuate and is constantly close to the Gaussian reference value ( $K_w \approx 3$ ); this is illustrated in Figures 1 and 2 for the runs with  $Fr = 0.03$  and  $= 0.28$ . One last important remark is that all the

runs in the intermittent regime identified here have buoyancy Reynolds number  $10 < R_B < 10^2$ , whereas values of the Lagrangian kurtosis  $K_{\tilde{w}}$  compatible with the Gaussian case are found for runs with  $R_B \sim 1$  as well as  $R_B \sim 10^3$  (Table I). To better understand the origin of the strong updrafts and downdrafts in the vertical velocity, and their variation with  $Fr$ , we now introduce a simple model.

#### IV. A MODEL FOR THE VERTICAL DRAFTS

It was found in [15] that the intermittent behavior observed in a stratified fluid can be explained by a 1D model for the vertical velocity and the temperature based on [19, 20]. In this model, the strong and fast events occur because of an amplification in the formation of vertical negative velocity gradients resulting from the interplay between the time scales of the waves and the nonlinearity. We generalize here this model adding both forcing and dissipation, in order to achieve a steady state and to control the growth of  $w$ . To this end we reduce Eqs. (1,2) to the 1D case, dependent only on the  $z$  coordinate, and with  $\mathbf{u}_\perp = 0$ . We derive the equations with respect to  $z$  using  $\partial_z(\partial_t a + w\partial_z a) = d_t(\partial_z a) + (\partial_z w)(\partial_z a)$  (for any field  $a$ , and where  $d_t$  is the Lagrangian derivative in the vertical direction), and finally we convert spatial derivatives to increments by assuming fields are smooth on an

arbitrary scale  $\ell_z$ , and thus  $\delta a \approx \partial_z a \ell_z$ . The resulting model has the same overall structure as the Boussinesq model, Eqs.(1,2), with viscous damping and mechanical forcing finally re-introduced in an empirical way:

$$\frac{d\delta w}{dt} = -\frac{\delta w^2}{\ell_z} - N\delta\theta - \nu\frac{\delta w}{\ell_z^2} + f \quad (4)$$

$$\frac{d\delta\theta}{dt} = -\frac{\delta w\delta\theta}{\ell_z} + N\delta w - \kappa\frac{\delta\theta}{\ell_z^2} \quad (5)$$

For a fixed value of  $\ell_z$  and for high enough  $N$ , waves prevail over turbulence, whereas for small  $N$ , turbulence prevails over waves. At intermediate values, a different behavior occurs, with a rapid increase of negative velocity field increments [15]. This model can be seen as a 1D approximation to Lagrangian trajectories in a stratified flow, and at fixed  $N$  with only one free parameter, the length scale  $\ell_z$  representing the dominant gradients. The model was integrated using  $N$ ,  $\nu$  and  $\kappa$  from the simulations (see Table I), and for each case we ran an ensemble of 20 realizations (or Lagrangian particles) up to  $t = 20$ , using a white-noise random forcing  $f$  with frequencies between  $N/8$  and  $N$  to mimic the flat Lagrangian spectrum of the vertical velocity observed in stably stratified turbulence, the so-called Garrett-Munk spectrum [21]. The amplitude of  $f$  is the only tunable parameter that is not taken directly from the DNS and it was fixed to lead to finite amplitude solutions even in the weakly stratified cases (i.e. for moderate  $N$ ). We adjusted the free parameter  $\ell_z$  by assuming that the extreme events are the result of local shear instabilities or overturning (see Fig. 3, right), and thus the vertical scale at which these events take place can be expected to be proportional to the Ozmidov scale in each run,  $\ell_z = \alpha \ell_{Oz}$  (note this scale also separates the boundary between wave- and eddy-dominated scales). In the following we use  $\alpha = 4$  which gives the best quantitative agreement with the DNS, but any choice for  $\alpha$  of order unity gives the same qualitative results. Other choices for  $\ell_z$ , such as  $\ell_z = L_B = 2\pi U/N$  do not give results compatible with the DNS, which can be expected since, at the buoyancy scale  $L_B$ , the vertical Froude number is unity, and thus the behavior of the model becomes independent of  $Fr$ . Figure 5 (top) shows the kurtosis  $K_{\bar{w}}$  of the Lagrangian vertical velocities for all the DNS runs of this parametric study, together with the kurtosis of the Lagrangian field  $\delta w$  generated by the 1D model initialized with the corresponding DNS parameters (red line). Each run is characterized by a different Froude number in a range of values spanning over one order of magnitude, from  $\approx 0.01$  to  $\approx 1$  (see Table I). Note the behavior of both kurtoses confirms the results in Fig. 1: for intermediate values of  $Fr$  the vertical velocity becomes very intermittent with values of the Lagrangian kurtosis  $K_{\bar{w}}$  larger than 10. Considering its simplicity, the model reproduces qualitatively remarkably well the behavior found in the DNS. All quantities display a sharp peak for  $Fr \approx 0.076$ , with a decrease for higher Froude numbers. What is striking here is the sharpness of the peak in  $Fr$  for all variables, as well as the asymmetry

between the rising and descending phases of this transition. Such a sharp variation in  $Fr \approx 0.076$  may be surprising; it evokes a wave resonance as occurs in critical layers when the flow velocity is equal to the wave phase speed, leading to the creation of jets. Indeed, similarly high values of kurtosis are found in atmospheric data in the upper boundary layer, and are interpreted as the signature of a global (large-scale) intermittency for a turbulence that is patchy and inhomogeneous [13]. In the model, both the peak and the asymmetry arise as the result of two competing effects: for large  $Fr$  the nonlinear term dominates, amplifying negative velocity increments on a time scale of the turnover time; for small  $Fr$  the linear term dominates, resulting in wave dynamics. But for intermediate values of  $Fr$  the time scales of the two terms are similar, with an acceleration in the nonlinear amplification resulting from the slightly faster wave time scale. To the right and to the left of the peak, the nature of the dominant terms is different. We stress that the transition discussed here strongly differs from that observed when the buoyancy Reynolds number,  $R_B$ , is varied; this transition affects the small-scale flow properties (see, e.g., [21–23]).

## V. STRUCTURES, OVERTURNING AND MIXING

Thanks to a combined implementation of global spatio-temporal Lagrangian statistics and instantaneous Eulerian statistics we are able to show how the broad distributions observed in previous sections can in fact be linked to physical structures. Fig. 3 (left) provides the three-dimensional rendering of the vertical velocity  $w$  for run 9,  $Fr = 0.076$ , at the time  $t'/\tau$  when a local maximum of the instantaneous Eulerian kurtosis is attained based on the curve  $K_w(t'/\tau)$  in Fig.2. The side plot in Fig. 3 (left) shows the variation of the kurtosis obtained from integrations of the statistics in a single horizontal plane, plotted as a function of altitude,  $K_w(z, t'/\tau)$ , which allow for the identification of the planes containing the strongest structures. On average in the flow, the variable is quasi-Gaussian, with  $K_w(z, t'/\tau) \sim 3$ , except at some rare vertical positions, where the fluctuations of  $w$  are much larger than the background fluctuations, with strong non-Gaussian properties. Similar conclusions can be drawn by analyzing the potential temperature  $\theta$  in physical space, shown in Fig. 4. This bursty behavior at the large scales, in space and in time, is stronger in runs 7 to 12, resulting in the observed non-stationarity of the instantaneous Eulerian PDFs (Fig. 1, middle, and Fig. 2) and in the emergence of structures, Fig.3 (left) and Fig. 4. The intermittent behavior also affects the smallest scales of the flow: the dissipation and the gradient fields also have rare, intense structures embedded in the quiet flow (not shown, see [15]).

Extreme updrafts and downdrafts affect the vertical transport. The product of the vertical temperature flux

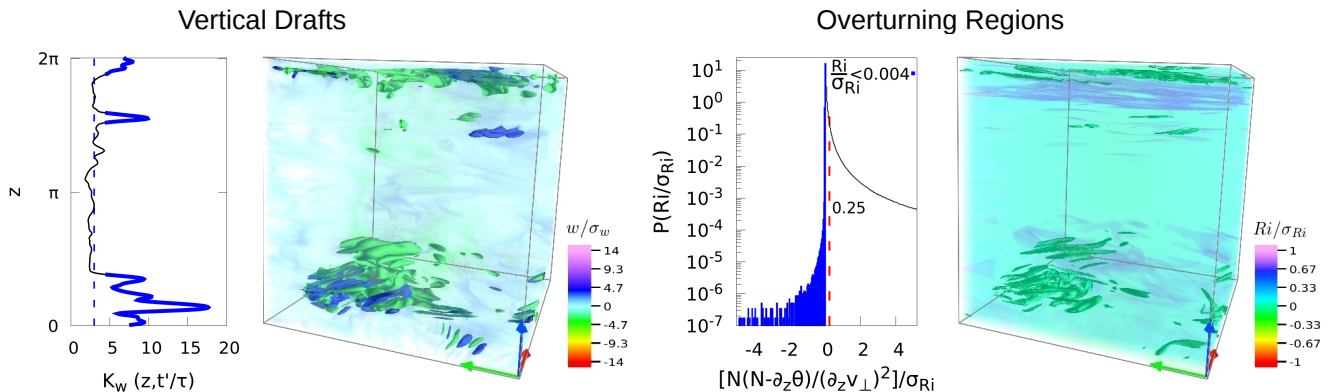


FIG. 3: *Left: Variation with height of the kurtosis of the Eulerian vertical velocity ( $w$ ), computed by plane for run 9 at fixed time ( $t'/\tau$ , relative maximum of  $K_w(t/\tau)$ , Fig.2), together with the rendering of  $w$  for the same run. A threshold is used to highlight the presence of intense vertical drafts ( $> 3\sigma_w$ ) which appear as large-scale structures emerging in distinct planes that correspond to those with the largest values of the kurtosis. Right: PDF of the gradient Richardson number ( $Ri = N(N - \partial_z \theta)/(\partial_z v_\perp)^2$ ) normalized by its variance ( $\sigma_{Ri}$ ), together with the rendering of its point-wise values where regions prone to develop overturning, with  $Ri/\sigma_{Ri} < 0.004$ , are visualized using opaque colors.*

with the Brunt-Väisälä frequency  $N$  is the so called buoyancy flux  $B_f = N \langle w\theta \rangle$ , routinely used to characterize mixing in stratified flows. There are several ways to define the mixing efficiency (see [22, 24, 25] and references therein), one possibility being to take the ratio of the buoyancy flux to the rate of kinetic energy dissipation  $\varepsilon_V$  in the momentum equation. Following [22, 26], we define here the irreversible mixing efficiency  $\hat{\Gamma}$  using the potential energy dissipation rate  $\varepsilon_P = \kappa(|\nabla\theta|^2)$  instead of  $B_f$ , so one can write  $\hat{\Gamma} = \varepsilon_P/\varepsilon_V$ . This definition is based on the assumption that the mixing efficiency should only account for the irreversible conversion of available potential energy into background potential energy, quantified by  $\varepsilon_P$ .

$\hat{\Gamma}$  is plotted in Fig. 5 (bottom) against the Froude number for all the runs in table I. Very interestingly, we find that in a parameter space compatible with regions of the atmosphere and the oceans, namely  $0.05 < Fr < 0.3$ , with  $R_B > 10$ , the irreversible mixing efficiency scales linearly with the Froude number ( $\hat{\Gamma} \propto Fr$ ) and it increases by roughly one order of magnitude, before dropping for  $Fr > 0.3$  consistently with [22, 26]. This is also the range of parameters in which maximal kurtosis of the Lagrangian vertical velocity  $\tilde{w}$  and large-scale intermittency attain as a result of our study (Fig. 5, top). Note that the scaling  $\hat{\Gamma} \propto Fr$  observed here for values of the Froude number of geophysical interest is different from the scaling reported in [26] ( $\hat{\Gamma} \propto Fr^{-2}$ ) obtained in the case of weak stratification ( $Fr > 1$ ). For  $Fr \ll 0.05$  we find a saturation value  $\hat{\Gamma}_0 \sim 10^{-1}$ , compatible with the proxy of the mixing efficiency commonly used in the ocean community ( $\approx 0.2$ ) [27].  $\hat{\Gamma}$  exhibits as well a non-monotonic dependence on the buoyancy Reynolds number (see table I), with a peak value obtained for  $R_B \sim 200$ , consistently with [25]. To complement our characterization of the mixing, we finally evaluated for all

runs the ratio of the volume-averaged kinetic to potential energies  $E_V/E_P$ , which can be linked to wave-eddy partition [28]. This quantity is plotted in the insert of Fig. 5 (bottom), together with the ratio of the volume-averaged horizontal kinetic to potential energies  $E_{V\perp}/E_P$ , versus the Froude number. These ratios provide the simplest measure of the partition of energy between kinetic and potential modes at all scales, which is another way to estimate the efficiency of the mixing. Both  $E_V/E_P$  and  $E_{V\perp}/E_P$  peak in the vicinity of the maximal value of  $K_{\tilde{w}}(Fr)$ , obtained for  $Fr \approx 0.076$  (Fig. 5, top). This suggests the possibility that in flows characterized by strong large-scale intermittency the mixing enhancement occurs due to large scale overturning, with a consequent increase of the kinetic over potential energy (both integrated over the volume and in Fourier space). It is also interesting to notice that  $E_V/E_P \approx E_{V\perp}/E_P$ , perhaps due to a more efficient generation of horizontal winds in this regime, that makes the horizontal kinetic energy dominate the ratio.

In order to investigate the tendency of stratified flows to develop local overturning and the link with the emergence of large scale intermittency and structures, we have analyzed the statistics of the point-wise gradient Richardson number  $Ri = N(N - \partial_z \theta)/(\partial_z v_\perp)^2$  computed on the instantaneous Eulerian fields. This analysis allowed to reveal a clear spatio-temporal correlation between the presence of structures in the velocity fields – originating from strong vertical drafts – and patches of the flow characterized by values of  $Ri$  indicating the most unstable regions of the domain. As an example, in Fig. 3 we propose the comparison between the rendering of the Eulerian vertical velocity  $w$  for run 9 – where only vertical drafts stronger than three standard deviations  $\sigma_w$  are visualized with opaque colors (left panel) – and the visualization of the point-wise gradient Richardson number for the same run, at the same time (right panel). Only the



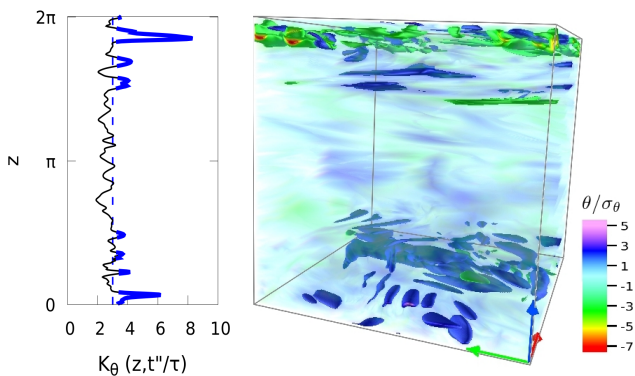


FIG. 4: Variation with height of the kurtosis of the potential temperature ( $\theta$ ), computed by plane for run 9 at fixed time ( $t''/\tau$ , relative maximum of  $K_w(t/\tau)$ , Fig.2), together with the rendering of  $\theta$  for the same run. A threshold is used to highlight with opaque colors the presence of hot and cold patches with temperature fluctuations larger than 3 standard deviations ( $\sigma_\theta$ ), corresponding here to the planes with the largest values of the kurtosis.

values below the threshold 0.004 in the PDF of  $Ri/\sigma_{Ri}$  (side plot in Fig. 3, right) are rendered without transparency, which makes it very clear the spatial correlation between overturning regions and vertical velocity structures in the flow. These structures are in turn responsible for the fat wings in the PDFs of the vertical Lagrangian and Eulerian velocities we discussed previously. This correlation pattern has been observed for runs in the range  $0.05 < Fr < 0.3$  and at different times in each run, being more evident in the proximity of the local maxima of  $K_w(t/\tau)$  (see Fig. 2).

## VI. DISCUSSION AND CONCLUSIONS

We have shown that very strong and intermittent large-scale vertical drafts can develop in stratified turbulence in a distinct range of Froude number that also reflects an abrupt change in the behavior of the vertical velocity statistics and fluid mixing properties. Similar results of bursty events in the vertical velocity have been obtained in [29] using DNS of the stable planetary boundary layers with comparable  $Re$ , no-slip boundary conditions in the vertical direction of a box with an aspect ratio  $\sim 10$ . These authors find a peak in the number of bursting events for Froude numbers compatible with the range we identified here ( $0.05 < Fr < 0.3$ ) in which we observe large-scale intermittency with a peak of the kurtosis of the Lagrangian vertical velocity ( $K_{\bar{w}}$ ) obtained for  $Fr \approx 0.76$ . Bursts in stably stratified turbulence were also reported in [15]. In the former case, the observed intermittency is mostly associated with interactions with the boundary, a situation which we do not have in the present study, while in the latter, albeit for only two values of  $Fr$ , similar extreme events were found.

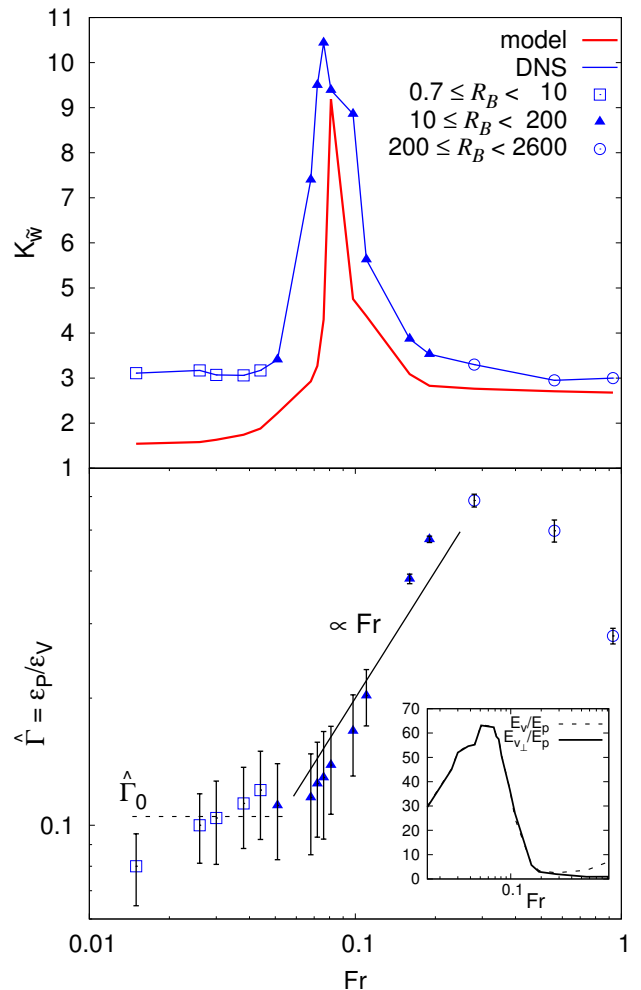


FIG. 5: Top: Kurtosis of the Lagrangian vertical velocity ( $\bar{w}$ ) from the DNS and ( $\delta w$ ) from the 1D model (red line), as a function of  $Fr$ . Bottom: irreversible mixing efficiency  $\hat{\Gamma}$ , with  $E_v/E_p$  and  $E_{v_\perp}/E_p$  in the inset, as a function of  $Fr$ , all from the DNS;  $\hat{\Gamma}_0$  is the estimated saturation value obtained in the limit of small Froude numbers. The different symbols are used to identify ranges in terms of the buoyancy Reynolds number  $R_B$  and highlight the non-monotonic trend of  $\hat{\Gamma}$  with  $Fr$  and  $R_B$ .

Also, in analysis of climatological data in the free troposphere, it was found that the fields with the strongest departure from Gaussianity are the vertical velocity, together with the specific humidity, and it has been speculated that extreme events in climate behavior such as recent heat waves may be linked to specific resonances in Rossby wave dynamics [30]. These results, however, lead to difficulties when mixing efficiency is parameterized. As reported in [32], results from experiments and numerical simulations attempting characterization of the mixing efficiency fail to converge in many cases. This may be related to the strong non-stationarity of the data for intermediate and small values of  $Fr$ , as we have shown

in Fig.2 ( $Fr = 0.076$ ) for the initial phase of evolution of the flow, well beyond the peak of the dissipation.

The present work provides evidence that even without the added complexity of climate processes (including moisture, boundaries and topography) extreme events can be observed in both the vertical velocity and the temperature fluctuations. We also showed how these events are linked to the emergence of structures which in turn correlate, in time and space, with those regions where the flow is more unstable and prone to develop overturning. Our results show that this behavior takes place in a range of Froude numbers relevant for atmospheric and oceanic flows and for values of the buoyancy Reynolds number  $> 10$ . Even though the values of  $Re$  considered remain small compared to the troposphere and the ocean, they are not too far off for the mesosphere lower thermosphere (MLT) [12, 28]. Recent numerical studies point also to the possibility that above certain thresholds in

$Re_B$ , trends for the mixing efficiency and dissipation represent realistic scenarios even if obtained at  $Re$  smaller than those observed in nature [22, 31]. Another important result of this Letter is that the observed behavior can be reproduced with a simple 1D model which is a truncation of the full system of governing equations in the Boussinesq framework; this indicates that the large scale intermittency range in  $Fr$  corresponds to a region in the parameter space in which the time scales of waves and nonlinearities near the Ozmidov length-scale are comparable, thus resulting in fast resonant amplification of velocity differences. Finally we found that the irreversible mixing efficiency parameter increases by roughly one order of magnitude (from  $\hat{\Gamma} \sim 0.1$  to  $\hat{\Gamma} \sim 1$ ) and scales linearly with the Froude number ( $\hat{\Gamma} \propto Fr$ ) in the range  $0.05 < Fr < 0.3$ , relevant for geophysical flows [32].

- 
- [1] Kolmogorov A.N. *Dokl. Akad. Nauk SSSR* **30** (1941) 9.  
[2] Kolmogorov A.N. *J. Fluid Mech.* **13** (1962) 82.  
[3] Frisch U. *Annals New York Acad. Sci.* **357** (1980) 359.  
[4] Fritts D.C. Wang L. *J. Geophys. Res.* **70** (2013) 3735.  
[5] Falkovich, G. Pumir, A. *J. Atmos. Sci.* **64** (2007) 4497.  
[6] Bodenschatz E., Malinowski S.P., Shaw R.A. Stratmann F. *Science* **326** (2010) 970-971.  
[7] Klymak J.M., Pinkel R. Rainville L. *J. Phys., Oceanography* **38** (2008) 380.  
[8] Pearson B. Fox-Kemper B. *Phys. Rev. Lett.* **120** (2018) 094501.  
[9] Barkley D., Song B., Mukund V., Lemoult G., Avila M. Hof B. *Nature* **526** (2015) 550.  
[10] Pumir A., Shraiman B. Siggia E.D. *Phys. Rev. Lett.* **66** (1991) 2984, Jayesh Warhaft, Z. *Phys. Rev. Lett.* **67** (1991) 3503.  
[11] Marino R., Sorriso-Valvo L., D’Amicis R., Carbone V., Bruno R. Veltri P. *Astrophys. J.* **750** (2012) 41.; Marino R., Sorriso-Valvo L., Carbone V., A. Noullez. Bruno R. B. Bavassano *Astrophys. J.* **677** (2008) L71.  
[12] Chau J.L., Stober G., Hall C.M., Tsutsumi M., Laskar F.I. Hoffmann P. *Radio Sci.* **52** (2017) 811.  
[13] Mahrt L. *J. Atmosph. Sci.* **46** (1989) 79.  
[14] D’Asaro E., Lee C., Rainville L., Harcourt R., Thomas L. *Science* **332** (2011) 318.  
[15] Rorai C., Mininni P.D. Pouquet A. *Phys. Rev. E* **89** (2014) 043002.  
[16] Rosenberg D., Pouquet A., Marino R. P. Mininni *Phys. Fluids* **90** (2015) 055105.  
[17] Marino R., Mininni P.D., Rosenberg D., Pouquet A. *Phys. Rev. E* **90** (2014) 023018., Marino R., Mininni P.D., Rosenberg D., Pouquet A. *Eur. Phys. Lett.* **102** (2013) 44006.  
[18] Mininni P.D., Rosenberg D., Reddy R. Pouquet A. *Parallel Computing* **37** (2011) 316.  
[19] Vieillefosse P. *Physica A* **125** (1984) 150.  
[20] Li Y. Meneveau C. *Phys. Rev. Lett.* **95** (2005) 164502.  
[21] Ivey G., Winters K. Koseff J. *Ann. Rev. Fluid Mech.* **40** (2008) 169.  
[22] Pouquet A., Rosenberg D., Marino R. Herbert C. *J. Fluid Mech.* **844** (2018) 519.  
[23] Shih L., Koseff J., Ivey G. Ferziger J. *J. Fluid Mech.* **525** (1005) 193.  
[24] Venayagamoorthy S.K. Koseff, J.R. *J. Fluid Mech.* **798** (2016) R1.  
[25] Mashayek, A., Salehipour, H., Bouffard, D., Caulfield, C.P., Ferrari, R., Nikurashin, M., Peltier, W.R. Smyth, W.D. *Geophys. Res. Lett.* **44** (2017) 6296.  
[26] Maffioli, A., Brethouwer, G. Lindborg, E. *J. Fluid Mech.* **794** (2016) R3.  
[27] Osborn T.R. 1980 *J. Phys. Oceanogr.* **10** (1980) 83-89  
[28] Marino R., Rosenberg D., Herbert C. Pouquet A. *Eur. Phys. Lett.* **112** (2015) 49001.  
[29] He P. Basu S. *Nonlin. Proc. Geophys.* **22** (2015) 447.  
[30] Petoukhov V., Petri S., Rahmstorf S., Coumou D., Kornhuber K. Schellnhuber H.J. *Proc. Nat. Acad. Sci.* **113** (2016) 6862.  
[31] Marino R., Pouquet A. Rosenberg D. *Phys. Rev. Lett.* **114** (2015) 114504.  
[32] Gregg M.C., D’Asaro E.A., Riley J.J. Kunze E. *Ann. Rev. Marine Sci.* **10** (2018) 9.

# Single-particle Lagrangian statistics from direct numerical simulations of rotating-stratified turbulence

D. Buaria,<sup>1,\*</sup> A. Pumir,<sup>2,1</sup> F. Feraco,<sup>3,4</sup> R. Marino,<sup>3</sup>  
A. Pouquet,<sup>5</sup> D. Rosenberg,<sup>6</sup> and L. Primavera<sup>4</sup>

<sup>1</sup>*Max Planck Institute for Dynamics and Self-Organization, 37077 Göttingen, Germany*

<sup>2</sup>*Laboratoire de Physique, ENS de Lyon, CNRS and Université de Lyon, 69007 Lyon, France*

<sup>3</sup>*Laboratoire de Mécanique des Fluides et d'Acoustique, École Centrale de Lyon, CNRS, Université Claude Bernard Lyon 1, INSA de Lyon, 69134 Écully, France*

<sup>4</sup>*Dipartimento di Fisica, Università della Calabria, 87036, Arcavacata di Rende, Italy*

<sup>5</sup>*Laboratory for Atmospheric and Space Physics, University of Colorado and National Center for Atmospheric Research, Boulder, CO 80309, USA*

<sup>6</sup>*288 Harper St., Louisville, CO 80027, USA*

(Dated: May 28, 2020)

Geophysical fluid flows are predominantly turbulent and often strongly affected by the Earth's rotation, as well as by stable density stratification. Using direct numerical simulations of forced Boussinesq equations, we study the influence of these effects on the motion of fluid particles. We perform a detailed study of Lagrangian statistics of acceleration, velocity and related quantities, focusing on cases where the frequencies associated with rotation and stratification (RaS),  $f$  and  $N$  respectively, are held at a fixed ratio  $N/f = 5$ . The simulations are performed in a periodic domain, at Reynolds number  $Re \approx 4000$ , and Froude number  $Fr$  in the range  $0.03 \lesssim Fr \lesssim 0.2$  (with Rossby number  $Ro = 5Fr$ ). As the intensity of RaS increases, a sharp transition is observed between a regime dominated by eddies to a regime dominated by waves, which corresponds to  $Fr \lesssim 0.07$ . For the given runs, this transition to a wave-dominated regime can also be seemingly described by simply comparing the time scales  $1/N$  and  $\tau_\eta$ , the latter being the Kolmogorov time scale based on the mean kinetic energy dissipation. Due to the known anisotropy induced by RaS, we consider separately the motion in the horizontal and vertical directions. In the regime  $N\tau_\eta < 1$ , acceleration statistics exhibit well known characteristics of isotropic turbulence in both directions, such as probability density functions (PDFs) with wide tails and acceleration variance approximately scaling as per Kolmogorov's theory. In contrast for  $N\tau_\eta > 1$ , they behave very differently, experiencing the direct influence of the imposed rotation and stratification. On the other hand, the Lagrangian velocity statistics exhibit visible anisotropy for all runs; nevertheless the degree of anisotropy becomes very strong in the regime  $N\tau_\eta > 1$ . We observe that in the regime  $N\tau_\eta < 1$ , rotation enhances the mean-square displacements in horizontal planes in the ballistic regime at short times, but suppresses them in the diffusive regime at longer times. This suppression of the horizontal displacements becomes stronger in the regime  $N\tau_\eta > 1$ , with no clear diffusive behavior. In contrast, the displacements in the vertical direction are always reduced. This inhibition is extremely strong in the  $N\tau_\eta > 1$  regime, leading to a scenario where particles almost appear to be trapped in horizontal planes.

## I. INTRODUCTION

Transport of material substances plays a crucial role in many geophysical processes [1, 2], e.g. dispersion of pollutants and contaminants [3, 4], droplet dynamics in clouds [5], mixing of planktons and other biomatter in the oceans [6]. The Lagrangian viewpoint following the motion of fluid particles [7] or analogous entities such as Brownian or inertial particles [8, 9], provides a natural description of such transport processes. Not only are most geophysical flows turbulent,

---

\* dhawal.buaria@ds.mpg.de; (present address: New York University, NY 11201, USA; dhawal.buaria@nyu.edu)

they are also often strongly influenced by anisotropies due to effects such as rotation (Coriolis force) and stratification (buoyancy force) or presence of magnetic fields [10]. While particle dispersion has been studied extensively in isotropic turbulence, e.g. see reviews [11–13], it has only recently started receiving attention in anisotropic flows. In particular, several studies have focused on flows considering either the effects of rotation [14–16] or stratification separately [17–19]. However, in many applications, adequately describing the observed flow physics necessitates examining the combined effects of rotation and stratification (RaS), e.g. in the southern abyssal oceans with particularly high mixing intensities [20–22].

Arguably the most challenging aspect of studying the combined effects of RaS in turbulence is the enormous range of spatial and temporal scales associated with such flows. In isotropic turbulence, typically the only governing parameter is the Reynolds number ( $Re$ ), which directly provides a measure of the range of scales in the flow. However, at least three additional parameters have to be considered in RaS turbulence, namely, the Rossby number ( $Ro$ ) and the Froude number ( $Fr$ ) which respectively measure the strength of RaS, and the Prandtl number ( $Pr$ ) which is the ratio of the fluid viscosity to the thermal diffusivity (see Section II for precise definitions). This leads to consideration of additional length and time scales – beyond the already wide range existing in isotropic turbulence – and makes the flow dynamics far more involved. In particular, it has been recognized that the interaction between linear and non-linear processes in such flows leads to a rich variety of complex behavior, such as spontaneous generation of helicity, dual cascading of energy and many more [23–25]. Advances in computing power in the last decade, has allowed for significant progress in understanding such flows, although mostly from the Eulerian perspective [26–31].

In this work, utilizing direct numerical simulations (DNS) of Boussinesq equations, our objective is to investigate the dispersion of fluid particles in RaS turbulence. In particular, we focus on the motion of single individual particles. In view of the very large parameter space associated with RaS turbulence, we limit our investigation to the case where  $Ro/Fr = 5$ , i.e., the strength of stratification is five times that of rotation, which is largely relevant to the southern abyssal oceans [20, 21]. We use the same grid sizes for all cases, giving  $Re \approx 4000 - 5000$ , and Froude numbers in the range  $0.03 \lesssim Fr \lesssim 0.2$ . This regime of  $Fr$  corresponds to the transitional regime, where both turbulent eddies and inertia-gravity waves are expected to play an important role [32]. As recently demonstrated in the case of purely stratified flows, the transition towards a wave dominated regime is accompanied by intermittent large-scale vertical drafts [33, 34]. We show that the presence of additional rotation does not, in general, prevent the manifestation of this intermittency and thereby also investigate its effect on Lagrangian statistics.

In studying the motion of single particles, in the spirit of earlier studies [11–13], we investigate the properties of both their acceleration and velocity. The intrinsic anisotropy of the flow makes it necessary to distinguish throughout between motion in the horizontal plane and in the vertical direction, which are respectively perpendicular and parallel to the direction of imposed stratification (and also the axis of rotation). However, the anisotropy of acceleration and velocity reveal strikingly different properties. For acceleration statistics, which are reflective of small-scales of turbulence, two distinct regimes are observed depending on the strength of imposed RaS. At weak or moderate RaS, the properties of acceleration are qualitatively similar to those documented in isotropic turbulence (with minor quantitative deviations), suggesting that the imposed anisotropy at large scales does not significantly affect the small-scales. On the other hand, when RaS becomes very strong, acceleration statistics are significantly affected and exhibit striking differences between the horizontal and vertical motions. In the range of parameters considered here, we observe a sharp transition between the two regimes, which can be simply quantified with the ratio of the Kolmogorov time scale and the stratification time scale (which is simply the inverse of the Brunt-Väisälä frequency). The qualitative change in the statistical properties of acceleration occurs

simultaneously with the appearance of intermittent bursts in the flow.

The Lagrangian velocity statistics, in contrast to acceleration, are always affected by the imposed RaS, with the degree of anisotropy expectedly increasing with the strength of the imposed RaS. However, the transition observed for acceleration statistics is also visible in velocity statistics, resulting in even stronger anisotropy in velocity statistics when RaS is very strong. Accordingly, we characterize the integral time scales based on velocity autocorrelations and investigate the displacement of particles. The particles move ballistically at short times. At long times, the emergence of a diffusive regime is evident for runs with moderate RaS. However for strong RaS, the dispersion, particularly in vertical direction is strongly suppressed, qualitatively consistent with earlier works on purely stratified flows.

This paper is organized as follows. In Section II, we discuss our numerical methods. Essential features of the underlying Eulerian flow are discussed in Section III. The statistics of acceleration are presented in Section IV. Section V presents our results on the Lagrangian autocorrelation functions of velocity along with results on how particles are displaced by the flow. Finally, Section VI contains our concluding remarks.

## II. NUMERICAL METHOD AND DATABASE

We simulate the Eulerian flow by numerically integrating the incompressible Boussinesq equations in a rotating frame, with constant solid body rotation rate  $\Omega$  (and frequency  $f = 2\Omega$ ) and gravity  $g$  anti-aligned in the vertical ( $z$ ) direction:

$$\partial \mathbf{u} / \partial t + \mathbf{u} \cdot \nabla \mathbf{u} = -\nabla P - f \mathbf{e}_z \times \mathbf{u} - N \theta \mathbf{e}_z + \nu \nabla^2 \mathbf{u} + \Phi \quad (1)$$

$$\partial \theta / \partial t + \mathbf{u} \cdot \nabla \theta = N w + \kappa \nabla^2 \theta \quad (2)$$

$$\nabla \cdot \mathbf{u} = 0 \quad (3)$$

Here,  $\mathbf{u} = (u, v, w)$  is the velocity field,  $\theta$  is the temperature fluctuation (in units of velocity),  $P$  is the pressure normalized by the background density,  $\nu$  is the kinematic viscosity,  $\kappa$  is the thermal diffusivity and  $N$  is the Brunt-Väisälä frequency, which characterizes the strength of imposed stratification. We take  $\nu = \kappa$ , assuming the Prandtl number to be unity. A large-scale stochastic forcing term,  $\Phi$ , is utilized to achieve and maintain a statistically stationary state. The forcing is random in time and isotropic in Fourier space, with the energy being injected in a spherical shell of wavenumbers given by  $2 < |\mathbf{k}| < 3$  [35], with the characteristic forcing length scale  $L_f = 2\pi/2.5$ . While the use of isotropic forcing to simulate innately anisotropic flows may appear unphysical in the present context, earlier comparisons with a quasi-geostrophic forcing have demonstrated that the precise nature of the forcing does not have any significant effect on the flow properties in the stationary state, at least in the regimes studied here [24, 28, 32, 36].

To characterize RaS, we introduce the dimensionless Rossby ( $Ro$ ) and Froude ( $Fr$ ) numbers defined as [10]:

$$Ro = \frac{U}{Lf}, \quad Fr = \frac{U}{LN} \quad (4)$$

where  $L$  and  $U$  are respectively the characteristic length and velocity scales of the large-eddies of the flow, defined as  $L = L_f$ , and  $U = \langle |\mathbf{u}|^2 \rangle^{1/2}$ , the mean amplitude of the velocity fluctuations. An important parameter is the ratio  $N/f$  ( $= Ro/Fr$ ), which measures the relative strength of RaS. As already mentioned, we maintain  $N/f = 5$  for all runs, as relevant in some oceanographic situations [20, 21].

In addition, we define the following dimensionless numbers

$$Re = \frac{UL}{\nu}, \quad R_{IB} = \frac{\langle \epsilon \rangle}{\nu N^2}, \quad R_B = ReFr^2, \quad Ro_\omega = \frac{\langle \omega^2 \rangle^{1/2}}{f}, \quad (5)$$

where  $\langle \epsilon \rangle$  is the mean dissipation rate of turbulent kinetic energy and  $\langle \omega^2 \rangle$  is the mean enstrophy density (with  $\omega$  being the magnitude of vorticity). It is worth noting that in homogeneous turbulence, as considered in this work, the two are related as  $\langle \omega^2 \rangle = \langle \epsilon \rangle / \nu = 1/\tau_\eta^2$ , where

$$\tau_\eta = (\nu/\langle \epsilon \rangle)^{1/2} \quad (6)$$

is the Kolmogorov time scale characterizing the motion of turbulent eddies [37]. Here,  $Re$  is the Reynolds number based on large scale. The parameter  $R_{IB}$ , often referred to as the buoyancy Reynolds number, provides a measure of the relative importance of the waves induced by stratification with respect to turbulent eddies in the flow (or alternatively, the relative importance of waves and non-linear processes), e.g. see [26, 38]. This is evident by considering the Ozmidov length scale  $\ell_{OZ} = (\langle \epsilon \rangle / N^3)^{1/2}$ , which characterizes the gravity waves and the Kolmogorov length scale,  $\eta = (\nu^3 / \langle \epsilon \rangle)^{1/4}$ , which characterizes the dissipation scale of turbulence, thereby giving  $R_{IB} = (\ell_{OZ} / \eta)^{4/3}$ . Alternatively,  $R_{IB}$  can be written as the ratio of two time scales:  $R_{IB} = (T_N / \tau_\eta)^2$ , where  $T_N = 1/N$  is the stratification time scale (and  $\tau_\eta$  is the Kolmogorov time scale), once again characterizing the relative importance of stratification to that of turbulent eddies. An alternative perspective is also offered by the asymptotic scaling analysis of [39], which suggests that  $R_{IB}$  can be interpreted as a replacement for the classical Reynolds number in strongly stratified turbulence – providing a relative measure of inertial and viscous forces. However, utilizing this interpretation in presence of rotation requires caution, since it invalidates the said asymptotic analysis (especially when rotation and stratification are comparable in strength).

A separate definition of the buoyancy Reynolds number [28, 32] is given by the parameter  $R_B$ . The two parameters are related as  $R_{IB} = \beta R_B$ , where  $\beta = \langle \epsilon \rangle L / U^3$ . In fully developed turbulence,  $\beta$  is expected to be constant as a consequence of the dissipation anomaly [40]. However, in the regimes considered here, it can be shown that  $\beta$  depends on the strength of stratification [32]. Hence in our analysis, we utilize  $R_{IB}$  to quantify the relative strength of stratification and turbulence. The relevance of this choice will become evident as our results are presented in later sections. Finally, in addition to the Rossby number  $Ro$  based on large scales, it is useful to define the micro-Rossby number  $Ro_\omega$ , which in contrast to  $R_{IB}$ , measures the relative strength of small-scale turbulent motions to that of the imposed rotation. However, using  $\langle \epsilon \rangle = \nu \langle \omega^2 \rangle$  due to statistical homogeneity,  $Ro_\omega$  can be simply related to  $R_{IB}$  as:  $Ro_\omega^2 / R_{IB} = (N/f)^2$ . Since  $N/f$  is held constant in this work, the parameters  $Ro_\omega$  and  $R_{IB}$  essentially provide the same information.

The database utilized in the current work, along with the main simulation parameters, is summarized in Table I. The simulations were carried out using the Geophysical High-Order Suite for Turbulence (GHOST) code, a versatile, highly parallelized, pseudo-spectral code, utilizing hybrid MPI-OpenMP programming model, with second order explicit Runge-Kutta time stepping [41]. All runs correspond to a  $(2\pi)^3$  periodic domain with  $512^3$  grid points. The parameters  $N$  and  $f$  are varied over a range of values keeping the ratio  $N/f$  fixed at 5. In addition, for a systematic comparison, we have also performed additional simulations by setting  $N = 0$  or  $f = 0$  or both. The simulation with  $N = f = 0$  (case 0) simply corresponds to homogeneous isotropic turbulence (HIT). All the runs reported were started from an initial condition, consisting of a few random modes in the velocity field, whereas the temperature field,  $\theta$ , was initialized to zero. The Boussinesq equations were integrated until a statistically stationary state was reached. For adequate statistical sampling, we considered a simulation period of at least  $10 - 20T_E$  in the stationary state for each case, where  $T_E = L/U$  is the large eddy turnover time. (Some additional details are available in the Supplementary Material [42]).

case	0 (HIT)	1	2	3	4	5	6	7 (s)	8 (r)
$N$	0	2.948	4.915	7.372	11.80	14.74	16.62	14.74	0
$f$	0	0.5896	0.9830	1.474	2.360	2.948	3.320	0	2.948
$\nu$	0.0015	0.001	0.001	0.001	0.001	0.001	0.001	0.001	0.001
$Fr$	$\infty$	0.168	0.114	0.086	0.069	0.063	0.045	0.030	$\infty$
$Ro$	$\infty$	0.840	0.570	0.430	0.345	0.315	0.225	$\infty$	0.140
$Re$	2379	3117	3537	3963	5199	5861	4744	3942	2645
$R_B$	$\infty$	90.1	42.9	26.9	24.7	23.2	9.61	3.0	$\infty$
$\langle \epsilon \rangle$	0.375	0.198	0.182	0.146	0.059	0.049	0.027	0.050	0.065
$R_{IB}$	$\infty$	22.8	7.53	2.69	0.422	0.226	0.096	0.229	$\infty$
$Ro_\omega$	$\infty$	23.9	13.7	8.22	3.25	2.38	1.55	$\infty$	2.73

TABLE I. DNS database used in the current work, with corresponding simulation parameters. All rotating-stratified runs (cases 1-6) correspond to  $N/f = 5$ . The cases 7 and 8, respectively with only stratification and only rotation, correspond to the  $N$  and  $f$  values of case 5. The case 0 corresponds to homogeneous isotropic turbulence (HIT) with  $N = f = 0$ . The mean dissipation of kinetic energy  $\langle \epsilon \rangle$  was obtained by averaging over all the grid points and the time over which particles were tracked in the simulations. Other parameters are defined in Eqs. (4) and (5).

In Table I, an important point to note is that the values of  $R_B$  and  $R_{IB}$  monotonically decrease as  $N$  and  $f$  are increased. Values of  $N$  and  $f$  higher than those shown are avoided, since the resulting regime would be completely dominated by waves [32]. The simulations with either  $N = 0$  or  $f = 0$  have their  $f$  or  $N$  value (respectively) corresponding to case 5, with one of the largest  $N$  and  $f$  values. However, as evident from Table I the values of the  $Fr$  (and  $Ro$ ) numbers corresponding to runs 5 and 7 (respectively runs 5 and 8) differ significantly, despite identical values of the stratification (respectively rotation rate). These variations are a consequence of our dynamical definition of  $U$ , which accounts for the subtle interplay between turbulence and RaS. In particular, they reflect the significant variation in  $U$  itself, which is discussed in Section III. Importantly, we observe that the value of  $R_{IB}$  is lower than 0.5 for Runs 4-6, as well as for the purely stratified run, 7, suggesting a dominant role of the waves in these runs. In contrast,  $R_{IB} > 2$  in all other runs, possibly pointing to a prevalent role of the eddies. This leads to two qualitatively different behaviors, as demonstrated by our results in the following sections.

Finally, in order to obtain Lagrangian statistics, the fluid particles are tracked in time along with the Eulerian flow in the stationary state, according to the basic equation of motion

$$\frac{d\mathbf{x}^+(t)}{dt} = \mathbf{u}^+(t) = \mathbf{u}(\mathbf{x}^+(t), t) \quad (7)$$

where the superscript + denotes a Lagrangian quantity and the fluid particle velocity is simply defined to be the Eulerian velocity field evaluated at the instantaneous particle position. For each run listed in Table I, we additionally tracked the motion of 1.5M particles ( $M=10^6$ ), which are randomly distributed throughout the entire domain at the time of injection. The number of fluid particles are held constant for all cases, since given the same grid size and approximately similar Reynolds numbers, their sampling requirements are also approximately the same. Similar to the Eulerian grid, the particles are distributed among parallel processors and tracked in time together with the velocity field using a second order Runge-Kutta scheme, and standard interpolation methods based on cubic splines [43, 44].

### III. EULERIAN VELOCITY FIELD

In this section, we provide a brief overview of the underlying Eulerian flow, which establishes the necessary framework for better understanding the Lagrangian statistics reported subsequently.

*Energy spectra:* We begin by considering the kinetic energy spectra, as shown in Fig. 1, which is one of the most common descriptor of Eulerian dynamics in turbulent flows [10]. The curves are normalized using the large scale variables  $U$  and  $L$ , and split into two sub-figures depending on the strength of weak rotation and stratification (RaS). Fig. 1a shows the spectra for the runs with relatively weak RaS, corresponding to  $Fr \geq 0.086$  and  $R_{IB} > 1$ , including the HIT and rotation-only runs. The main observation is that all the spectra demonstrate an approximate  $k^{-5/3}$  Kolmogorov-like scaling in an intermediate range of  $k$ . This expectation is justified for the HIT run, as well as the  $R_{IB} > 1$  runs, for which there is a sufficient scale separation between  $\ell_{OZ}$  and  $\eta$  (note  $R_{IB} = (\ell_{OZ}/\eta)^{4/3}$  as discussed earlier), to recover Kolmogorov-like turbulence [39, 45]; although systematic deviations from the scaling are clearly evident as  $R_{IB}$  decreases. In fact, as shown later in this section, the large scales for  $R_{IB} > 1$  runs are still predominantly anisotropic, though their impact on small-scales is weak.

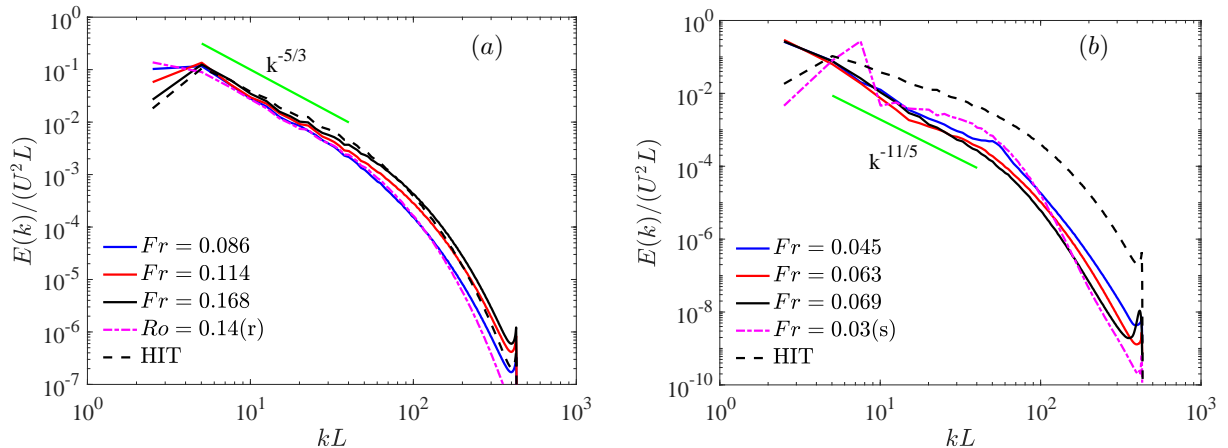


FIG. 1. The kinetic energy spectrum  $E(k)$  normalized by  $U^2 L$  as a function of  $kL$ , where  $U$  and  $L$  are the large scale velocity and length scales respectively. The curves correspond to cases listed in Table I. Solid green lines indicating a spectral slope of  $k^{-5/3}$  and  $k^{-11/5}$  in (a) and (b) respectively are drawn for reference.

On the other hand, in Fig. 1b, the spectra for runs with stronger stratification, corresponding to  $Fr \leq 0.069$  and  $R_{IB} < 1$  are shown. The spectrum for the HIT run (dashed black line) is also included for comparison. As evident, this regime significantly differs from that at weaker stratification, with the spectra exhibiting a spectral slope steeper than  $k^{-5/3}$  (since  $R_{IB} < 1$  and hence  $\ell_{OZ} < \eta$  precludes Kolmogorov's theory from being applicable). It has been observed in the closely related context of a time-dependent flow [28, 46] that the spectra followed the Bolgiano-Obukhov prediction [47, 48]. In this regime, energy transfer is strongly affected by the temperature fluctuations (potential energy). The straight line in Fig. 1b indicates the corresponding  $k^{-11/5}$  prediction. Given the small range of spatial scales available in our simulations, however, it is difficult to conclusively demonstrate that the spectra shown indeed conform to a  $k^{-11/5}$  scaling (and the fact that the precise exponent can depend on the Froude number [49]). Nevertheless, the change in spectral slopes clearly evidences that the energy transfer between scales is strongly perturbed in runs with  $R_{IB} < 1$ , and much less so in runs with  $R_{IB} > 1$ . In fact, this demarcation



based on  $R_{IB}$  becomes increasingly prominent as more results are discussed in later sections. The spectra of the temperature fluctuations (not shown) follow similar trends as that of velocity.

*Anisotropy of velocity fluctuations:* The above transition between strong hydrodynamic turbulence and regimes dominated by RaS, as evidenced from the energy spectra, clearly warrant further inspection. An important aspect of the flows in this study is the existence of a strong anisotropy of velocity fluctuations. Namely, the presence of RaS induces very different properties of the velocity fluctuations in the horizontal plane and in the vertical direction. This anisotropy has been investigated in many earlier studies, in particular by analyzing the longitudinal and transverse energy spectra [10, 28, 39]. In the present work, we limit our discussion to the velocity components  $u_{\perp}$  and  $u_{\parallel}$ , respectively in the horizontal and vertical directions (perpendicular and parallel to gravity). The statistics involving  $u_{\perp}$  are obtained by averaging the two components in the x-y horizontal plane (which is also the plane of rotation), whereas  $u_{\parallel}$  simply corresponds to the vertical z-component. An obvious manifestation of the anisotropy between the two directions is in variances of  $u_{\perp}$  and  $u_{\parallel}$ , as shown in Table II. It is evident that apart from the HIT run (case 0) and to a large extent the rotation only run (case 8), the variances for both components are very different. To precisely quantify the anisotropy, we consider the ratio  $\xi^u = [\langle u_{\perp}^2 \rangle / \langle u_{\parallel}^2 \rangle]^{1/2}$ , also shown in Table II. Expectedly, this ratio is unity for case 0 and very close to unity for case 8. However, for all runs with stratification, the ratio is always greater than 1. For cases 1-3, the ratio increases slowly with decreasing  $Fr$ , whereas a sharp increase occurs for cases 4-6 (and also case 7). Clearly, this transition corresponds to the change in spectral slope observed for the spectra in Fig. 1. The runs with smaller  $\xi^u$  correspond to spectra which show  $k^{-5/3}$  scaling, whereas runs with sharp increase of  $\xi^u$  correspond to spectra with steeper Bolgiano-like scaling. In these flows, the fluctuations of  $u_{\parallel}$  are essentially suppressed when the imposed RaS are strong. We note that the values shown here are consistent with the results of some earlier runs [32].

case	0	1	2	3	4	5	6	7	8
$Fr$	$\infty$	0.168	0.114	0.086	0.069	0.063	0.045	0.030	$\infty$
$Ro$	$\infty$	0.840	0.570	0.430	0.345	0.315	0.225	$\infty$	0.140
$\langle u_{\perp}^2 \rangle$	0.68	0.62	0.92	1.2	2.2	2.8	1.7	0.55	0.39
$\langle u_{\parallel}^2 \rangle$	0.67	0.28	0.17	0.097	0.022	0.019	0.005	0.0077	0.28
$\xi^u$	1.01	1.48	2.33	3.52	10.0	12.0	18.4	8.4	1.18
$K_{u_{\perp}}$	2.9	2.9	2.9	2.9	3.1	3.4	3.05	2.5	3.1
$K_{u_{\parallel}}$	2.9	3.3	3.8	4.7	6.4	8.4	10.9*	3.2	3.1

TABLE II. Variance and kurtosis of velocity components. We use  $\xi^u = \langle u_{\perp}^2 \rangle^{1/2} / \langle u_{\parallel}^2 \rangle^{1/2}$ , to measure the anisotropy, whereas  $K_{u_{\parallel}}$  and  $K_{u_{\perp}}$  are the kurtosis of  $u_{\parallel}$  and  $u_{\perp}$  respectively. The skewness of these components (not shown) is consistent with 0. The value(s) of kurtosis marked with an asterisk correspond to relatively low accuracy.

To further investigate the anisotropy, we next consider higher order moments of the velocity components. Since the probability density functions (PDFs) of individual velocity components are symmetric (due to underlying symmetry of Boussinesq equations), we note that the values of the third moments of the velocity fluctuations are expected to be zero. Our results, not shown here, are compatible with this. Thus, we consider the fourth-order moment, through the kurtosis, defined as  $K_{u_i} = \langle u_i^4 \rangle / \langle u_i^2 \rangle^2$ . It is known that the PDFs of individual velocity components in HIT are approximately Gaussian, which implies that the kurtosis is approximately 3. Consistent with that, we find that the value of the kurtosis is very close to 3 in the case HIT, (see Table II). In the case of a purely stratified flow, however, it was found that the distribution of the velocity component parallel to the direction of stratification,  $u_{\parallel}$ , could be significantly wider than Gaussian [33, 34]. The strong deviations from a Gaussian distribution have been shown to originate from intermittent

case	0	1	2	3	4	5	6	7	8
$Fr$	$\infty$	0.168	0.114	0.086	0.069	0.063	0.045	0.030	$\infty$
$Ro$	$\infty$	0.840	0.570	0.430	0.345	0.315	0.225	$\infty$	0.140
$\langle a_{\perp}^2 \rangle$	16.4	6.9	6.3	5.4	5.4	9.3	6.21	0.48	2.1
$\langle a_{\parallel}^2 \rangle$	16.3	8.9	8.6	6.7	1.9	2.0	0.43	1.1	1.9
$\xi^a$	1.01	0.88	0.85	0.90	1.67	2.11	3.80	0.66	1.05
$K_{a_{\perp}}$	19.3	29.8	37.1	46.9*	6.52	7.50	14.3	4.38	22.8
$K_{a_{\parallel}}$	19.6	22.3	27.2	40.5*	17.9	11.8	16.2	3.27	35.6*
$\xi^u/\xi^a$	1.0	1.68	2.74	3.9	6.0	5.7	4.8	12.7	1.1

TABLE III. Variance and kurtosis of acceleration components, perpendicular and parallel to the axis of rotation/stratification.  $\xi^a = [\langle a_{\perp}^2 \rangle / \langle a_{\parallel}^2 \rangle]^{1/2}$  measures the anisotropy, whereas the kurtosis,  $K_{a_{\perp}}$  and  $K_{a_{\parallel}}$ , characterizes the extent of the PDFs (see Fig. 3). The underlying symmetry of the problem imposes that the skewness (not shown) is zero. The values of kurtosis marked with an asterisk correspond to relatively low accuracy.

vertical drafts [34]. On the other hand, the kurtosis of  $u_{\perp}$  is always found to be approximately 3. Our values, as shown in Table II, are consistent with these trends. We find that  $K_{u_{\perp}}$  is slightly smaller than 3 at low stratification, and slightly larger than 3 for runs with strong stratification ( $Fr \lesssim 0.07$ ), with PDFs (not shown) being approximately Gaussian. In the vertical direction,  $K_{u_{\parallel}}$  increases very significantly beyond 3 as strength of RaS increases.

It is worthwhile to compare the dependence of  $K_{u_{\parallel}}$  in our RaS runs with the stratification-only runs reported in [34] (see in particular their Fig.5). While the sharp transition in  $K_{u_{\parallel}}$  appears to be qualitatively similar, quantitatively the large values of  $K_{u_{\parallel}}$  for RaS runs occur at slightly lower  $Fr$  values than in [34]. For even smaller  $Fr$  (not considered in this work), in a wave-dominated regime, one can expect that  $K_{u_{\parallel}}$  for RaS runs will again become 3 [34], as it was the case for the stratification-only run (case 7) discussed here. Additional discussion of  $K_{u_{\parallel}}$  will be presented in the following section, in relation with acceleration statistics.

#### IV. ACCELERATION STATISTICS

The acceleration experienced by a fluid element, defined by the rate of change of velocity in the Lagrangian frame, i.e.,  $\mathbf{a}^+ = d\mathbf{u}^+/dt$  (where  $\mathbf{u}^+$  is defined in Eq. (7)) and resulting from the balance of forces acting on it, is arguably the simplest descriptor of its motion, as also directly reflected in the governing fluid equations. In addition to its fundamental importance in turbulence theory [13], a key motivation to study acceleration comes from its central role in stochastic modeling of turbulent dispersion [50]. In the following sub-sections, we study different aspects related to acceleration, namely, acceleration variance and kurtosis, the probability density functions and Lagrangian autocorrelations and frequency spectra. As already mentioned, the anisotropy of the flow makes it necessary to distinguish between the horizontal and vertical components of acceleration, denoted by  $a_{\perp}^+$  and  $a_{\parallel}^+$  respectively. In this section, we demonstrate that the anisotropy properties of the acceleration components strongly differ from those of the velocity discussed in the previous section. For convenience, we will henceforth omit the superscript '+' from our notation, since our subsequent results only involve Lagrangian quantities.

### A. Acceleration variance

Extending the earlier analysis of the Eulerian velocity field, we first examine the anisotropy in acceleration by considering the second and fourth order moments, namely, the variance and kurtosis respectively. The moments are listed in Table III. Due to the underlying symmetry of the Boussinesq equations, the third and all other odd moments of acceleration components are zero (similar to the velocity components). As can be seen from cases 1-6, the properties of  $a_{\perp}$  and  $a_{\parallel}$  show striking differences. While the variances of  $a_{\parallel}$  rapidly decrease with decreasing  $Ro$  (and  $Fr$ ), the variances of  $a_{\perp}$  do not change that much. To better understand this behavior, we consider the anisotropy ratio  $\xi^a = [\langle a_{\perp}^2 \rangle / \langle a_{\parallel}^2 \rangle]^{1/2}$ . For the HIT run (case 0), the ratio, as expected, is equal to 1, whereas for rot-strat cases two separate behaviors are visible.

The first corresponds to cases 1-3 with relatively weak rotation and stratification (RaS), where the ratio  $\xi^a$  is approximately constant, and slightly smaller than 1. The ratio being close to unity suggests that the effect of anisotropy on small scales is only minor. Furthermore, a simple explanation for the ratio slightly smaller than unity can be provided based on the knowledge that the relative strength of stratification is significantly stronger compared to that of rotation (since  $N/f = 5$ ). For that reason, the acceleration variance in the vertical direction is likely to be slightly more enhanced (due to stratification) than that in the horizontal direction (due to rotation). On the other hand, runs 4-6 correspond to significantly stronger RaS, which leads to a different behavior, with  $\xi^a > 1$  and further increasing with decreasing  $Fr$  (and  $Ro$ ). Since runs 4-6 correspond to  $R_{IB} < 1$ , they are in a regime where waves play a stronger role, compared to (turbulent) eddies. With strong stratification, the motion in the vertical direction is strongly suppressed, as also reflected in  $\xi^u$  values (see Table II). With relative weaker effect of rotation, the acceleration in the horizontal direction is still affected by turbulent eddies, resulting in  $\xi^a$  to become greater than 1. Thereafter, the effect becomes even more pronounced with further increase in strength of RaS.

It is instructive to compare the acceleration variances for case 5 (with strong RaS), to case 7, with exactly the same stratification,  $N$ , but no rotation and to case 8, with the same rotation,  $f$ , but no stratification. The variances of  $a_{\perp}$  and  $a_{\parallel}$  are stronger in the presence of both RaS, than with either of the two effects taken separately. The anisotropy ratio  $\xi^a$  also shows a very striking difference, when comparing runs 5, 7 and 8. For rotation-only (run 8), we observe  $\xi^a \approx 1$ , implying little to no small-scale anisotropy. This can be viewed as consistent with the observation that the flow spectrum for run 8 is overall comparable to the Kolmogorov spectrum (see Fig. 1a), so the flow is dominated by eddies. On the other hand, the anisotropy ratio is  $\xi^a < 1$  (0.66) for run 7, implying stronger acceleration variances in the vertical than in the horizontal direction, but an opposite situation in the presence of both RaS:  $\xi^a > 1$  (2.1). This difference can be traced back to the much larger value of  $\langle a_{\perp}^2 \rangle$  in the presence of rotation, a consequence of the enhancement of the horizontal component of acceleration due to the Coriolis force.

In comparing the anisotropy of acceleration components with that of velocity (see Table II), we find that  $\xi_a$  is always smaller than  $\xi_u$ , and additionally very close to unity when  $R_{IB} > 1$ . This can be explained by realizing that velocity is sensitive to the large scales of the flow and is directly influenced by the imposed anisotropy. On the other hand, acceleration mostly samples the small scales, and is not likely sensitive to the imposed anisotropy (at large scales), provided the scale separation between the large and small scales is sufficiently wide – consistent with the notion of local isotropy as dictated by Kolmogorov’s theory [7]. In the current scenario, this is realized when  $R_{IB} > 1$ , resulting in  $\xi^a$  being nearly unity (and also a  $k^{-5/3}$  range in the intermediate  $k$  range as demonstrated earlier). Whereas for  $R_{IB} < 1$ , local isotropy is clearly violated, but still the anisotropy of acceleration is significantly weaker than that of velocity.

Additional insight can be obtained by considering the ratio  $\xi^u / \xi^a$ , also shown in Table III. For

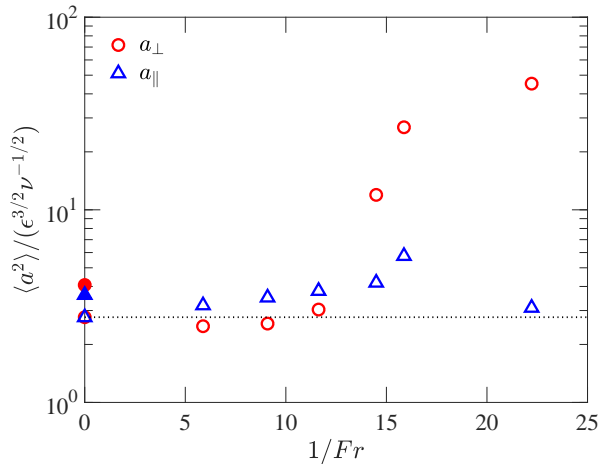


FIG. 2. Kolmogorov-scaled acceleration variance, as defined by Eq. 8, plotted as a function of  $1/Fr$ . The parallel (vertical) and perpendicular (horizontal) components of accelerations are shown in blue triangles and red circles respectively. The HIT run corresponds to  $1/Fr = 0$ . In addition the rotation-only run also corresponds to  $1/Fr = 0$ , but is shown in solid symbols.

HIT, this ratio is unity, but with increasing strength of RaS, we observe  $\xi_u/\xi_a$  increases, peaking at around 6 for case 4, and thereafter decreasing slightly with further increase in strength of RaS. A limiting value can be obtained in the case where RaS is very strong, such that the flow is dominated by linear processes (with turbulent eddies playing a very weak role). This would lead to  $\xi^u/\xi^a \approx N/f$ , by assuming that  $a_{\perp} \sim u_{\perp}f$  and  $a_{\parallel} \sim u_{\parallel}N$ . The value for case 6, with  $\xi^u/\xi^a = 18.4/3.8 \approx 5$ , appears to be consistent with this consideration, though it remains to be further tested for different  $N/f$  values.

Given that the statistics of acceleration appear to conform with local isotropy for  $R_{IB} > 1$ , we consider the following relation from classical turbulence:

$$\langle a^2 \rangle = a_0 \langle \epsilon \rangle^{3/2} \nu^{-1/2} \quad (8)$$

which results from the application of Kolmogorov's similarity theory to acceleration variance [7]. Here,  $a_0$  is a dimensionless constant, which is plausibly universal for HIT. Empirical evidence based on studies of isotropic turbulence has shown that  $a_0$  increases slowly with Reynolds numbers [51], which can be possibly viewed as a manifestation of small-scale intermittency, unaccounted for in Kolmogorov's 1941 theory. In contrast, for RaS turbulence, one may expect additional deviations because of the imposed anisotropy, especially if  $Re$  is not very large.

Fig. 2 shows the values of the  $a_0^{\perp}$  and  $a_0^{\parallel}$  as a function of  $Fr$  for cases 1 through 6, together with the value obtained for case 0, in the absence of RaS. The values of  $a_0^{\parallel}$  and  $a_0^{\perp}$  do not vary very much for  $1/Fr \gtrsim 12.5$ , and sharply increase, especially in the perpendicular direction, at large values of  $1/Fr$ . In particular, the value of  $a_0^{\perp}$  at  $1/Fr \approx 16$  exceeds that in the HIT case by a factor larger than  $\sim 10$ . This points to a strong difference of the small-scale properties between runs 4-6 and the HIT run (case 0). In comparison, and despite the larger value of  $N$  ( $N/f = 5$  for runs 1-6), the value of  $a_0^{\parallel}$  remains comparable to that obtained in the HIT case. In the purely stratified case (run 7), the value of  $a_0^{\parallel}$  is slightly reduced compared to case 5 in the presence of both RaS ( $a_0^{\parallel} \approx 3.1$ ). On the other hand, the value of  $a_0^{\perp} \approx 1.4$  for case 7 is reduced by over an order of magnitude compared to case 5. For the rotation-only run,  $a_0$  is not very different compared to the HIT case, suggesting that the small scales are still dominated by turbulence, even though the large scales are highly anisotropic. This once again demonstrates that acceleration becomes progressively dominated, as

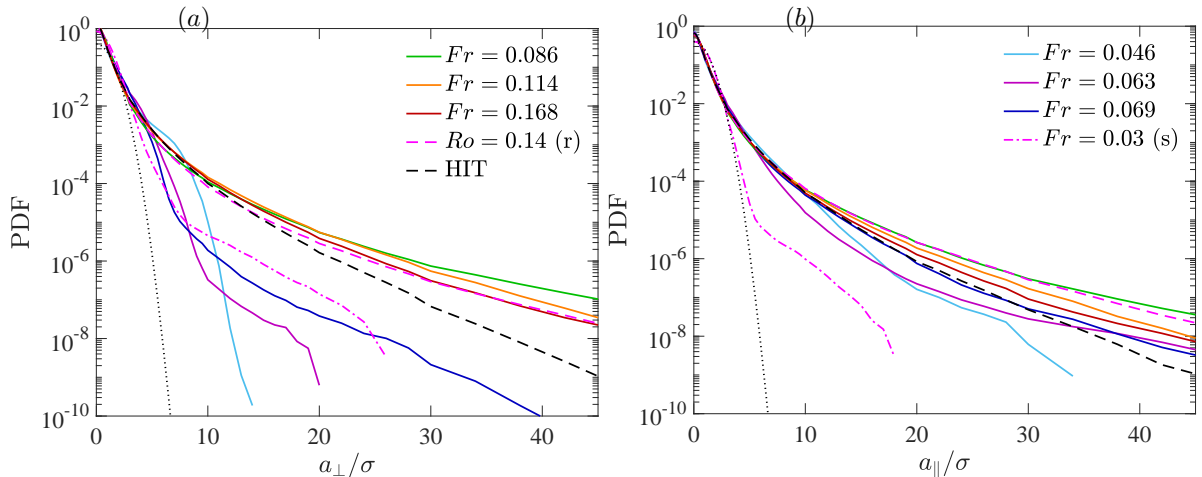


FIG. 3. Standardized probability density functions (PDFs) of (a) the perpendicular (horizontal) and (b) the parallel (vertical) components of acceleration, i.e.,  $a_{\perp}$  and  $a_{\parallel}$  respectively.  $\sigma$  denotes the corresponding standard deviation. The dotted line shows the standardized Gaussian distribution for comparison. The legend is split over two panels, but applies to each panel individually.

$Ro$  and  $Fr$  decrease, by the frequencies associated with rotation/buoyancy. As a consequence, the values of  $a_0$  shown in Fig. 2 do not reflect only the small-scale structure of the flow, but also its global properties.

## B. Acceleration PDFs

The analysis of acceleration variance can be generalized by considering the probability density functions (PDFs) of acceleration components. In HIT, similar to Eulerian velocity gradients, acceleration is also characterized by extremely large fluctuations reflected in broad tails of the PDF, which further broaden with increasing Reynolds number [13, 37]. In this subsection, we study the effect of imposed RaS on the PDFs of acceleration, especially focusing on the long tails. Once again, we separate out the contributions  $a_{\parallel}$  and  $a_{\perp}$ .

Fig. 3a and b respectively show the standardized PDFs of  $a_{\perp}$  and  $a_{\parallel}$  for all the runs listed in Table III. Two very distinct behaviors can be observed once again. At moderate RaS (and for  $R_{IB} > 1$ ) the PDFs of acceleration exhibit very broad tails, and in this sense, they differ only quantitatively from those obtained in the HIT case. This property is also reflected by the values of the kurtosis of the distributions, shown in Table III, which are all  $\gtrsim 20$ , even larger than the values obtained for the HIT case. The run corresponding to pure rotation also exhibits very high kurtosis of the acceleration. Note that the accuracy of the estimates of kurtosis indicated in the table are of the order of 10% or less, except for values marked with an asterisk, which exhibited very large fluctuations, leading to higher error bars for runs 3 and 8 (of about 20 – 30%).

In contrast for the runs with strong RaS (with  $R_{IB} < 1$ ), the tails of the PDFs are significantly suppressed. As shown in Table III, the corresponding kurtosis values are also quite small, although still larger than the Gaussian value of 3. This is particularly clear for the horizontal component  $a_{\perp}$  of acceleration, see Fig. 3a, and to a lesser extent, for the vertical component  $a_{\parallel}$  (Fig. 3b). The tendency of the PDFs to become narrower in runs with strong RaS appears to be a consequence of the strong stratification, as the PDFs of acceleration in the run with pure rotation are only weakly

modified. In regimes dominated by waves, weak turbulence theory suggests that the velocity and acceleration should be close to Gaussian [52]. However, we observe that the kurtosis of acceleration components are significantly larger than the corresponding Gaussian value of 3 (with a stronger kurtosis for the vertical, than for the horizontal component of acceleration). This unexpected phenomenon can also be associated with the observation of bursts of vertical velocity, manifested by the large values of  $K_{u_{\parallel}}$  listed in Table II, particularly for runs 4-6. These bursts are related to the phenomenon observed in [34] in the case of purely stratified flows, in comparable domains of parameters. We expect that the mechanisms are similar in the presence of a relatively weak rotation ( $N/f = 5$ ), as it is the case in the present study.

### C. Acceleration autocorrelation and frequency spectra

Essential information on the motion of tracers can be obtained from the autocorrelation function of quantities fluctuating along Lagrangian trajectories. For example, the autocorrelation function can be used to determine relevant time scales and to form the frequency spectrum via Fourier transform [53]. Since our analysis is concerned with statistically stationary signals, the autocorrelation only depends on the chosen time lag. The autocorrelation  $\rho^a(\tau)$  is defined as

$$C^a(\tau) = \langle a(t + \tau)a(t) \rangle, \quad \rho^a(\tau) = C^a(\tau)/C^a(0) \quad (9)$$

where  $\tau$  is the time lag and  $C^a$  is the autocovariance. Statistical stationarity implies  $\rho^a(-\tau) = \rho^a(\tau)$  and also imposes that the integral of the acceleration autocorrelation must be zero, i.e.,  $\int_0^{\infty} \rho^a(\tau) d\tau = 0$  [53]. The frequency spectrum of acceleration  $E^a$ , which is the Fourier transform of  $C^a(\tau)$  can be defined as

$$E^a(\omega) = \int_0^{\infty} C^a(\tau) \exp^{-i\omega\tau} d\tau \quad (10)$$

By definition, the integral of the spectrum gives the variance of the signal. Yet again, we consider  $a_{\perp}$  and  $a_{\parallel}$  separately.

*Perpendicular component:* Fig. 4 shows the autocorrelation function  $\rho_{\perp}^a(\tau)$  for all the runs with RaS. In Fig. 4a, the time lag is normalized with  $\tau_{\eta}$ , the Kolmogorov time scale characterizing the small-scale motion. We also include the HIT case (dashed line) and the pure rotation case (dash-dotted line) as a reference. For HIT, the acceleration autocorrelation is known to decay rapidly, becoming zero at  $\tau \approx 2\tau_{\eta}$  and thereafter becoming negative and slowly approaching zero again at very large time lags [54] – as readily seen in Fig. 4a. Interestingly, we observe that the runs with relatively weak RaS, i.e.,  $Fr \geq 0.114$ , and also the run with only rotation, behave very similarly to the HIT case (see inset of Fig. 4a), albeit with minor variation in the zero-crossing point. For the rot-strat run with  $Fr = 0.086$ , the autocorrelation function shows a similar behavior up to very small time lags, but thereafter deviates with the zero-crossing extending to  $\tau \approx 8\tau_{\eta}$ . The large time behavior is markedly different with very low frequency oscillations. On the other hand, for runs with strong RaS, i.e.,  $Fr \leq 0.07$ , a very different behavior is observed right from small time lags. The autocorrelation shows strong oscillations which are eventually damped out at large time lags. Furthermore, the zero-crossing point also is strongly dependent on  $Fr$ , moving to smaller time lags with decreasing  $Fr$ .

Plotting  $\rho_{\perp}^a$  as a function of  $\tau f/2\pi$ , see Fig. 4b, shows that the period of the damped oscillations is close to  $2\pi/f$  (with small but significant deviation). For comparison, we also show in Fig. 4b the function  $\rho_{\perp}^a$  for the case of a purely rotating flow. Somewhat surprisingly, the tendency to oscillate at a frequency  $\sim f$  is not as strong as in the case where both RaS are present. A similar trend was observed in [14]. We notice, however, that the stronger stratification ( $N = 5f$  in runs 1-6) implies

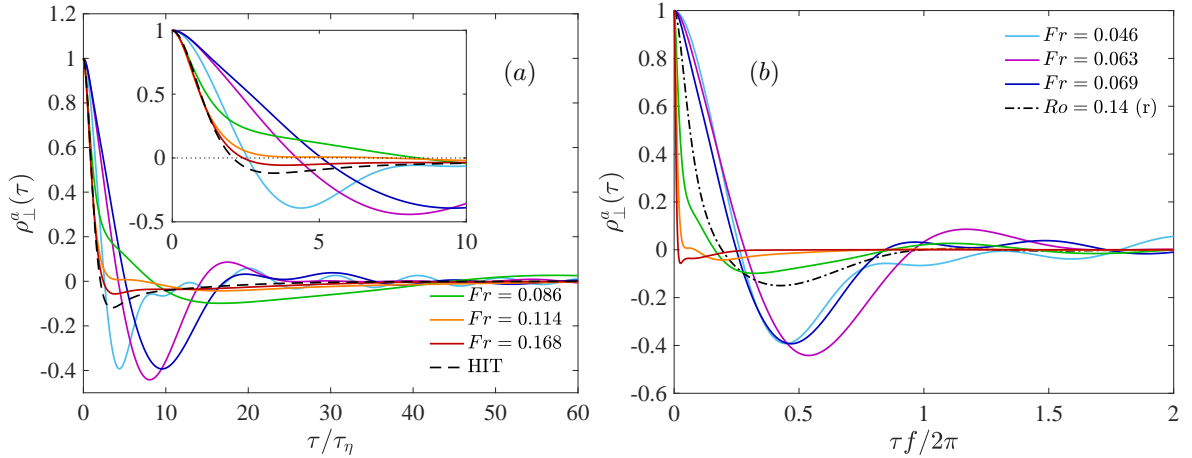


FIG. 4. Lagrangian autocorrelation of the perpendicular (horizontal) component of acceleration  $\rho_{\perp}^a(\tau)$  against the time lag  $\tau$  normalized by the Kolmogorov time scale  $\tau_{\eta}$  in (a) and by the rotation period  $2\pi/f$  in (b). Inset in (a) shows a zoomed view at small time lag. The legend is split over two panels, but applies to each panel individually.

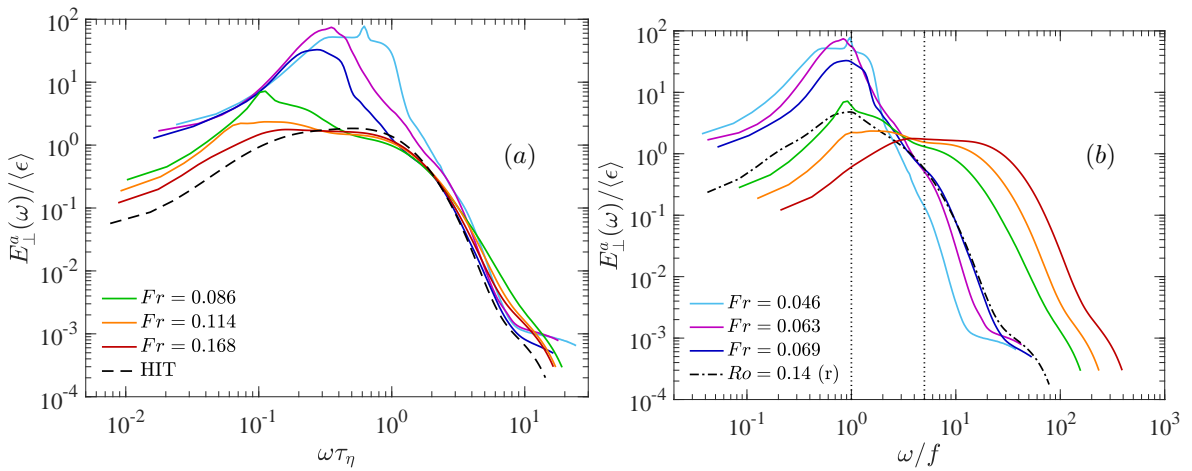


FIG. 5. Lagrangian frequency spectrum of the perpendicular (horizontal) component of acceleration  $E_{\perp}^a(\omega)$  against the frequency  $\omega$  normalized by the Kolmogorov time scale  $\tau_{\eta}$  in (a) and by the rotation frequency  $f$  in (b). The spectra are non-dimensionalized using the mean kinetic energy dissipation rate  $\langle\epsilon\rangle$ . Vertical dotted lines in (b) correspond to frequencies  $\omega = f$  and  $N$  (note  $N = 5f$ ). The legend is split over two panels, but applies to each panel individually.

the presence of faster waves than in a purely rotating flow at the same  $Ro$  number, involving in particular high values of  $k_{\perp}$ , since the dispersion law for inertia-gravity waves can be written as  $k^2\omega_{IG}^2 = N^2k_{\perp}^2 + f^2k_{\parallel}^2$  [1].

To better identify the frequencies present in the autocorrelation function, it is apt to take its Fourier transform to obtain the frequency spectrum. Fig. 5 shows the spectrum  $E_{\perp}^a$ . The spectra have been made dimensionless by dividing by the mean kinetic energy dissipation rate  $\langle\epsilon\rangle$ . In Fig. 5a, the frequency is normalized by  $\tau_{\eta}$ , whereas in Fig. 5b, we use the rotation frequency  $f$ .

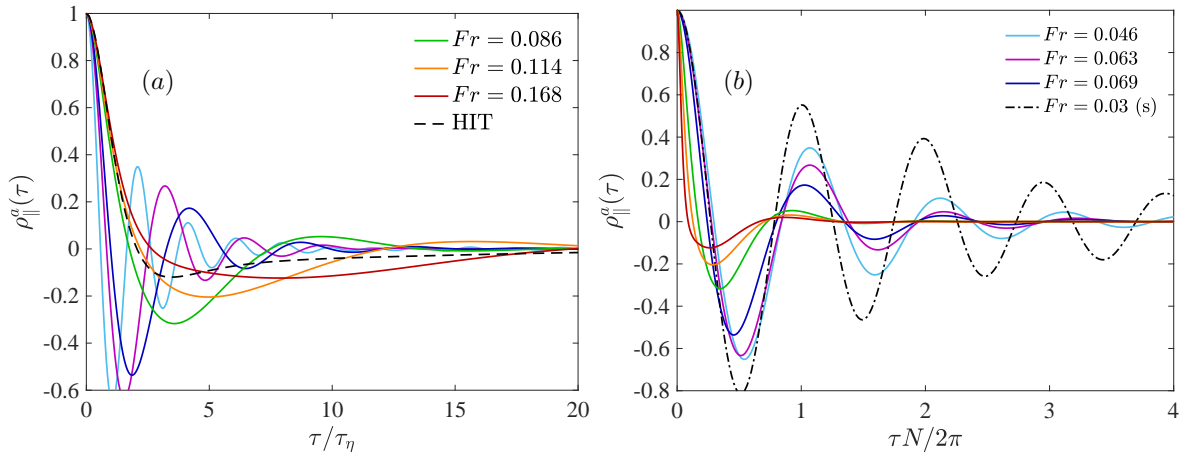


FIG. 6. Lagrangian autocorrelation of the parallel (vertical) component of acceleration  $\rho_{\parallel}^a(\tau)$  against the time lag  $\tau$  normalized by the Kolmogorov time scale  $\tau_{\eta}$  in (a) and by the Brunt-Väisälä period  $2\pi/N$  in (b). The legend is split over two panels, but applies to each panel individually.

Note that the runs shown in Fig. 5a and b correspond to the same runs shown respectively in Fig. 4a and b. For the HIT run in Fig. 5a, Kolmogorov scaling would imply that the spectrum  $E^a$  is constant in the inertial range (defined as  $\tau_{\eta}/T_E \lesssim \omega\tau_{\eta} \lesssim 1$ ). While the validity of Kolmogorov's similarity hypotheses to Lagrangian statistics is debatable, DNS studies suggest that the above scaling law, i.e.,  $E^a \sim \langle \epsilon \rangle$ , still may be approximately satisfied [55]. Consistent with this, we find that for our HIT run, the spectrum  $E_{\perp}^a(\omega)$  is approximately flat over a limited range of values of  $\omega$ .

With addition of weak RaS, the changes in the structure of the spectrum appear to be relatively minor. In particular, for runs with  $Fr \geq 0.086$ , the differences in spectra, relative to the HIT case, only become significant for  $\omega\tau_{\eta} \lesssim 0.2$ . For the particular case of  $Fr = 0.086$ , a small peak emerges around  $\omega\tau_{\eta} \approx 0.1$ . With increasing strength of RaS, the differences become more pronounced, with all the cases for  $Fr \leq 0.086$  now showing a prominent peak (which is relatively broad). This observation is consistent with the behavior of the autocorrelation function at small times, as observed in Fig. 4. In addition, the increase in values of  $E_{\perp}^a/\langle \epsilon \rangle$  also corresponds to the strong increase in the value of  $a_0$  for small  $Fr$  cases, as shown in Fig. 2 (for the perp. data points). Interestingly, the decay of spectra for all cases are somewhat similar at very large frequencies (and not very different from the HIT case). This possibly confirms that the role of turbulent eddies in the horizontal direction is still relevant as compared to the vertical direction, at least in the parameter range covered in this work (note once again the fact that  $N/f = 5$ , plays an important role, since it renders the effect of rotation relatively weaker than that of stratification).

Fig. 5b shows the spectra as a function of  $\omega/f$ . As expected, the peaks observed at low frequencies in Fig. 5a, are all centered around  $\omega/f \approx 1$ . For the runs with strong RaS, the frequency corresponding to stratification, i.e.,  $\omega/f = N/f = 5$ , does not seem to play any particularly important role.

*Parallel component:* While the role of rotation was dominant in the perpendicular direction, we can in turn expect stratification to dominate in the parallel direction. In Fig. 6a and b, we show the autocorrelation in the parallel direction  $\rho_{\parallel}^a$  as a function of  $\tau/\tau_{\eta}$  and of  $\tau(N/2\pi)$  respectively. As it was the case for the perpendicular component of acceleration, the deviation of the autocorrelation function from the reference homogeneous isotropic case, shown as a dashed line, increases gradually



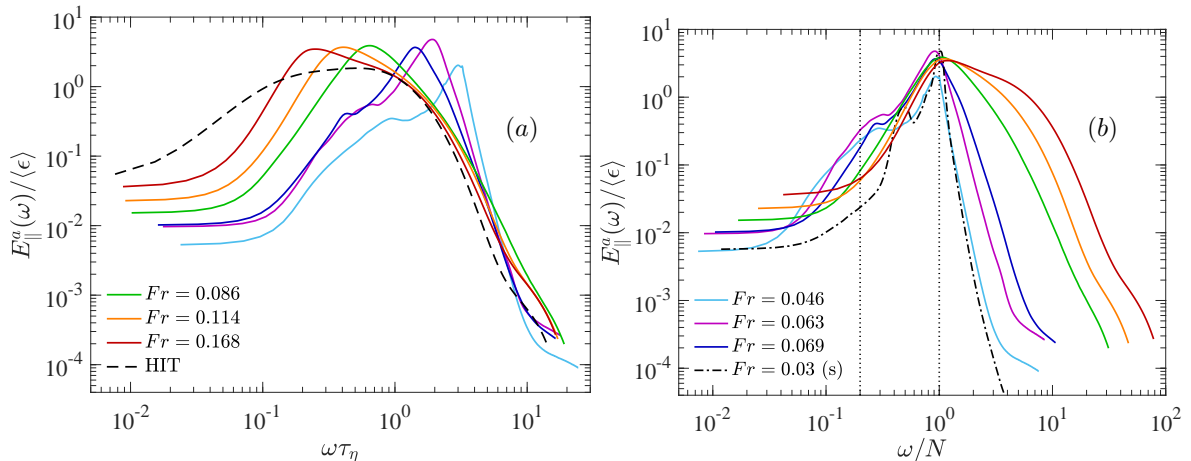


FIG. 7. Lagrangian frequency spectrum of the parallel (vertical) component of acceleration  $E_{\parallel}^a(\omega)$  against the frequency  $\omega$  normalized by the Kolmogorov time scale  $\tau_{\eta}$  in (a) and by the Brunt-Väisälä frequency  $N$  in (b). The spectra are non-dimensionalized using the mean kinetic energy dissipation rate  $\langle \epsilon \rangle$ . Vertical dotted lines in (b) correspond to frequencies  $\omega = f$  and  $N$  (with  $N = 5f$ ). The legend is split over two panels, but applies to each panel individually.

when  $Fr$  decreases. However, contrary to  $\rho_{\perp}^a$ ,  $\rho_{\parallel}^a$  tends to decay significantly faster than in the HIT case when  $Fr$  diminishes. In addition, for all cases, overshooting oscillations are clearly visible, with a particularly strong amplitude for cases with  $Fr \leq 0.086$ . While the zero-crossing of  $\rho_{\parallel}^a$  for cases with weak RaS still appears to be close to  $\tau \approx 2\tau_{\eta}$  (with minor deviations), for cases with strong RaS, the zero-crossing shifts to even smaller time lags of  $\tau \approx 0.5\tau_{\eta}$ . This is in contrast to  $\rho_{\perp}^a$ , where the zero-crossing first shifted to higher time lags, and then moved to smaller time lags with decreasing  $Fr$ . Fig. 6b clearly reveals that the period of the oscillations is equal to the Brunt-Väisälä period,  $2\pi/N$ . This strongly suggests that the motion in the parallel direction is dominated by stratification, and that turbulence plays a much smaller role for the vertical motion (in comparison to horizontal motion, where even at strongest rotation rate, the role of turbulence still could not be ignored). For comparison, the autocorrelation function  $\rho_{\parallel}^a$  is shown in Fig. 6b for the run with a strong stratification,  $Fr = 0.03$ . The tendency to oscillate is even stronger in this run, an effect amplified by the low value of  $Fr$  (and  $R_{IB}$ ) in this case (see Table II).

The corresponding frequency spectra  $E_{\parallel}^a(\omega)$  are plotted as a function of  $\omega\tau_{\eta}$  and of  $\omega/N$  in Fig. 7a and b respectively. The spectra are again non-dimensionalized by  $\langle \epsilon \rangle$ . Unlike in the case of  $E_{\perp}^a$ , we observe that deviations from the HIT run are already prominent even for runs with weak RaS. All spectra are characterized by the presence of a peak, with the peak becoming more sharp and prominent as  $Fr$  decreases. An inspection of spectra in Fig. 7b clearly shows that all these peaks correspond to  $\omega/N \approx 1$ , i.e., the respective Brunt-Väisälä frequencies, conforming with the dominant role of stratification in the vertical direction. Note the peak for the stratification-only run is even more pronounced. For runs with strong RaS, i.e.,  $Fr \leq 0.069$ , a very minor enhancement of the spectra is visible in the band of frequencies  $\omega/N \approx 0.2$  (or  $\omega/f \approx 1$ ).

Another point to note is that even though the peaks in  $E_{\parallel}^a$  become sharper with decreasing  $Fr$ , their amplitudes do not vary much, in contrast to  $E_{\perp}^a$ , where the peaks vary by more than an order of magnitude. This can be explained by the variation of acceleration variance as seen in Fig. 2. While the  $a_0^{\perp}$  sharply shoots up for runs with  $Fr \leq 0.069$ , the  $a_0^{\parallel}$  only shows a minor variation in comparison.

The results of this Subsection complement the conclusions of Subsections IV A and IV B, as well as those of Section III, which were pointing to two qualitatively different regimes, dominated by waves for  $R_{IB} < 1$ , and by eddies  $R_{IB} > 1$ . Whereas in the latter regime, the variances and the PDFs of accelerations were showing only moderate deviations compared to HIT flow, Fig. 5b and 7b reveals the role of  $N$  and  $f$  in the horizontal and vertical motion closer to the transition, when  $R_{IB} \gtrsim 1$  ( $R_{IB} = 2.69$  for run 3). The transition to a wave-dominated regime for  $R_{IB} < 1$  corresponds to the formation of peaks, which are much more intense (see Fig. 5b) or much sharper (see Fig. 7b), leading to a qualitatively very different dynamics.

## V. LAGRANGIAN VELOCITY AND DISPERSION STATISTICS

The spread or dispersion of a material under the action of turbulence is of obvious importance and can be directly studied from the investigation of the Lagrangian velocity along trajectories. In this regard, we briefly summarize the classical theory below [7].

Single-particle dispersion is best understood by considering the mean-square displacement of a particle from its initial position. From Eq. (7), we can write for each direction:

$$\langle Y_i^2(t) \rangle = \langle u_i(0)^2 \rangle \int_0^t \int_0^t \rho^{u_i}(t', t'') dt' dt'' \quad (11)$$

where  $Y_i(t) = x_i(t) - x_i(0)$  is the displacement of the particle from its position  $x_i(0)$  at  $t = 0$  to its position  $x_i(t)$  at time  $t$ , and  $\rho^{u_i}(t', t'')$  is the velocity autocorrelation. For statistical stationarity, the autocorrelation function at  $t'$  and  $t''$  only depends on  $\tau = |t' - t''|$ , allowing Eq. (11) to be rewritten as

$$\langle Y_i^2(t) \rangle = 2\langle u_i^2 \rangle \int_0^t (t - \tau) \rho^{u_i}(\tau) d\tau \quad (12)$$

Once again, we treat separately the horizontal and vertical components, as explained before. The expression for the dispersion, Eq. (12), simplifies in the limit of short and long times, respectively to

$$\langle Y_{\perp, \parallel}^2(t) \rangle = \langle u_{\perp, \parallel}^2 \rangle t^2 \quad \text{for } t \ll \tau_K, \quad (13)$$

$$\langle Y_{\perp, \parallel}^2(t) \rangle = D_{\perp, \parallel} t \quad \text{for } t \gg T_L^{\perp, \parallel}, \quad (14)$$

where  $D_{\perp, \parallel} = 2\langle u_{\perp, \parallel}^2 \rangle T_L^{\perp, \parallel}$  are the diffusion coefficients and

$$T_L^{\perp, \parallel} = \int_0^\infty \rho_{\perp, \parallel}^u(\tau) d\tau \quad (15)$$

are the Lagrangian integral times. In the following subsections, we discuss separately the behavior of the autocorrelation functions, integral time scales and then the mean-square displacements.

### A. Velocity autocorrelation and integral time scales

In this subsection, we investigate the behavior of the velocity autocorrelations and the corresponding integral time scales derived from them. Similar to the acceleration spectra, the velocity frequency spectra can be obtained through a Fourier transform of the velocity autocorrelations. However, the velocity spectra can also be simply derived from the acceleration spectra using the simple relation  $E^u(\omega) = E^a(\omega)/\omega^2$  [53]. Consequently, we do not discuss the results for  $E^u$  in this section (since they provide similar information as  $E^a$ ). Instead, we have briefly summarized them in the Supplementary Material [42].

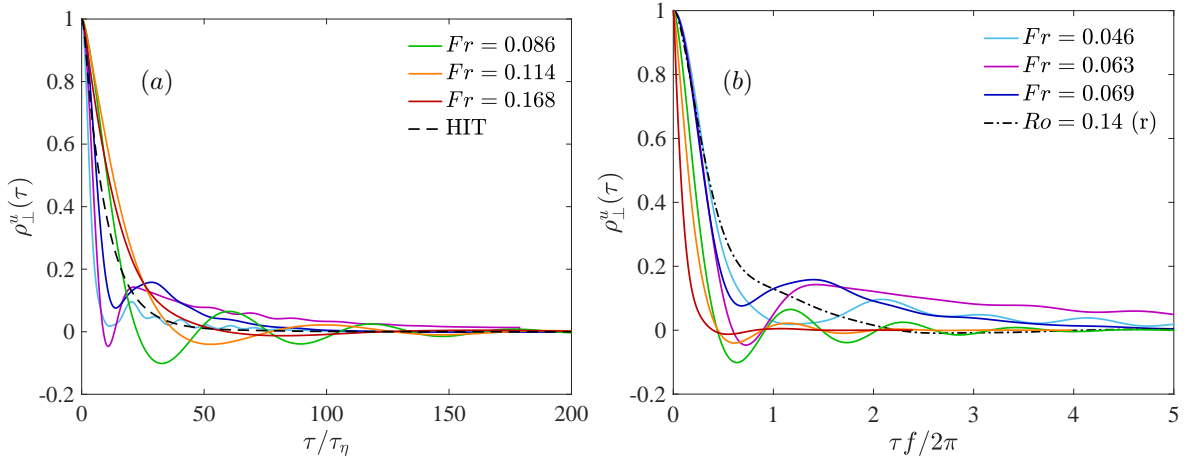


FIG. 8. Lagrangian autocorrelation  $\rho_{\perp}^u(\tau)$  of the perpendicular (horizontal) component of the velocity. Similar normalizations as Fig. 4 are used. The legend is split over two panels, but applies to each panel individually.

*Perpendicular component:* Fig. 8a-b shows the autocorrelation functions  $\rho_{\perp}^u(\tau)$ ; similar to results for the perpendicular component of acceleration, the time lag  $\tau$  is normalized first by  $\tau_{\eta}$  and then by  $f$ . The correlation function  $\rho_{\perp}^u$ , plotted as a function of  $\tau/\tau_{\eta}$ , see Fig. 8a, shows only weak deviations from the HIT case (shown in black dashed line) when RaS are moderate (runs 1-3). We recall that in the HIT case, the long time behavior of the velocity autocorrelation can be well represented by an exponential functional form,  $\rho^u \sim \exp^{-\tau/T_L}$  [12]. We notice that the runs with RaS are fundamentally different from the HIT run with appearance of oscillations resulting in negative values of the correlation function. These deviations become stronger with imposed RaS.

To better understand these oscillations, Fig. 8b shows the autocorrelation as a function of  $\tau f/2\pi$ . Although an oscillatory behavior can be seen in the runs with the highest values of RaS rates, the frequency is close to, but differs from  $f$ . On the other hand,  $\rho_{\perp}^u$  in the flow with rotation only (shown in black dash-dotted line in Fig. 8b), appears to be monotonically decreasing (no oscillations).

*Parallel component:* The autocorrelations and spectra corresponding to the parallel component of velocity are shown in Fig. 9. We first consider the autocorrelation  $\rho_{\parallel}^u$  as a function of  $\tau/\tau_{\eta}$  in Fig. 9a. In all the cases with RaS,  $\rho_{\parallel}^u$  strongly differs from the HIT case (indicated by a black dashed line). Two patterns are distinctly visible. First, all the autocorrelation functions decay rapidly. In terms of the dimensionless time  $t/\tau_{\eta}$ , the decay rate becomes increasingly larger when  $Fr$  decreases (especially in comparison to perpendicular component shown in Fig. 8a). Second, the autocorrelations all overshoot to become strongly negative and show distinct oscillations. The primary period of these oscillations corresponds to the stratification frequency, as demonstrated by Fig. 9b, which shows the autocorrelations as a function of  $\tau N/2\pi$ . In addition, Fig. 9b also shows that all cases superpose reasonably well for the initial decay of the autocorrelation, These results clearly demonstrate that stratification plays a dominant role in the vertical motion, and in comparison turbulence plays a weaker role. The fast dynamics in the vertical direction is dominated by the strong vertical gradients arising from the constraint that the vertical Froude number be of order unity [56], and leading to strong spatial and temporal intermittency, dissipation and mixing [57]. This is true, even for the runs at weak RaS ( $Fr \gtrsim 0.08$ ). A similar behavior was obtained for the vertical acceleration correlation function, see Section IV C. We notice that in the case of a

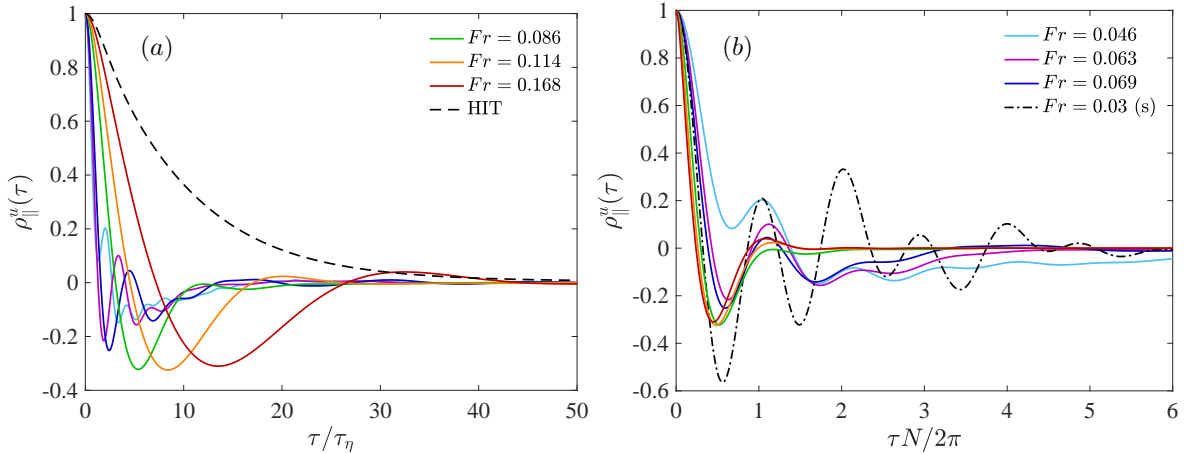


FIG. 9. Lagrangian autocorrelation  $\rho_{||}^u(\tau)$  of the parallel (vertical) component of the velocity. Similar normalizations as Fig. 6 are used. The legend is split over two panels, but applies to each panel individually.

purely stratified run, without any rotation, the autocorrelation function  $\rho_{||}^u$  clearly oscillates, with a modulation at twice the Brunt-Väisälä period.

case	0	1	2	3	4	5	6	7	8
$Fr$	$\infty$	0.168	0.114	0.086	0.069	0.063	0.045	0.030	$\infty$
$Ro$	$\infty$	0.840	0.570	0.430	0.345	0.315	0.225	$\infty$	0.140
$T_L^\perp/\tau_\eta$	11	14	14	10	12	4.1	5.8	$\infty$	8.2
$T_L^\parallel/\tau_\eta$	10	0.59	0.23	0.11	$6.4 \cdot 10^{-2}$	$2.7 \cdot 10^{-2}$	$5.5 \cdot 10^{-2}$	$3.6 \cdot 10^{-2}$	8.4
$T_L^\parallel N/(2\pi)$	0	$2.0 \cdot 10^{-2}$	$1.4 \cdot 10^{-2}$	$1.1 \cdot 10^{-2}$	$1.6 \cdot 10^{-2}$	$9.0 \cdot 10^{-3}$	$2.8 \cdot 10^{-2}$	$1.2 \cdot 10^{-2}$	0

TABLE IV. Integral time scales of the velocity,  $T_L^\perp$  and  $T_L^\parallel$  respectively based on the perpendicular (horizontal) component and parallel (vertical) component (see Eq. (15) for definition). The integral time scales are also compared with the Kolmogorov time  $\tau_\eta$ , and of the Brunt-Väisälä period,  $2\pi/N$ , for the vertical motion, and of the rotation period,  $2\pi/f$ , for the horizontal motion. (A more detailed table is provided in the Supplementary Material [42]).

*Integral time scales:* As highlighted by Eqs. (14) and (15), the Lagrangian integral time scale  $T_L$ , characterizes the particle dispersion at large times and is simply obtained by integrating the autocorrelation function:  $T_L = \int_0^\infty \rho^u d\tau$ . We begin by noticing that many of the correlation functions shown in Figs. 8 and 9 exhibit an oscillatory behavior. This makes the calculation of their integrals generally prone to statistical errors. As such, the values of  $T_L^{\perp,\parallel}$ , listed in Table IV, are subject to large relative errors, the more so as the values of  $T_L^{\perp,\parallel}$  are small.

Over the range of  $Re$  considered here, the variation of  $T_L^\perp$  is found to be rather weak at moderate RaS ( $Fr \gtrsim 0.08$ ). In particular, the ratio  $T_L^\perp/\tau_\eta$ , is of the order of 10 for the HIT run, and remains approximately constant for cases 1-4 and also for the run 8, which corresponds to a flow with rotation only. For cases 5-6 with strong RaS, the ratio sharply drops by a factor  $\sim 2$ , which can be attributed to a sharp decrease in the mean dissipation  $\langle \epsilon \rangle$  (hence causing a sharp increase in  $\tau_\eta$ ). The above observations are consistent with earlier results which also highlight a sharp transition to wave-dominated regime as  $R_{IB}$  significantly decreases. We note that for the run with pure stratification (case 7), the velocity autocorrelation in the horizontal direction converges extremely slowly to zero at large time lags, pointing to an extremely large value of  $T_L^\perp$ . A similar behavior

has been noticed in [19]. In this regard, the presence of rotation plays a crucial role. In particular, the dispersion relation and the structure of the eigenmodes, underlying the wave motion is strongly modified by rotation.

On the other hand, the integral time  $T_L^{\parallel}$  is substantially smaller than  $T_L^{\perp}$  for all runs with stratification (cases 1-7). The ratio  $T_L^{\parallel}/\tau_{\eta}$  is still around 10 for the HIT and purely rotating flows (cases 0 and 8 respectively), but is greatly reduced for all runs with stratification. This can be evidently attributed to the strongly oscillating nature of the velocity autocorrelation functions for cases 1-7 (see Fig. 9b), which results in significant cancellation when calculating  $T_L^{\parallel}$ . The ratio  $T_L^{\parallel}/\tau_{\eta}$  drops by more than an order of magnitude in going from HIT to case 1, which corresponds to the weakest RaS. Thereafter, with increasing strength of RaS, the ratio further decreases. Interestingly, the ratio  $T_L^{\parallel}N/2\pi$  shows a much reduced variation, and remains in the range 0.01-0.02 for all cases with stratification. This suggests that despite the strong oscillations in the autocorrelation the time scale,  $T_L^{\parallel}$ , is not strictly zero, but instead scales inversely with  $N$ , consistent with earlier predictions for purely stratified flows [58].

### B. Mean-square displacement

Fig. 10 shows the mean-square displacement for horizontal and vertical directions as a function of time (both axes normalized appropriately by Kolmogorov scales). At small times, a clear  $t^2$  scaling is visible for all runs in both components, as expected from Eq.(13). The displacement in the horizontal direction is enhanced by RaS, whereas inhibited in the vertical direction. This can be readily explained by considering the variance of the components of the velocity  $\langle v_{\perp}^2 \rangle$  and  $\langle v_{\parallel}^2 \rangle$ , as shown in Table II (see also Eq. (13)).

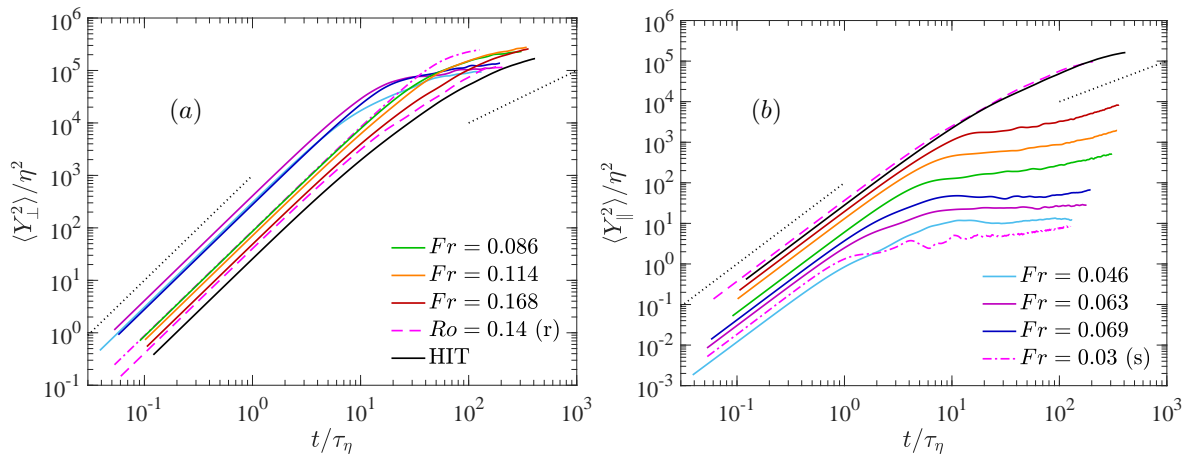


FIG. 10. Mean square displacement as a function of time in the (a) perpendicular (horizontal) direction and (b) parallel (vertical) direction. All quantities normalized by Kolmogorov scales. The dotted lines represent slopes 2 and 1 at short and long times respectively. The legend is split over two panels, but applies to each panel individually.

At long times, transition to a diffusive regime, given by Eq. (14), is expectedly seen in the HIT run [53], for both horizontal and vertical components. A similar behavior is also visible for runs with weak RaS ( $Fr \gtrsim 0.08$ ), when considering the horizontal component. In comparison, the growth of the vertical component at long times for these runs is significantly inhibited, nevertheless

still showing a very slow approach to a diffusive regime. Our results are generally consistent with those obtained earlier for a comparable parameter range ( $N/f = 10$ ,  $Fr \approx 0.16$ ) [59]. Note the rotation-only run, behaves like the HIT run, consistent with the small degree of anisotropy in both velocity and acceleration statistics as noted earlier.

On the other hand, for runs with strong RaS ( $Fr \lesssim 0.07$ ), the growth of both horizontal and vertical components appears to be slower than a linear behavior. This is particularly clear for the vertical displacements  $\langle Y_{\parallel}^2 \rangle$ , which appear to increase extremely slowly with time, if at all. In fact, the values of  $\langle Y_{\parallel}^2 \rangle / \eta^2$  remain small, of the order of  $\sim 10$ , over a very long time. The absence of a clear diffusive regime for  $\langle Y_{\parallel}^2 \rangle$  is arguably not very surprising, given the small values of  $T_{\parallel}^L$  and  $\langle v_{\parallel}^2 \rangle$ , hence of the diffusion coefficient  $D = \langle v_{\parallel}^2 \rangle T_{\parallel}^L$ . Assuming that  $T_{\parallel}^L$  is inversely proportional to  $N$  (multiplied with a small prefactor), the expected diffusive behavior will likely be visible only after an extremely long time. Consistent with our own results, the near constancy of  $\langle Y_{\parallel}^2 \rangle$  was also reported in purely stratified flows [17–19].

Contrary to the very low values of  $T_{\parallel}^L$  for runs with strong RaS (see Table IV), the values of  $T_{\perp}^L$  do not appear to be particularly small. This makes the lack of a clear diffusive regime for runs 4-6 for the horizontal displacement much more surprising. It has been noticed in the context of stratified flows, that the horizontal displacement could grow as  $t^2$  [17]. Here, our results show that, in a regime dominated by waves (runs 4-6), the growth of  $\langle Y_{\perp}^2 \rangle$  is slower than  $t^1$  over a long time. This suggests a strong interaction between the horizontal and vertical directions owing to the presence of rotation (and inertia-gravity waves), which was also visible in autocorrelations of acceleration and velocity. However, given the large values of  $T_{\perp}^L$ , it can be expected that the diffusive regime is ultimately reached at sufficiently longer times.

Finally, we note that the strong vertical drafts responsible for high kurtosis of  $u_{\parallel}$  (see Section III), and increased mixing efficiency [34], do not appear to cause an appreciable growth in  $\langle Y_{\parallel}^2 \rangle$  for the runs considered here. This is not inconsistent given the kurtosis is a normalized fourth-order moment, whereas  $\langle Y_{\parallel}^2 \rangle$  goes as the variance of vertical velocity and the integral scale  $T_{\parallel}^L$ , both of which are strongly suppressed. It is likely that at higher Reynolds numbers than considered here, the effect of the vertical drafts is felt more directly on the vertical displacement of fluid particles.

## VI. DISCUSSION AND CONCLUSIONS

Motivated by the well established effect of both rotation and stratification (RaS) in numerous geophysical flows, and by the observation of Lagrangian tracers, such as buoys in the ocean [60], we have investigated the properties of particle trajectories in such flows. We have utilized direct numerical simulations of the Boussinesq equations in a periodic domain, with both stratification and the axis of rotation aligned in the vertical direction, in a statistically stationary regime maintained by an external forcing. We have focused on cases where the corresponding rotation and stratification frequencies,  $f$  and  $N$  respectively, are held in a fixed ratio  $N/f = 5$ , as relevant in oceanographic situations [21]. The usual computer limitations have restricted the Reynolds numbers to approximately around 4000 in our runs, which are smaller than those observed in nature, but still large enough to allow turbulence to adequately develop. The Froude numbers investigated are in the range  $0.03 \lesssim Fr \lesssim 0.2$ , with corresponding Rossby number  $Ro = 5Fr$ , compatible with geophysical fluid flows. Our results illustrate the complex physical effects involved in a turbulent flow under the combined action of RaS. Whereas the corresponding physical effects have been recently investigated in an Eulerian context in many studies, we have documented the elementary properties of particle trajectories, in particular concerning acceleration, velocity and displacement

statistics. Due to the imposed large-scale anisotropy, we differentiate between motion in the horizontal plane and in the vertical direction. We also appropriately compare with rotation-only and stratification-only runs and also with the well studied case of isotropic turbulence.

While the parameters  $Fr$  and  $Ro$  vary smoothly with the strength of imposed RaS, we observe a sharp change in the nature of the flow when  $Fr \lesssim 0.07$  for the runs considered, corresponding to a regime where waves appear to dominate over the non-linearities, as also observed in [34] for stratification-only runs. An inspection of the Eulerian energy spectra (and the temperature spectra), shows a clear transition from a Kolmogorov  $k^{-5/3}$  like behavior to a Bolgiano  $k^{-11/5}$  like behavior at intermediate wavenumbers. The transition also corresponds to the peak of intermittent disruption of shear layers, with a maximum of the kurtosis of the vertical velocity. In this context, our work extends the stratification-only results of [34]. Interestingly, we find that this transition to wave-dominated regime can be given by a simple condition of  $R_{IB} < 1$  based on the buoyancy Reynolds number  $R_{IB}$ .

The effect of this transition is also evident in Lagrangian statistics. For acceleration statistics, the effect of imposed RaS appears very weak before the transition, suggesting the imposed anisotropy does not affect the small-scale isotropy significantly. The probability density functions (PDFs) of acceleration in both horizontal and vertical direction display wide tails very similar to isotropic turbulence, and the variance of acceleration can be approximately scaled with Kolmogorov variables. The Lagrangian autocorrelations and frequency spectra also appear to behave in a similar fashion, although a weak effect of RaS is still visible at low frequencies in the spectra (when  $R_{IB} \gtrsim 1$ ). However, the sharp transition at  $R_{IB} \lesssim 1$  leads to a very strong anisotropy between the horizontal and vertical directions, with the particle motion strongly dominated by RaS instead of turbulent eddies. The PDFs of acceleration show suppressed tails, and acceleration variance shows no clear scaling. Moreover, the autocorrelations and frequency spectra clearly reflect the dominant roles of frequencies  $N$  and  $f$ .

On the other hand, Lagrangian velocity statistics are always affected by the imposed RaS. Anisotropy is already evident for weak RaS; however the degree of anisotropy becomes very strong with the said transition at  $R_{IB} \lesssim 1$ . This is most readily seen in the integral time scale based on the autocorrelations from vertical velocity and hence also reflected in long time behavior of mean-square displacement of particles in the vertical direction. Similar effects had been observed in the case of purely stratified flows [19]. In such flows, it is known that stratification leads to the formation of horizontal layers, that inhibits the transport in the vertical direction. In the presence of both RaS, slanted layers appear [23] which somewhat inhibit transport in both the vertical and the horizontal directions.

It is interesting to consider that the transitional behavior observed in this work is possibly also linked to the enhanced vertical velocities that develop in strongly stably stratified turbulent flows, such as in the nocturnal planetary boundary layer [61], and warrant further examination. The resulting dispersion of Lagrangian particles must feel these hot spots of strong vertical velocity and strong local dissipation linked to localized shear instabilities, as also observed in the ocean. Several studies point to a local Richardson number, measuring stratification with respect to the internal shear associated with vertically sheared horizontal winds, to be mostly in the vicinity of the value for linear instability [28, 57, 62]. This leads to flows which are altogether close to criticality, and strongly anisotropic, intermittent and dissipative [57]. We expect that the observed similarity between the statistical properties of acceleration when the flow is dominated by eddies (for  $R_{IB} > 1$ ), and those in HIT, may be very useful in modeling the dispersion of particles in turbulent flows in the presence of RaS.

Whereas  $R_{IB}$  seems to provide a clear criterion to distinguish between the different regimes observed here, alternative ways [32] have been proposed to describe the transition between wave-dominated flows, and flows where waves and eddies interact. Namely, it was found that the

transition occurs around  $R_B \sim 10$ , where  $R_B = ReFr^2$ . In this sense, the flows studied here are all in the regime of interacting waves and eddies, although run 6 is very close to the transition towards a wave-dominated flow.

We conclude by mentioning that many interesting issues remain to be addressed for particle motion in such flows. For example, the problem of separation of pairs, or of clusters of particles, both forward and backward in time [63, 64] or considering the effects of particle inertia or molecular diffusion. In addition, we stress that the picture we have drawn is based on runs at a relative moderate Reynolds numbers. Exploring higher Reynolds numbers, and also higher Prandtl/Schmidt numbers [65], along with different values of  $N/f$  will help in better understanding the parameter space and how the results from current work translate to practical geophysical applications.

### ACKNOWLEDGMENTS

The computing resources utilized in this work were provided by PSMN at the Ecole Normale Supérieure de Lyon. D. Buaria and A. Pumir acknowledge support from the European High-performance Infrastructure in Turbulence (EuHIT) program and the Max Planck Society. A. Pumir acknowledges additional support from the IDEXLYON project (Contract ANR-16-IDEX-0005) under University of Lyon auspices. R. Marino acknowledges support from the program PALSE (Programme Avenir Lyon Saint-Etienne) and IMPULSION of the University of Lyon, in the framework of the program *Investissements d’Avenir* (ANR-11-IDEX-0007), from the Inge’LySE (Lyon-Saint-Etienne) and from ERCOFTAC. A. Pouquet gratefully acknowledges support from Laboratory for Atmospheric and Space Physics (LASP), in particular Bob Ergun, at the University of Colorado, Boulder.

- 
- [1] J. Pedlosky, *Geophysical Fluid Dynamics* (Springer, 1979).
  - [2] J. B. Weiss and A. Provenzale, *Transport and mixing in geophysical flows*, Vol. 744 (Springer, 2007).
  - [3] J. C. Wyngaard, “Atmospheric turbulence,” *Annu. Rev. Fluid Mech.* **24**, 205–234 (1992).
  - [4] A. Stohl, S. Eckhardt, C. Forster, P. James, and N. Spichtinger, “On the pathways and timescales of intercontinental air pollution transport,” *J. Geophysical Research: Atmospheres* **107**, ACH-6 (2002).
  - [5] R. A. Shaw, “Particle-turbulence interactions in atmospheric clouds,” *Ann. Rev. Fluid Mech.* **35**, 183–227 (2003).
  - [6] J. S. Guasto, R. Rusconi, and R. Stocker, “Fluid mechanics of planktonic microorganisms,” *Annu. Rev. Fluid Mech.* **44**, 373–400 (2012).
  - [7] A. S. Monin and A. M. Yaglom, *Statistical Fluid Mechanics. Vol. I*, Vol. 1 (MIT Press, 1971).
  - [8] D. Buaria, P. K. Yeung, and B. L. Sawford, “A Lagrangian study of turbulent mixing: forward and backward dispersion of molecular trajectories in isotropic turbulence,” *J. Fluid Mech.* **799**, 352–382 (2016).
  - [9] A. Pumir and M. Wilkinson, “Collisional aggregation due to turbulence,” *Annu. Rev. Condens. Matter Phys.* **7**, 141–170 (2016).
  - [10] P. A. Davidson, *Turbulence in Rotating, Stratified and Electrically Conducting Fluids* (Cambridge University Press, 2013).
  - [11] B. Sawford, “Turbulent relative dispersion,” *Annu. Rev. Fluid Mech.* **33**, 289–317 (2001).
  - [12] P. K. Yeung, “Lagrangian investigations of turbulence,” *Ann. Rev. Fluid Mech.* **34**, 115–142 (2002).
  - [13] F. Toschi and E. Bodenschatz, “Lagrangian properties of particles in turbulence,” *Annu. Rev. Fluid Mech.* **41**, 375–404 (2009).
  - [14] L. DelCastello and H. J. H. Clercx, “Lagrangian acceleration of passive tracers in statistically steady rotating turbulence,” *Phys. Rev. Lett.* **107**, 214502 (2011).
  - [15] L. DelCastello and H. J. H. Clercx, “Lagrangian velocity autocorrelations in statistically steady rotating turbulence,” *Phys. Rev. E* **83**, 056316 (2011).



- [16] A. Naso and F. S. Godeferd, “Statistics of the perceived velocity gradient tensor in a rotating turbulent flow,” *New J Phys* **125002**, 7558–7563 (2012).
- [17] M. van Artrijk, H. J. H. Clercx, and K. B. Winters, “Single-particle, particle-pair, and multiparticle dispersion of fluid particles in forced stably stratified turbulence,” *Phys. Fluids* **20**, 025104 (2008).
- [18] G. Brethouwer and E. Lindborg, “Numerical study of vertical dispersion by stratified turbulence,” *J. Fluid Mech.* **631**, 149–163 (2009).
- [19] N. E. Sujovolsky, P. D. Mininni, and M. P. Rast, “Single-particle dispersion in stably stratified turbulence,” *Phys. Rev. Fluids* **3**, 034603 (2018).
- [20] A. C. N. Garabato, K. L. Polzin, B. A. King, K. J. Heywood, and M. Visbeck, “Widespread intense turbulent mixing in the southern ocean,” *Science* **303**, 210–213 (2004).
- [21] M. Nikurashin, G. K. Vallis, and A. Adcroft, “Routes to energy dissipation for geostrophic flows in the southern ocean,” *Nat. Geosci.* **6**, 48–51 (2012).
- [22] H. van Haren and L. Gostiaux, “Convective mixing by internal waves in the Puerto Rico Trench,” *J. Mar. Res.* **74**, 161–173 (2016).
- [23] R. Marino, P. D. Mininni, D. Rosenberg, and A. Pouquet, “Emergence of helicity in rotating stratified turbulence,” *Phys. Rev. E* **87**, 033016 (2013).
- [24] A. Pouquet and R. Marino, “Geophysical turbulence and the duality of the energy flow across scales,” *Phys. Rev. Lett.* **111**, 234501 (2013).
- [25] G. Haller, “Lagrangian coherent structures,” *Annu. Rev. Fluid Mech.* **47**, 137–162 (2015).
- [26] G. Ivey, K. Winters, and J. Koseff, “Density stratification, turbulence but how much mixing?” *Ann. Rev. Fluid Mech.* **40**, 169 (2008).
- [27] E. Deusebio, P. Augier, and E. Lindborg, “Third-order structure functions in rotating and stratified turbulence: a comparison between numerical, analytical and observational results,” *J. Fluid Mech.* **755**, 294–313 (2014).
- [28] D. Rosenberg, A. Pouquet, R. Marino, and P. D. Mininni, “Evidence for Bolgiano-Obukhov scaling in rotating-stratified turbulence using high-resolution direct numerical simulations,” *Phys. Fluids* **27**, 055105 (2015).
- [29] E. Lindborg and A. V. Mohanan, “A two-dimensional toy model for geophysical turbulence,” *Phys. Fluids* **29** (2017).
- [30] M. L. Waite, “Random forcing of geostrophic motion in rotating stratified turbulence,” *Phys. Fluids* **29** (2017).
- [31] M.C. Gregg, E.A. D’Asaro, J.J. Riley, and E. Kunze, “Mixing efficiency in the ocean,” *Ann. Rev. Marine Sci.* **10**, 9.1–9.31 (2018).
- [32] A. Pouquet, D. Rosenberg, R. Marino, and C. Herbert, “Scaling laws for mixing and dissipation in unforced rotating stratified turbulence,” *J. Fluid Mech.* **844**, 519–545 (2018).
- [33] C. Rorai, P. D. Mininni, and A. Pouquet, “Turbulence comes in bursts in stably stratified flows,” *Physical Review E* **89**, 043002 (2014).
- [34] F. Feraco, R. Marino, A. Pumir, L. Primavera, P. D. Mininni, A. Pouquet, and D. Rosenberg, “Vertical drafts and mixing in stratified turbulence: sharp transition with the Froude number,” *Europhys. Lett.* **123**, 44002 (2018).
- [35] R. Marino, P. D. Mininni, D. Rosenberg, and A. Pouquet, “Inverse cascade in rotating stratified turbulence: fast growth of large scales,” *Europhys. Lett.* **102**, 44006 (2013).
- [36] A. Pouquet, D. Rosenberg, J. Stawarz, and R. Marino, “Helicity dynamics, inverse, and bidirectional cascades in fluid and magnetohydrodynamic turbulence: A brief review,” *Earth Space Sci.* **6**, 1–19 (2019).
- [37] D. Buaria, A. Pumir, E. Bodenschatz, and P. K. Yeung, “Extreme velocity gradients in turbulent flows,” *New J. Phys.* **21**, 043004 (2019).
- [38] R. Marino, D. Rosenberg, C. Herbert, and A. Pouquet, “Interplay of waves and eddies in rotating stratified turbulence and the link with kinetic-potential energy partition,” *EuroPhys. Lett.* **112**, 49001 (2015).
- [39] G. Brethouwer, P. Billant, E. Lindborg, and J. M. Chomaz, “Scaling analysis and simulations of strongly stratified flows,” *J. Fluid Mech.* **585**, 343–368 (2007).
- [40] T. Ishihara, T. Gotoh, and Y. Kaneda, “Study of high-Reynolds number isotropic turbulence by direct numerical simulations,” *Ann. Rev. Fluid Mech.* **41**, 165–80 (2009).

## Chapter 3

# Observation of vertical drafts in the Earth's upper atmosphere

In stratified flows as in the Earth's atmosphere and in the oceans [30, 63], intermittency is observed not only in phenomena related to the field variations at the smallest-scales, but strong enhancements of the fields occur also at scales comparable to that of the mean flow [31, 24, 39]. The origin of large-scale intermittent phenomena in geophysical flows is not clear though recent studies based on numerical simulations [16, 65] and theoretical modeling [73, 74] provided major insights on the dynamics underlying the sudden amplification of the potential temperature  $\theta$  and of the vertical component of the velocity  $w$  in stably stratified turbulent flows. These rare and powerful events developing in  $w$  and  $\theta$  have been explained in terms of the interplay of gravity waves and turbulent motions (see Chap. 2) [16, 65]. In the previous chapter we investigated the large-scale intermittent behaviour of the velocity and temperature in DNSs of the Boussinesq equations in a range of the governing parameters of geophysical interest. PDFs of the fields characterized by high values of the fourth order statistical moment, namely the kurtosis  $K_x = \langle (x - \bar{x})^4 \rangle / \langle (x - \bar{x})^2 \rangle^2$  (with  $x = w, \theta$ ), have been observed in a range of Froude and Buoyancy Reynolds numbers compatible with that of the MLT ( $Fr \sim 10^{-1} - 10^{-2}, R_B > 10$ ). The occurrence of these large-scale bursts was explained through a simple one-dimensional model [16, 65] able to reproduce the extreme events emerging in stratified flows within a sharp range of values of  $Fr$  (and  $R_B$ ), as well as the abrupt transition observed in DNS between Gaussian and non-Gaussian statistics when the system shifts from a wave dominated dynamics ( $R_B < 10$ ) to a state where gravity waves and turbulent motions coexist in stratified flows ( $R_B > 10$ ) [16].

These extreme events have been interpreted as the result of a resonant interaction of the gravity waves and the turbulent motions which can develop in the flow when the time scale of the two is comparable.

In this chapter I present an extreme event observed in the MLT with the Middle Atmosphere Alomar Radar System (MAARSY) through the polar mesospheric summer echoes (PMSE) (see section 1.12.2) on July 16, 2016 [10]. This reported event showed an extreme vertical draft with an amplitude five standard deviation larger than the ambient velocity. The event resembled previously observed mesospheric bores and showed a sizeable vertical extent that is also associated with moderate horizontal wind shear.

The evidence that led to the identification of the extreme event are shown here and its analogies with the drafts observed in the DNSs will be highlighted. A description of the radars used to obtain the wind velocity shown in this chapter can be found in section 1.12.2.

### 3.1 Evidence of extreme vertical wind velocities in the mesosphere and lower thermosphere

The observation of this extreme vertical draft was possible using MAARSY (see section 1.12.2) and represents the first and unique evidence of an extreme vertical draft in the mesosphere by means of PMSE. The event was observed at an altitude around 86 km within an illuminated volume of a 5 km radius.

The data collected by MAARSY during the occurrence of the extreme event is shown in Fig. 3.1. Fig. 3.1 (b) displays the mean estimated vertical velocities (in colors) as functions of altitude and time. We note from this panel two main regions which are associated to extreme events, one around 86 km of altitude and the other around 82 km. The estimated vertical wind in these regions is quite strong, reaching 60 m/s, while the expected values of the vertical wind are of  $\sim 5$  m/s. Fig. 3.1 (a) shows the mean Signal-to-Noise Ratio (SNR) (in colors) as functions of altitude and time. SNR is the ratio of the power of the desired signal to the power of the background noise. SNR can also be expressed in decibels (dB):

$$SNR_{dB} = 10 \log_{10} \frac{P_{sig}}{P_{noise}}, \quad (3.1)$$

where  $P_{sig}$  is the power of the detected signal and  $P_{noise}$  is the power of the background noise. Higher values of the SNR imply a better quality of the signal. In our case, between the two regions with high vertical velocity shown in Fig. 3.1 (a), only for one of them the SNR is positive. Thus, we will only consider the region around 86 km in Fig. 3.1 (b) due to the good quality of the detected signal. The spread of the power spectrum of the velocity detected, the full spectral widths, are shown in Fig. 3.1 (c). They provide a measure of velocity fluctuations and higher values of the spectral widths are associated to turbulent regions. This is the case for the signal detected at 86 km of altitude. Finally, Fig. 3.1 (d-t) show the normalized spectra for altitudes around 86 km and for selected times. The dashed red lines indicate the  $3\sigma$  of the vertical velocity computed at each altitude over the data collected in two months. Again, we note how powerful positive and negative vertical drafts develop, reaching absolute values as high as 60 m/s ( $\sim 5\sigma$ ) (panel h).

The horizontal wind velocity was also estimated during the occurrence of the extreme vertical draft by means of Specular Meteor Radars (SMRs) (see 1.12.2). Using these measurements, the profile of the averaged horizontal vertical wind velocity and its vertical gradient were obtained. Fig. 3.2 shows the profiles of magnitude and direction of the mean horizontal velocity and its mean vertical gradient as a function of the altitude. The symbols in each panel identify the time at which each profile is obtained. The profiles shown are the ones obtained when the extreme event identified from Fig. 3.1 (b) develops in the vertical velocity. Around 86 km of altitude, we find that a moderate horizontal wind shear (third panel of Fig. 3.2) occurs at the same time as the vertical draft. Thus, thanks to the estimates of both vertical and horizontal winds obtained using PMSE and SMRs, we conclude that the extreme vertical draft observed was found in correspondence of a moderately strong horizontal shear. Finally, by means of radar imaging we were able to determine that the vertical draft observed in Fig. 3.1 (b) is mainly localized in horizontal planes, possessing a vertical extension of  $\sim 10$  km. A movie showing the time evolution of two-dimensional spatial cuts of PMSE when the extreme event was detected can be found at [79].

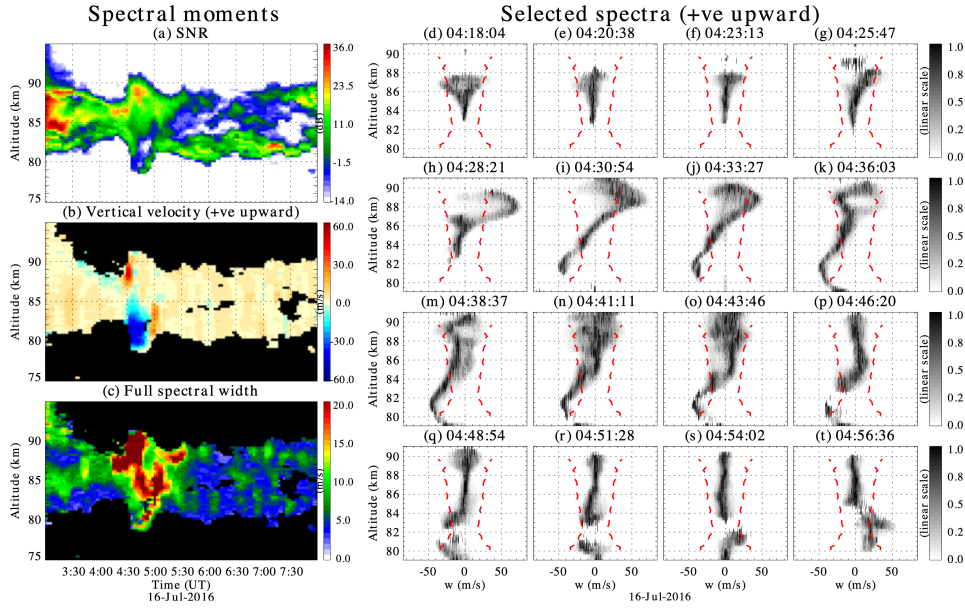


FIGURE 3.1: Left: Range-time plots of: (a) signal-to-noise ratio (SNR), (b) radial velocity (positive upward) and (c) total spectral width, observed with a vertical pointing beam on July 16, 2020. These parameters have been obtained using a spectral moment method. Right: Normalized spectra as a function of  $w$ . The normalization is in power spectra amplitude for each altitude with respect to its maximum. Three-sigma levels ( $3\sigma_w$ ) based on June-July 2016 observations are plotted in dashed red lines. [10]

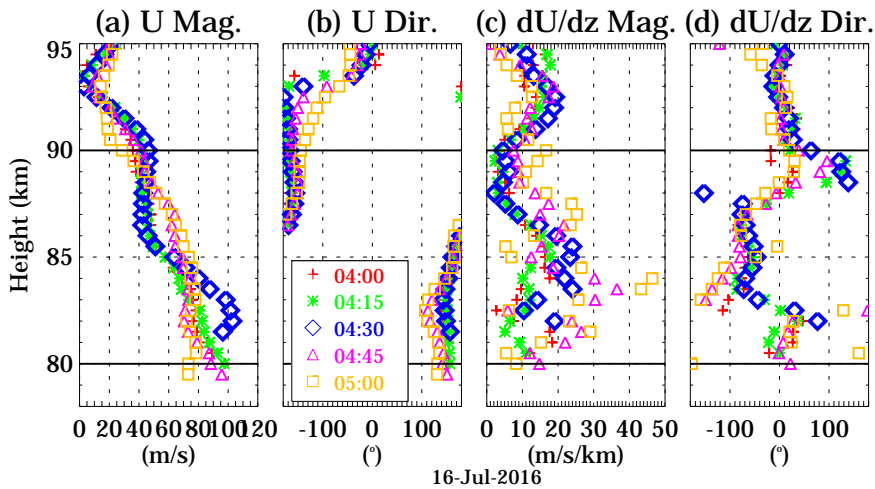


FIGURE 3.2: Horizontal winds profiles obtained with a collocated radar that observe specular meteor echoes around 0430 UT on July 16, 2016:  $U_x$ , and  $U_y$  components, their vertical gradients, and the horizontal wind magnitude and phase with their respective vertical gradients. The colors indicate time in minutes with respect to 0430 UT. [10]

### 3.2 The role of horizontal shears in the statistics of vertical drafts

We will now examine some of the features emerging from radar observations by means of DNSs of stratified turbulent flows. This will help determining whether the characteristics of the extreme event observed through the PMSE are analogous to those

developing in the DNSs. We will first investigate the correlation between vertical drafts and horizontal shear. We define a point-wise horizontal shear parameter  $S$  as the derivative of the horizontal velocity with respect to the  $z$  direction:

$$S = \frac{\partial u_{\perp}}{\partial z} \quad (3.2)$$

where  $u_{\perp} = \sqrt{u^2 + v^2}$  is the horizontal velocity. We then compute the pointwise value of the vertical velocity normalized by the instantaneous standard deviation  $\sigma_w$  computed from the whole domain,  $\hat{w} = w/\sigma_w$  and associate each value to the horizontal shear  $\hat{S} = S/\sigma_S$ , averaged over horizontal planes and normalized by its standard deviation  $\sigma_S$ . With the values obtained we built the joint probabilities to observe the extreme events in the vertical velocity conditioned to the values of horizontal wind shear averaged over the plane displayed in Fig. 3.3. This joint statistics is based on the full DNS integration interval of a purely stratified run with  $Fr = 0.076$  ( $\sim 400\tau_{NL}$ ) and clearly shows that the probability to observe extremely strong vertical drafts ( $(|\hat{w}| \gtrsim 6)$ ) is very close to zero in planes where the horizontal wind shear is vanishing or very small ( $|\hat{S}| < 0.35$ ). On the other hand, as  $|\hat{S}|$  increases, it becomes more probable to observe extreme vertical drafts. In particular, the probability to observe vertical drafts with  $6 \lesssim |\hat{w}| \lesssim 8$  increases from  $|\hat{S}| \sim 0.7$  to  $|\hat{S}| \sim 1.2$ . For  $|\hat{S}| \geq 1.2$  the probability to observe drafts with  $6 \lesssim |\hat{w}| \lesssim 8$  decreases. However, if we consider the most extreme events developing ( $|\hat{w}| \gtrsim 10$ ) in the flow, we note how the probability to observe them saturates very quickly around  $\hat{S} \sim 0.8$ . After this saturation, the probability remains constant, showing no variation when  $|\hat{S}|$  further increases. From these results, we conclude that in the absence of a strong horizontal shear, vertical drafts would not develop. Fig. 3.3 also shows the cumulative probability (%)  $C(|\hat{S}|)$  to observe any values of the vertical velocity  $|\hat{w}|$  larger than 5.5 with a dashed black line. We observe that  $C(|\hat{S}|)$  is smaller than the 1% for  $\hat{S} < 0.7$ , which strengthens the previous statement that strong horizontal wind shears are a necessary condition in order for the flow to develop extreme vertical drafts. The correlation between vertical drafts and strong horizontal shear observed using radars for the event reported in [10] is thus reproduced even in our DNSs and seems to be a characteristic feature.

To verify the presence of more analogies with the wind velocity observed through the PMSE by MAARSY we also investigated qualitatively the morphological features of the simulated velocity field. We do so by means of three-dimensional renderings of the vertical velocity field using VAPOR (see section 1.12.1). Using this tool we can impose a threshold on the vertical velocity field  $w$  in three-dimensional visualizations to highlight extreme vertical drafts as isosurfaces. These isosurfaces consist of several point-wise extreme values of the vertical velocity which, together, appear as coherent structures of different length scales in the vertical velocity field. Fig. 3.4 (a) shows a horizontal slice of the vertical velocity in units of the standard deviation  $\hat{w} = w/\sigma_w$  and in Fig. 3.4(b) a vertical slice of  $\hat{w}$  showing only 1/4 of the total vertical extension of the domain. The vertical slice is taken along the thick dashed line shown in Fig. 3.4 (a). Extreme values of  $\hat{w}$  are highlighted in Fig.3.4 (a, b) with dark-red for updrafts and dark-blue for downdrafts. We note from Fig. 3.4 (a) how the extreme events usually appear in the form of elongated and thin structures (finger-like) in the horizontal plane, possessing several characteristic length-scales up to  $\sim 1/4$  of the simulation domain. This feature emerged also in observations, where the horizontal extension of the vertical draft observed was greater than the vertical one. From the vertical cut (Fig.3.4 (b)) we observe that the extreme events usually appear in pairs, displaying an alternation of updrafts and downdrafts. We also note how for a given structure,

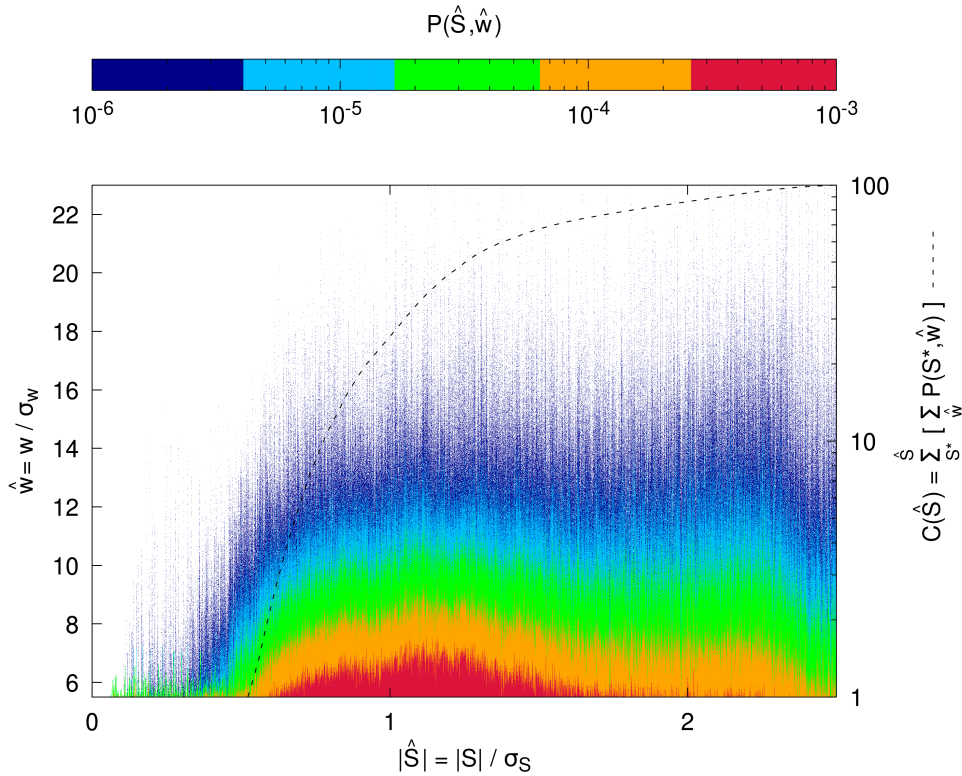


FIGURE 3.3: Probability to observe extreme events in the vertical velocity,  $\hat{w}$ , conditioned to the values of the vertical shear of the horizontal wind velocity  $\hat{S}$ . The dashed black line indicated the cumulative probability (%)  $C(|\hat{S}|)$  to observe any values of the vertical velocity  $w$  larger than  $5.5\sigma_w$ . Values larger than  $\hat{S} = 2.5$  were also found but have been discarded as the statistics is not resolved enough.

the most extreme values of the vertical velocity are found at the center of the volume, with values gradually becoming less intense towards its borders (see Fig. 3.4 (b)). Finally, Fig. 3.4 (c) contains the vertical profile of the horizontal averaged wind shear  $\hat{S} = \langle \partial_z u_{\perp} \rangle_h$  (where the average is performed over horizontal planes) together with the number of grid points for each horizontal plane (thus for a fixed height  $z$ ) where the value of the vertical velocity  $w$  exceeds  $5.5\sigma_w$ . The thin dashed black line represents the height at which the cut for the  $xy$  plane of Fig. 3.4 (a) is made. The accumulation of the events with  $w > 5.5\sigma_w$ , indicated by the red line in Fig. 3.4 (c), occurs for values of the  $z$ -coordinate corresponding to high local values of the shear ( $\hat{S} = S/\sigma_S$ ), as also seen from Fig. 3.3. We also note from Fig. 3.4 (c) that the highest number of events is found in correspondence of a strong shear, in agreement with Fig. 3.3. However, we observe how not all the planes with horizontal shears develop extreme events. This suggests that, while it is necessary to develop extreme events (as noted by the observation made using PMSE and from the statistics obtained from DNSs of Fig. 3.3), a strong horizontal shear does not necessarily implies the generation of extreme events.

Due to the many similarities, we can therefore speculate that the event identified using radar presented at the beginning of this chapter could be of the same nature as the ones developing in the DNSs. The statistics collected by means of DNSs seem to indicate that the presence of a horizontal shear is indeed necessary for the generation of strong vertical drafts. A moderately strong shear was indeed measured by means of SMRs during the occurrence of the extreme event observed in the mesosphere.

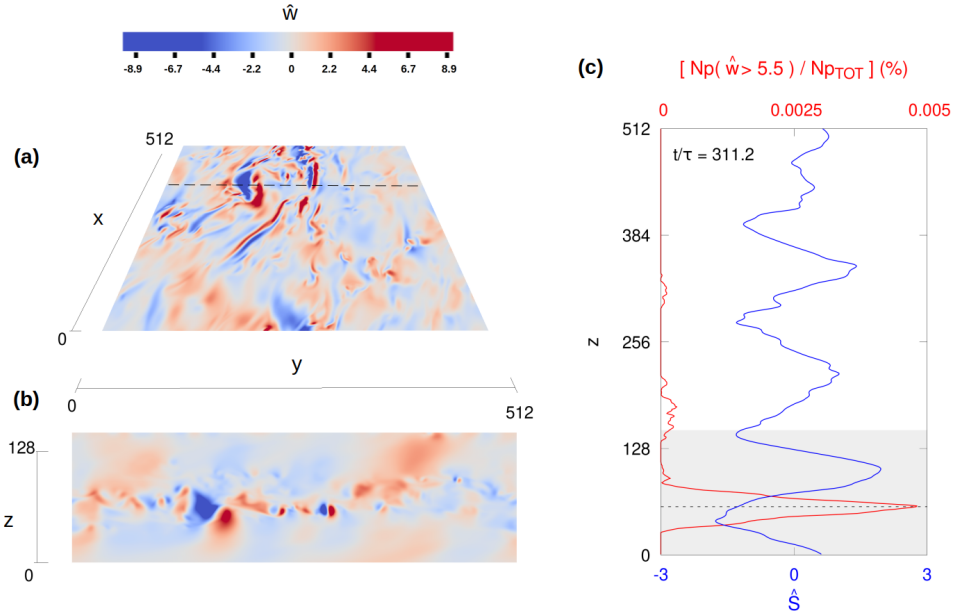


FIGURE 3.4: Two dimensional renderings of the normalized vertical velocity  $\hat{w} = w/\sigma_w$  from the DNS: a)  $xy$  cut at fixed  $z$  and b)  $xz$  cut fixed  $y$ , the locations of the cuts being indicated with dashed lines in panel a) and c). Panel c) shows the horizontal wind shear vertical profile  $\hat{S} = S/\sigma_S$  (with  $S = \langle \partial_z u_{\perp} \rangle_h$ , where the average is performed over horizontal planes) together with the by-plane percentage of extreme events in the vertical velocity (defined as the grid points with  $w > 5.5\sigma_w$ ).

The morphology of the extreme event identified using PMSE resembles previously observed instabilities called bores [20]. Our MLT event, however, displayed a much larger vertical velocity, since in previous mesospheric bores that was less than 10 m/s [37]. Several works tried to explain how mesospheric bores are generated and some may also apply to our case, like, for example, the interaction of gravity waves with the mean flow [13]. A larger number of extreme events, however, is needed in order to draw definitive conclusions. This is a challenging task since due to the large values of the vertical velocity and their short duration, they may appear as outliers at first sight. Thus, in light of what we discovered here, we envisage a reprocessing of the data collected by means of PMSE and SMRs in order to identify a greater number of extreme drafts in the mesosphere. Moreover, mesospheric bores are not unique to the polar mesosphere but have also been observed at other latitudes [28]. It would thus be interesting to investigate the occurrence of extreme vertical drafts at other latitudes, using tools different from the ones employed for our study, in order to provide a better understanding of this phenomenon. Finally, we expect such extreme events to show up also in other atmospheric variables, such as temperature, which we already saw being intermittent at large-scale in Chap. 2.

# Geophysical Research Letters



## RESEARCH LETTER

10.1029/2021GL094918

### Key Points:

- First observations of extreme vertical velocities in the polar summer mesosphere
- The observed solitary wave in a varicose mode resembles a mesospheric bore, with large vertical extent and vertical velocities
- Such extreme events might have been missed or ignored in previous observations of vertical velocities or other mesospheric observations

### Supporting Information:

Supporting Information may be found in the online version of this article.

### Correspondence




J. L. Chau,  
chau@iap-kborn.de

### Citation:

Chau, J. L., Marino, R., Feraco, F., Urco, J. M., Baumgarten, G., Lübken, F.-J., et al. (2021). Radar observation of extreme vertical drafts in the polar summer mesosphere. *Geophysical Research Letters*, 48, e2021GL094918. <https://doi.org/10.1029/2021GL094918>

Received 23 JUN 2021  
Accepted 22 JUL 2021

## Radar Observation of Extreme Vertical Drafts in the Polar Summer Mesosphere

J. L. Chau<sup>1</sup> , R. Marino<sup>2</sup>, F. Feraco<sup>2,3</sup>, J. M. Urco<sup>1,4</sup>, G. Baumgarten<sup>1</sup>, F.-J. Lübken<sup>1</sup> , W. K. Hocking<sup>5</sup>, C. Schult<sup>1</sup>, T. Renkowitz<sup>1</sup>, and R. Latteck<sup>1</sup> 

<sup>1</sup>Leibniz-Institute of Atmospheric Physics at the University of Rostock, Kühlungsborn, Germany, <sup>2</sup>Laboratoire de Mécanique des Fluides et d'Acoustique, CNRS, École Centrale de Lyon, Université Claude Bernard Lyon 1, INSA de Lyon, Écully, France, <sup>3</sup>Dipartimento di Fisica, Università della Calabria, Rende, Italy, <sup>4</sup>Department of Electrical and Computer Engineering and Coordinated Science Laboratory, University of Illinois Urbana-Champaign, Urbana, IL, USA, <sup>5</sup>Department of Physics and Astronomy, University of Western Ontario, London, ON, Canada

**Abstract** The polar summer mesosphere is the Earth's coldest region, allowing the formation of mesospheric ice clouds. These ice clouds produce strong polar mesospheric summer echoes (PMSE) that are used as tracers of mesospheric dynamics. Here, we report the first observations of extreme vertical drafts ( $\pm 50 \text{ ms}^{-1}$ ) in the mesosphere obtained from PMSE, characterized by velocities more than five standard deviations larger than the observed vertical wind variability. Using aperture synthesis radar imaging, the observed PMSE morphology resembles a solitary wave in a varicose mode, narrow along propagation (3–4 km) and elongated ( $> 10 \text{ km}$ ) transverse to propagation direction, with a relatively large vertical extent ( $\sim 13 \text{ km}$ ). These spatial features are similar to previously observed mesospheric bores, but we observe only one crest with much larger vertical extent and higher vertical velocities.

**Plain Language Summary** Extreme events are ubiquitous in geophysical flows. Examples of these events are tornadoes and rogue waves in the lower atmosphere and oceans, respectively. In the mesosphere, the boundary of Earth's atmosphere and outer space, extreme events can also occur, although this region is poorly observed. Here, we present the first observations of extreme vertical velocities ( $\pm 50 \text{ ms}^{-1}$ ) in the mesosphere, that are more than five times their expected standard deviation. These observations are possible by tracking and imaging strong mesospheric radar echoes that occur in the summer at polar latitudes, with a radar used in a radio camera mode. The morphology of our observations resembles previously observed instabilities called bores or wave walls, but with much larger vertical velocities and vertical extents.

## 1. Introduction

Extreme events are ubiquitous in geophysical flows, for example, tornadoes or rogue waves (e.g., Adcock & Taylor, 2014; Tippett & Cohen, 2016). In the mesosphere (60–90 km), extreme events can also exist. This region is difficult to observe since it is too high for meteorological balloons, and too low for satellites to fly through and make in situ measurements. Therefore, observations of extreme events and their respective impacts in this region are not easy to identify and study. Nonetheless, this atmospheric region hosts a number of interesting optical and radio phenomena like noctilucent clouds (NLCs) and polar mesospheric summer echoes (PMSE) (e.g., Ecklund & Balsley, 1981; Hoppe et al., 1988; Thomas & Olivero, 1986).

During summer months at mid and high latitudes, the mesosphere is the coldest place on Earth with temperatures as low as 130K due to dynamical processes that drive the atmosphere away from a radiatively controlled state (e.g., Lübken et al., 1999). One of the most challenging, important, and intriguing mesospheric measurements is vertical winds. Vertical winds are usually smaller than horizontal winds, but they have significant effects on the atmospheric dynamics, composition, electrodynamics, and mixing (e.g., Larsen & Meriwether, 2012; Pouquet et al., 2017). Their mean synoptic-scale values are expected to be in the order of centimeters per second and are difficult to measure directly (e.g., Gudadze et al., 2019). On the other hand measurements made with ground-based radars, passive optics, lidars, as well as in situ chemical traces, show high values varying by up to  $\pm 10 \text{ ms}^{-1}$  (e.g., Gardner & Liu, 2007; Hoppe & Fritts, 1995; Lehmacher et al., 2011; Woodman & Guillén, 1974). Similar and even higher values have been observed at

© 2021. The Authors.  
This is an open access article under the terms of the [Creative Commons Attribution-NonCommercial-NoDerivs License](https://creativecommons.org/licenses/by/4.0/), which permits use and distribution in any medium, provided the original work is properly cited, the use is non-commercial and no modifications or adaptations are made.



higher altitudes in the thermosphere (e.g., Larsen & Meriwether, 2012). These high values can occur with the same sign for minutes to hours.

Although part of this variability is attributed to Kelvin-Helmholtz, mesospheric bores, and other instabilities (e.g., Chau et al., 2020), the drivers for the majority of observations of large and/or persistent values are not obvious. Waves propagating through the region appear to be connected to the vertical wind variability; either they come from below or are generated locally via instabilities, nonlinear interaction with other waves or turbulence (e.g., Fritts et al., 2004; Gardner et al., 1995; Herbert et al., 2016; Larsen & Meriwether, 2012). Moreover, high variability in vertical winds has been reproduced in direct numerical simulations (DNS) in flows similar to those in the mesosphere (Marino et al., 2015), including extreme values in a certain range of the governing parameters of the flow (Feraco et al., 2018). Understanding and characterizing the vertical wind variability of the mesosphere and higher altitudes (thermosphere) are important for explaining their effects on the dynamics, composition, chemistry, and electrodynamics of these regions (e.g., Larsen & Meriwether, 2012).

In this study, we focus on extreme vertical drafts observed in the polar summer mesosphere. These observations have been made with the Middle Atmosphere Alomar Radar System (MAARSY) located in northern Norway (69.30°N, 16.04°E). Observations of PMSE have been routinely made with MAARSY since 2010 (Latteck et al., 2012). After more than 20 years of active research, the physics behind PMSE is well understood. Their signal strength depends on electron density, turbulence, and charged-ice particles (e.g., Rapp & Lübken, 2004) and they are good tracers of atmospheric winds (e.g., Sato et al., 2017).

The event we present is extreme as the vertical velocities measured are more than five times the standard deviation ( $\sigma_w$ ) of continuous measurements over two summers. The paper is structured as follows: Section 2 describes the observing modes and Section 3 presents the observations. These observations and possible connections to previously observed mesospheric instabilities are discussed in Section 4.

## 2. Radar Observing Modes

MAARSY is an active phased array that consists of 433 three-element cross-polarized Yagi antennas and operates at 53.5 MHz. Its main beam one-way half-power beam-width is 4°. On reception, either all 433 elements, or up to seven groups of 49 elements, or up to 15 out of 55 groups of seven elements can be used (e.g., Latteck et al., 2012, for more details).

PMSE are routinely observed with MAARSY using two quasi-simultaneous main modes: (a) multi-beam, and (b) radar imaging (e.g., Gudadze et al., 2019; Urco et al., 2019). These modes have been used during the summers of 2016 and 2017, except for a few days where other modes were used to support special requests. Both modes run with 1 ms interpulse period. Since horizontal winds are expected to be within  $\pm 150 \text{ ms}^{-1}$ , the multi-beam mode has been configured to allow a Nyquist velocity of  $\pm 35 \text{ ms}^{-1}$ . On the other hand, the radar imaging mode allows a Nyquist velocity of  $\pm 175 \text{ ms}^{-1}$ , suitable to study other echoes, for example, nonspecular meteor echoes (Chau et al., 2014).

Given the velocity aliasing in the multi-beam mode, in this work we use only data from the radar imaging mode, which observes for 30 s every 180 s. This mode uses only one vertically pointing transmitting beam using all 433 elements, while 16 antenna groups are used on reception, 15 of them for radar imaging. A spectral moment method has been implemented to obtain: signal, mean radial velocity, and spectral width. Radial velocities from slightly off-vertical locations could have contributions from horizontal velocities. However, unrealistic supersonic horizontal winds (more than  $1,500 \text{ ms}^{-1}$ ) would be required to generate the large ( $\sim 50 \text{ ms}^{-1}$ ) observed velocities.

Radar imaging has been obtained by applying the Maximum Entropy method on the cross-spectral data from combinations of receiving antenna pairs (e.g., Hysell & Chau, 2006; Urco et al., 2019). Since the selected 15 receiving antennas do not have the same beam width, the imaging inversion has been performed only within  $\pm 8^\circ$  zenith angles. This angular coverage also allows for the observation of PMSE outside the main illuminated area, if strong echoes are present there.

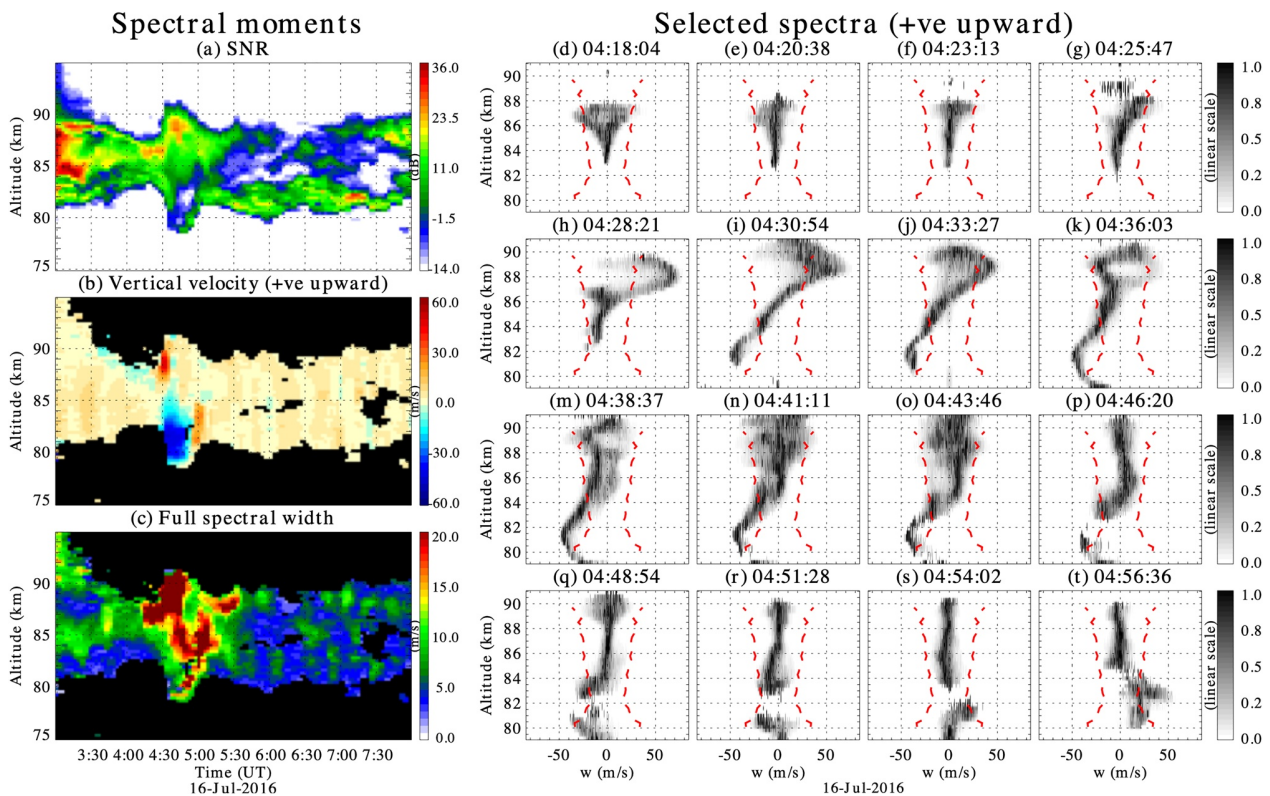


**Figure 1.** (left) Range-time plots of: (a) signal-to-noise ratio (SNR), (b) vertical velocity (positive upward), and (c) total spectral width, observed with a vertical pointing beam on July 16, 2016. Note the relative large scales being shown for vertical velocities ( $\pm 60 \text{ ms}^{-1}$ ). (right) Normalized spectra as a function of  $w$ , where  $w = -f\lambda / 2$ ,  $f$  is Doppler frequency in Hz, and  $\lambda$  the radar wavelength in meters. The normalization is in power spectra amplitude for each altitude with respect to its maximum. Three-sigma levels ( $3\sigma_w$ ) based on June–July 2016 observations are plotted in dashed red lines.

Besides the PMSE observations, in this work we also used the horizontal wind observations with a specular meteor radar (SMR) located also in Andoya (e.g., Chau et al., 2017). This system consists of one single element Yagi antenna on transmission and five single element antennas on reception arranged in an interferometer configuration. On reception echoes from meteor trails perpendicular to the line of sight are detected and identified. The radial velocity and location (range and angle) of each meteor trail within selected altitude and temporal bins are used to estimate a mean horizontal wind vector for that bin (e.g., Hocking et al., 2001). Such vector components are obtained assuming a homogeneous wind inside the illuminated area, that is, a circle of approximately 400 km diameter at 86 km altitude.

### 3. Results

The extreme vertical draft event occurs on July 16, 2016 and is shown in Figures 1a–1c. Figure 1a shows the signal-to-noise ratio (SNR) as a function of altitude and time. The vertical velocities and spectral widths are shown in Figures 1b and 1c, respectively.

The event in question occurred between 04:25 and 05:00 universal time (UT) and is characterized by: (a) episodes of large vertical updrafts and downdrafts lasting a few minutes at around 86 km, (b) large spectral widths, and (c) echoes appearing to move up and down according to the measured mean vertical velocities, and (d) their strength increasing (decreasing) when going up (down). Outside this time interval, the PMSE spectral moments behave within expected values, that is, vertical velocities within  $\pm 5 \text{ ms}^{-1}$ , spectral widths below  $5 \text{ ms}^{-1}$ , and echoes occurring in multiple layers.

Normalized spectrograms for selected times around the extreme event are shown in Figures 1d–1t. Each spectrum is obtained from  $\sim 30$  s continuous observations. The striking features in this figure are the large

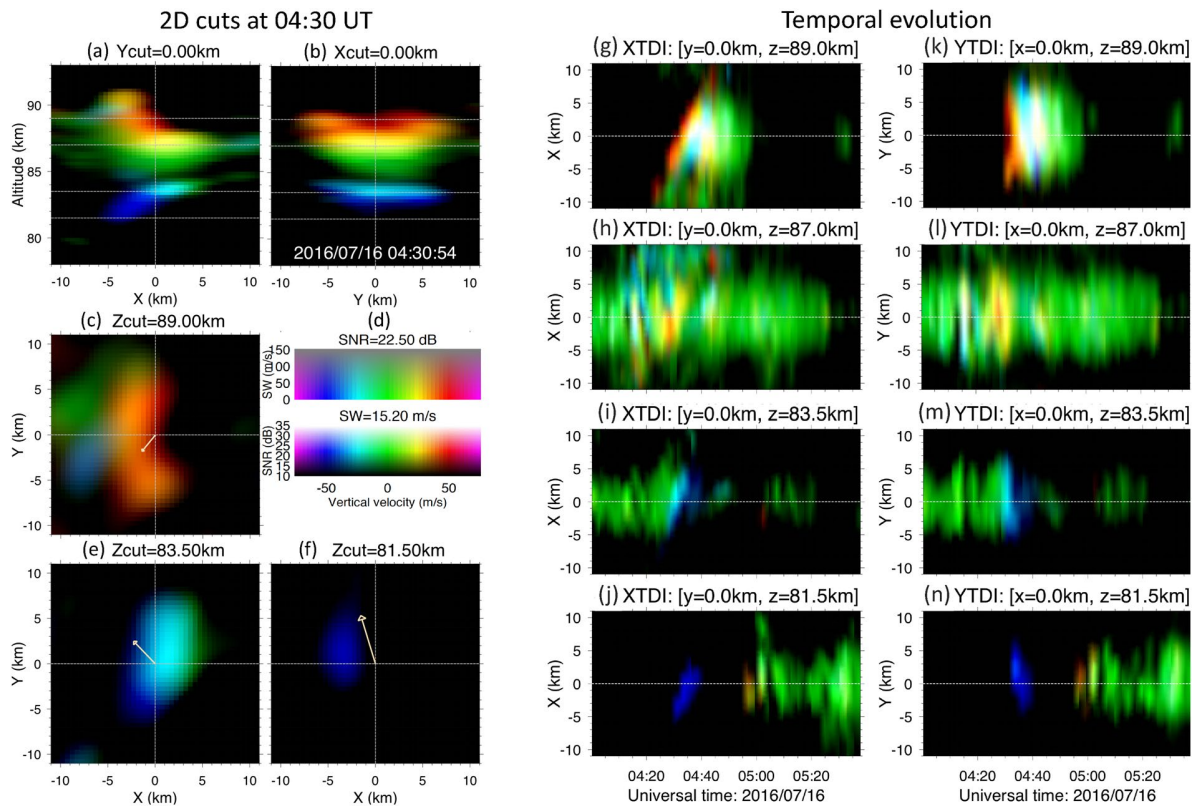


**Figure 2.** (left) Two dimensional spatial cuts of polar mesospheric summer echoes inside the illuminated volume on July 16, 2016 around 04:30 UT.  $xz$  and  $yz$  cuts at  $x = 0$  and  $y = 0$  km in panels (a) and (b), respectively.  $xy$  cuts at altitudes 89.0, 83.5, and 81.5 km in panels (c), (e), and (f), respectively. The intensity indicates signal strength of the echoes, while the color shows vertical velocity. Red (blue) values represent upward (downward) velocities greater (smaller) than  $25$  ( $-25$ )  $\text{ms}^{-1}$ , while green values represent velocities in between (see panel d). The 30-min horizontal wind from the specular meteor radar is indicated with a yellow arrow in the center of each  $xy$  cut. (right) Space-time cuts at altitudes 89.0, 87.0, 83.5, and 81.5 km, of  $xy$  cuts in the left panel: (g–j)  $x$  versus time for  $y = 0$ , and (k–n)  $y$  versus time for  $x = 0$ .

positive and negative vertical drafts well outside  $3\sigma_w$ , reaching high absolute values (e.g.,  $65 \text{ ms}^{-1}$  at 04:28:21 UT or  $-45 \text{ ms}^{-1}$  at 04:36:03 UT). Except for the spectra at 04:41:11 (1o) and 04:43:46 (1n) UT, the spectra are composed of one or two velocity peaks at a given altitude. Given that the illuminated volume has a radius of about 5 km in the horizontal direction at these altitudes, the multi-peak features are a result of multiple regions of enhanced backscattering within the illuminated volume. The presence of multiple peaks gives rise to large values of spectral widths. The red dashed lines indicate the  $3\sigma_w$  based on 2 months of continuous observations in 2016.

From radar imaging, we have obtained spatial information of features within the illuminated volume. Figures 2a–2f show selected 2D spatial planes of imaging around 04:30:54 UT. The large-scale 30-min averaged horizontal winds obtained from a closely located SMR are shown in arrows as a reference. Radar imaging results clearly indicate that the extreme updrafts and downdrafts are localized in horizontal space, with 3–4 km width along the  $x$  axis, and at least 8–12 km elongation along the  $y$  axis, where  $x$ -axis and  $y$ -axis are rotated  $50^\circ$  East of North. Note that the elongation along  $y$  axis could be larger but our observations are limited to the radar illuminated area. An animation of similar frames from 04:00 to 05:30 UT every 150–170 s can be seen in Movie S1. The imaging results are also used to verify that the inferred vertical velocities are mainly due to vertical wind and not to a horizontal wind contamination, since areas of large vertical drafts are observed at or close to overhead inside the vertical transmitting beam. For typical mesospheric horizontal winds ( $\pm 150 \text{ ms}^{-1}$ ), their contamination in our vertical estimates would be at most within  $\pm 4 \text{ ms}^{-1}$ .

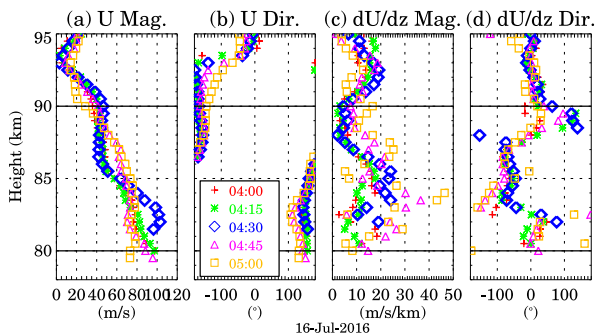


**Figure 3.** Horizontal winds profiles obtained with a collocated radar that observe specular meteor echoes around 04:30 UT on July 16, 2016: horizontal wind magnitude and direction with their respective vertical gradients. The direction is with respect to  $x$ , positive anti-clockwise. The colors indicate time in minutes with respect to 04:30 UT. The central time values are marked with black diamonds.

The temporal evolution of these spatial features is summarized in Figures 2g–2n as a function of  $x$  (i.e., X-Time Doppler-Intensity, XTDI) (left) and  $y$  (YTDI) (right) for selected altitudes. The extreme drafts are elongated along  $y$  at all altitudes, and drift along  $x$ . At 89 km, the updraft is observed to drift over the field of view at least 16–20 km in  $x$ , appearing around 04:20 and disappearing around 04:45 UT. The irregularities causing these echoes move up from around 86 km and stay at 89 km for at least 25 min. At 81.5 km, downdrafts are also elongated along the  $y$  axis and drift generally along  $x$ . However, they are only observed for 2–4 km along  $x$  and last less than 5 min. The echoes at the lower altitudes are weaker and disappear after a few minutes. Later the echoes appear again around 04:55 due to irregularities coming from below and remain present at least until 05:30 UT. Both regions of updrafts and downdrafts drift at  $\sim 11 \text{ ms}^{-1}$  along  $x$ , North-East, with respect to an observer on the ground. Note that regions of large drafts are observed for a longer time in these plots than in the spectra plots in Figure 1, since the spectra were obtained using all 433 elements on transmission and reception. The duration, elongation, and horizontal extent of the event should be taken as minimum

values, given the relatively small observing volume, when compared to other imaging observations (e.g., airglow imagers).

Figure 3 shows profiles of horizontal wind magnitude and direction as well as their vertical gradients. These profiles were obtained with the SMR described above, around the time of the event. A moderate horizontal wind shear ( $24 \text{ ms}^{-1} \text{ km}^{-1}$ ), occurs at the altitude where the extreme updrafts and downdrafts begin, that is, 86 km. Recall that these are mean values representing an area of approximately 400 km diameter at 86 km obtained.

## 4. Discussion

The main features of the kilometer-scale extreme event presented here can be summarized as follows: (a) vertical drafts close to  $5\sigma_w$  occur during a limited time of  $\sim 30$  min on July 16, 2016 around 04:30 UT; (b) they occur between 80 and 90 km, (c) updrafts (downdrafts) up to 65 (45)  $\text{ms}^{-1}$  occur above (below) 86 km, are observed for long (short) time, and their associated echoes present larger (smaller) SNR than echoes at 86 km where they begin; (d) it is localized in horizontal space with widths of 3–4 km in the  $x$  axis, and elongated along the  $y$  axis; (e) at the center altitude, the vertical gradient of the background horizontal wind is the largest ( $24 \text{ ms}^{-1} \text{ km}^{-1}$ ); (f) the PMSE layer thickness changes from 3 km (before the event) to 13 km (at the central time), (g) both drafts drift across the observing volume apparently against the mean horizontal wind at  $\sim 11 \text{ ms}^{-1}$ , therefore the duration, elongation and horizontal extent of the event should be taken as minimum values.

### 4.1. Verification of Our Observations

Since our reported vertical velocities are not expected and might be controversial, in this section we summarize briefly some of the actions we have performed to verify the validity of our vertical velocity estimates. The first obvious check was range aliasing. Our unambiguous range is 300 km, echoes coming from 380 km might be range aliased, however, their range, temporal, and spectral features do not correspond to such altitude. For example, if they were echoes from radar aurora, they would cover a much larger range (e.g., Chau & St.-Maurice, 2016). Moreover, plasma instabilities have been ruled out since (a) the ionosphere was quiet for a few hours around the event, and (b) the altitude is too low for plasma instabilities to be generated (e.g., St.-Maurice & Chau, 2016). The former indicates that strong electric fields are not expected, while the latter is supported by high collision frequencies around 86 km.

Horizontal velocity contamination is a usual suspect on vertical velocity studies, particularly when studying their mean values (e.g., Gudadze et al., 2019). As we mentioned above without considering radar imaging, unrealistic huge supersonic horizontal velocities would be needed to explain the reported vertical velocities.

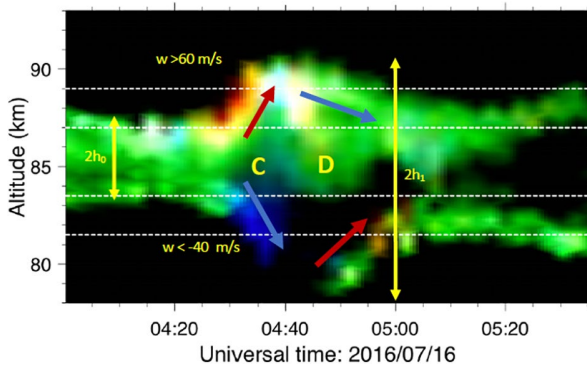


**Figure 4.** Closeup of the observations shown in Figure 1 to sketch the dynamics accompanying our event. The color code is the same as the one in Figure 2d. The regions of strong updraft (downdraft) are indicated with red (blue) arrows. Letter C and D represent horizontal wind convergence and divergence, respectively. Yellow vertical arrows indicate relevant vertical scales (see text).

Moreover in the imaging results, at a given altitude they would be shown with a transition from red to blue as the scattering center passes the beam center if the vertical velocity is very small. Figure 2g clearly shows that the upper/lower altitude regions are red/blue as the event transits the beam. At most we expect the horizontal contamination to be within  $\pm 4$   $\text{ms}^{-1}$ .

The vertical velocity profile is not constant at all altitudes at the central time of the event (i.e., 04:30), instead, it shows a maximum upward value around 89 km, zero at 86 km, and maximum downward value around 82 km. If one assumes this vertical velocity profile to be constant for a few minutes, the resulting vertical displacement of a scattering region at 86 km is consistent with the observed vertical extent.

#### 4.2. Connection to Previous Mesospheric Observations

A sketch based on the observations is shown in Figure 4. The SNR, vertical velocity, and spectral width from Figure 1 are combined into an altitude-time-Doppler intensity plot (e.g., Chau et al., 2020), with superimposed arrows indicating  $w$  directions, and expected regions of horizontal

wind convergence (C) and divergence (D) (see below). Our observed event resembles a solitary wave oscillating in varicose mode, that is, where the upper part is rising, the lower part is falling, and vice versa. This varicose mode is expected in internal bores (e.g., Dewan & Picard, 2001) and has been directly observed in mesospheric bores (e.g., Fritts et al., 2020).

Our sketch together with the spatial features shown in Figure 2 resembles the mesospheric bore features of Bore 1 reported by Fritts et al. (2020), where they combined 2D images of PMC and lidar vertical profiling. As in the case of Fritts et al. (2020), we also expect that the observed vertical velocity divergence (convergence) ahead of (behind) the extreme event is accompanied by horizontal wind convergence (divergence). This horizontal wind behavior, unfortunately, could not be directly measured in our case. However, using vertical velocities from Figure 1i, the continuity equation and assuming an incompressible flow, the estimated local horizontal wind convergence is  $\sim 14 \text{ ms}^{-1} \text{ km}^{-1}$ , which is more than 100 times the measured mesoscale horizontal divergence in this region (Chau et al., 2017). This large local horizontal wind convergence/divergence is expected at the central altitude and not where the high vertical velocities are observed. Our assumption of incompressibility might not be totally correct given the high observed vertical velocities, possibly accompanied by local horizontal velocities larger than the speed of sound. Therefore, the estimated horizontal divergence/convergence values should be considered as upper values.

The vertical dimensions of our event are more than two times larger than those reported by Fritts et al. (2020), that is,  $2h_1 \sim 13$  and  $2h_0 \sim 3.0$  km, instead of 4.7 and 2.8 km, respectively, where  $2h_1$  and  $2h_0$  are the vertical extensions during the peak of the perturbation and before the perturbation, respectively. These dimensions imply a normalized bore amplitude  $\beta = (h_1 - h_0) / h_0 \sim 3.33$  which is much larger than previously measured or inferred characteristics of mesospheric bores or wall waves (e.g., Fritts et al., 2020; Li et al., 2007; Smith et al., 2003, 2017; Taylor et al., 1995). Vertical velocities in previous mesospheric bores have been expected or measured to be less than  $10 \text{ ms}^{-1}$  (e.g., Li et al., 2007).

Morphologically our extreme event resembles a mesospheric bore, but given its vertical dimensions, observed vertical velocities, and single observed crest, our event is unique. Unfortunately, temperature and density profiles are not available for this event. However, as in the case of typical mesospheric bores, we expect that our event is a consequence of an instability occurring in some type of ducting (Doppler, thermal, or a combination of both). Ducting regions are ubiquitous, but mesospheric bores are not. Possible mechanisms that have been invoked to explain mesospheric bores might also explain our observations, for example, interaction of gravity waves with the mean flow at a critical level (e.g., Dewan & Picard, 1998), nonlinear internal gravity waves trapped within a thermal inversion layer (e.g., Seyler, 2005), and so on. Interesting to note is that run 8 in Seyler (2005, Table 1), reproduces a single-crest bore with larger amplitudes

and Bore speeds than the other runs. However, none of the previous theories aimed to explain an event with the large  $\beta$  and very high vertical velocities that characterized our observations.

DNS results of stratified flows have predicted extreme vertical velocities localized in space and time under particular values of stratification, specifically with Froude number  $\sim 0.1 - 0.01$  (Feraco et al., 2018). Although a one-to-one comparison with our event is difficult, the DNS results indicate that the resonant interaction between gravity waves and turbulent motions responsible for the simulated DNS results, might play a role in explaining our event. Such comparison with DNS results and possibly more events will be pursued in future work.

#### 4.3. How Often Mesospheric Extreme Events Occur?

We have presented only one event showing extreme vertical velocities. At this point, it is difficult to infer if this is an isolated one-of-a-kind event, or if they occur more often but, due to their high velocities and spatio-temporal characteristics, have been ignored.

In the case of previous PMSE observations with MAARSY, the great majority were done with Nyquist velocities less than  $30 \text{ ms}^{-1}$ . Therefore, extreme drafts have been filtered out or were Doppler aliased, and cannot be recovered by their velocity values. In cases where larger Nyquist velocities have been used, they were presumably treated as outliers given their large values and relatively short duration (e.g., Gudadze et al., 2019, Figure 4). In the latter cases, a careful reprocessing should be pursued to search for additional extreme drafts. Data obtained with small Nyquist might still be useful, if one looks for sudden vertical excursions (up and down).

Mesospheric bores are not unique to the polar summer mesosphere and have been observed at other latitudes (Hozumi et al., 2019). If the observed extreme vertical velocities are indeed related to mesospheric bores one should search for extreme vertical velocities at other latitudes, seasons, with a variety of instruments. For example, mesospheric solitary waves (solitons) reported from foil chaff experiments in the past, might have sampled a small spatial and temporal portion of an extreme event like the one reported here (Widdel, 1991).

Although our work is focused on vertical velocities, such extreme events should show up in other atmospheric variables, for example, temperatures, airglow intensities, NLC brightness, and so on. As far as we know, extreme events based on these parameters have not been reported so far, or they might have been ignored.

#### 4.4. Potential Impacts

In the particular case of the polar summer mesosphere, ice particles exist and they are the main reason for the presence of NLC and PMSE (e.g., Rapp & Lübken, 2004; Thomas & Olivero, 1986). Using expected temperature and pressure profiles from empirical models (e.g., Murphy & Koop, 2005; Picone et al., 2002) as well as the observed vertical drafts, we find that in our specific case the temperature increases significantly in the downdraft regions. This increase causes the reduction of ice particle radius in time scales of a few minutes (see Figure S1). More details of these calculations can be found in the supplemental information. In the case of PMSE, their volume reflectivity is mainly determined by the Schmidt number, which is proportional to the square of ice particle radius (e.g., Rapp & Lübken, 2004). Therefore a reduction of ice particle radius would mean a weaker PMSE. In Figure 1a, the strength of echoes decreases or echoes even disappears for the regions experiencing downdrafts. In the updraft regions, the strength of echoes increases but based on our calculations this increase is not related to the ice particle radius, instead it could be due to an increase in electron density. These simple calculations indicate that indeed ice particle radius is affected by extreme vertical drafts, and so are clouds and echoes relying on it.

As in the case of ice particles, other mesospheric species would also experience significant changes in altitude, and therefore their mixing ratios might change at a given altitude. The transport of photochemically inactive species across the turbopause by vertical winds enhances their concentration much more rapidly compared to turbulent mixing, which implies that extreme vertical updrafts are an effective mechanism to transport trace gases into the lower thermosphere. For example, if Argon and molecular Nitrogen are

brought to higher altitudes, from 90 to 110 km, it could take up to 3 h to fully mix these components, that is, much longer than if these species would have stayed at 90 km (e.g., Von Zahn et al., 1990).

## 5. Conclusions

We report the first observations of extreme vertical drafts ( $\pm 50 \text{ ms}^{-1}$ ) in the mesosphere which show characteristics that resemble a solitary wave behavior in varicose mode. Although their horizontal and spatial structures resemble those of previously observed mesospheric bores, our event shows only one crest with a much larger vertical extent than previous observations.

Our current poor knowledge on these extreme drafts (formation, occurrence rate, duration, and predictability) as well as limited observing capabilities in the mesosphere, should not impede the exploration of impacts on other fields where kilometer-scale perturbations and instabilities and high vertical drafts might be important. If they occur frequently, a better understanding and characterization would contribute to the roles of kilometer-scale dynamics in a number of parameters requiring their parameterization in large-scale general circulation weather and climate models (e.g., Fritts et al., 2014, 2020). Further observations as well as theory and modeling efforts are still needed to find and identify the specific sources of our reported event.

## Data Availability Statement

Open Research Data Statement PMSE radar spectra and imaging data as well as meteor wind data can be found here <https://dx.doi.org/10.22000/396>.

## References

- Adcock, T. A. A., & Taylor, P. H. (2014). The physics of anomalous ('rogue') ocean waves. *Reports on Progress in Physics*, 77(10), 105901. <https://doi.org/10.1088/0034-4885/77/10/105901>
- Chau, J. L., & St-Maurice, J.-P. (2016). Unusual 5 m E region field-aligned irregularities observed from Northern Germany during the magnetic storm of 17 March 2015. *Journal of Geophysical Research: Space Physics*, 121(10), 310–316. <https://doi.org/10.1002/2016ja023104>
- Chau, J. L., Stober, G., Hall, C. M., Tsutsumi, M., Laskar, F. I., & Hoffmann, P. (2017). Polar mesospheric horizontal divergence and relative vorticity measurements using multiple specular meteor radars. *Radio Science*, 52(7), 811–828. <https://doi.org/10.1002/2016RS006225>
- Chau, J. L., Strelnikova, I., Schult, C., Oppenheim, M. M., Kelley, M. C., Stober, G., & Singer, W. (2014). Nonspecular meteor trails from non-field-aligned irregularities: Can they be explained by presence of charged meteor dust? *Geophysical Research Letters*, 41(10), 3336–3343. <https://doi.org/10.1002/2014GL059922>
- Chau, J. L., Urco, J. M., Avsarkisov, V., Vierinen, J. P., Latteck, R., Hall, C. M., & Tsutsumi, M. (2020). Four-dimensional quantification of Kelvin-Helmholtz instabilities in the polar summer mesosphere using volumetric radar imaging. *Geophysical Research Letters*, 47(1), D09S12. <https://doi.org/10.1029/2019GL086081>
- Dewan, E. M., & Picard, R. H. (1998). Mesospheric bores. *Journal of Geophysical Research*, 103(D6), 6295–6305. <https://doi.org/10.1029/97jd02498>
- Dewan, E. M., & Picard, R. H. (2001). On the origin of mesospheric bores. *Journal of Geophysical Research*, 106, 2921–2927. <https://doi.org/10.1029/2000JD900697>
- Ecklund, W. L., & Balsley, B. B. (1981). Long-term observations of the Arctic mesosphere with the MST radar at Poker Flat, Alaska. *Journal of Geophysical Research*, 86, 7775–7780. <https://doi.org/10.1029/JA086iA09p07775>
- Feraco, F., Marino, R., Pumir, A., Primavera, L., Mininni, P. D., Pouquet, A., & Rosenberg, D. (2018). Vertical drafts and mixing in stratified turbulence: Sharp transition with Froude number. *Europhysics Letters*, 123(4), 44002. <https://doi.org/10.1209/0295-5075/123/44002>
- Fritts, D. C., Baumgarten, G., Wan, K., Werne, J., & Lund, T. (2014). Quantifying Kelvin-Helmholtz instability dynamics observed in noctilucent clouds: 2. Modeling and interpretation of observations. *Journal of Geophysical Research: Atmospheres*, 119(15), 9359–9375. <https://doi.org/10.1002/2014JD021833>
- Fritts, D. C., Kaifler, N., Kaifler, B., Geach, C., Kjellstrand, C. B., Williams, B. P., et al. (2020). Mesospheric bore evolution and instability dynamics observed in PMC Turbo imaging and Rayleigh Lidar profiling over Northeastern Canada on 13 July 2018. *Journal of Geophysical Research: Atmospheres*, 125, e2019JD032037. <https://doi.org/10.1029/2019JD032037>
- Fritts, D. C., Williams, B. P., She, C. Y., Vance, J. D., Rapp, M., Lübken, F. J., & Goldberg, R. A. (2004). Observations of extreme temperature and wind gradients near the summer mesopause during the MacWAVE/MIDAS rocket campaign. *Geophysical Research Letters*, 31, L24S06. <https://doi.org/10.1029/2003GL019389>
- Gardner, C. S., & Liu, A. Z. (2007). Seasonal variations of the vertical fluxes of heat and horizontal momentum in the mesopause region at Starfire Optical Range, New Mexico. *Journal of Geophysical Research*, 112, D09113. <https://doi.org/10.1029/2005JD006179>
- Gardner, C. S., Tao, X., & Papen, G. C. (1995). Simultaneous lidar observations of vertical wind, temperature, and density profiles in the upper mesosphere: Evidence for nonseparability of atmospheric perturbation spectra. *Geophysical Research Letters*, 22, 2877–2880. <https://doi.org/10.1029/95GL02783>
- Gudadze, N., Stober, G., & Chau, J. L. (2019). Can VHF radars at polar latitudes measure mean vertical winds in the presence of PMSE? *Atmospheric Chemistry and Physics*, 19(7), 4485–4497. <https://doi.org/10.5194/acp-19-4485-2019>
- Herbert, C., Marino, R., Rosenberg, D., & Pouquet, A. (2016). Waves and vortices in the inverse cascade regime of stratified turbulence with or without rotation. *Journal of Fluid Mechanics*, 806, 165–204. <https://doi.org/10.1017/JFM.2016.581>
- Hocking, W. K., Fuller, B., & Vandeppeer, B. (2001). Real-time determination of meteor-related parameters utilizing modern digital technology. *Journal of Atmospheric and Solar-Terrestrial Physics*, 63(2), 155–169. [https://doi.org/10.1016/s1364-6826\(00\)00138-3](https://doi.org/10.1016/s1364-6826(00)00138-3)

## Acknowledgments

This study was partially supported by the Deutsche Forschungsgemeinschaft (German Research Foundation) under project LU1174/8-1 (PACOG) of the research unit FOR1898, and under SPP 1788 (CoSIP) project CH1482/3-1 (CS-PMSE-MIMO). R. Marino acknowledges support from the project "EVENTFUL" (ANR-20-CE30-0011), funded by the French "Agence Nationale de la Recherche"—ANR through the program AAPG-2020. The authors would like to thank Nikoloz Gudadze for suggesting us to look at the PMSE observations from July 16, 2016, and Dr. Miguel Larsen for his valuable suggestions. Open access funding enabled and organized by Projekt DEAL.

- Hoppe, U.-P., & Fritts, D. C. (1995). High-resolution measurements of vertical velocity with the European incoherent scatter VHF radar: 1. Motion field characteristics and measurement biases. *Journal of Geophysical Research*, *100*(D8), 16813–16825. <https://doi.org/10.1029/95JD01466>
- Hoppe, U.-P., Hall, C., & Röttger, J. (1988). First observations of summer polar mesospheric backscatter with a 224 MHz radar. *Geophysical Research Letters*, *15*(1), 28–31. <https://doi.org/10.1029/GL0151001p00028>
- Hozumi, Y., Saito, A., Sakanoi, T., Yamazaki, A., Hosokawa, K., & Nakamura, T. (2019). Geographical and seasonal variability of mesospheric bores observed from the International Space Station. *Journal of Geophysical Research: Space Physics*, *124*(5), 3775–3785. <https://doi.org/10.1029/2019JA026635>
- Hysell, D. L., & Chau, J. L. (2006). Optimal aperture synthesis radar imaging. *Radio Science*, *41*, RS2003. <https://doi.org/10.1029/2005RS003383>
- Larsen, M. F., & Meriwether, J. W. (2012). Vertical winds in the thermosphere. *Journal of Geophysical Research*, *117*(9), A09319. <https://doi.org/10.1029/2012JA017843>
- Latteck, R., Singer, W., Rapp, M., Vandeppeer, B., Renkwitz, T., Zecha, M., & Stober, G. (2012). MAARSY: The new MST radar on Andøya—System description and first results. *Radio Science*, *47*(1), RS1006. <https://doi.org/10.1029/2011RS004775>
- Lehmacher, G. A., Scott, T. D., Larsen, M. F., Bilén, S. G., Croskey, C. L., Mitchell, J. D., et al. (2011). The Turbopause experiment: Atmospheric stability and turbulent structure spanning the turbopause altitude. *Annales Geophysicae*, *29*, 2327–2339. <https://doi.org/10.5194/angeo-29-2327-2011>
- Li, F., Swenson, G. R., Liu, A. Z., Taylor, M., & Zhao, Y. (2007). Investigation of a “wall” wave event. *Journal of Geophysical Research*, *112*(D4), D04104. <https://doi.org/10.1029/2006JD007213>
- Lübken, F.-J., Jarvis, M. J., & Jones, G. O. L. (1999). First in situ temperature measurements at the Antarctic summer mesopause. *Geophysical Research Letters*, *26*(24), 3581–3584. <https://doi.org/10.1029/1999GL010719>
- Marino, R., Rosenberg, D., Herbert, C., & Pouquet, A. (2015). Interplay of waves and eddies in rotating stratified turbulence and the link with kinetic-potential energy partition. *Europhysics Letters*, *112*(4), 49001. <https://doi.org/10.1209/0295-5075/112/49001>
- Murphy, D. M., & Koop, T. (2005). Review of the vapour pressures of ice and supercooled water for atmospheric applications. *Quarterly Journal of the Royal Meteorological Society*, *131*, 1539–1565. <https://doi.org/10.1256/qj.04.94>
- Picone, J. M., Hedin, A. E., Drob, D. P., & Aikin, A. C. (2002). NRLMSISE-00 empirical model of the atmosphere: Statistical comparisons and scientific issues. *Journal of Geophysical Research*, *107*(A12), SIA151–SIA1516. <https://doi.org/10.1029/2002JA009430>
- Pouquet, A., Marino, R., Mininni, P. D., & Rosenberg, D. (2017). Dual constant-flux energy cascades to both large scales and small scales. *Physics of Fluids*, *29*(11), 111108. <https://doi.org/10.1063/1.5000730>
- Rapp, M., & Lübken, F.-J. (2004). Polar mesosphere summer echoes (PMSE): Review of observations and current understanding. *Atmospheric Chemistry and Physics*, *4*, 2601–2633. <https://doi.org/10.5194/acp-4-2601-2004>
- Sato, K., Kohma, M., Tsutsumi, M., & Sato, T. (2017). Frequency spectra and vertical profiles of wind fluctuations in the summer Antarctic mesosphere revealed by MST radar observations. *Journal of Geophysical Research: Atmospheres*, *122*(1), 3–19. <https://doi.org/10.1002/2016JD025834>
- Seyler, C. E. (2005). Internal waves and undular bores in mesospheric inversion layers. *Journal of Geophysical Research*, *110*(D9), D09S05. <https://doi.org/10.1029/2004jd004685>
- Smith, S. M., Stober, G., Jacobi, C., Chau, J. L., Gerding, M., Mlynarczyk, M. G., et al. (2017). Characterization of a double mesospheric bore over Europe. *Journal of Geophysical Research: Space Physics*, *122*(9), 9738–9750. <https://doi.org/10.1002/2017JA024225>
- Smith, S. M., Taylor, M. J., Swenson, G. R., She, C. Y., Hocking, W., Baumgardner, J., & Mendillo, M. (2003). A multidagnostic investigation of the mesospheric bore phenomenon. *Journal of Geophysical Research*, *108*(A2), 1–18. <https://doi.org/10.1029/2002JA009500>
- St-Maurice, J.-P., & Chau, J. L. (2016). A theoretical framework for the changing spectral properties of meter-scale Farley-Buneman waves between 90 and 125 km altitudes. *Journal of Geophysical Research: Space Physics*, *121*(10), 310–341. <https://doi.org/10.1002/2016ja023105>
- Taylor, M. J., Turnbull, D. N., & Lowe, R. P. (1995). Spectrometric and imaging measurements of a spectacular gravity wave event observed during the ALOHA-93 Campaign. *Geophysical Research Letters*, *22*(20), 2849–2852. <https://doi.org/10.1029/95GL02948>
- Thomas, G. E., & Olivero, J. J. (1986). The heights of polar mesospheric clouds. *Geophysical Research Letters*, *13*(13), 1403–1406. <https://doi.org/10.1029/GL013i013p01403>
- Tippett, M. K., & Cohen, J. E. (2016). Tornado outbreak variability follows Taylor’s power law of fluctuation scaling and increases dramatically with severity. *Nature Communications*, *7*, 10668. <https://doi.org/10.1038/ncomms10668>
- Urco, J. M., Chau, J. L., Weber, T., & Latteck, R. (2019). Enhancing the spatio-temporal features of polar mesosphere summer echoes using coherent MIMO and radar imaging at MAARSY. *Atmospheric Measurement Techniques*, *12*, 955–969. <https://doi.org/10.5194/amt-12-955-2019>
- Von Zahn, U., Lübken, F. J., & Putz, C. (1990). BUGATTI experiments: Mass spectrometric studies of lower thermosphere eddy mixing and turbulence. *Journal of Geophysical Research*, *95*(D6), 7443–7465. <https://doi.org/10.1029/JD095iD06p07443>
- Widdel, H.-U. (1991). Experimental evidence for solitary waves in the middle atmosphere. *Journal of Geophysical Research*, *96*(A9), 15931–15942. <https://doi.org/10.1029/91ja01396>
- Woodman, R. F., & Guillén, A. (1974). Radar observations of winds and turbulence in the stratosphere and mesosphere. *Journal of the Atmospheric Sciences*, *31*(2), 493–505. [https://doi.org/10.1175/1520-0469\(1974\)031<0493:roowat>2.0.co;2](https://doi.org/10.1175/1520-0469(1974)031<0493:roowat>2.0.co;2)





## Chapter 4

# Enhancement of small-scale intermittency and dissipation in stratified flows

This chapter focuses on the link between small- and large-scale intermittency in stratified turbulence and how the large-scale extreme events affect the way energy is dissipated in the flow. Small-scale (or internal) intermittency is a key feature of turbulent flows. We discussed in Chap. 1 how its characteristic feature is a strong deviation from Gaussian statistics of the PDFs of velocity and temperature gradients. In geophysical flows, small-scale intermittency is widely observed in the form of intense fluctuations of the dissipation, localized in space and in time. However, we mentioned that intermittency is also observed at large-scale in the atmosphere and in the oceans. Indeed, when in Chap. 2 we characterized large-scale intermittency using the kurtosis by means of DNSs, we observed that vertical velocity and temperature display large-scale intermittent phenomena which affect the mixing properties of the flow in a range of Froude number of geophysical interest. Moreover, in Chap. 3, with data collected by radars we provided evidence of their occurrence in the MLT and along with the data from the DNSs we observed a link between extreme vertical drafts and strong horizontal shear. In this chapter I will introduce the results of a work ([15] and [42]) in which we show the link between large-scale extreme drafts, small-scale intermittency and enhanced dissipation in stratified flows by means of DNSs. We first investigate how large-scale drafts influence the small scales in a certain range of Froude numbers and then how they enhance local dissipation.

### 4.1 The link between large- and small-scale intermittency

As was presented in Chap. 2, the parameter we use to characterize intermittency is the kurtosis:  $K_x = \langle (x - \bar{x})^4 \rangle / \langle (x - \bar{x})^2 \rangle^2$ , where this time  $x = \partial_i u_j, \partial_i \theta$ . The overall behaviour of the small-scale kurtoses does resemble the ones of  $w$  and  $\theta$  observed in Chap. 2. In particular, from Fig. 4.1 we note a peak in almost all of the kurtoses of the gradients at the intermediate values of  $Fr$ , where large-scale extreme events develop in  $w$  and  $\theta$ . This hints at a possible enhancement of the classical small-scale intermittency due to the presence of the large-scale extreme events. However, contrary to what was found for the large-scale fields, the estimated kurtoses are always non-Gaussian, consistently with the small-scale intermittency observed in HIT (see Chap. 1). The enhancement of the small scale intermittency is observed even for  $u$  and  $v$ , which, as expected are Gaussian at large-scale, suggesting the recovery of isotropy at small-scales. Only  $K_{\partial_z u}, K_{\partial_z v}$  and  $K_{\partial_z \theta}$  do not show a trend with  $Fr$ .

This is associated to the imposed condition of stable stratification, therefore vertical variations of  $u$ ,  $v$  and  $\theta$  are bounded and cannot grow indefinitely.

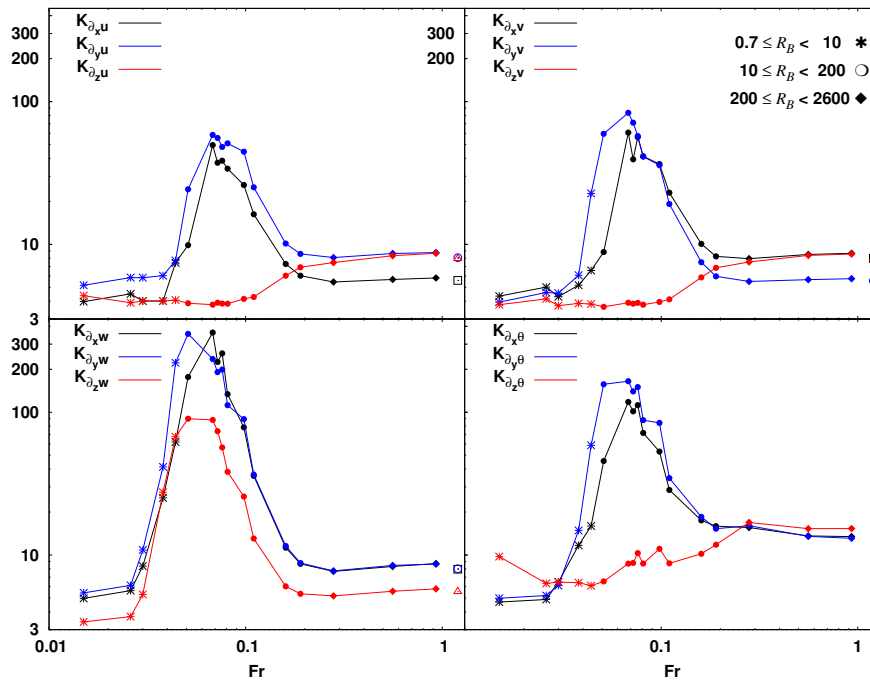


FIGURE 4.1: Kurtosis of the gradients of  $u$  (top-left),  $v$  (top-right),  $w$  (bottom-left) and  $\theta$  (bottom-right) as a function of  $Fr$ .  $K_{\partial_x u}$ ,  $K_{\partial_z v}$ , and  $K_{\partial_z \theta}$  are the only ones not showing any sizable dependence with  $Fr$ . Empty symbols placed at  $Fr > 1$  represent the values of the HIT run.

Using VAPOR we produced two-dimensional renderings to highlight the spatial correlation between extreme values in the large- and in the small-scale fields. In particular, we note the correlation between regions characterized by intermittency and regions with negative values of the gradient Richardson number  $Ri$ . The observed correlations cannot all be explained with the simple one-dimensional model presented in Chap. 2, however, they are captured by the analytical system of equations presented in [73]. We saw in Chap. 2 that  $Ri$  can be used to identify regions of the flow more prone to develop local overturning, and that these correlate with the regions where extreme drafts develop. Moreover, in Chap. 3 we found that strong horizontal shears are needed in order to develop the strongest extreme events in the flow. Thus, the generation of the extreme events in the fields may be related to the presence of vertically sheared horizontal winds (VSHWs) [18] in the flow. From these consideration we propose a mechanism which explain the generation of extreme vertical deafts from local overturning. Based on that, vertical drafts would originate from the shear generated by the VSHWs, the latter creating the conditions for Kelvin-Helmholtz instabilities to develop, which in turn generate gradients of  $\theta$ . If we consider the equation for  $\partial_z \theta$  along fluid trajectories, obtained from the analytical model presented in [73] we have:

$$D_t(\partial_z \theta) = (N - \partial_z \theta) \partial_z w - (\partial_x \theta)(\partial_z u) - (\partial_y \theta)(\partial_z v). \quad (4.1)$$

with  $D_t$  being the Lagrangian derivative. From 4.1 we see that  $\partial_z \theta$  is linked to the variations in the horizontal strain given by the second and third term on the right side of the equation,  $(\partial_x \theta)(\partial_z u)$  and  $(\partial_y \theta)(\partial_z v)$  respectively.  $\partial_z \theta$  can then be produced by strain and local rotation or by buoyancy. Thus, if  $\partial_z \theta$  grows and approaches  $N$ ,

buoyancy fluctuations reverse the background stratification, the flow becomes unstable and local convection takes place generating fast and strong large-scale drafts: the extreme events observed in the vertical velocity field. These motions also generate vorticity  $\omega$  as

$$D_t\omega \approx -N(\partial_y\theta\hat{x} - \partial_x\theta\hat{y}). \quad (4.2)$$

A correlation between the extreme events of large- and small-scale fields with  $\omega$  was indeed also observed. This provides a mechanism producing vorticity in stably stratified turbulence without resorting to vortex stretching. This generation of vorticity enhances dissipation, as the dissipation of kinetic energy is proportional to the enstrophy which depends on the spatial average of  $\omega^2$ . Thus, vorticity feeds the small-scale intermittency, acting as a link between large-scale extreme events and small-scale intermittency.

## 4.2 Modulation of local energy dissipation by vertical drafts

We now investigate in detail how dissipation is affected by the presence of extreme vertical drafts.

In the attempt to characterize the effects of the vertical drafts on local (kinetic and potential) energy dissipation, we first assess when they develop within the flow from the temporal evolution of the kurtosis of the vertical velocity  $K_w$  in DNSs of stratified flows. This analysis emphasizes the bursty behaviour of the kurtosis over time in the resonant regime,  $Fr \in [0.07 : 0.1]$  identified in Chap. 2. In particular, we observe for the runs with  $Fr = 0.076$  and  $Fr = 0.081$  spikes of  $K_w$ , where it can reach values up to  $\sim 11$ , separated by short time intervals where the kurtosis drops to  $\sim 3$ . We also note that such behaviour is no longer observed if we keep the same value of  $Fr$  but lower  $Re$ , therefore  $R_B$ , leading to a smoother signal of the kurtosis. We recall that  $R_B$  has been proved to be useful in identifying different regimes in stratified turbulence as mentioned in Chap. 2. By analyzing the kinetic and potential energy spectra,  $E_V(k)$  and  $E_P(k)$  respectively, we note how the same flow, with the same global parameters, but at different times, displays a significant difference in the power spectral density (PSD) at the small-scales. Indeed, the small-scale PSDs of  $E_V(k)$  and  $E_P(k)$  appear to be modulated by the kurtosis of  $w$ , displaying a difference of up to four orders of magnitude. In order to assess the effects of the extreme vertical drafts we compute the statistics of the dissipation in horizontal planes (i.e. averaged over horizontal planes of constant height), so that we can compare it with the by-plane kurtosis  $K_w(z, t)$ . We evaluated the point-wise kinetic and potential energy dissipation,  $\varepsilon_V = \nu|\nabla\mathbf{u}|^2$  and  $\varepsilon_P = \kappa|\nabla\theta|^2$ , respectively and computed their PDF on horizontal planes,  $\hat{\varepsilon}_V(z, t)$  and  $\hat{\varepsilon}_P(z, t)$  respectively, observing that they are indeed modulated by  $K_w(z, t)$ . A comparison between the vertical profile of  $K_w(z)$  and  $\hat{\varepsilon}_V$  reveals how planes with strong value of the dissipation display a peak also in the kurtosis. On the other hand, regions with moderate and weak values of the dissipation are associated to a lower kurtosis. Moreover, the PDFs of  $P[\log(\varepsilon_V)]$  are similar when computed on regions with comparable values of  $K_w(z)$ , further proof that the statistical distribution of the kinetic energy dissipation is modulated by the presence of extreme vertical drafts. The correspondence between peaks in the kurtosis and in the dissipation is shown for several times around  $T^*$  in the top and mid-top panel of Fig. 4.2. Here, the vertical profiles of the by-plane kurtosis  $K_w(z, t)$  and of the normalized kinetic energy dissipation  $\hat{\varepsilon}_V(z, t)$ , as a function of time for the run with  $N = 8$  are displayed on a three-dimensional color map. From these panels, a good qualitative correlation between the peaks (orange/red in the color map) of  $K_w(z, t)$  and of  $\hat{\varepsilon}_V(z, t)$  can be

observed. The strongest peaks in  $\hat{\varepsilon}_V(z, t)$  are found around the same height  $z$  and the same time  $t$  as the peak in  $K_w(z, t)$ , meaning that the flow is developing extreme vertical drafts. A joint PDF built with all the values of  $K_w(z, t)$  and  $\hat{\varepsilon}_V(z, t)$  for all times and heights of the run with  $N = 8$  is shown in the bottom panel of Fig. 4.2. The solid red line indicates the conditional average of the dissipation in bins of the kurtosis,  $\langle \hat{\varepsilon}_V(z, t) | K_w(z, t) \rangle$ . We observe from the average of the dissipation that the values assumed by  $\hat{\varepsilon}_V(z, t)$  scale linearly with  $K_w(z, t)$  up to  $K_w(z, t) \sim 5$ . After that,  $\hat{\varepsilon}_V(z, t)$  saturates and shows no further evolution with the kurtosis. We find that the quantities rendered in Fig. 4.2 are maximally correlated for a time delay of  $\phi \approx \tau_{NL}/3$ . The good correlation resulting from the statistics of the joint PDF, the conditional average of the dissipation, clearly showing a modulation due to the value of the kurtosis of  $w$ , and the evidence that local maxima of  $\hat{\varepsilon}_V(z, t)$  are anticipated by peaks in  $K_w(z, t)$  indicate a causation between the emergence of vertical drafts and the enhancement of the dissipation. Similar results are obtained for the other runs where vertical drafts arise in the flow.

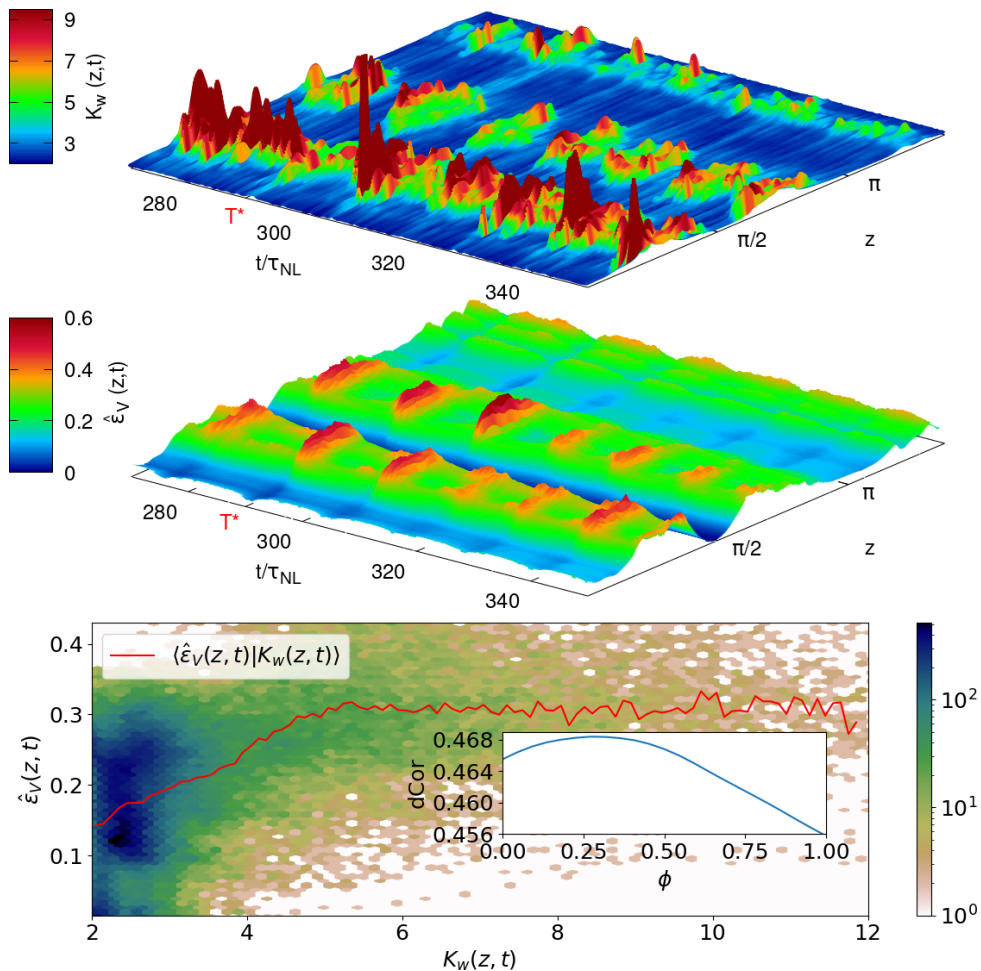


FIGURE 4.2: Temporal evolution in units of  $\tau_{NL}$  for the run with  $N = 8$  of (top) the vertical profile of the by-plane kurtosis  $K_w(z, t)$ , and (mid-top) the normalized kinetic energy dissipated in horizontal planes  $\hat{\varepsilon}_V(z, t)$ . The bottom panel gives the joint PDF of  $K_w(z, t)$  and  $\hat{\varepsilon}_V(z, t)$  for the entire run with  $N = 8$ . The solid red line indicates the average of  $\hat{\varepsilon}_V$  conditioned on  $K_w$ . Inset: evolution of the distance correlation coefficient  $dCor$  between  $K_w(z, t)$  and  $\hat{\varepsilon}_V(z, t + \phi)$ , as a function of a temporal lag  $\phi$  between the two signals. Note that the highest correlation is obtained for  $\phi \approx \tau_{NL}/3$ .

These results indicate that the occurrence of extreme drafts determines the local properties and statistics of strong dissipative events. The efficiency of the local energy dissipation can be further characterized by computing the minimal domain volume needed to achieve a given percentage of the total energy dissipation at a given time. By comparing this quantity between runs which develop extreme events and the ones where they do not develop we can provide an estimate of how much the extreme vertical drafts enhance the dissipation efficiency. We define the kinetic (potential) energy dissipation efficiency  $V_{\varepsilon_V}$  ( $V_{\varepsilon_P}$ ) as the minimum number of (grid) points needed to achieve the 50% level of the total kinetic (potential) energy dissipation at that time step. The lower  $V_{\varepsilon_V}$  ( $V_{\varepsilon_P}$ ), the more efficient will be the local dissipation of the kinetic (potential) energy. For each time step we associate the value of  $V_{\varepsilon_V}$  ( $V_{\varepsilon_P}$ ) with the global (i.e. computed from the whole domain) kurtosis of the vertical velocity  $K_w$ . By doing this, we obtain couples made of  $V_{\varepsilon_V}$  (or  $V_{\varepsilon_P}$ ) and  $K_w$ . For each run we average the values of  $V_{\varepsilon_V}$  ( $V_{\varepsilon_P}$ ) in bins of  $K_w$ , obtaining the top (bottom) panel of Fig. 4.3. We note from Fig. 4.3 that the HIT case (black cross in the top panel) has one of the largest kinetic energy dissipation efficiencies: only  $\approx 16\%$  of the most dissipative regions within the volume are in fact needed to achieve 50% of the global kinetic energy dissipation. Comparing the HIT run to the stratified runs in the same bin of  $K_w$  shows that in the former the dissipation of kinetic energy is more efficient. However, runs with  $N = 7.37$  and with  $N = 8$  (red pentagons and blue triangles respectively) in Fig. 4.3 are able to achieve similar values  $V_{\varepsilon_V}$ . The values  $V_{\varepsilon_V}$  of these runs become comparable to the one found for the HIT run only when developing extreme vertical drafts, as observed from the scaling of  $V_{\varepsilon_V}$  with  $K_w$  shown in Fig. 4.3. In these cases,  $V_{\varepsilon_V}$  decreases linearly with the kurtosis, reaching values comparable to the HIT run when  $K_w \gtrsim 7$ . Indeed,  $V_{\varepsilon_V}$  for these two runs can be respectively as low as  $\approx 14\%$  and  $\approx 11\%$ , which is smaller than the  $\approx 16\%$  of the HIT case. Large-scale vertical drafts are then needed in stratified turbulent flows for the energy to be locally dissipated as efficiently as in the HIT case at equivalent Reynolds numbers. Moreover, runs with  $N = 7.37$  and with  $N = 8$  belong to the resonant regime [16] discussed in Chap. 2, and have a  $Fr$  compatible with values found in some regions of the ocean and the atmosphere. Thus, these drafts are responsible for the local and efficient enhancement of the kinetic energy dissipation  $\varepsilon_V$ , which would be otherwise weakened by stratification. Indeed, without drafts, dissipation efficiency is significantly smaller. The most stratified runs in our study are unable to develop significant drafts, therefore they have an almost Gaussian kurtosis (i.e.  $K_w \sim 3$ ), and they are both characterized by an efficiency  $V_{\varepsilon_V} \approx 26\%$ , more than twice that of the most dissipative cases. On the opposite limit, when stratification is weak,  $V_{\varepsilon_V}$  approaches the value of the HIT case even though  $K_w \sim 3$ . The local potential energy dissipation efficiency  $V_{\varepsilon_P}$  exhibits a behaviour similar to that of  $V_{\varepsilon_V}$  (Fig. 4.3, bottom) and even in this case runs with  $N = 7.37$  and with  $N = 8$  are the most dissipative when they reach high values of  $K_w$ . The present result is consistent with the findings of [55], where by modeling the global ocean they find that the  $\sim 10\%$  of the ocean is responsible for  $\sim 90\%$  of the global dissipation. Finally, the volume of the flow needed to achieve the 50% of the total potential dissipation is significantly smaller in this case. In fact, the values of  $V_{\varepsilon_P}$  are smaller than those of  $V_{\varepsilon_V}$ , suggesting that stratified flows are more efficient in dissipating potential energy than kinetic energy. This could be related to the well-known stronger small-scale intermittency of (passive) scalars as they easily form frontal structures [6, 58, 75].

We leave for future works a similar investigation for the stratified and rotating case. The addition of rotation in the flow may, in fact, have an effect on the observed

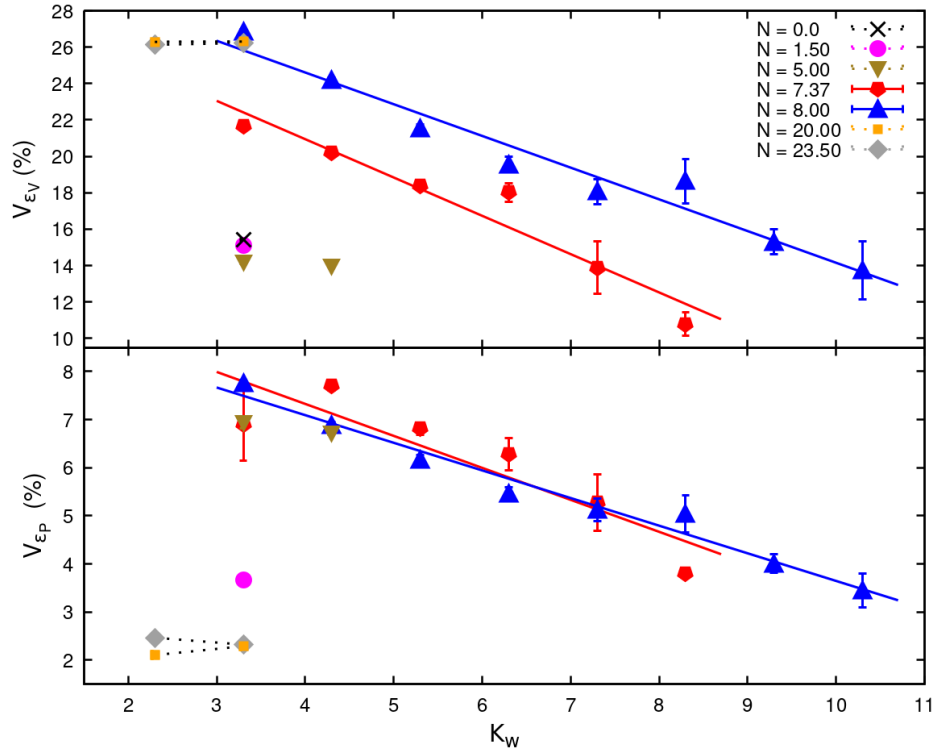


FIGURE 4.3: Kinetic and potential energy dissipation efficiency as a function of  $K_w$  measured in terms of the minimal domain volume percentage  $V_{\epsilon_V}$  and  $V_{\epsilon_P}$  needed to achieve 50% of respectively the total kinetic and potential energy dissipation.

generation of small-scale turbulence and on the dissipation. In that case, however, a higher spatial resolution will be required in order to obtain broader spectra. The stratified and rotating case is also of interest since the presence of an inverse cascade, transferring energy from small- to large-scales, has been observed along the usual “direct” cascade (from large- to small-scale) [41].



**HAL**  
open science

## Connecting Large-Scale Velocity and Temperature Bursts with Small-Scale Intermittency in Stratified Turbulence

F Feraco, R Marino, L Primavera, Alain Pumir, P D Mininni, D Rosenberg, A Pouquet, R Foldes, E Lévêque, E Camporeale, et al.

► **To cite this version:**

F Feraco, R Marino, L Primavera, Alain Pumir, P D Mininni, et al.. Connecting Large-Scale Velocity and Temperature Bursts with Small-Scale Intermittency in Stratified Turbulence. EPL - Europhysics Letters, European Physical Society/EDP Sciences/Società Italiana di Fisica/IOP Publishing, 2021, 10.1209/0295-5075/135/14001 . hal-03412913

**HAL Id: hal-03412913**

**<https://hal.archives-ouvertes.fr/hal-03412913>**

Submitted on 3 Nov 2021

**HAL** is a multi-disciplinary open access archive for the deposit and dissemination of scientific research documents, whether they are published or not. The documents may come from teaching and research institutions in France or abroad, or from public or private research centers.

L'archive ouverte pluridisciplinaire **HAL**, est destinée au dépôt et à la diffusion de documents scientifiques de niveau recherche, publiés ou non, émanant des établissements d'enseignement et de recherche français ou étrangers, des laboratoires publics ou privés.



# Connecting Large-Scale Velocity and Temperature Bursts with Small-Scale Intermittency in Stratified Turbulence

F. FERACO<sup>1,2</sup>, R. MARINO<sup>1</sup>, L. PRIMAVERA<sup>2</sup>, A. PUMIR<sup>3</sup>, P.D. MININNI<sup>4</sup>, D. ROSENBERG<sup>5</sup>, A. POUQUET<sup>6</sup>, R. FOLDES<sup>7</sup>, E. LÉVÊQUE<sup>1</sup>, E. CAMPOREALE<sup>8</sup>, S. CERRI<sup>9</sup>, H. CHARUVIL ASOKAN<sup>9</sup>, J.L. CHAU<sup>9</sup>, J.P. BERTOGLIO<sup>1</sup>, P. SALIZZONI<sup>1</sup>, M. MARRO<sup>1</sup>

<sup>1</sup> *Laboratoire de Mécanique des Fluides et d'Acoustique, CNRS, École Centrale de Lyon, Université Claude Bernard Lyon 1, INSA de Lyon, F-69134 Écully, France*

<sup>2</sup> *Dipartimento di Fisica, Università della Calabria, Italy*

<sup>3</sup> *École Normale Supérieure de Lyon, Lyon France*

<sup>4</sup> *Departamento de Física, Facultad de Ciencias Exactas y Naturales, Universidad de Buenos Aires, and IFIBA, CONICET, Buenos Aires 1428, Argentina*

<sup>5</sup> *288 Harper St., Louisville, CO 80027, USA*

<sup>6</sup> *Laboratory for Atmospheric and Space Physics, University of Colorado, Boulder, CO 80309, USA, and National Center for Atmospheric Research, P.O. Box 3000, Boulder, CO 80307, USA*

<sup>7</sup> *Università degli studi dell'Aquila, Italy*

<sup>8</sup> *CIRES, University of Colorado, Boulder, CO 80309, USA, and Centrum Wiskunde & Informatica, 1098 XG Amsterdam, The Netherlands*

<sup>9</sup> *Department of Astrophysical Sciences, Princeton University, 4 Ivy Lane, Princeton, NJ 08544, USA*

<sup>10</sup> *Leibniz Institute of Atmospheric Physics, University of Rostock, Kühlungsborn, Germany*

PACS 47.55.Hd – Stratified flows

PACS 47.35.Bb – Gravity waves

PACS 42.68.Bz – Atmospheric turbulence effects

**Abstract** – Non-Gaussian statistics of large-scale fields are routinely observed in data from atmospheric and oceanic campaigns and global models. Recent direct numerical simulations (DNSs) showed that large-scale intermittency in stably stratified flows is due to the emergence of sporadic, extreme events in the form of bursts in the vertical velocity and the temperature. This phenomenon results from the interplay between waves and turbulent motions, affecting mixing. We provide evidence of the enhancement of the classical small-scale (or internal) intermittency due to the emergence of large-scale drafts, connecting large- and small-scale bursts. To this aim we analyze a large set of DNSs of the stably stratified Boussinesq equations over a wide range of values of the Froude number ( $Fr \approx 0.01 - 1$ ). The variation of the buoyancy field kurtosis with  $Fr$  is similar to (though with smaller values than) the kurtosis of the vertical velocity, both showing a non-monotonic trend. We present a mechanism for the generation of extreme vertical drafts and vorticity enhancements which follows from the exact equations for field gradients.

**Introduction.** – A characteristic feature of turbulent flows, including geophysical flows, is the so-called internal (or small-scale) intermittency, producing localized intense variations of the energy dissipation and of field gradients [1], as observed in many instances in the atmosphere [2], the ocean [3, 4], and in laboratory experiments and in direct numerical simulations (DNSs). The Kolmogorov refined theory [5] of homogeneous isotropic turbulence (HIT)

relates this phenomenon to the anomalous scalings of the structure functions [5]. Internal intermittency is also at the origin of the non-Gaussian behavior of the probability distribution functions (PDFs) of small-scale turbulent velocity fluctuations. But an accurate modeling of intermittency in turbulence remains a challenging question. Numerous attempts have been made to model this departure from Gaussianity, as for instance with log-normal or

log-Lévy models [6]. When shear waves are present, it was shown that intermittency is again a major feature of the small-scale behavior in these flows [7], although the anomalous exponents differ from those obtained in HIT, showing a lack of dependence with the imposed shear.

More generally, intermittent events at large scales have been observed in clear air turbulence with patches that can span up to 100 km horizontally and 1 km vertically [9], in the vertical velocity and temperature in atmospheric mesoscales [10], in the mesosphere-lower thermosphere [11], in the ocean (in observations [12] and models [16]), and in DNSs [13, 14, 19] where large-scale bursts develop in a certain parameter space. Indeed, [14] (F18 hereafter) demonstrated that the vertical velocity  $w$  and the buoyancy  $\theta$  (proportional to potential temperature fluctuations) are highly intermittent at large scales in DNSs of the Boussinesq equations. This phenomenon takes place in a range of the Froude number  $Fr$  compatible with values in the atmosphere and the oceans. Large-scale intermittency was found both for Eulerian and Lagrangian velocities, demonstrating the importance of large-scale flow structures. In turn, these structures were shown to be associated with the most unstable regions within the fluid, affecting its mixing properties [14]. More recently it was shown that large-scale intermittency is present also in rotating stratified turbulent flows, including situations in quasi-geostrophic balance [15, 21].

The purpose of this study is to connect large- and small-scale intermittency in stably stratified turbulence, using the DNS database of purely stratified flows from F18. We analyze fourth-order moments of the Eulerian velocity and buoyancy fields. With these fields we show the connection between intermittent dynamics at different scales, and how intermittency and the emergence of structures in the flow are modulated by the Froude number.

**Methods.** – The results presented here are based on several DNSs of the Navier-Stokes equations in the Boussinesq framework in presence of stable stratification. To ensure incompressibility, the velocity field  $\mathbf{u}$  satisfies the condition  $\nabla \cdot \mathbf{u} = 0$ . The dimensionless equations are:

$$\partial_t \mathbf{u} + (\mathbf{u} \cdot \nabla) \mathbf{u} = -\nabla p - N\theta \hat{z} + \mathbf{F} + \nu \nabla^2 \mathbf{u} \quad (1)$$

$$\partial_t \theta + \mathbf{u} \cdot \nabla \theta = Nw + \kappa \nabla^2 \theta, \quad (2)$$

where  $\nu$  and  $\kappa$  are respectively the kinematic viscosity and the thermal diffusivity. For all the runs the Prandtl number is  $Pr = \nu/\kappa = 1$  with  $\nu = 10^{-3}$ .  $N$  is the Brunt-Väisälä frequency, associated to the background potential temperature stratification, kept constant throughout the computational domain, thus representing the parameter governing the imposed stable stratification. The initial conditions consist of vanishing buoyancy fluctuations ( $\theta = 0$ ) and a velocity field with kinetic energy randomly distributed on spherical shells with wavenumbers  $k_F \in [2, 3]$  in Fourier space. A random isotropic mechanical forcing  $\mathbf{F}$  is applied to the velocity field at the

same wavenumbers [20]. We define the dimensionless parameters  $Re = UL/\nu$  and  $Fr = U/LN$  respectively as the Reynolds and Froude numbers, where  $U$  and  $L$  are the flow characteristic velocity and integral scale. The buoyancy Reynolds number  $R_B \equiv Re Fr^2$  measures the relative strength of buoyancy to dissipation and is commonly used to identify regimes where waves ( $R_B \leq 10$ ) or turbulence ( $R_B \geq 10^2$ ) dominate. We integrated the equations numerically using the Geophysical High-Order Suite for Turbulence (GHOST), a hybrid MPI-, OpenMP- and CUDA-parallelized pseudo-spectral code [18] that can generate flows in a triply-periodic domains (as in the runs under study) or with non-periodic boundary conditions in one direction [17]. Seventeen runs were performed on isotropic grids of  $512^3$  points, with the size of the periodic three-dimensional computational box equal to  $2\pi$ , each run with a different value of  $N$ . The statistics of  $\mathbf{u} = (u, v, w)$  and  $\theta$  are characterized by their dimensionless fourth-order moment, the kurtosis,

$$K_\alpha = \frac{\langle (\alpha - \bar{\alpha})^4 \rangle}{\langle (\alpha - \bar{\alpha})^2 \rangle^2}, \quad (3)$$

with  $\alpha = u, v, w, \theta$ , or field gradients. Averages were taken in all cases over the entire spatial domain and for  $\approx 8$  turnover times  $\tau_{NL} = L/U$  after the peak of dissipation was reached. The reference value of the kurtosis for Gaussian processes is 3, thus values  $K_\alpha > 3$  correspond to leptokurtic PDFs with fat tails and a higher probability of extreme values. As seen in F18,  $u$  and  $v$  show no large-scale intermittency, their kurtosis never exceeding 3, and thus with nearly Gaussian PDFs as in HIT, or, in fact, slightly sub-Gaussian up to  $Fr \approx 0.2$ . However, in F18 it was shown that  $w$  and  $\theta$  develop strong events in the range  $0.07 \leq Fr \leq 0.1$ , with  $K_{w,\theta} > 3$ . Table 1 gives relevant quantities and the governing parameters for each run.

**Results.** – The Eulerian vertical velocity  $w$  kurtosis for runs in Table 1 follows a non-monotonic dependence on  $Fr$  with a peak at  $Fr \approx 0.08$ ; see Fig. 1 (top). The figure also shows that  $K_\theta$  exhibits a qualitatively similar dependence with a peak at  $Fr \approx 0.08$ . The value of  $K_\theta$  at the peak, however, is significantly smaller than that of  $K_w$ . The buoyancy field  $\theta$  is therefore intermittent at large scales, with the emergence of localized bursts making its PDF non-Gaussian in the range  $Fr \in [0.07 - 0.1]$ , corresponding to runs 7 to 12 in Table 1. As a reference, in the atmosphere at horizontal scales of 100 km,  $Fr \approx 0.01$  on the average, but values in the range mentioned above are not unusual (e.g., up to 0.5 in clear air turbulence [9] with turbulent patches of 1 to 100 km).

The PDFs of both  $w$  and  $\theta$  are shown in Fig. 2 (left) for run 9, exhibiting fatter tails than the Gaussian reference. The small asymmetry of the PDFs is a consequence of the limiting sampling, and is expected to disappear if statistics are accumulated over much longer times. A Gaussian behavior, to the extent that  $K_\alpha \approx 3$  ( $\alpha = w, \theta$ ), is recovered in the runs with large  $Fr$  (weakly stratified) and for

Run	1	2	3	4	5	6	7	8	9	10	11	12	13	14	15	16	17
$Re/10^3$	3.9	3.8	3.8	3.8	3.8	3.8	3.9	3.8	3.8	3.8	3.7	3.6	3.0	2.6	2.6	2.8	2.9
$Fr$	0.015	0.026	0.030	0.038	0.044	0.051	0.068	0.072	0.076	0.081	0.098	0.11	0.16	0.19	0.28	0.56	0.93
$R_B$	0.87	2.5	3.4	5.6	7.3	10.2	17.7	19.7	22.1	25.2	35.9	47.5	75.2	90.9	201	895	2560
$K_u$	2.3	2.4	2.3	2.1	2.3	2.3	2.3	2.3	2.3	2.3	2.3	2.3	2.5	2.6	2.9	2.8	2.8
$K_v$	2.2	2.3	2.2	2.3	2.1	2.0	2.1	2.1	2.1	2.1	2.1	2.1	2.6	2.8	2.7	2.8	2.8
$K_w$	3.1	3.2	3.1	3.1	3.2	3.6	7.3	8.6	10.4	9.1	8.8	5.3	3.9	3.5	3.3	3.0	2.9
$K_\theta$	3.3	3.4	3.4	3.5	3.5	3.6	4.0	4.3	4.3	4.1	4.1	3.6	3.1	2.9	2.8	2.7	2.7
$K_{\partial_x\theta}$	4.7	4.9	6.5	11.7	16.0	45.6	118.0	101.5	112.2	71.7	53.0	28.6	17.5	15.9	15.6	13.6	13.5
$K_{\partial_y\theta}$	5.0	5.2	6.1	14.9	58.7	157.0	165.0	140.0	150.1	88.1	84.2	34.5	18.5	15.3	16.0	13.5	13.1
$K_{\partial_z\theta}$	9.8	6.3	6.5	6.4	6.1	6.5	8.7	8.8	10.3	8.7	11.1	8.7	10.2	11.8	16.9	15.3	15.3
$K_{\partial_x u}$	4.0	4.5	4.0	4.0	7.4	9.9	49.6	37.3	38.6	33.9	26.0	16.3	7.3	6.03	5.5	5.7	5.8
$K_{\partial_y v}$	3.9	4.6	4.6	6.1	22.7	59.5	83.5	71.2	57.4	41.2	35.9	19.2	7.5	6.0	5.5	5.7	5.8
$K_{\partial_z w}$	3.4	3.7	5.3	27.5	67.4	90.1	88.4	73.7	56.7	38.3	25.6	13.0	6.0	5.4	5.2	5.6	5.8
$K_{\partial_y u}$	5.2	5.9	5.8	6.0	7.7	24.3	58.5	55.7	48.2	51.0	44.6	25.1	10.1	8.6	8.1	8.6	8.8
$K_{\partial_z u}$	4.4	3.9	4.0	4.0	4.01	3.9	3.8	3.9	3.9	3.8	4.2	4.3	6.0	6.9	7.5	8.3	8.7
$K_{\partial_x v}$	4.3	5.0	4.3	5.2	6.6	8.8	60.7	39.4	56.4	41.4	36.5	23.0	10.1	8.2	7.9	8.5	8.7
$K_{\partial_z v}$	3.8	4.2	3.7	3.9	3.8	3.7	3.9	3.8	3.9	3.8	4.0	4.1	5.9	6.9	7.5	8.4	8.6
$K_{\partial_x w}$	5.0	5.6	8.4	25.1	61.9	176.5	361.6	225.0	258.4	133.8	78.4	35.8	11.3	8.7	7.7	8.3	8.7
$K_{\partial_y w}$	5.4	6.1	10.8	41.4	222.1	354.0	236.0	191.1	199.1	112.1	89.5	36.6	11.6	8.8	7.7	8.5	8.6

Table 1: Governing parameters for each run, namely the Reynolds number  $Re$ , the Froude number  $Fr$ , and the buoyancy Reynolds number  $R_B$ , and kurtosis of the fields and their gradients,  $K_\alpha$  ( $\alpha = u, v, w, \theta$ , and spatial derivatives  $\partial_x, \partial_y$  and  $\partial_z$  of all these quantities) for all the runs. Values are averaged for  $\approx 8$  turnover times after the peak of dissipation in each run.

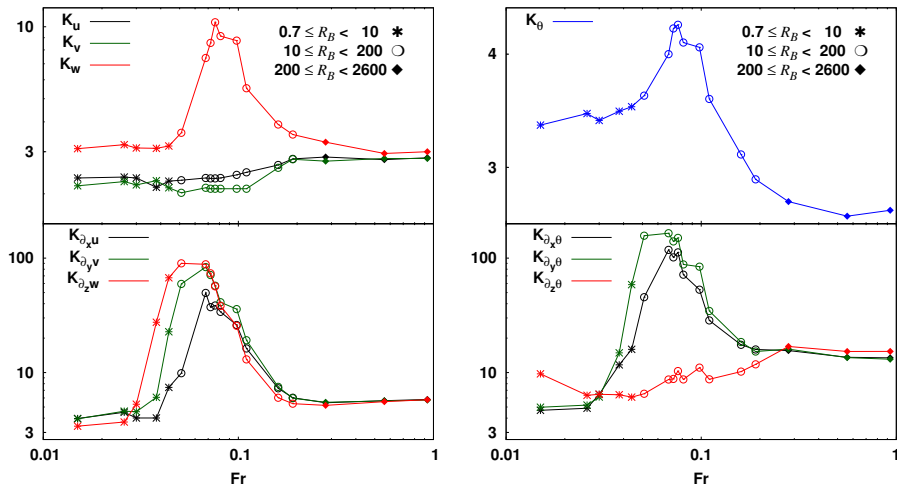


Figure 1: For all runs in Table 1, the figure shows as a function of  $Fr$ : the kurtosis of  $u, v, w$  (top-left) and  $\theta$  (top-right); the kurtosis of the diagonal elements of the velocity gradient tensor  $\partial_x u, \partial_y v, \partial_z w$  (bottom-left), and of the components of the buoyancy gradient  $\partial_x \theta, \partial_y \theta$ , and  $\partial_z \theta$ . Note that  $K_u, K_v$ , and  $K_{\partial_z \theta}$  do not show any sizable dependence with  $Fr$ , the first two being always compatible with Gaussian or sub-Gaussian statistics.

$Fr < 0.04$  (strongly stratified). The kurtosis of  $u$  and  $v$  on the other hand show almost no dependence on  $Fr$ , with values of  $K_u$  and  $K_v$  close to 3 for all runs (see Fig. 1). The corresponding PDFs (not shown) are in good agreement with Gaussian or sub-Gaussian distributions. To characterize the spatial distribution of the intermittent extreme events in  $w$  and  $\theta$ , emerging within the flow with the passage of the time, we computed two-dimensional (2D) histograms of these fields accumulated in time (i.e., using several DNS temporal outputs), displayed in Fig. 3 for runs 3, 9, and 15. Events are counted as a function of their height and of the standardized values (i.e., normal-

ized to have zero mean and unitary standard deviation) of  $w$  and  $\theta$ , and the counts normalized to get a probability. The standard deviation  $\sigma_\alpha$  ( $\alpha = w, \theta$ ) used to normalize each field is computed on the three-dimensional domain at the time of each output. In this representation, in the absence of extreme events, assuming a Gaussian statistics, over 99.7% of all the points would accumulate in a vertical stripe of the histograms between  $\pm 3\sigma_\alpha$ . However, velocity and buoyancy bursts induce the presence of many events with  $|\alpha|/\sigma_\alpha > 3$ . Histograms for run 9 are shown in particular in Fig. 3 (middle) and provide several relevant information: (1) The values of vertical velocity and

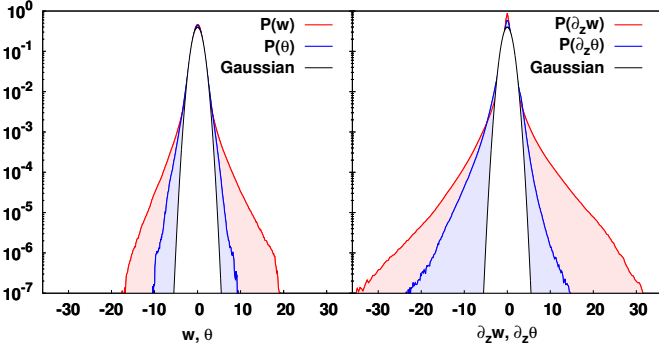


Figure 2: (Left) PDFs of  $w$  and  $\theta$  for run 9 with  $K_w = 10.4$ ,  $K_\theta = 4.3$ . (Right) PDFs of  $\partial_z w$  and  $\partial_z \theta$  for the same run, with  $K_{\partial_z w} = 56.7$ ,  $K_{\partial_z \theta} = 10.3$ . Shaded areas exceeding the Gaussian PDF (black lines) indicate the probability for extreme values in the fields and their gradients. Fields are normalized by their standard deviation to allow direct comparison.

buoyancy with the highest probability to occur are those between  $\pm 3\sigma_\alpha$ . However, extreme events (outside that range) are rather abundant for both  $w$  and  $\theta$  for all the runs within the peak of the plot of kurtosis vs.  $Fr$  (Fig. 1, top), and this is true in particular for run 9, for which the probability to observe events larger than  $3\sigma_\alpha$  is 1.06% for  $\alpha = w$  and 0.85% for  $\alpha = \theta$ , therefore significantly larger than what expected in the Gaussian case (0.27%). (2) Extreme events have a higher probability to develop in  $w$  than in  $\theta$ . Moreover, non-zero probabilities are observed in  $w$  up to  $\approx 13\sigma_w$ , whereas in  $\theta$  only up to  $\approx 9\sigma_\theta$ . This is in agreement with the fact that peak values of  $K_\theta$  are lower than those of  $K_w$  (see Fig. 1, top). Such difference is probably due to the coupling between  $w$  and  $\theta$ , which is modulated also by other parameters of the system such as  $Re$  and  $Fr$ . (3) The pattern described above is also observed in the histograms of the other runs within the range  $Fr \in [0.07 - 0.1]$  (not shown), demonstrating in all cases that extreme events in  $w$  and  $\theta$  have a probability to develop over time which is rather independent of height, as expected given the flow homogeneity.

Top and bottom panels in Fig. 3 also show the histograms for two cases outside the peaks of  $K_{w,\theta}$  in Fig. 1, respectively at lower and higher Froude numbers:  $Fr = 0.038$  (run 3), and  $Fr = 0.28$  (run 15). The pattern here is significantly different from the one observed for run 9, with these histograms having almost no points in the region  $|\alpha/\sigma_\alpha| > 7$  ( $\alpha = w, \theta$ ), consistent with the low  $K_\alpha$  detected and the absence of extreme events in the vertical velocity and buoyancy in these runs. Next we provide evidence of the connection between the large-scale intermittency materializing through the emergence of these bursts of vertical velocity and buoyancy [13, 14], and the classical internal or small-scale intermittency (evaluated through the kurtosis of the fields and their gradients). From 1 we first note that the kurtosis of all components of the velocity gradient tensor  $\partial_i u_j$  (except for  $\partial_z u$  and  $\partial_z v$ ) follow a trend with the Froude number resembling that of the kurtosis of  $w$  and  $\theta$ , with peaks close to  $Fr \approx 0.08$ . The

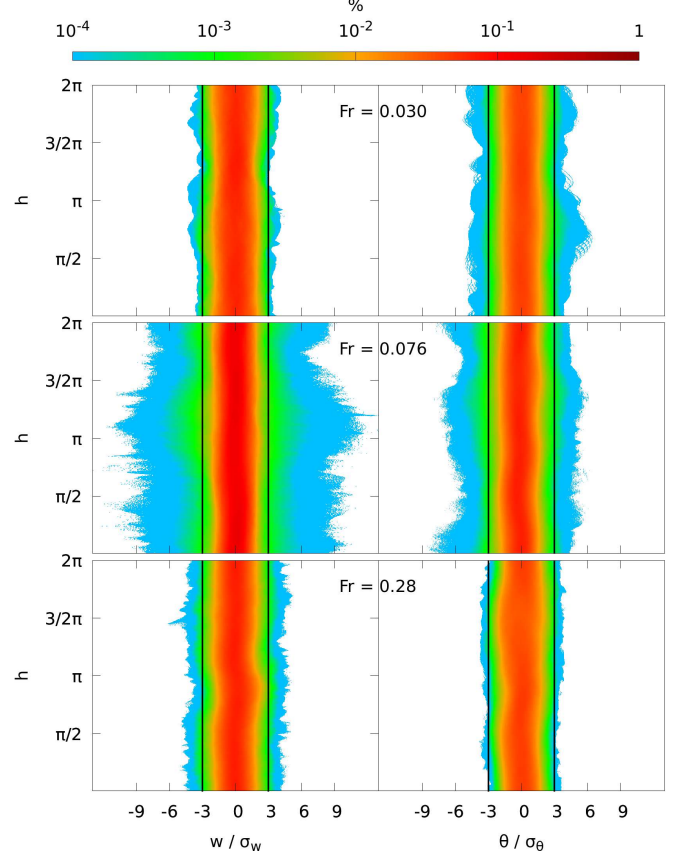


Figure 3: 2D histograms of  $w$  (left) and  $\theta$  (right) for three Froude numbers, in bins of their standardized values and of the height  $h$  (the  $z$ -coordinate and direction of gravity). The color palette shows the probability that a particular field value has to occur in the plane at altitude  $h$ . Red is for the most common values, light-blue for the rarest (see color bar). The mid panel corresponds to run 9 which displays extreme events in  $w$  and  $\theta$ . Top and bottom panels correspond respectively to runs 3 and 15, in which extreme events rarely evelop.

kurtosis of the diagonal components of the tensor,  $K_{\partial_x u}$ ,  $K_{\partial_y v}$ , and  $K_{\partial_z w}$  are reported in Fig. 1 (bottom), whereas kurtosis of the off-diagonal terms are in Table 1, showing how most peak values achieved by  $K_{\partial_i u_j}$  are about one order of magnitude larger than the peak values of  $K_w$  and  $K_\theta$ . A similar trend is followed by the kurtosis of the horizontal buoyancy gradient,  $K_{\partial_x \theta}$  and  $K_{\partial_y \theta}$ . Surprisingly  $K_{\partial_z \theta}$  (see Fig. 1, bottom), as the vertical derivatives  $K_{\partial_z u}$  and  $K_{\partial_z v}$ , do not exhibit any definite trend. This can be understood as  $\partial_z \theta$  is dynamically bounded and cannot take arbitrarily large values. For  $\partial_z \theta \geq N$  buoyancy fluctuations reverse the background stratification, and the flow becomes unstable, developing local convection. Thus, as soon as  $\partial_z \theta \approx N$  the flow destabilizes, generating fast and strong large-scale drafts, and  $\partial_z \theta$  decreases again [22]. Indeed, neglecting viscous effects and with  $D_t$  the Lagrangian derivative,

$$D_t(\partial_z \theta) = (N - \partial_z \theta)(\partial_z w) - (\partial_x \theta)(\partial_z u) - (\partial_y \theta)(\partial_z v). \quad (4)$$

Strain in horizontal winds ( $\partial_z u$  and  $\partial_z v$ ) can change  $\partial_z \theta$ ,

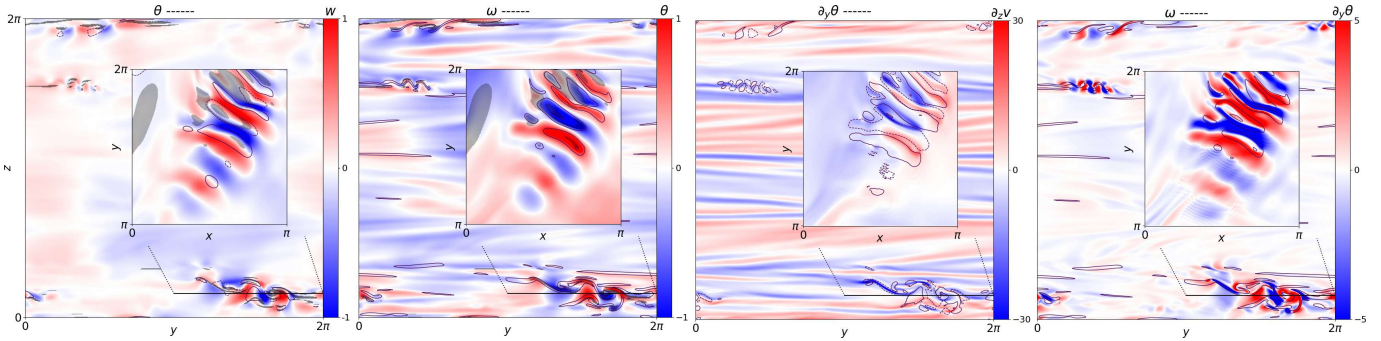


Figure 4: Vertical 2D slices (with the insets showing a horizontal slice of 1/4 of the domain at the region of the extreme event) for run 9. Correlations of  $\theta$  and  $w$ ,  $\omega = |\boldsymbol{\omega}|$  and  $\theta$ ,  $\partial_y \theta$  and  $\partial_z v$ , and  $\omega$  and  $\partial_y \theta$  are shown (the first quantity in colors, the second with contours). Contours are at  $\pm 3\sigma_\theta$  for  $\theta$ , and  $\pm 4\sigma$  for all other fields. Gray shaded areas indicate regions with  $\partial_z \theta > N$ .

but the first term on the r.h.s. tends to saturate  $\partial_z \theta$  as it approaches  $N$  [22], albeit for this value other gradients grow explosively as the local instability develops. Given the estimated values of the kurtosis, the PDFs of most gradient tensor elements cannot be Gaussian, as seen in Fig. 2 (right) for run 9. This is a universal feature in turbulent fluids, and a manifestation of small-scale intermittency, with or without stratification. But in this case, the large-scale intermittency and extreme events in  $w$  and  $\theta$  also enhance the extreme values of the field gradients, thus also enhancing small-scale intermittency. It is also worth noticing that the statistics of the horizontal velocities  $u$  and  $v$  are always Gaussian (or slightly sub-Gaussian) for all the DNSs in this study, pointing to the fact that the large-scale intermittent behavior of the sole vertical component of the velocity  $w$  (and/or of the buoyancy) is able to enhance small-scale intermittency, as seen from the spatial derivatives both of the velocity and of the buoyancy. What is then the origin of the large-scale extreme events, and the link between large-scale intermittent structures and classical small-scale intermittency?

Large-scale extreme events are generated through a buoyancy driven instability, which also connects large- and small-scale dynamics. The visualization in Fig. 4 (left) shows localized bursts of  $w$ , the vertical velocity component, and  $\theta$  (left), with an essentially periodic structure in the horizontal plane (inset), with a phase difference of  $\approx \pi/2$  between the two fields. Fig. 4 (center left) also reveals that intense values of  $\theta$  coincide with locations where vorticity,  $|\boldsymbol{\omega}|$ , is very strong. These structures can be understood as a result of an instability in the following terms. Vertically sheared horizontal winds (VSHWs) [23] are ubiquitous in the flow, as revealed by Fig. 4 (center right, with  $\partial_z v$  and  $\partial_y \theta$ ), appearing as horizontal streaks with strong values of  $\partial_z v$ . The resulting shear is prone to Kelvin-Helmholtz instabilities, which creates vertical modulations of the layers, and passively generate horizontal gradients of  $\theta$ . A nonlinear amplification of the vertical gradients results from the coupling with the velocity gradient, as readily seen from Eq. (4). The induced correlation between, e.g.,  $\partial_z v$  and  $\partial_y \theta$  is clearly seen in the inset of this figure. This mechanism may even lead to val-

ues of  $\partial_z \theta \geq N$ , therefore bringing heavier fluid on top of lighter one, resulting in the formation of intense up- and down-drafts, and to very strong vertical velocity fluctuations (indeed, extreme regions in Fig. 4 also coincide with regions with  $\partial_z \theta \geq N$ , as shown by the shaded regions in the first two insets). This process however saturates as the first term on the r.h.s. of Eq. (4) prevents  $\partial_z \theta$  from becoming too large (i.e., the background stratification opposes vertical gradients of  $\theta$ ). Also, from Eqs. (1,2), a fluid element going up (down) results in an increase (decrease) of  $\theta$  following the fluid element, opposing  $w$ , and thus large updrafts (downdrafts) tend to have a phase shift between  $w$  and  $\theta$ . These motions generate vorticity as  $D_t \boldsymbol{\omega} \approx -N(\partial_y \theta \hat{\mathbf{x}} - \partial_x \theta \hat{\mathbf{y}})$  (where viscous effects, forcing and vortex stretching were neglected), resulting in a correlation between  $|\boldsymbol{\omega}|$  and horizontal gradients of  $\theta$ , clearly seen in Fig. 4 (right, with  $|\boldsymbol{\omega}|$  and  $\partial_y \theta$ ). In turn, the generation of vorticity feeds the small-scale intermittency, giving the link between large-scale events and internal intermittency. This results in enhanced dissipation, as volumetric dissipation of kinetic energy is proportional to the enstrophy which depends on the spatial average of  $\omega^2$ . And this also explains the conspicuous absence of vortex filaments in stably stratified turbulence, despite their ubiquity in HIT. In these flows, vortex stretching is *not* the main mechanism producing vorticity (as shown, e.g., by the absence of the Vieillefosse tail [27] in diagrams of invariants of the field gradients [19,22]). Instead, generation of vorticity is the result of buoyancy, through a mechanism reminiscent of a large-scale local baroclinic instability.

Thus, large-scale extreme values feed stronger small-scale intermittency through the generation of vorticity. And also the small-scale intermittency can be the precursor of the large-scale extreme values of  $w$  and  $\theta$ , through the billows in the horizontal winds and the amplification of  $\partial_z \theta$ .

Indeed, this also provides an explanation for the decrease of large-scale intermittency for  $Fr < 0.04$ . As  $Fr$  decreases,  $N$  increases, and it becomes more difficult for points in the fluid to reach  $\partial_z \theta \approx N$ . The counterpart of this process in spectral space, and the coupling of these two types of intermittency, could be studied using tools as

those used in [24, 25] for HIT. Similarities in the behavior of  $K_{\partial_x u}$ ,  $K_{\partial_y v}$ , and  $K_{\partial_z w}$  (and in the kurtosis of the off-diagonal components of  $\partial_i u_j$ ) also suggest that the small scales of the large-scale drafts are in a more mixed state, and in some sense more isotropic (albeit this should not be confused with a recovery of isotropy as in HIT, as, e.g., the vertical velocity has extreme values while horizontal velocities do not, and passive scalars are known in some cases not to return, or to return very slowly, to isotropy), whereas regions outside these patches are less mixed and even more anisotropic. Such more mixed states enforce the connection between these patches and local instabilities.

Finally, this intermittent dynamics at large and small scales is modulated by different regimes explored by the flow, which can be viewed in terms of the relative strength of waves and turbulent motions as measured by  $R_B$  (see the labels in Fig. 1, indicating the range of  $R_B$  for the runs). All simulations with larger values of kurtosis have  $R_B \in [10, 200]$ . While several theoretical models of small-scale intermittency for the velocity field in HIT have been devised, the intermittency considered here couples multiple scales and combines such intermittency with large-scale bursts. It is thus not clear *a priori* how these models perform in geophysical applications or in the presence of waves. It was shown in [13] and in F18 that a simple one-dimensional model stemming from the original work of Vieillefosse [27], to which the wave terms were added, behaves remarkably well in reproducing the peak of the kurtosis of the vertical velocity (Fig. 1). There are also models that tackle the dynamics of the passive scalar. For example, in [26], the dispersion of turbulent plumes in a boundary layer is considered through a model which allows for a prediction of the PDF of the scalar density distribution (see also [28]). A generalization of such models to the Boussinesq framework was presented in [19, 22], and it would be of interest to further extend these models to properly capture the coupling of small-scale and large-scale intermittency in stratified flows.

**Discussion.** – The aim of the present study was to investigate the large-scale intermittency properties of the velocity and buoyancy fields in forced stably stratified turbulence, and to show its connection with the more classical small-scale (or internal) intermittency. To achieve this goal we exploited a large set of forced DNSs where solutions of the Boussinesq equations were analyzed using statistical tools; in particular, the large-scale intermittency of the velocity and buoyancy fields was evaluated by means of their fourth-order distribution moments (or kurtosis), while the small-scale intermittency was quantified through the kurtosis of field gradients.

Our analysis shows that the buoyancy field  $\theta$  (proportional to potential temperature variations) is intermittent at large scales with its kurtosis following the same non-monotonic trend with Froude number as the kurtosis of the vertical component of the velocity  $w$ . Thus, well-defined peaks of the kurtosis of both  $w$  and  $\theta$  appear for

$Fr \approx 0.07 - 0.1$ , with values significantly larger than the Gaussian reference of 3, indicating the emergence of bursts of both quantities in stratified turbulence. From the analysis in Fig. 3 we conclude that the extreme events responsible for this large-scale intermittent behavior in stratified flows can take place at any height and are uniformly distributed along the direction of stratification for long-enough DNS integration times.

Moreover, we showed that small-scale intermittency (i.e., in field gradients) is enhanced in the same range of  $Fr$  as large-scale intermittency, with the peaks of their kurtosis occurring for  $Fr \approx 0.07 - 0.1$ , and that in individual simulations their extreme values takes place at the same spatial locations as the large-scale patches. We also provided a mechanism for the generation of the large-scale events through the growth of billows in the winds, the amplification of vertical buoyancy gradients through strain, the development of overturning, and the generation of vorticity through baroclinicity which feeds the small scales. This mechanism is consistent with the exact equations for the evolution of the field gradients. Thus, we showed the connection between large-scale extreme events, and small-scale intermittency in the fields  $\partial_x u$ ,  $\partial_y v$ ,  $\partial_z w$ , the vorticity, and other off-diagonal elements of the velocity gradient, as well as in  $\partial_x \theta$  and  $\partial_y \theta$ .

Beyond the specific objectives of this study, weather and climate codes in use today require sophisticated modeling through parameterizations of the unresolved small scales. Unraveling the link between small-scale intermittency and large-scale enhancement of vertical velocity and buoyancy is an important element to incorporate in sub-grid models of geophysical flows, and that raise questions for future studies. For example, can these strong vertical shear layers in stratified turbulence (including in the presence of rotation [21]) be modeled adequately with the sub-grid parameterization developed for plane-channel flows, e.g., in [29], improving on the classical Smagorinsky eddy-viscosity? The fact that the rapid intensification phase of a hurricane is best predicted by following vertical velocity enhancements leads to think that the small-scale and large-scale connection through intermittency is also a factor to be taken into consideration in such models. This might also allow for a more detailed understanding of the interplay between the intermittency observed in some cases in the ocean or in the atmosphere far from the atmospheric or oceanic boundary layers, and the high skewness and kurtosis found in recent oceanic simulations [4]. For the atmosphere, based on the range of Froude numbers for which strong events develop, typical scales are of the order of 100 km, while in the ocean the scale is of 10 km. We conclude by stressing that the significance of extreme events in the atmosphere goes well beyond the scales considered here [30].

\*\*\*

*R. Marino acknowledges support from the project*

“EVENTFUL” (ANR-20-CE30-0011), funded by the French “Agence Nationale de la Recherche” - ANR through the program AAPG-2020, and IRP IVMF (CNRS and CONICET). Numerical simulations were done on the cluster “Newton” of the High Performance Computing Center of the University of Calabria, supported by EU FP7 2007-13 through the MATERIA Project (PONA3\_00370) and EU Horizon 2020 through the STAR\_2 Project (PON R&I 2014-20, PIR01\_00008). AP is thankful to LASP and Bob Ergun.

## References

- [1] FRISCH U., Fully developed turbulence and intermittency. *Annals New York Acad. Sci.* **1980**, 357, 359.
- [2] FRITTS D.C. and WANG L., Gravity wave-fine structure interactions. Part I: Influences of fine structure form and orientation on flow evolution and instability. *J. Geophys. Res.* **2013**, 70, 3735.
- [3] VAN HAREN H., CIMATORIBUS A. and GOSTIAUX L., Where large deep-ocean waves break. *Geophys. Res. Lett.*, **2015**, 42, 2351– 2357.
- [4] PEARSON B. and FOX-KEMPER B., Log-normal turbulence dissipation in global ocean models. *Phys. Rev. Lett.* **2018**, 120, 094501.
- [5] KOLMOGOROV A.N., A refinement of previous hypotheses concerning the local structure of turbulence in a viscous incompressible fluid at high Reynolds number. *J. Fluid Mech.* **1962**, 13, 82.
- [6] SHE Z-S. and LÉVÊQUE E., Universal scaling laws in fully developed turbulence. *Phys. Rev. Lett.* **1994**, 72, 336.
- [7] TOSCHI F., LÉVÊQUE E. AND RUIZ-CHAVARRIA G., Shear Effects in Nonhomogeneous Turbulence. *Phys. Rev. Lett.* **2000**, 85, 1436.
- [8] MAHRT L., Intermittency of atmospheric turbulence. *J. Atmosph. Sci.* **1989**, 46, 79.
- [9] BRAMBERGER M., DÖRNBRACK A., WILMS H., EWALD F., AND SHARMAN, R., Mountain-Wave Turbulence Encounter of the Research Aircraft HALO above Iceland. *Journal of Applied Meteorology and Climatology* **2020**, 59, 567.
- [10] LYU R., HU F., LIU L., XU J. and CHENG X., High-order statistics of temperature fluctuations in an unstable atmospheric surface layer over grassland. *Advances in Atmospheric Sciences* **2018**, 35, 1265.
- [11] CHAU J.L., STOBBER G., HALL C.M., TSUTSUMI M., LASKAR F.I. and HOFFMANN P., Polar mesospheric horizontal divergence and relative vorticity measurements using multiple specular meteor radars. *Radio Science* **2017**, 52, 811.
- [12] D’ASARO E., LIEN R. and HENYEFY F., High-Frequency internal waves on the Oregon continental shelf. *J. of Phys. Oceanogr.* **2011**, 332, 318.
- [13] RORAI C., MININNI P.D. and POUQUET A., Turbulence comes in bursts in stably stratified flows. *Phys. Rev. E* **2014**, 89, 043002.
- [14] FERACO F., MARINO R., PUMIR A., PRIMAVERA L., MININNI P.D., POUQUET A. and ROSENBERG D., Vertical drafts and mixing in stratified turbulence: Sharp transition with Froude number. *Eur. Phys. Lett.* **2018**, 123, 44002.
- [15] D. BUARIA, A. PUMIR, F. FERACO, R. MARINO, A. POUQUET, D. ROSENBERG, and L. PRIMAVERA, Single-particle Lagrangian statistics from direct numerical simulations of rotating-stratified turbulence. *Phys. Rev. Fluids* **2020**, 5, 064801.
- [16] CAPET X., MCWILLIAMS J.C., MOLEMAKER M.J. and SHCHEPETKIN A.F., Mesoscale to submesoscale transition in the California current system. Part I: flow structure, eddy flux, and observational tests. *J. Phys. Oceanogr.* **2008**, 38, 29.
- [17] FONTANA M., BRUNO P.O., MININNI P.D. and DMITRUK P., Fourier continuation method for incompressible fluids with boundaries. *Computer Physics Communications* **2020**, 256, 107482.
- [18] ROSENBERG D., MININNI P.D., REDDY R. and POUQUET, A., GPU Parallelization of a Hybrid Pseudospectral Geophysical Turbulence Framework Using CUDA. *Atmosphere* **2020**, 11, 00178.
- [19] SUJOVOLSKY N.E. and MININNI P.D., Invariant manifolds in stratified turbulence. *Phys. Rev. Fluids* **2019** 4,052402.
- [20] MARINO R., MININNI P.D., ROSENBERG D., POUQUET A., Large-scale anisotropy in stably stratified rotating flows. *Phys. Rev. E*, **2014**, 90, 023018.
- [21] POUQUET A., ROSENBERG D. and MARINO, R., Linking dissipation, anisotropy and intermittency in rotating stratified turbulence. *Phys. Fluids* **2019**, 31, 105116.
- [22] SUJOVOLSKY, N.E. and MININNI, P.D., From waves to convection and back again: The phase space of stably stratified turbulence, *Phys. Rev. Fluids*, **2020**, 5, 064802.
- [23] FITZGERALD J. G. and FARRELL B. F., Vertically Sheared Horizontal Flow-Forming Instability in Stratified Turbulence: Analytical Linear Stability Analysis of Statistical State Dynamics Equilibria, *Journal of the Atmospheric Sciences*, **2018**, 75(12), 4201-4227.
- [24] ALEXAKIS A., MININNI P.D. and POUQUET A., Imprint of large-scale flows on Navier-Stokes turbulence. *Phys. Rev. Lett.* **2005**, 95, 264503.
- [25] MININNI P.D., ALEXAKIS A. and POUQUET A., Nonlocal interactions in hydrodynamic turbulence at high Reynolds numbers: The slow emergence of scaling laws. *Phys. Rev. E* **2008**, 77, 036306.
- [26] MARRO M., SALIZZONI P., SOULHAC, L. and CASSIANI, M., Dispersion of a Passive Scalar Fluctuating Plume in a Turbulent Boundary Layer. Part III: Stochastic Modelling. *Bound. Layer Met.* **2018**, 167, 349.
- [27] VIEILLEFOSSE P., *Physica A* **125** (1984) 150.
- [28] BERTAGNI, M.B., MARRO, M., SALIZZONI, P. and CAMPOREALE, C., Solution for the statistical moments of scalar turbulence. *Phys. Rev. Fluids* **2019**, 4, 124701.
- [29] LÉVÊQUE, E., TOSCHI, F., SHAO, L. and BERTOGLIO, J.-P., Shear-improved Smagorinsky model for large-eddy simulation of wall-bounded turbulent flows. *J. Fluid Mech.* **2007**, 570, 491.
- [30] RAHMSTORF, S. and COUMOU, D., Increase of extreme events in a warming world. *PNAS* **2011**, 108, 17905-17906.

# Turbulence generation by large-scale extreme vertical drafts and the modulation of local energy dissipation in stably stratified geophysical flows

Raffaele Marino,<sup>1</sup> Fabio Feraco,<sup>1,2</sup> Leonardo Primavera,<sup>2</sup> Alain Pumir,<sup>3</sup> Annick Pouquet,<sup>4</sup> Duane Rosenberg,<sup>5</sup> and Pablo D. Mininni<sup>6</sup>

<sup>1</sup>*Laboratoire de Mécanique des Fluides et d'Acoustique, CNRS, École Centrale de Lyon, Université Claude Bernard Lyon 1, INSA de Lyon, F-69134 Écully, France.*

<sup>2</sup>*Dipartimento di Fisica, Università della Calabria, Italy.*

<sup>3</sup>*Laboratoire de Physique, UMR5672, École Normale Supérieure de Lyon and CNRS, 46 Allée d'Italie, F-69007, Lyon, France.*

<sup>4</sup>*Laboratory for Atmospheric and Space Physics, University of Colorado, Boulder, CO 80309, USA.*

<sup>5</sup>*288 Harper St. Louisville, CO 80027 USA.*

<sup>6</sup>*Departamento de Física, Facultad de Ciencias Exactas y Naturales, Universidad de Buenos Aires, and IFIBA, CONICET, Buenos Aires 1428, Argentina.*

We observe the emergence of strong vertical drafts in direct numerical simulations of the Boussinesq equations in a range of parameters of geophysical interest. These structures, which appear intermittently in space and time, generate turbulence and enhance kinetic and potential energy dissipation, providing a possible explanation for the observed variability of the local energy dissipation in the bulk of oceanic flows, and the modulation of its probability distribution function. We show how, due to the extreme drafts, in runs with Froude numbers observable in geophysical scenarios, roughly 10% of the domain flow can account for up to 50% of the global volume dissipation, reminiscent of estimates based on oceanic models.

## I. INTRODUCTION

The combination of turbulent eddies and waves, due to stratification and rotation, leads to the formation of surprising features in geophysical flows, from oval structures and jets on Jupiter [1], to hurricanes and tornadoes in our atmosphere [2], or strong currents and dual energy cascades in the ocean [3–14]. The interplay between such structures is not fully understood, in particular their dependence on control parameters such as the Reynolds and Froude numbers [15–18] (see definitions below). But it is known that extreme events associated with these structures can play an important role in the dynamics and dissipation. For example, sudden and significant enhancements of the vertical velocity (hereafter “drafts”) have been observed in geophysical flows, in the planetary boundary layer [19–21], as well as far from boundaries in the mesosphere and lower thermosphere (MLT) [22, 23] and in the ocean at depths close to that of the mixed layer [24]. Moreover, in the ocean, vast regions of rather constant energy dissipation  $\varepsilon_0$  are observed together with local patches of turbulence dissipating  $10^2\varepsilon_0$  to  $10^4\varepsilon_0$ , as in the vicinity of the Hawaiian ridge [4] or of the Puerto-Rico trench [25], with large values of the vertical velocity [24, 26]. Similarly, in frontal structures, gradients of tracers such as pollutants are characterized by very large fluctuations, with



a kurtosis (the normalized fourth moment of the distribution) reaching values of several hundreds [27]. All these extreme events are characterized by non-Gaussian statistics.

The occurrence of many of these extreme events is associated with turbulence. Unexpectedly, early seminal studies of stratified flows [28–31] revealed that stably stratified turbulence, as found, e.g., at intermediate scales in the nocturnal atmosphere and in the oceans, is more complex than quasi-geostrophic dynamics and very different from homogeneous and isotropic turbulence (HIT). This is evidenced, e.g., by the formation of anisotropic horizontal structures and their effect on turbulent transport [32, 33], or by the complex structure of the spectra, characterizing the kinetic and potential energy of the flow [8, 34, 35]. Stably stratified turbulence is also dependent on the Reynolds number [36], the possible flow regimes being controlled by the product of the Reynolds and the squared Froude number [37], the so-called buoyancy Reynolds number (see [38] for a review, and for an alternate definition to the one used in this work). These results led to the emergence of a physical picture for strongly stratified turbulence, in which an anisotropic and forward energy cascade is associated with highly anisotropic vortical structures, and with the development of breakdown events on small scales where the flow becomes super-critical, feeding into local patches of more isotropic dynamics (see, e.g., [34, 39–41]). Concerning extreme events, it is known that stably stratified turbulence displays intermittency [42–46], but only recently it was found that the amount of large-scale intermittency (to distinguish it from the classical small-scale intermittency considered in several studies [43]) depends sharply on the Froude number, with some regimes being in fact more intermittent than HIT, and displaying extreme values of the large-scale vertical flow velocity [42, 44, 46], as also observed for example in reanalysis of climate data [47, 48]. These latter events are of a different nature than the small-scale extreme events, as they involve directly the velocity instead of velocity gradients. However, their effect on the energy dissipation, and how these extreme vertical drafts interact with and affect the turbulence, remain unclear.

Recent numerical work based on the Boussinesq equations has confirmed that the vertical component of the velocity field ( $w$ ) indeed exhibits a large-scale intermittent behavior, in both space and time, for values of Froude numbers of geophysical interest [44], with a connection existing between large- and small-scale intermittency in stratified turbulent flows [46]. In particular, direct numerical simulations (DNSs) of stably stratified turbulent flows were found to systematically develop powerful vertical drafts that make the statistics of  $w$  strongly non-Gaussian in the energy-containing eddies. This is interpreted as a result of the interplay between gravity waves and turbulent motions, and it occurs in a resonant regime of the governing parameters where vertical velocities are enhanced much faster than in the analogous HIT case [42, 44, 46]. It can also be understood as a result of complex phase-space dynamics in a reduced model for the velocity and temperature gradients [49]. The present study establishes that extreme drafts emerge in a recurrent manner in stratified flows, producing localized turbulence, and ultimately bursts of dissipation at small-scale, as observed for example in oceanic data and DNSs [50] (see also [45]).

## II. SIMULATIONS AND PARAMETERS

We performed a series of DNSs in a triply-periodic domain of side  $2\pi L_0$  with  $512^3$  grid points for up to  $t \approx 500\tau_{NL}$  ( $\tau_{NL} = L/U$  being the turnover time,  $U$  and  $L$  the flow characteristic velocity and integral scale respectively in units of a simulation unit length  $L_0$  and a unit velocity  $U_0$  with  $T_0 = L_0/U_0$ ). In these units, in all the simulations considered

below, the velocity  $u$  is  $U \approx 1$  to 1.5, and the flow integral scale is  $L \approx 2\pi/\bar{k}_f \approx 2.5$  in all cases, with  $\bar{k}_f$  the mean forced wavenumber; for practical purposes the typical velocity  $U$  and length  $L$  can be considered  $\mathcal{O}(1)$ . Some of these flows were analyzed in [44] over a limited time span (up to  $\approx 25\tau_{NL}$ ), while other simulations analyzed herein are new. It was shown in [44, 46] that the kurtosis of  $w$  could reach high values in a narrow regime of parameters around a Froude number  $\text{Fr} = U/(LN) \approx 0.08$ , with  $N = [-(g/\rho_0)\partial_z\bar{\rho}]^{1/2}$  the Brunt-Väisälä frequency,  $g$  the gravitational acceleration,  $\rho_0$  the mean density, and  $\bar{\rho}$  the background linear density profile. Simulation parameters are listed in Table I. Runs P3 to P5, with  $5 \leq NT_0 \leq 8$ , correspond to the resonant regime mentioned above. In all the simulations with  $N \neq 0$ ,  $NT_0$  varies from 1.5 to 23.5. As a reference, a typical velocity in the ocean of  $U_0 = 0.1 \text{ ms}^{-1}$ , and a unit length of 1 km (thus for a computational domain of  $\approx 6.3$  km), results in  $N \approx 2 \times 10^{-3} \text{ s}^{-1}$  (for run P7) to  $N \approx 10^{-4} \text{ s}^{-1}$  (for run P2). These values are reasonable for oceanic scales and situations in which the hydrostatic approximation breaks down [51].

The Boussinesq equations for the velocity  $\mathbf{u}$  and the density fluctuation  $\rho'$  around the stable linear background are

$$\partial_t \mathbf{u} + (\mathbf{u} \cdot \nabla) \mathbf{u} = -\nabla(p/\rho_0) - (g/\rho_0)\rho' \hat{z} + \mathbf{F}_u + \nu \nabla^2 \mathbf{u}, \quad (1)$$

$$\partial_t \rho' + \mathbf{u} \cdot \nabla \rho' = (\rho_0 N^2/g)w + \kappa \nabla^2 \rho', \quad (2)$$

where  $\kappa$  is the thermal diffusivity and  $\nu$  the kinematic viscosity, with  $\kappa = \nu$  for all runs. Both values, in units of  $L_0 U_0$  in Table I, are not realistic for geophysical flows and come as a result of computational constraints, and should thus be considered as effective transport coefficients. In spite of this, in the simulations presented here, turbulence is strong enough for the typical nonlinear dynamics observed in the atmosphere and in the oceans to develop. We take the convention that the vertical coordinate,  $z$ , points upwards, and gravity downwards. The total fluid density is  $\rho = \bar{\rho}(z) + \rho'$ , with  $\langle \rho' \rangle = 0$ , and uniform  $\partial_z \bar{\rho} < 0$ , expressing that the background density decreases linearly with  $z$  ( $\langle \bar{\rho}(z) \rangle = \rho_0$ ). These equations can also be written using a scaled density fluctuation  $\zeta = g\rho'/(N\rho_0)$ , with units of velocity  $U_0$ , as

$$\partial_t \mathbf{u} + (\mathbf{u} \cdot \nabla) \mathbf{u} = -\nabla p' - N\zeta \hat{z} + \mathbf{F}_u + \nu \nabla^2 \mathbf{u}, \quad (3)$$

$$\partial_t \zeta + \mathbf{u} \cdot \nabla \zeta = Nw + \kappa \nabla^2 \zeta, \quad (4)$$

where  $p' = p/\rho_0$ . This latter form is convenient as the kinetic and potential energy (per unit mean density  $\rho_0$ ) are then given respectively by  $E_V = \int u^2/2 dV$  and  $E_P = \int \zeta^2/2 dV$ .

The Reynolds and buoyancy Reynolds numbers are  $\text{Re} = UL/\nu$  and  $\text{R}_B = \text{Re} \text{Fr}^2$ .  $\text{R}_B$  is a measure of the relative strength of the buoyancy to the dissipation, and allows for the identification of three regimes: one controlled by gravity waves ( $\text{R}_B \leq 10$ ), a transitional regime, and another dominated by turbulence ( $\text{R}_B \geq 10^2$ ) [16, 37, 44].  $\text{Fr}$ ,  $\text{Re}$ , and  $\text{R}_B$  are computed for each run close to the peak of dissipation. A HIT run is also performed. The flows evolve under the action of a random forcing  $\mathbf{F}_u$ , with constant amplitude, delta-correlated in time, isotropic in Fourier space, and centered on a spherical shell of wavenumbers  $2 \leq k_f L_0 \leq 3$ . Simulations were performed with the GHOST code (Geophysical High Order Suite for Turbulence), a highly parallelized pseudo-spectral framework that hosts a variety of solvers [52–54] to study anisotropic classic and quantum fluids, as well as plasmas.

Run	P1	P2	P3	P4	P5	P6	P7	P8	P9
Re [ $\times 10^3$ ]	2.4	2.6	3.6	3.8	3.8	3.8	3.8	1.2	0.8
Fr [ $\times 10^{-1}$ ]	$\infty$	2.8	1.1	0.81	0.76	0.3	0.26	0.76	0.71
$R_B$	$\infty$	206	43.8	24.8	22.1	3.4	2.6	6.8	4.2
$\nu[\times 10^{-3}L_0U_0]$	1.5	1	1	1	1	1	1	3	4
$N [U_0/L_0]$	0	1.5	5	7.37	8	20	23.5	7.37	7.37
$U [U_0]$	1.4	1.0	1.4	1.5	1.5	1.5	1.5	1.4	1.3
$t_{tot}/\tau_{NL}$	30	55	103	452	406	91	62	526	422

TABLE I. Parameters of the runs, with Re, Fr, and  $R_B$  respectively the Reynolds, Froude, and buoyancy Reynolds numbers, and  $\nu$ ,  $N$ ,  $U$ , and  $t_{tot}/\tau_{NL}$  the kinematic viscosity, the Brunt-Väisälä frequency, the flow typical (r.m.s.) velocity, and the temporal extension of the runs in units of  $\tau_{NL}$ . In all runs  $L \approx 2.5L_0$ , and  $\tau_{NL} = L/U$ .

### III. GENERATION OF TURBULENCE BY EXTREME VERTICAL DRAFTS

The operative definition as well as the identification of the drafts in the DNSs performed in this study are obtained in terms of the statistical moments of the vertical components of the Eulerian velocity  $w$ . Specifically, we consider as drafts regions where the vertical velocity ( $w$ ) is significantly larger than 3 standard deviations ( $\sigma_w$ ). The presence of the drafts in the simulations is then confirmed through the analysis of the temporal evolution of the kurtosis of the vertical velocity,  $K_w = \langle (w - \langle w \rangle)^4 \rangle / \langle (w - \langle w \rangle)^2 \rangle^2$ , computed as a function of time from the DNSs. We recall that the kurtosis of a Gaussian distribution is  $K = 3$ , so values of  $K_w > 3$  are indicative of the presence of extreme events in  $w$ . Fig. 1 displays  $K_w$  vs.  $t/\tau_{NL}$  for runs P4, P5, P8, and P9. The Froude number for these runs is close to  $Fr \approx 0.08$ , for which  $K_w$  was found to be maximum from calculations at  $Re \approx 3800$  in [44]. It is worth mentioning that the values of Fr and  $R_B$  of the main DNSs considered in this study are compatible with estimates of these parameters for some regions of the atmosphere and of quiet parts of the ocean interior. To characterize how these extreme drafts affect the flow energetics, we accumulate the statistics for several hundreds  $\tau_{NL}$  (see Table I). Together with the investigation of this global quantity, our study will later consider statistical tools which are more local, either in Fourier or in physical space.

Starting from the top panel of Fig. 1 we observe that, for  $N = 8.0U_0/L_0$ , the flow is characterized by strong spikes of the kurtosis reaching values as high as  $K_w \approx 11$ , and separated by short time intervals with values of  $K_w$  close to the Gaussian reference. The temporal analysis of the high-order spatial statistics allows us to conclude that in the presence of large-scale intermittent drafts not only the flow is non-homogeneous due to the irregular emergence of these structures, but furthermore, global properties of the flow exhibit wide fluctuations. A similar situation has been observed in other flows, such as turbulent homogeneous shear flows [55, 56]. The fluctuations of  $K_w$  are smaller for  $N = 7.37U_0/L_0$  (Fig. 1, middle panel), which is still close to  $Fr \approx 0.08$  and also appears to show fluctuations of large scale quantities. Keeping  $N = 7.37U_0/L_0$  but lowering the Reynolds number to  $Re \approx 1200$  changes drastically the dependence of  $K_w$  on  $t/\tau_{NL}$ : it becomes a smooth signal interrupted by sporadic bursts. The signal is almost completely smooth and stationary for  $Re \approx 800$  (Fig. 1, bottom panel). Since Fr for the three runs in Fig. 1 is roughly the same,

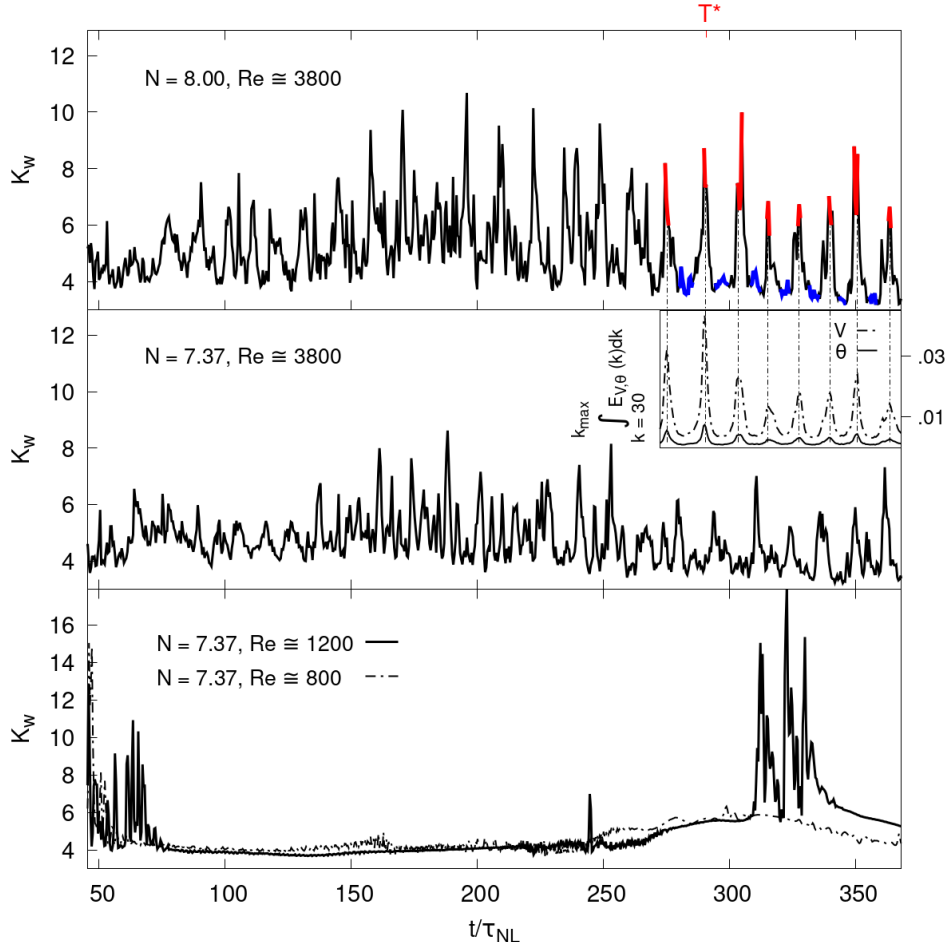


FIG. 1. Kurtosis  $K_w$  of the vertical velocity  $w$  as a function of time, in units of the turn-over time  $\tau_{NL}$ , for runs  $P5$  (top panel),  $P4$  (middle panel), as well as (bottom panel)  $P8$  (solid line) and  $P9$  (dashed line). Red and blue identify respectively the portions of the signal across relative maxima and minima used to compute the spectra in Fig. 2.  $T^* \approx 290\tau_{NL}$  is the reference time used in Figs. 3. The inset in the middle panel shows the small-scale kinetic (V) and potential (P) energies at late times for run  $P5$ , obtained through the integration of the corresponding spectra from  $k = 30$  to  $k_{max} \simeq 512/3$ .

this transition appears therefore to be led by the buoyancy Reynolds number  $R_B$ .

To investigate how strong vertical drafts affect the generation of turbulence, we performed a systematic study of the isotropic kinetic and potential energy spectra, respectively  $E_V(k)$  and  $E_P(k)$ . The results indicate a substantial enhancement of the power spectral density (PSD) in the small scales when  $K_w$  is maximal. This can be clearly inferred from the spectra computed at local maxima and minima of the kurtosis  $K_w$ , as shown in Fig. 2 for run  $P5$  (corresponding to times highlighted in red and blue in Fig. 1). Note that these spectra correspond to the same flow, thus to a run with the same global parameters, but at different times. The small-scale PSD of  $E_V(k)$  and  $E_P(k)$  computed at the local maxima can be up to four orders of magnitude larger than the corresponding PSD for neighboring local minima (see Fig. 2). This indicates that vertical drafts excite small-scale turbulent

structures, developing in patches within the flow, and powerful enough to modify the spectral distribution of the energy, plausibly with a  $k^{-5/3}$  dependence over an inertial range of scales at the times when  $K_w$  peaks (see insets in Fig. 2). Conversely, the energy spectra computed at the local minima are much lower for  $k > 10$ , and in fact steeper, plausibly with a  $k^{-2}$  scaling at intermediate scales. The integral of  $E_V(k)$  and  $E_P(k)$  for  $k > 30$ , act as proxies respectively of the small-scale kinetic and potential energy; they are shown in the inset of Fig. 1. Their correlation with the local maxima and minima of  $K_w$  confirms that enhancements of the small-scale PSD are modulated by the extreme vertical drafts.

#### IV. MODULATION OF KINETIC ENERGY DISSIPATION

A study of the statistics of the kinetic and potential energy dissipation rates (respectively  $\varepsilon_V = \nu(\partial u_i/\partial x_j)(\partial u_i/\partial x_j)$  and  $\varepsilon_P = \kappa|\nabla\zeta|^2$ ) reveals that the extreme vertical drafts strongly feedback on  $\varepsilon_V$  and  $\varepsilon_P$ , and play a major role in the way the energy is dissipated in stratified turbulence. Fig. 3 shows the instantaneous vertical profile of the kurtosis  $K_w(z, T^*)$  (i.e., averaged over horizontal planes of constant height) in run P5, at time  $T^* \approx 290\tau_{NL}$ , when  $K_w(T^*)$  is at a maximum (see Fig. 1). The figure also shows the vertical profile of the kinetic energy dissipation rate  $\hat{\varepsilon}_V(z, T^*)$  achieved in horizontal planes, normalized by its value in the entire volume (so that  $\int_0^{2\pi} \hat{\varepsilon}_V(z, T^*) dz = 1$ ), and the probability density functions (PDFs) of  $\hat{\varepsilon}_V$  in regions at different heights. A comparison between the profiles of  $K_w$  and  $\hat{\varepsilon}_V$  reveals some correlation between their peaks (Fig. 3, right). The PDFs for

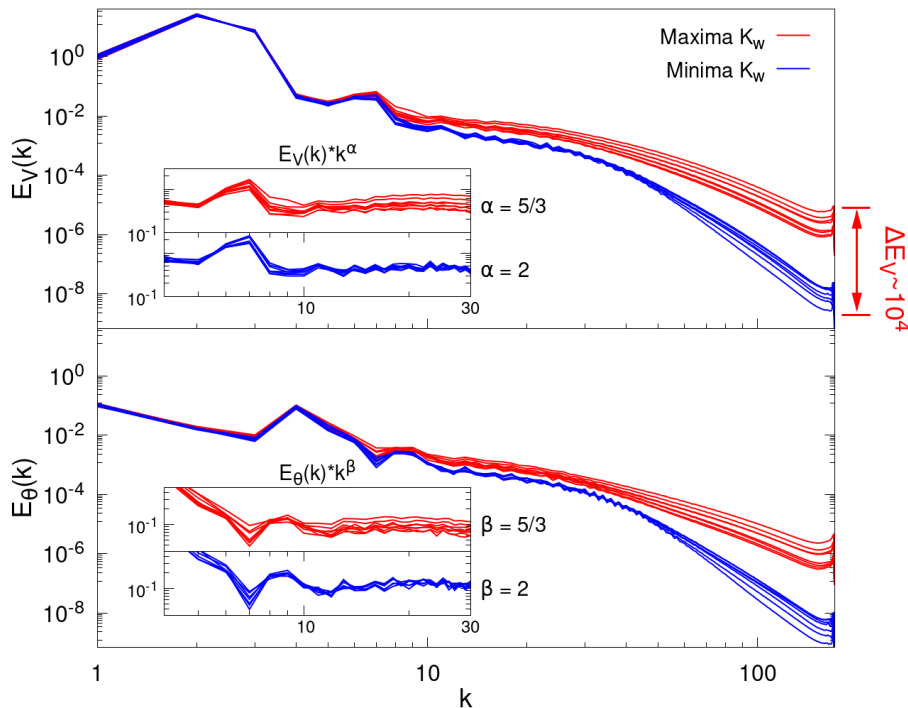


FIG. 2. Kinetic (top) and potential (bottom) energy spectra computed for run P5 at the relative maxima (red) and minima (blue) of  $K_w$  (see Fig. 1). Insets show  $\alpha$  or  $\beta$ -compensated spectra respectively for  $E_V$  or  $E_P$ , with  $\alpha, \beta$  either  $5/3$  or  $2$ .

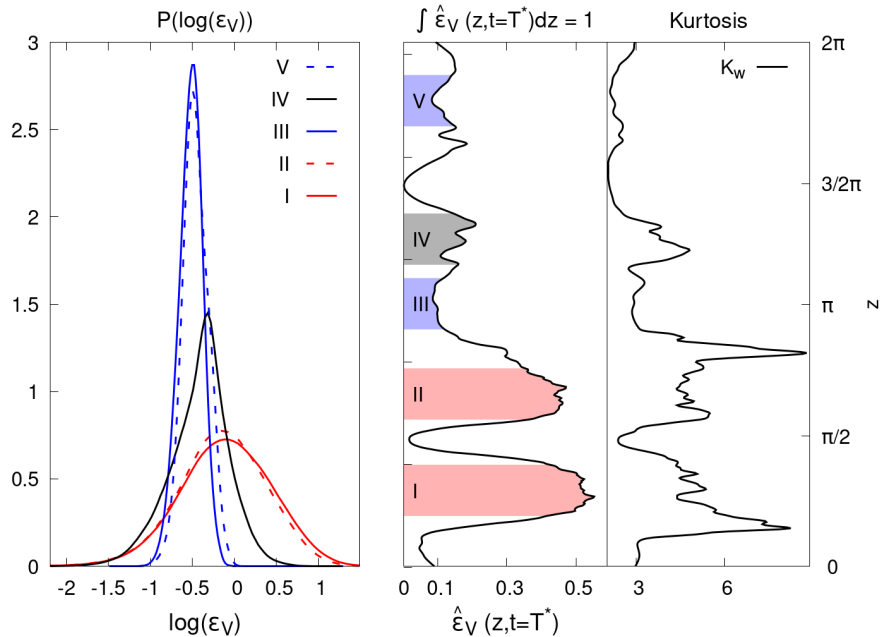


FIG. 3. Left: PDFs of the kinetic energy dissipation computed in the regions indicated by the shaded areas in the middle panel, for run P5. Middle: profile of the normalized kinetic energy dissipation  $\hat{\epsilon}_V(z, t)$  in individual horizontal planes, at fixed time  $T^* \approx 290\tau_{NL}$  (see Fig. 1), and as a function of  $z$ . Right: vertical profile of the by-plane kurtosis  $K_w(z, t)$ .

regions with strong (I, II), moderate (IV) and weak (III, V) local dissipation show that the statistical distribution of the kinetic energy dissipation is modulated by the presence of extreme vertical drafts (Fig. 3, left). Indeed  $P[\log(\epsilon_V)]$  is similar between regions with comparable values of  $K_w$ .

In the top and middle panels, Fig. 4 provides the vertical profiles of the by-plane kurtosis  $K_w(z, t)$  and of the normalized kinetic energy dissipation  $\hat{\epsilon}_V(z, t)$ , as a function of time (around  $T^*$ ) for run P5. These visualizations emphasize the spatial correlation along the vertical axis  $z$  between the emergence of drafts (detected through the amplitude of the kurtosis) and the enhancement of the kinetic energy dissipation, as well as the temporal correlation between these two phenomena. The large peaks of dissipation occur in the same layer of the flow immediately after strong vertical drafts develop. Although the small temporal shift cannot be appreciated from the visualized signals, its existence is demonstrated in the bottom panel of Fig. 4, that shows how the (point-wise) values of the quantities rendered in the top-mid panels are maximally correlated for a time delay of  $\phi \approx \tau_{NL}/3$ , as it results from the analysis of the distance correlation coefficient  $dCor_{XY}$ , defined next. The latter measures both linear and nonlinear correlations between  $X = K_w(z, t)$  and  $Y = \hat{\epsilon}_V(z, t + \phi)$ , for different temporal shifts  $\phi$  (shown in the inset in the bottom panel of Fig. 4):

$$dCor_{XY} = \frac{\mu_{XY}}{(\mu_{XX}^2 \mu_{YY}^2)^{1/4}}, \quad (5)$$

where  $\mu_{XY}$ ,  $\mu_{XX}$  and  $\mu_{YY}$  are correlation and autocorrelation functions defined as in [57, 58]. It is worth noticing that the overall distance correlation is always rather high, even for  $\phi = 0$ . Finally, the joint PDF of  $K_w(z, t)$  and of  $\hat{\epsilon}_V(z, t)$  for all times and heights available for P5 is

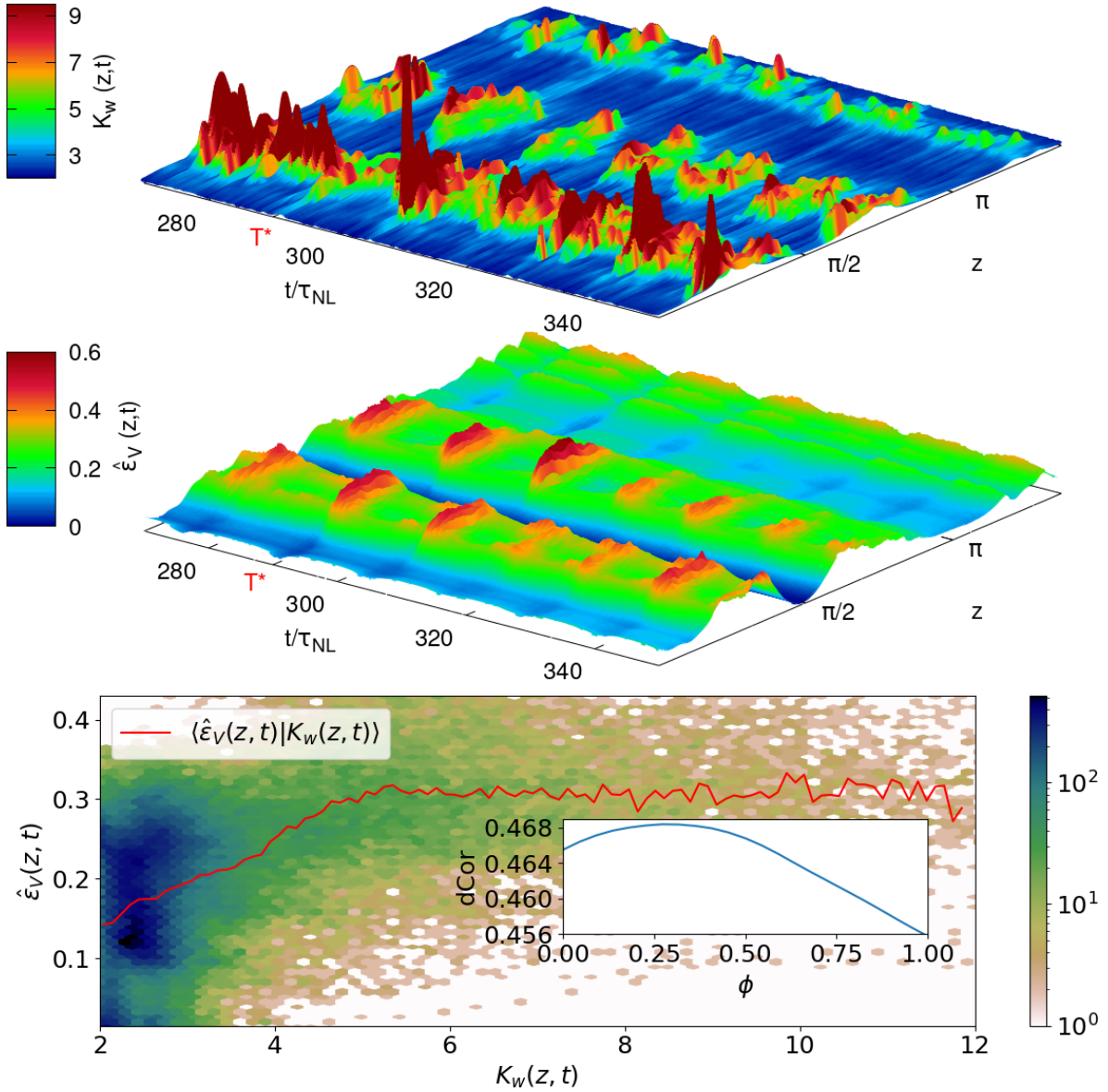


FIG. 4. Temporal evolution in units of  $\tau_{NL}$  for run *P5* of (top) the vertical profile of the by-plane kurtosis  $K_w(z,t)$ , and (mid-top) the normalized kinetic energy dissipated in horizontal planes  $\hat{\varepsilon}_V(z,t)$ . The bottom panel gives the joint PDF of  $K_w(z,t)$  and  $\hat{\varepsilon}_V(z,t)$  for all *P5* data, the solid red line indicating averages of  $\hat{\varepsilon}_V$  conditioned on  $K_w$ . Inset: evolution of the distance correlation coefficient  $dCor$  between  $K_w(z,t)$  and  $\hat{\varepsilon}_V(z,t+\phi)$ , as a function of a temporal lag  $\phi$  between the two signals. Note that the highest correlation obtains for  $\phi \approx \tau_{NL}/3$  (not for  $\phi = 0$ ), thus indicating causation.

shown in the bottom panel of Fig. 4, together with the conditional average of the dissipation in bins of the kurtosis,  $\langle \hat{\varepsilon}_V(z,t) | K_w(z,t) \rangle$  (red line). Note that, locally in space and time, larger values of  $K_w$  correspond to larger dissipation rates up to  $K_w \approx 6$ , while for  $K_w > 6$   $\hat{\varepsilon}_V(z,t)$  saturates, these high  $K_w$  regions being very efficient at dissipating kinetic energy. The good correlation resulting from the above statistics, together with the evidence that local

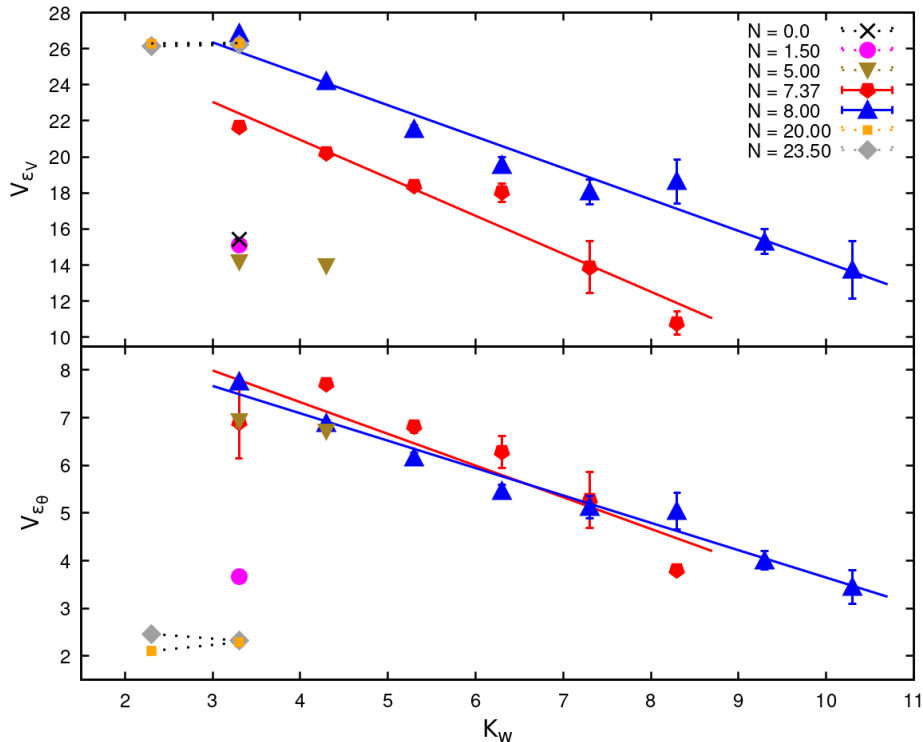


FIG. 5. Kinetic and potential energy dissipation efficiency as a function of  $K_w$  (for high-Re runs P1–P7), measured in terms of the minimal domain volume percentage  $V_{\epsilon_V}$  (%) and  $V_{\epsilon_P}$  (%) needed to achieve 50% of respectively the global kinetic and potential energy dissipation.

maxima of  $\hat{\epsilon}_V(z, t)$  are anticipated by peaks in  $K_w(z, t)$  – the latter occurring  $\sim \tau_{NL}/3$  earlier than the former in run P5 – indicate a causation between the emergence of vertical drafts and the enhancement of the dissipation. Similar results are obtained for other simulations (not shown). Overall, these evidences indicate that the local occurrence of extreme drafts determines the local properties and statistics of strong dissipative events. An analysis of the time evolution of the extreme drafts done through renderings of run P5, shows that right after the occurrence of bursts in the vertical velocity, entire horizontal layers of the flow become turbulent displaying strong fluctuations of all the components of the velocity field, both at large- and at small-scales (see movie in the supplemental material [59]).

## V. ENHANCED LOCAL DISSIPATION EFFICIENCY

The efficiency of the local energy dissipation can be further characterized by computing the minimal domain volume needed to achieve a given percentage of the global (kinetic and/or potential) energy dissipation at a given time. We therefore evaluate the local kinetic and potential energy dissipation efficiency, respectively  $V_{\epsilon_V}$  and  $V_{\epsilon_P}$ , by classifying the temporal outputs of each run in terms of their domain kurtosis  $K_w$ , and then computing the minimal volume percentage needed to achieve the 50% level of the global energy dissipation.

The outcome of this analysis is shown in Fig. 5 for the runs with  $2400 \leq Re \leq 3800$  (thus within a relatively narrow range of values of the Reynolds number) in order to avoid any



Reynolds number dependence of  $V_{\varepsilon_V}$  and  $V_{\varepsilon_P}$ . First, we note that the HIT case has one of the highest kinetic energy dissipation efficiencies: only  $\approx 15\%$  of the most dissipative regions within the volume are in fact needed to achieve 50% of the global kinetic energy dissipation (Fig. 5, top). Strongly stratified flows are unable to achieve a similar  $V_{\varepsilon_V}$  except when they develop extreme vertical drafts, powerful enough for the domain kurtosis to be  $K_w \gtrsim 7$ , attainable in our study only for Froude numbers within the resonant regime delineated in [44] (runs P4 and P5), a regime compatible with values found in some regions of the ocean and the atmosphere. Indeed,  $V_{\varepsilon_V}$  for these two runs can be respectively as low as  $\approx 14\%$  and  $\approx 11\%$ , smaller in fact than for the HIT case. Thus, not only do the large-scale vertical drafts generate small-scale turbulence, but they are also responsible for the local and efficient enhancement of the kinetic energy dissipation  $\varepsilon_V$ . These extreme drafts are therefore needed in stratified turbulent flows, when stratification is strong enough ( $Fr \lesssim 0.1$ ), for the energy to be locally dissipated as efficiently as in the HIT case at equivalent Reynolds numbers.

Indeed, without drafts, dissipation efficiency is significantly smaller. The most stratified runs in our study (runs P7 and P8) are unable to develop significant drafts, and they are both characterized by an efficiency  $V_{\varepsilon_V} \approx 26\%$ , more than twice that of the most dissipative cases of runs P4 and P5. On the opposite limit, when stratification is weak, as for runs P2 and P3,  $V_{\varepsilon_V}$  approaches the value of the HIT case (in fact from below) even though  $K_w \approx 3$ . The local potential energy dissipation efficiency  $V_{\varepsilon_P}$  exhibits a behaviour similar to that of  $V_{\varepsilon_V}$  (Fig. 5, bottom) except for the most stratified runs P7 and P8, that appear to be the most dissipative, although characterized by low kurtosis  $K_w$ . Moreover, values of  $V_{\varepsilon_P}$  are smaller than those of  $V_{\varepsilon_V}$ , suggesting that stratified flows are more efficient in dissipating potential energy than kinetic energy. This could be related to the well-known stronger small-scale intermittency of (passive) scalars as they easily form frontal structures [60, 61] (see also [43]).

## VI. DISCUSSION

### A. A model of intermittency

We showed that the generation of large-scale intermittent vertical drafts in stratified turbulence [44] can lead to recurrent strong modulations of the flow over duration of up to  $\approx 500 t/\tau_{NL}$ . These extreme events produce, possibly through instabilities, strong localized (potential and) kinetic energy dissipation  $\varepsilon_V$  and modulate the overall distribution  $P(\varepsilon_V)$ , whose shape depends on the region of the flow considered. The presence of vertical drafts is also needed for stably stratified turbulence to achieve a localized dissipation efficiency comparable to that of homogeneous isotropic turbulence. In particular, we showed that, at the peak in  $Fr$  of the resonant regime identified in [44], roughly 10% of the domain volume ( $V_{\varepsilon_V}$ ) is sufficient to account for 50% of the global kinetic energy dissipation.

The kind of intermittency reported here, with slow but strong recurrent modulations, differs from the small-scale intermittency reported in other studies [43]. The former can be reproduced with a simple model, as we now illustrate. Specifically, we consider a modification

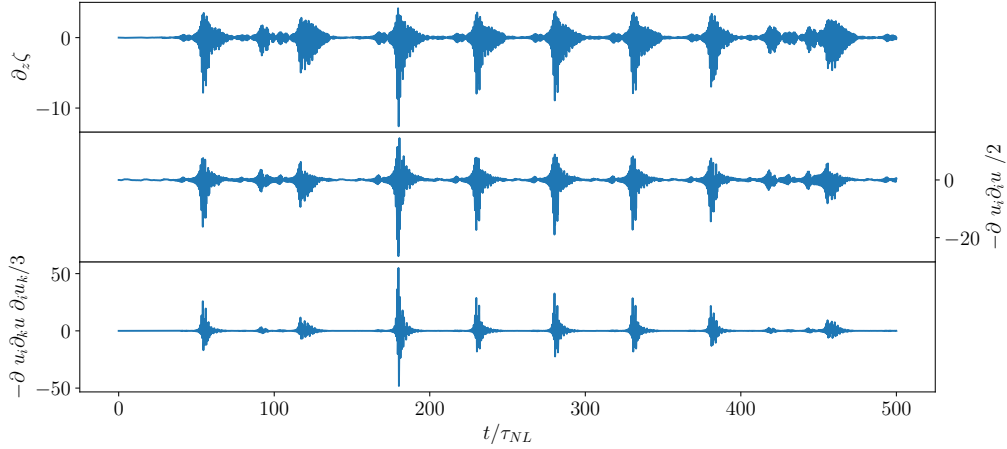


FIG. 6. Time evolution of the vertical gradients of the scaled density fluctuations,  $\partial_z \zeta$ , and of two different combinations of the velocity field gradients ( $Q$  and  $R$ , two quantities relevant for the evolution of fluid elements and of dissipation in reduced Euler models [62, 63]), in a reduced model of field gradients in stratified flows with parameters compatible with run P5.

of a reduced model for field gradients in stratified turbulence presented in [49, 64],

$$\begin{aligned}
 \dot{Q} &= -3R + NT + f - \gamma Q, \\
 \dot{R} &= 2Q^2/3 + 2NSQ/3 + NR_\zeta - \gamma R, \\
 \dot{R}_\zeta &= 5QT/3 + 3RS - 4NST/3 - NQA - NR - \gamma R_\zeta, \\
 \dot{B} &= 2QA/3 + 2R - NAS/3 - NT - \gamma B, \\
 \dot{T} &= -2R_\zeta - 2SQ/3 + NB - 2NS^2/3 - \gamma T, \\
 \dot{A} &= -B - 2Q/3 - 2NS/3 - \gamma A, \\
 \dot{S} &= NA - T - \gamma S,
 \end{aligned}$$

where  $N$  is the Brunt-Väisälä frequency as before,  $Q = (\partial_j u_i)(\partial_i u_j)/2$ ,  $R = (\partial_j u_i)(\partial_k u_j)(\partial_i u_k)/3$ ,  $R_\zeta = (\partial_i \zeta)(\partial_j u_i)(\partial_z u_j)$ ,  $B = (\partial_i u_z)(\partial_z u_i)$ ,  $T = (\partial_i \zeta)(\partial_z u_i)$ ,  $A = \partial_z u_z$ , and  $S = \partial_z \zeta$  (i.e., all combinations of field gradients). Viscous damping (controlled by  $\gamma$ ) and forcing were added phenomenologically. These equations (for  $f = \gamma = 0$ ) can be derived from Eqs. (3) and (4) following fluid trajectories [49]. We integrate these equations with  $f$  given by a superposition of harmonic oscillations with frequencies centered around the Brunt-Väisälä frequency  $N$  and with very small amplitude ( $= 0.08$ ), and with  $\gamma = \nu/L_{Oz}^2$ , where  $L_{Oz}$  is the Ozmidov length. This length is defined as  $L_{Oz} = \sqrt{\varepsilon_V/N^3}$ ; it can be viewed as partitioning the flow between larger scales governed by quasi geostrophic dynamics which progressively gives way, at smaller scales, to strong stratified turbulence. The values of  $N$ ,  $\nu$ , and  $L_{Oz}$  were chosen as in run P5. The result is shown in Fig. 6. Note the system is bursty with a behavior reminiscent of so-called on-off intermittency [65–67]: it displays long periods of very small oscillations, followed by non-regular (but repetitive) bursts reminding those observed in Fig. 1, which are separated by times much larger than the typical time scales in the system. Also, both  $\partial_z \theta$  as well as  $\partial_z w$  (not shown) have bursts, as well as  $Q$  and  $R$ , two quantities relevant in many reduced Euler models [62, 63] to describe vortex stretching

and dissipation. The bursts, amplifying the forcing by orders of magnitude, take place as the system evolves between two slow manifolds [49], and the overall behavior is compatible with a stochastic resonance [68].

## B. Conclusion

The observation of the strong spatial localization of the dissipation in our DNSs is reminiscent of results presented in [69] using global oceanic simulations. Indeed, Pearson and Fox-Kemper have shown that macroscopic features of the PDF of  $\varepsilon_V$  in their simulations (i.e., the mean and standard deviation) depend on the depth and the sub-domains considered, concluding that most of the dissipation at oceanic mesoscales occurs in a small number of high-dissipation locations corresponding to a fraction of the ocean volume. It is worth noticing, however, that the model used in [69] includes subgrid modelling of the dissipation, plus the effect of topography as well as other relevant effects for global oceanic modelling. By showing that large-scale intermittent structures emerging in the bulk of stratified flows are associated with enhanced kinetic energy dissipation, our work indicates that the underlying mechanism associated with the development of regions of extreme dissipation may be a fundamental property of turbulence in the presence of stable stratification, as also suggested by the simple model that reproduces the recurrent bursts (see §VI). Our results shed also light on the link between intermittency and dissipation recently emphasized in [70].

The way energy is dissipated in geophysical flows remains an important open problem; our study indicates that in a certain region of parameter space, vertical drafts and the associated steepening of gravity waves can lead to enhanced local-in-time-and-space dissipation, ultimately leading to an inadequacy of the description of the system in terms of solely weakly interacting waves, even when the global Froude number is small. The state of marginal instability and its relationship with the efficiency of energy dissipation and mixing, also in the context of ocean dynamics, has been analyzed recently [71]. Using a model, it was shown that it may be governed by regions of the flow close to a margin of instability for the Richardson number, consistently with results obtained from other reduced models [49]. Finally, we mention important extensions of this work. With its focus on intermittency, our study is necessarily of a statistical nature, as quantities such as the kurtosis are only defined by averages. As a result, the present analysis could show that stratified turbulence can dissipate energy as efficiently as homogeneous and isotropic turbulence for some values of the Froude number, but it cannot pinpoint individual structures responsible for the dissipation, or characterize the dynamics of such structures. From the point of view of out-of-equilibrium statistical mechanics, the origin of these events can be understood, with the help of simple dynamical models involving a nonlinear resonant-like amplification of waves by eddies [42, 44, 46], as a self-organized critical process in which the strong events lead to a cascade of smaller scale extreme events [41, 45]. Another way to analyze the dynamics is by postulating the existence of two slow manifolds in the dynamics (one associated with waves, the other with the overturning instability) with fluid elements evolving fast from one available state to the other [49], as in the model briefly discussed in this section. A study of the fluid dynamics of the evolution of individual structures, in the spirit of traditional studies of stably stratified turbulence as, e.g., in [32, 33], or in [30] considering the role of conserved quantities, is left for the future.

## ACKNOWLEDGMENTS

R. Marino acknowledges support from the project “EVENTFUL” (ANR-20-CE30-0011), funded by the French “Agence Nationale de la Recherche” - ANR through the program AAPG-2020. A. Pouquet is thankful to LASP and in particular to Bob Ergun.

- 
- [1] P. S. Marcus, “Jupiter’s great red spot and other vortices,” *Annu. Rev. Astron. Astrophys.* **31**, 523–573 (1993).
  - [2] K. Emanuel, “Increasing destructiveness of tropical cyclones over the past 30 years,” *Nature* **436**, 686–688 (2005).
  - [3] R.B. Scott and F. Wang, “Direct evidence of an oceanic inverse kinetic energy cascade from satellite altimetry,” *J. Phys. Oceanogr.* **35**, 1650–1666 (2005).
  - [4] J.M. Klymak, R. Pinkel, and L. Rainville, “Direct breaking of the internal tide near topography: Kaena Ridge, Hawaii,” *J. Phys. Oceanogr.* **38**, 380–399 (2008).
  - [5] P. Klein, B.L. Hua, G. Lapeyre, X. Capet, S. Le Gentil, and H. Sasaki, “Upper ocean turbulence from high-resolution 3D simulations,” *J. Phys. Oceanogr.* **38**, 1748–1763 (2008).
  - [6] R. Marino, P.D. Mininni, D. Rosenberg, and A. Pouquet, “Inverse cascades in rotating stratified turbulence: Fast growth of large scales,” *Eur. Phys. Lett.* **102**, 44006 (2013).
  - [7] A. Pouquet and R. Marino, “Geophysical turbulence and the duality of the energy flow across scales,” *Phys. Rev. Lett.* **234501**, 111 (2013).
  - [8] R. Marino, P.D. Mininni, D. Rosenberg, and A. Pouquet, “Large-scale anisotropy in stably stratified rotating flows,” *Phys. Rev. E* **90**, 023018 (2014).
  - [9] R. Marino, A. Pouquet, and D. Rosenberg, “Resolving the paradox of oceanic large-scale balance and small-scale mixing,” *Phys. Rev. Lett.* **114**, 114504 (2015).
  - [10] A. Pouquet, R. Marino, P.D. Mininni, and D. Rosenberg, “Dual constant-flux energy cascades to both large scales and small scales,” *Phys. Fluids* **29**, 111108 (2017).
  - [11] A. Pouquet, D. Rosenberg, J.E. Stawarz, and R. Marino, “Helicity dynamics, inverse, and bidirectional cascades in fluid and magnetohydrodynamic turbulence: A brief review,” *Earth and Space Science* **6**, 351–369 (2019).
  - [12] A. Pouquet, D. Rosenberg, J. Stawarz, and R. Marino, “Helicity dynamics, inverse, and bidirectional cascades in fluid and magnetohydrodynamic turbulence: A brief review,” *Earth Space Sci.* **6**, 1–19 (2019).
  - [13] J.H. Xie and O. Bühler, “Two-dimensional isotropic inertia–gravity wave turbulence,” *J. Fluid Mech.* **872**, 752–783 (2019).
  - [14] J.H. Xie and O. Bühler, “Exact third-order structure functions for two-dimensional turbulence,” *J. Fluid Mech.* **851**, 672–686 (2018).
  - [15] R. Marino, D. Rosenberg, C. Herbert, and A. Pouquet, “Interplay of waves and eddies in rotating stratified turbulence and the link with kinetic-potential energy partition,” *Eur. Phys. Lett.* **112**, 49001 (2015).
  - [16] A. Pouquet, D. Rosenberg, R. Marino, and C. Herbert, “Scaling laws for mixing and dissipation in unforced rotating stratified turbulence,” *J. Fluid Mech.* **844**, 519–545 (2018).
  - [17] H. Wang and O. Bühler, “Ageostrophic corrections for power spectra and wave–vortex decomposition,” *J. Fluid Mech.* **882**, A16 (2020).
  - [18] C. Herbert, R. Marino, D. Rosenberg, and A. Pouquet, “Waves and vortices in the inverse

- cascade regime of stratified turbulence with or without rotation,” *Journal of Fluid Mechanics* **806**, 165–204 (2016).
- [19] D. H. Lenschow, M. Lothon, S. D. Mayor, P. P. Sullivan, and G. Canut, “A comparison of higher-order vertical velocity moments in the convective boundary layer from Lidar with in situ measurements and Large-Eddy Simulation,” *Bound. Lay. Met.* **143**, 107–123 (2012).
- [20] L. Mahrt and N. Gamage, “Observations of turbulence in stratified flow,” *J. Atmos. Sci.* **44**, 1106–1122 (1987).
- [21] L. Mahrt, “Intermittency of atmospheric turbulence,” *J. Atmos. Sci.* **46**, 79 – 95 (1989).
- [22] H.L. Liu, “On the large wind shear and fast meridional transport above the mesopause,” *Geophys. Res. Lett.* **34**, L08815 (2007).
- [23] J.L. Chau, R. Marino, F. Feraco, J.M. Urco Cordero, G. Baumgarten, F-J. Luebken, W.K. Hocking, C. Schult, T. Renkwitz, and R. Latteck, “Radar observation of extreme vertical drafts in the polar summer mesosphere,” *Geophys. Res. Lett.* **48**, e2021GL094918 (2021).
- [24] E. D’Asaro, R-C. Lien, and F. Henyey, “High-frequency internal waves on the oregon continental shelf,” *J. Phys. Oceanogr.* **37**, 1956–1967 (2007).
- [25] H. van Haren and L. Gostiaux, “Convective mixing by internal waves in the Puerto Rico Trench,” *J. Mar. Res.* **74**, 161–173 (2016).
- [26] X. Capet, J. McWilliams, M. Molemaker, and A. Shchepetkin, “Mesoscale to submesoscale transition in the california current system. part i: Flow structure, eddy flux, and observational tests,” *J. Phys. Oceanogr.* **38**, 29–43 (2008).
- [27] J.M. Klymak, W. Crawford, M.H. Alford, J.A. MacKinnon, and R. Pinkel, “Along-isopycnal variability of spice in the North Pacific,” *J. Geophys. Res.* **120**, 2287–2307 (2015).
- [28] J.J. Riley, R.W. Metcalfe, and M.A. Weissman, “Direct numerical simulations of homogeneous turbulence in density-stratified fluids,” *AIP Conference Proceedings* **76**, 79–112 (1981).
- [29] J.R. Herring and O. Métais, “Numerical experiments in forced stably stratified turbulence,” *J. Fluid Mech.* **202**, 97–115 (1989).
- [30] K.B. Winters, P.N. Lombard, J.J. Riley, and E. D’Asaro, “Available potential energy and mixing in density-stratified fluids,” *J. Fluid Mech.* **289**, 115–128 (1995).
- [31] O. Métais, P. Bartello, E. Garnier, J.J. Riley, and M. Lesieur, “Inverse cascade in stably stratified rotating turbulence,” *Dynamics of Atmospheres and Oceans* **23**, 193–203 (1996).
- [32] Y. Kimura and J.R. Herring, “Diffusion in stably stratified turbulence,” *J. Fluid Mech.* **328**, 253–269 (1996).
- [33] P. Billant and J-M. Chomaz, “Experimental evidence for a new instability of a vertical columnar vortex pair in a strongly stratified fluid,” *J. Fluid Mech.* **418**, 167–188 (2000).
- [34] J.J. Riley and S.M. de Bruyn Kops, “Dynamics of turbulence strongly influenced by buoyancy,” *Physics of Fluids* **15**, 2047–2059 (2003).
- [35] E. Lindborg, “The energy cascade in a strongly stratified fluid,” *J. Fluid Mech.* **550**, 207–242 (2006).
- [36] J-P. Laval, J.C. McWilliams, and B. Dubrulle, “Forced stratified turbulence: successive transitions with Reynolds number,” *Physical Review E* **68**, 036308 (2003).
- [37] P. Bartello and S.M. Tobias, “Sensitivity of stratified turbulence to the buoyancy Reynolds number,” *J. Fluid Mech.* **725**, 1–22 (2013).
- [38] G. Ivey, K. Winters, and J. Koseff, “Density stratification, turbulence but how much mixing?” *Ann. Rev. Fluid Mech.* **40**, 169–184 (2008).
- [39] G. Brethouwer, P. Billant, E. Lindborg, and J-M. Chomaz, “Scaling analysis and simulation of strongly stratified turbulent flows,” *J. Fluid Mech.* **585**, 343–368 (2007).

- [40] P.A. Davidson, Turbulence in rotating, stratified and electrically conducting fluids (Cambridge University Press, 2013).
- [41] A. Pouquet, D. Rosenberg, and R. Marino, “Linking dissipation, anisotropy and intermittency in rotating stratified turbulence,” *Phys. Fluids* **31**, 105116 (2019).
- [42] C. Rorai, P.D. Mininni, and A. Pouquet, “Turbulence comes in bursts in stably stratified flows,” *Phys. Rev. E* **89**, 043002 (2014).
- [43] S.M. de Bruyn Kops, “Classical scaling and intermittency in strongly stratified Boussinesq turbulence,” *J. Fluid Mech.* **775**, 436–463 (2015).
- [44] F. Feraco, R. Marino, A. Pumir, L. Primavera, P.D. Mininni, A. Pouquet, and D. Rosenberg, “Vertical drafts and mixing in stratified turbulence: sharp transition with Froude number,” *Eur. Phys. Lett.* **123**, 44002 (2018).
- [45] W.D. Smyth, J.D. Nash, and J.N. Moum, “Self-organized criticality in geophysical turbulence,” *Scientific reports* **9**, 3747 (2019).
- [46] F. Feraco, R. Marino, L. Primavera, A. Pumir, P.D. Mininni, D. Rosenberg, A. Pouquet, R. Foldes, E. Lévêque, E. Camporeale, S.S. Cerri, H. Charuvil Asokan, J.L. Chau, J.P. Bertoglio, P. Salizzoni, and M. Marro, “Connecting large-scale velocity and temperature bursts with small-scale intermittency in stratified turbulence,” *Eur. Phys. Lett.* **135**, 14001 (2021).
- [47] V. Petoukhov, A.V. Eliseev, R. Klein, and H. Oesterle, “On statistics of the free-troposphere synoptic component: an evaluation of skewnesses and mixed third-order moments contribution to the synoptic-scale dynamics and fluxes of heat and humidity,” *Tellus* **60A**, 11–31 (2008).
- [48] P. Sardeshmukh, G.P. Compo, and C. Penland, “Need for caution in interpreting extreme weather statistics,” *J. Climate* **28**, 9166–9185 (2015).
- [49] N.E. Sujovolsky and P.D. Mininni, “From waves to convection and back again: The phase space of stably stratified turbulence,” *Phys. Rev. F* **5**, 064802 (2020).
- [50] H. Salehipour, W.R. Peltier, C.B. Whalen, and J.A. MacKinnon, “A new characterization of the turbulent diapycnal diffusivities of mass and momentum in the ocean,” *Geophys. Res. Lett.* **43**, 3370–3379 (2016).
- [51] G.K. Vallis, Atmospheric and oceanic fluid dynamics (Cambridge University Press, 2017).
- [52] P.D. Mininni, D. Rosenberg, R. Reddy, and A. Pouquet, “A hybrid MPI-OpenMP scheme for scalable parallel pseudospectral computations for fluid turbulence,” *Parallel Computing* **37**, 316–326 (2011).
- [53] M. Fontana, O.P. Bruno, P.D. Mininni, and P. Dmitruk, “Fourier continuation method for incompressible fluids with boundaries,” *Comp. Phys. Comm.* **256**, 107482 (2020).
- [54] D. Rosenberg, P.D. Mininni, R. Reddy, and A. Pouquet, “GPU parallelization of a hybrid pseudospectral geophysical turbulence framework using CUDA,” *Atmosphere* **11**, 178 (2020).
- [55] A. Pumir, “Turbulence in homogeneous shear flows,” *Phys. Fluids* **8**, 3112–3127 (1996).
- [56] A. Sekimoto, S. Dong, and J. Jiménez, “Direct numerical simulation of statistically stationary and homogeneous shear turbulence and its relation to other shear flows,” *Phys. Fluids* **28**, 035101 (2016).
- [57] G.J. Székely, M.L. Rizzo, and N.K. Bakirov, “Measuring and testing dependence by correlation of distances,” *The Annals of Statistics* **35**, 2769–2794 (2007).
- [58] D. Edelman, T.F. Móri, and G.J. Székely, “On relationships between the Pearson and the distance correlation coefficients,” *Statistics & Probability Letters* **169**, 108960 (2021).
- [59] See Supplemental Material at [URL will be inserted by publisher] for a movie showing the time evolution of typical extreme events developing in run P5. In the left panel of the movie

it is rendered one of the horizontal components of the velocity ( $u$ ), while the right panel displays the values of the vertical velocity ( $w$ ) exceeding four standard deviations, namely the extreme vertical drafts corresponding to  $w > 4\sigma_w$ . The movie shows the time evolution of the standardized flow fields over an interval of  $\sim 26\tau_{NL}$ .

- [60] A. Pumir, “A numerical study of the mixing of a passive scalar in three dimensions in the presence of a mean gradient,” *Phys. Fluids* **6**, 2118–2132 (1994).
- [61] N.E. Sujovolsky, P.D. Mininni, and A. Pouquet, “Generation of turbulence through frontogenesis in sheared stratified flows,” *Phys. Fluids* **30**, 086601 (2018).
- [62] P. Vieillefosse, “Internal motion of a small element of fluid in an inviscid flow,” *Physica A: Statistical Mechanics and its Applications* **125**, 150–162 (1984).
- [63] Charles Meneveau, “Lagrangian dynamics and models of the velocity gradient tensor in turbulent flows,” *Annual Review of Fluid Mechanics* **43**, 219–245 (2011).
- [64] N. E. Sujovolsky, G. B. Mindlin, and P. D. Mininni, “Invariant manifolds in stratified turbulence,” *Physical Review Fluids* **4**, 052402(R) (2019).
- [65] Y. Pomeau and P. Manneville, “Intermittent transition to turbulence in dissipative dynamical systems,” *J. de Physique* **41**, 1235–1243 (1980).
- [66] E. Ott and J. C. Sommerer, “Blowout bifurcations: The occurrence of riddled basins and on-off intermittency,” *Phys. Lett. A* **188**, 39–47 (1994).
- [67] Arindam Saha and Ulrike Feudel, “Riddled basins of attraction in systems exhibiting extreme events,” *Chaos* **28**, 033610 (2008).
- [68] Roberto Benzi, Giorgio Parisi, Alfonso Sutera, and Angelo Vulpiani, “Stochastic resonance in climatic change,” *Tellus* **34**, 10–15 (1982).
- [69] B. Pearson and B. Fox-Kemper, “Lognormal turbulence dissipation in global ocean models,” *Phys. Rev. Lett.* **120**, 094501 (2018).
- [70] J. Isern-Fontanet and A. Turiel, “On the connection between intermittency and dissipation in ocean turbulence: a multifractal approach,” *Journal of Physical Oceanography* , <https://doi.org/10.1175/JPO-D-20-0256.1> (2021).
- [71] W.D. Smyth, “Marginal instability and the efficiency of ocean mixing,” *J. Phys. Oceano.* **50**, 2141–2150 (2020).

## Chapter 5

# Modeling of the probability density function of a passive scalar concentration in a turbulent flow: a preliminary study

In this Chapter I am presenting a study of the dispersion of a passive scalar in a homogeneous and isotropic turbulent flow. This work is preliminary to a future investigation where passive scalars will be injected in stratified flows developing extreme vertical drafts, as discusses in the previous chapters. Passive scalars are quantities which are transported by the flow without affecting its dynamics or altering its properties. The modeling of the dispersion of a passive scalar has many different applications, going from industrial to biological and environmental flows. Understanding how passive scalars are transported is necessary to model, for example, the dispersion of pollutants in the oceans or toxic, flammable or explosive substances in the atmosphere. Due to the turbulent nature of the natural flows that carries the passive scalar, its concentration is usually studied with a statistical approach, like in the case of the velocity or temperature field. The statistical characterization of the concentration fluctuations of a passive scalar can be modeled by different distributions, depending on the dynamics of the system. In particular, the gamma distribution has been shown to be the more suitable for the modeling of dispersion and mixing in the atmosphere [8, 83]. In the study I am presenting, the statistics obtained from the DNSs of the Navier-Stokes equations are compared to the results of an experiment carried out in the wind tunnel at of the Laboratoire de Mécanique des Fluides et d'Acoustique at the École Centrale de Lyon in France [50]. A description of the experimental setup can be found in section 1.12.3. Here I will describe the numerical setup used to perform the DNSs and discuss the results obtained. After that, a comparison with the experimental measurements from [50] will be shown.

### 5.1 Evolution of the PDF of the passive scalar concentration and mixing phases

The numerical simulations have been carried out using GHOST (see section 1.12.1), which can integrate the equation describing the evolution of the concentration of a passive scalar. A puff of passive scalar is injected at an arbitrary time in a homogeneous and isotropic fluid (with no mean flow) after it reached a statistically stationary state. The concentration of a puff,  $c$ , injected, follows a Gaussian distribution peaked at the center of the simulation box. Due to the periodic boundary conditions, the



volume averaged concentration,  $\bar{c}$ , will remain constant. After the injection, the passive scalar is free to evolve within the flow. From the output of the simulation we obtain the pointwise values of concentration, which we use to study the statistics of the concentration fluctuations intensity:

$$i_c = \frac{\sigma_c}{\langle c \rangle}, \quad (5.1)$$

defined as the ratio of the standard deviation of the concentration,  $\sigma_c$ , to its mean value  $\langle c \rangle$ . The evolution in time of the concentration of passive scalar  $c$  is shown through visualization of the simulation domain (made using VAPOR) and through its PDF in Fig. 5.1.

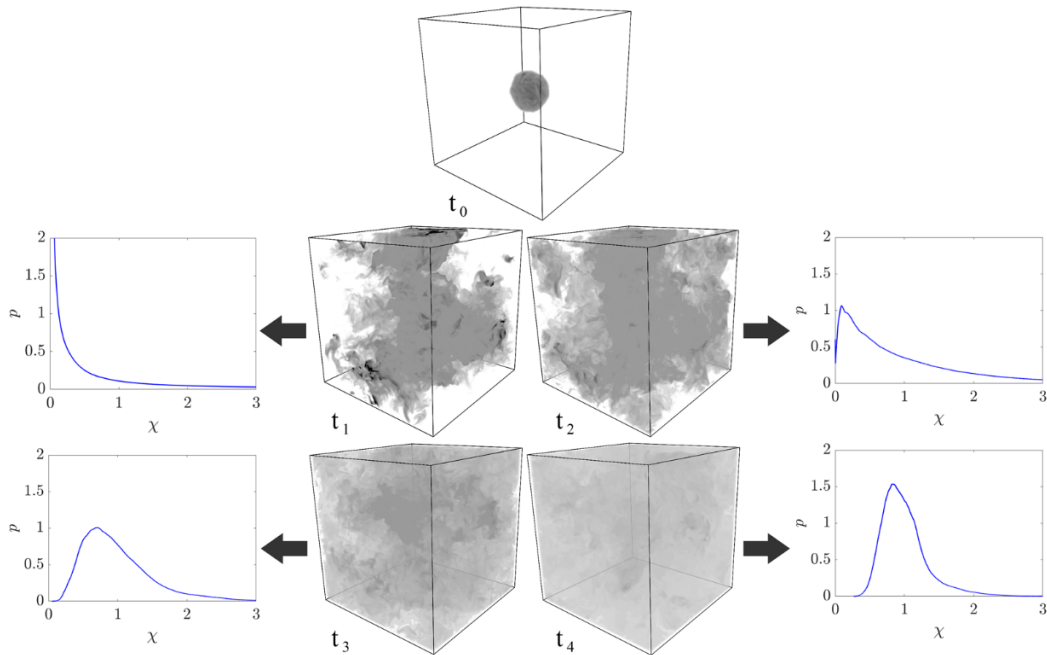


FIGURE 5.1: Visualization at different time steps of three-dimensional renderings of the concentration  $c$  and the corresponding PDFs of run S1. The initial condition ( $t_0$ , top) consists of a puff of passive scalar injected after the flow reached a statistically stationary state. At  $t_4$  (bottom right) the passive scalar is almost completely homogeneously distributed in the domain. [53]

In the renderings of Fig. 5.1,  $c$  is displayed with a grey color-palette. Dark-grey indicates regions with high concentration while white is used for regions where the concentration is 0. Fig. 5.1 ( $t_0$ ) shows the initial condition, with the injected puff at the center of the cubic box. We then observe, from the evolution of  $i_c$ , two different phases. During the first phase, the scalar is progressively transported throughout the domain, as seen in Fig. 5.1( $t_1$ ). In this phase, the PDF of  $c$  displays an exponential-like shape and the volume-averaged value of  $i_c$  is found to be greater than 1. The second phase observed is instead characterized by a volume-averaged value of  $i_c$  smaller than 1. At the beginning of this phase, see Fig. 5.1, the PDF of  $c$  is well approximated by a log-normal distribution, as shown in Fig. 5.1( $t_2$ ) and Fig. 5.1( $t_3$ ). In Fig. 5.1( $t_4$ ) the passive scalar is almost completely homogeneously distributed in the domain. This homogenization induces a further transition of the PDF which becomes more similar to a clipped Gaussian. In past years, several distributions have been proposed to

model the PDF of the concentration of a passive scalar. We use here the Kullback-Leibler divergence  $D_{KL}$  [35] in order to identify which one can better approximate the PDFs of our study among the gamma, the lognormal and the Weibull  $2p$  distribution.  $D_{KL}$  is defined as:

$$D_{KL}(p \parallel q) = \sum_i p_i \log_2 \left( \frac{p_i}{q_i} \right), \quad (5.2)$$

where  $p$  is the observed distribution and  $q$  is the model tested. The best agreement is found when  $p \sim q$ , hence when  $D_{KL} \sim 0$ . By estimating  $D_{KL}$  at different time steps we find that the gamma distribution shows the overall better agreement with the statistics of our DNSs.

## 5.2 Validation of a model distribution in DNSs and wind tunnel experiments

We now compare the results of the DNSs with the experimental measurements of a passive scalar concentration performed in [50]. The evolution of the PDF of the concentration of a continuously released passive scalar was obtained from fixed point measurements. Time series of such measurements (plume) allowed to investigate the evolution of the PDF as the distance from the source increased. Before comparing the results obtained using the two methods, we provide an explanation on why the PDF computed from the whole simulation domain at a fixed time step of the DNSs can be compared to the PDFs obtained from the fixed-point time series measurements of the plume in the experiment. We can consider each time step of the DNSs as possible realizations of the plume at a fixed distance from the source in the wind tunnel experiment. By invoking the ergodicity in both systems we can compare the spatial statistics of the simulations with the single-point temporal statistics of the experiment. Thus, we consider the temporal evolution of the puff of passive scalar from the DNSs as a reproduction of the evolution of the plume of passive scalar in the wind tunnel as it get translated horizontally by the mean flow. We then proceed with the comparison of the results. In [50] it is shown that the distribution of a plume of passive scalar can be well approximated at any distance by a Gamma distribution, which we also observed from the results of the DNSs. By comparing the PDFs of the concentration, normalized to its mean value, obtained in [50] and ours we find a good agreement between the two. The comparison is shown Fig. 5.2, where a Gamma distribution is added as a reference.

We note that, although we carefully conceived this comparison between DNSs and experiment, the characteristics of the turbulence that develops in the wind tunnel and the one in the simulations are rather different. Indeed, while using DNSs it is relatively easy to simulate a homogeneous and isotropic flow without a mean flow and no boundary effects, this is not possible in the wind tunnel. In fact, a mean flow does exist in the wind tunnel and the boundary layer cannot be considered homogeneous and isotropic. In our case, even though the measurements have been taken at the centreline of the wind tunnel to minimize its effects, they cannot be completely neglected. However, the good agreement obtained between the two results means that, in any case, part of the dynamics of the passive scalar dispersion in a boundary layer is recovered in our DNSs of a homogeneous and isotropic flow. This motivates us in pursuing for future works a characterization of the concentration of a passive scalar in stratified turbulent flows by means of DNSs with the aim of studying

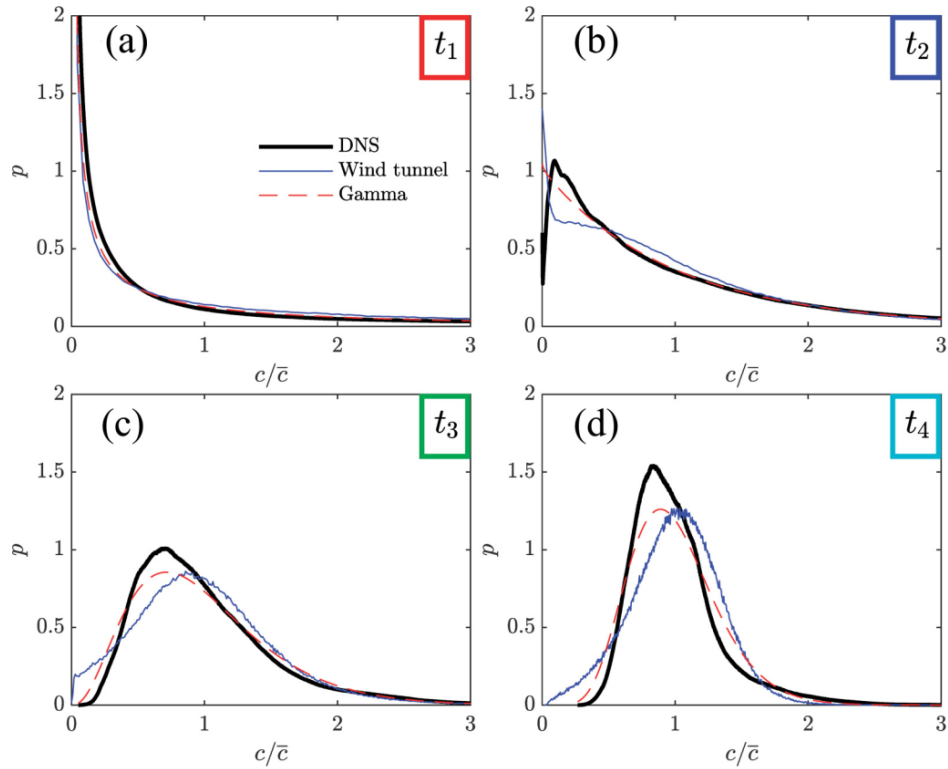


FIGURE 5.2: Comparison between the normalized PDFs of the passive scalar concentration from the DNS, the wind-tunnel measurements from [50] and the gamma distribution. Each panel corresponds to a different value of  $i_c$ : (a)  $i_c = 2.25$ , (b)  $i_c = 1$ , (c)  $i_c = 0.53$  and (d)  $i_c = 0.33$ . [53]

the feedback of the system to the extreme vertical drafts characterized throughout the present work.



**HAL**  
open science

## Scalar mixing in homogeneous isotropic turbulence: A numerical study

Michel Orsi, Lionel Soulhac, Fabio Feraco, Massimo Marro, Duane Rosenberg, Raffaele Marino, Maurizio Boffadossi, Pietro Salizzoni

### ► To cite this version:

Michel Orsi, Lionel Soulhac, Fabio Feraco, Massimo Marro, Duane Rosenberg, et al.. Scalar mixing in homogeneous isotropic turbulence: A numerical study. *Physical Review Fluids*, American Physical Society, 2021, 6 (3), 10.1103/PHYSREVFLUIDS.6.034502 . hal-03451996

**HAL Id: hal-03451996**

**<https://hal.archives-ouvertes.fr/hal-03451996>**

Submitted on 28 Nov 2021

**HAL** is a multi-disciplinary open access archive for the deposit and dissemination of scientific research documents, whether they are published or not. The documents may come from teaching and research institutions in France or abroad, or from public or private research centers.

L'archive ouverte pluridisciplinaire **HAL**, est destinée au dépôt et à la diffusion de documents scientifiques de niveau recherche, publiés ou non, émanant des établissements d'enseignement et de recherche français ou étrangers, des laboratoires publics ou privés.

**Scalar mixing in homogeneous isotropic turbulence: A numerical study**

Michel Orsi <sup>1</sup>, Lionel Souhac <sup>2</sup>, Fabio Feraco <sup>2,3</sup>, Massimo Marro <sup>2</sup>, Duane Rosenberg <sup>4</sup>,  
Raffaele Marino <sup>2</sup>, Maurizio Boffadossi <sup>1</sup> and Pietro Salizzoni <sup>2</sup>

<sup>1</sup>*Department of Aerospace Engineering, Politecnico di Milano, 34 via La Masa, 20158 Milano, Italy*

<sup>2</sup>*Laboratoire de Mécanique des Fluides et d'Acoustique, University of Lyon, CNRS UMR 5509, École Centrale de Lyon, INSA Lyon, Université Claude Bernard, 36 Avenue Guy de Collongue, 69134 Écully, France*

<sup>3</sup>*Dipartimento di Fisica, Università della Calabria, Italy*

<sup>4</sup>*1401 Bradley Drive, Boulder 80305, Colorado, USA*



(Received 19 April 2020; accepted 3 March 2021; published 19 March 2021)

The understanding of the mechanics of turbulent dispersion is of primary importance in estimating the effects of mixing processes involved in a variety of events playing a significant role in our daily life. This motivates research on the characterization of statistics and the complex temporal evolution of passive scalars in turbulent flows. A key aspect of these studies is the modeling of the probability density function (PDF) of the passive scalar concentration and the identification of its link with the mixing properties. In order to investigate the dynamics of passive scalars as observed in nature and in laboratory experiments, we perform here direct numerical simulations of a passive tracer injected in the stationary phase of homogeneous isotropic turbulence flows in a setup mimicking the evolution of a fluid volume in the reference frame of the mean flow. In particular, we show how the gamma distribution proves to be a suitable model for the PDF of the passive scalar concentration and its temporal evolution in a turbulent flow throughout the different phases of the mixing process. Then, assuming a gamma distribution, we develop a simple mixing model by which we can estimate a mixing timescale, which regulates the decay rate of the intensity of the concentration fluctuations.

DOI: [10.1103/PhysRevFluids.6.034502](https://doi.org/10.1103/PhysRevFluids.6.034502)

## I. INTRODUCTION

Turbulent dispersion and mixing of passive scalars are ubiquitous in nature. As is well known, the turbulent character of the high Reynolds ( $Re$ ) number flows is reflected on the fluctuations of the passive scalar concentration occurring over a wide range of spatial and temporal scales [1]. The statistical characterization of these fluctuations is essential for the modeling of several processes occurring in industrial, biological, and environmental flows (see Fig. 1 as examples). To this aim, over the years this issue has been tackled by several authors considering a large variety of flow configurations [2–8].

In a number of applications of interest in physics, chemistry, biology, and engineering, a key aspect is the prediction of the spatial variability of the one-point probability density function (PDF) of the scalar field. Previous works have shown that, depending on the flow configuration, this can be modeled by different distributions [2–9], including the Weibull, the lognormal, and the gamma distributions. Notably, the latter was shown to be a suitable model for both dispersion and mixing in internal flows [2–7] and in the atmosphere [6–8, 10–14].

The present paper aims at further exploring the above features, through the investigation of concentration statistics and mixing in a framework mimicking the evolution of the passive scalar in a homogeneous isotropic turbulent flow. To this purpose, we performed direct numerical simulations

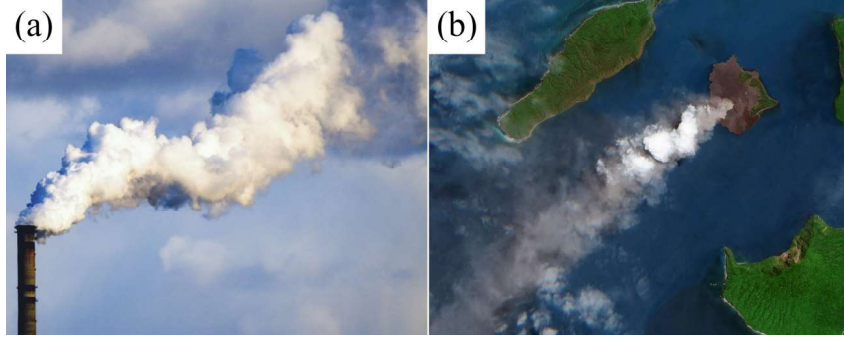


FIG. 1. (a) Plume generated by a chimney (i.e., an elevated continuous source in a nonisotropic and nonhomogeneous turbulent flow field); (b) volcanic ash and steam in the Sunda Strait released by the Anak Krakatau volcano in Indonesia 3 months before its eruption in December 2018.

(DNSs) of a stationary turbulent velocity field (with zero mean) where a puff of passive scalar was released and let evolve to get insights on its diffusion and mixing properties (Sec. II). In Sec. III concentration statistics and PDF computed on the pointwise simulated fields were first checked to ascertain their reliability and then linked to the main mechanisms involving the mixing. Finally, we discuss the consistency between spatial statistics computed by the DNS (seeing the puff as evolving in a Lagrangian framework moving with the mean flow) and the temporal statistics based on one-point wind-tunnel measurements (Sec. IV).

## II. NUMERICAL SIMULATION

In order to investigate the dispersion and mixing of a passive scalar in homogeneous isotropic turbulence (HIT), the Navier-Stokes equations for an incompressible fluid together with the convection-diffusion equation for the concentration are integrated by means of the geophysical high-order suite for turbulence code [15], a highly parallelized (hybrid MPI-OPENMP) pseudospectral framework with second-order explicit Runge-Kutta time stepping. The Navier-Stokes equations have been integrated on a cubic grid of  $512^3$  points (corresponding to a box whose linear size in adimensional units is  $L_0 = 2\pi$ ) with periodic boundary conditions. A stochastic forcing  $\mathbf{F}$  was used to inject energy into the velocity field to achieve and maintain a statistically stationary state. The forcing is random in time and isotropic in Fourier space with the energy being injected at large scales in a spherical shell of wave-numbers  $2 \leq |k_i| \leq 3$ . A puff of a passive scalar modeled with a Gaussian concentration peaked in the center of the box is injected at an arbitrary time in the statistically stationary state of the simulation and is let to diffuse. The full system of equations implemented is reported here

$$\begin{aligned} \nabla \cdot \mathbf{u} &= 0, \\ \partial_t \mathbf{u} + (\mathbf{u} \cdot \nabla) \mathbf{u} &= -\nabla p + \mathbf{F} + \frac{1}{\text{Re}} \nabla^2 \mathbf{u}, \\ \partial_t c + \mathbf{u} \cdot \nabla c &= \frac{1}{\text{Pr Re}} \nabla^2 c, \end{aligned} \quad (1)$$

$\mathbf{u}$  being the velocity field,  $p$  is the pressure, and  $c$  is the passive scalar concentration. The DNS governing parameters are the Prandtl (Pr) and the Reynolds (Re) numbers. The former, defined as  $\text{Pr} \equiv \nu/\kappa$ , is set equal to 1 (being  $\nu$  and  $\kappa$  the kinematic viscosity and the diffusivity, respectively). The latter is instead  $\text{Re} \equiv \frac{UL}{\nu}$ , where  $U = \sqrt{3\sigma_u^2}$  (being  $\sigma_u^2 = \sigma_v^2 = \sigma_w^2 \sim 1$  the variances of the three velocity components averaged over the computational domain) and  $L = \frac{2\pi}{k_i \sim 2.5}$ , respectively, are the characteristic velocity and the integral length scale of the background fluid (the latter being

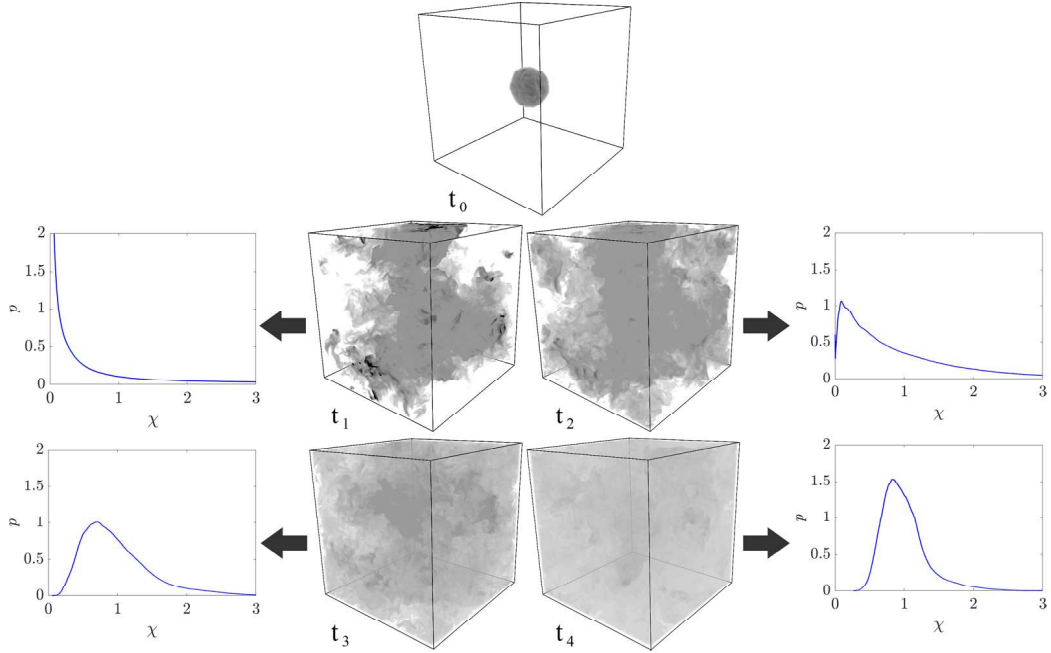


FIG. 2. Visualization of different instants of the DNS solutions and corresponding concentration PDFs: at the top ( $t_0$ ), the initial condition can be observed; at the bottom right ( $t_4$ ), the passive scalar homogenizes itself within the box.

estimated as the scale at which energy is injected into the system). Based on these quantities we can estimate the turnover time  $t^* \equiv L/U$ , the characteristic timescale of the simulation, whose total extension is about  $10t^*$ . The simulations have been performed at two Reynolds numbers, namely, 3000 and 3500. For  $\text{Re} = 3000$  the Kolmogorov length scale is  $\eta = (\nu^3/\varepsilon)^{1/4} = 8.15 \times 10^{-3}$  ( $\varepsilon$  is the turbulent kinetic-energy dissipation rate), which is three orders of magnitude lower than the integral length scale ( $\eta/L = 3.24 \times 10^{-3}$ ). Note that the (periodic) boundary conditions induce the concentration averaged over the domain ( $\bar{c}$ ) to be constant throughout the simulation duration.

### III. RESULTS

The concentration statistics provided by the DNS results allow the temporal evolution of the mixing process to be investigated. To that purpose, we focus on two main statistical indicators: the shape of the PDF of the spatial distribution of the concentration and the (volume-averaged) concentration fluctuations intensity  $i_c$  (defined as the ratio between the standard deviation of the concentrations  $\sigma_c$  and  $\bar{c}$ ). The first feature that is worth noting is the strict connection between the temporal evolutions of these two indicators.

Notably, once excluded the early transient of the simulation (lasting less than one turnover time  $t^*$ ) during which the system progressively “loses memory” of the initial concentration distribution (Fig. 2,  $t_0$ ), we can identify two main stages of the process by linking the shape of the PDFs (Fig. 2) to  $i_c$  (Fig. 3). To allow the reader to suitably capture this connection between the concentration PDF and  $i_c$ , we provided a movie as Supplemental Material [16]. During the first phase, starting at the inflection point of  $i_c$ , the scalar is progressively transported throughout the domain as shown in Fig. 2 at  $t_1$ . This stage presents specific features: (i)  $i_c$  is larger than 1, (ii) the concentration PDF is characterized by a large number of zero values (mostly distributed at the edge of the evolving puff), and (iii) it approximates an exponential-like shape. The second phase begins when the domain

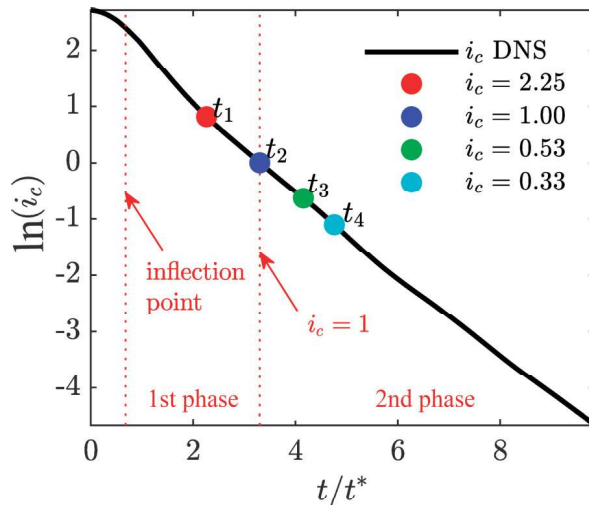


FIG. 3. Behavior of the concentration fluctuations intensity  $i_c$  over time: four instants  $t_1$ ,  $t_2$ ,  $t_3$ , and  $t_4$  are highlighted.

gets completely filled by the passive scalar (Fig. 2 at  $t_2$ ) and  $i_c = 1$  (Fig. 3), and it is mostly characterized by the diffusion. During this stage the scalar field progressively homogenizes (as shown in Fig. 2 at  $t_3$ ) and the concentration PDFs assume a lognormal-like shape. The increasing scalar homogenization (Fig. 2 at  $t_4$ ) induces a further transition of the PDFs towards a clipped Gaussian [13].

The results of the simulations performed with two different Reynolds numbers (i.e.,  $Re = 3000$  and  $Re = 3500$ ) did not show any relevant difference one to the other. In what follows we will, therefore, present results for the case of  $Re = 3000$ . Concentration statistics recover those obtained with the smaller blob as  $t/t^* > 2$ .

#### A. Concentration PDF

In order to identify the statistical distribution showing the best agreement with the presented numerical results, we tested different models for the scalar PDF. To do this, we, therefore, computed the PDF of the concentration for each time step. The agreement between the PDFs obtained from the DNS and the analytical model distributions is estimated here using the Kullback-Leibler divergence  $D_{KL}$  [17], defined as

$$D_{KL}(p \parallel q) \equiv - \sum p \log_2 \left( \frac{p}{q} \right), \quad (2)$$

where  $p$  is the PDF from the DNS and  $q$  is the distribution assumed as a model. According to this definition, the best agreement is observed when  $p/q \rightarrow 1$ , i.e., for  $D_{KL} \rightarrow 0$ .

We tested three different distributions which have been proposed over the years as suitable models for the passive scalar concentration PDF within a turbulent flow [2–9]. These are as follows:

- (1) the gamma distribution,

$$p(\chi|\lambda, \theta) = \frac{1}{\Gamma(\lambda)\theta} \left( \frac{\chi}{\theta} \right)^{\lambda-1} \exp \left( -\frac{\chi}{\theta} \right), \quad (3)$$

where  $\chi$  is the sample space variable for the concentration,  $\Gamma(\cdot)$  is the Gamma special function [18], and  $\lambda = i_c^{-2}$  and  $\theta = \sigma_c^2/\bar{c}$  are the shape and scale parameters, respectively. It is worth noting that normalizing the distribution as  $\chi' \equiv \chi/\bar{c}$  allows us to reduce the problem to only the shape parameter  $\lambda$  [2,19,20];



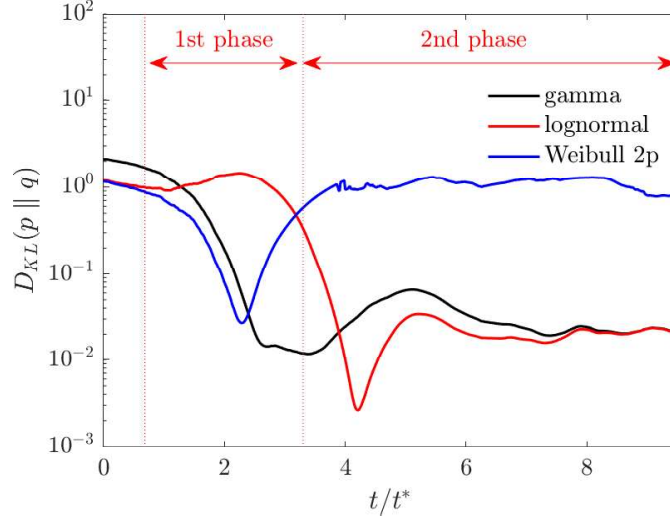


FIG. 4. Kullback-Leibler divergence of the PDF from the DNS results (semilogarithmic plot): comparison among the gamma, the lognormal, and the Weibull  $2p$  distributions. The two vertical dashed lines indicate different phases of the mixing processes as defined in Sec. III. The KL divergence of the gamma distribution presents a good overall behavior, and it is the most suitable choice for modeling the scalar-field PDF for all the time steps.

(2) the lognormal distribution,

$$p(\chi|\mu_l, \sigma_l) = \frac{1}{\chi \sigma_l \sqrt{2\pi}} \exp\left[-\frac{(\ln \chi - \mu_l)^2}{2\sigma_l^2}\right] \quad (4)$$

for  $\chi > 0$  and with the parameters,

$$\begin{aligned} \mu_l &= \ln(\bar{c}^2 / \sqrt{\sigma_c^2 + \bar{c}^2}), \\ \sigma_l &= \sqrt{\ln(\sigma_c^2 / \bar{c}^2 + 1)}, \end{aligned} \quad (5)$$

(3) the Weibull  $2p$  distribution,

$$p(\chi|a_w, b_w) = \frac{b_w}{a_w} \left(\frac{\chi}{a_w}\right)^{b_w-1} \exp\left[-\left(\frac{\chi}{a_w}\right)^{b_w}\right], \quad (6)$$

being  $a_w$  and  $b_w$  the scale and the shape parameters, respectively, set as

$$\begin{aligned} i_c^2 + 1 - \frac{\Gamma(1 + \frac{2}{b_w})}{[\Gamma(1 + \frac{1}{b_w})]^2} &= 0, \\ a_w &= \frac{\bar{c}}{\Gamma(1 + \frac{1}{b_w})}. \end{aligned} \quad (7)$$

We point out that the computation of  $b_w$  requires to solve the nonlinear Eq. (8). We mention that for practical application the shape parameters can be conveniently approximated as  $b_w \approx (1/i_c)^{1.086}$  e.g., Ref. [21].

As shown in Fig. 4, close to  $t_0$  the lognormal distribution is not appropriate since it is not able to reproduce the effects of the meandering process in the near field as observed close to the scalar source in wind-tunnel experiments. Conversely, it provides accurate estimates of the scalar PDF

after the homogenization process induced by the relative dispersion. The Weibull  $2p$  distribution performs suitable approximations of the concentration PDF in the near field, whereas it fails to model the distribution of the scalar at large values of  $t/t^*$ .

The gamma distribution shows a more accurate overall behavior providing a good agreement with the numerical solutions both in the near and in the far field. Such behavior suggests that the gamma PDF is a robust model being able to replicate the main features of the mixing process over the entire DNS.

### B. Mixing

As a second step, we discuss here the implications of a mixing process due to the interaction of pollutant particles, assuming, based on the results presented in the previous paragraph, that the PDF of the concentration within our reference volume is a gamma distribution. In order to analyze the mixing process, we focus on the fluctuations intensity  $i_c$ , that progressively goes to zero. Note that because of the imposed boundary conditions (Sec. II), the decay of  $i_c$  is entirely due to the reduction of the standard deviation  $\sigma_c$  since the spatially averaged concentration  $\bar{c}(t)$  remains unaltered.

We represent the passive-scalar puff as constituted of an ensemble of “marked” fluid particles so that the mixing process is modeled as a “discrete” phenomenon resulting by the interaction of pairs of marked fluid particles. This is a classical pattern in PDF methods for the prediction of concentration fluctuations (referred to as micromixing models) implemented in Lagrangian one-particle dispersion models [9,22]. In this kind of model, each fluid particle exchanges mass with the surrounding particles and, as a consequence, the concentration statistics defined by an ensemble of neighboring particles evolve in time. Then, following this analogy, the concentrations of the fluid particles can be considered as single realizations of the same random variable whose statistical behavior is modeled by a distribution that we assume to be a gamma PDF. The two fluid particles, denoted as 1 and 2, exchange mass each other so that the temporal evolution of their concentrations develops as a system of two ordinary differential equations,

$$\begin{aligned}\frac{dc_1}{dt} &= -\frac{c_1 - c_2}{\tau_m}, \\ \frac{dc_2}{dt} &= -\frac{c_2 - c_1}{\tau_m},\end{aligned}\tag{8}$$

here  $\tau_m$  is the characteristic timescale of the mixing process. The solution of the system above in the time-interval  $[t', t' + \Delta t]$  is as follows:

$$\begin{aligned}c_1(t' + \Delta t) &= (1 - \alpha)c_1(t') + \alpha c_2(t'), \\ c_2(t' + \Delta t) &= \alpha c_1(t') + (1 - \alpha)c_2(t'),\end{aligned}\tag{9}$$

where

$$\alpha \equiv \frac{1}{2} \left[ 1 - \exp\left(-2\frac{\Delta t}{\tau_m}\right) \right].\tag{10}$$

Generalizing this approach to any pair of fluid particles  $i$  and  $j$  within the domain, we conclude that predicting the effect of mixing is equivalent to estimate the PDF of a new random variable  $c_k$  given by a weighted sum of  $c_i$  and  $c_j$ ,

$$c_k(t' + \Delta t) = (1 - \alpha)c_i(t') + \alpha c_j(t').\tag{11}$$

The PDF of  $c_k$  is then given by the convolution of the PDFs for  $c_i$  and  $c_j$ . Since  $c_i(t')$  and  $c_j(t')$  are both distributed according to the same gamma PDF  $p(\lambda, \theta)$ , we have that

$$\begin{aligned}(1 - \alpha)c_i(t') &\text{ follows } p_i[\lambda, (1 - \alpha)\theta], \\ \alpha c_j(t') &\text{ follows } p_j[\lambda, \alpha\theta].\end{aligned}\tag{12}$$

As far as we are aware, simple expressions for the convolution of two gamma distributions having different scale parameters [as in Eq. (13)] are not known. Moschopoulos [23] and Sim [24] provided the exact convolution as a sum of infinite terms, and Mathai [25] and Akkouchi [26] proposed some complicated formulas. An alternative approach was investigated in Stewart *et al.* [27] who showed that the sum of gamma PDFs is suitably approximated by a gamma distribution if the scale parameters differ no more than a factor of 10, and the shape parameters are not below 0.1. In our case these conditions are generally satisfied. The first condition is fulfilled for  $\Delta t \geq 0.2 \tau_m$ , and the second one is fulfilled for  $i_c \lesssim 3.2$ . Therefore, the PDF  $p_k(\lambda_k, \theta_k)$  of  $c_k$  [Eq. (11)] is suitably approximated as a gamma distribution [27], and its scale and shape parameters can be determined by computing mean and variance as follows:

$$\begin{aligned}
 \bar{c}_k &= \lambda_k \theta_k \\
 &= \lambda(1 - \alpha)\theta + \lambda\alpha\theta \\
 &= \lambda\theta, \\
 \sigma_{c,k}^2 &= \lambda_k \theta_k^2 = \lambda(1 - \alpha)^2 \theta^2 + \lambda\alpha^2 \theta^2 \\
 &= \lambda\theta^2[(1 - \alpha)^2 + \alpha^2], \\
 \theta_k &= \frac{\sigma_{c,k}^2}{\bar{c}_k} \\
 &= \theta[\alpha^2 + (1 - \alpha)^2], \\
 \lambda_k &= \frac{\bar{c}_k^2}{\sigma_{c,k}^2} \\
 &= \frac{\lambda}{\alpha^2 + (1 - \alpha)^2}.
 \end{aligned} \tag{13}$$

As a consequence of the mixing process, the first two moments of the concentration PDF evolve as (dropping the indices for clarity),

$$\begin{aligned}
 \bar{c}(t' + \Delta t) &= \bar{c}(t'), \\
 \sigma_c^2(t' + \Delta t) &= \beta \sigma_c^2(t'),
 \end{aligned} \tag{14}$$

where

$$\beta \equiv \alpha^2 + (1 - \alpha)^2 = \frac{1}{2} \left[ 1 + \exp\left(-4 \frac{\Delta t}{\tau_m}\right) \right]. \tag{15}$$

Performing a limited development of this process for short intervals and neglecting the higher-order terms, we obtain the evolution of the characteristics of the distribution between  $t'$  and  $t' + \Delta t$ ,

$$\begin{aligned}
 \bar{c}(t' + \Delta t) &= \bar{c}(t') \\
 \sigma_c^2(t' + \Delta t) &= \left(1 - 2 \frac{\Delta t}{\tau_m}\right) \sigma_c^2(t').
 \end{aligned} \tag{16}$$

Since Eq. (17) represents the incremental ratio of  $\sigma_c$ , we can write the time derivative of the concentration variance as

$$\lim_{\Delta t \rightarrow 0} \frac{\sigma_c^2(t' + \Delta t) - \sigma_c^2(t')}{\Delta t} = \frac{d\sigma_c^2}{dt} = -\frac{2}{\tau_m} \sigma_c^2, \tag{17}$$

which essentially expresses the dissipation rate of the scalar variance  $\varepsilon_c \equiv -2\nu \langle \partial c' / \partial x_i \rangle^2$ .

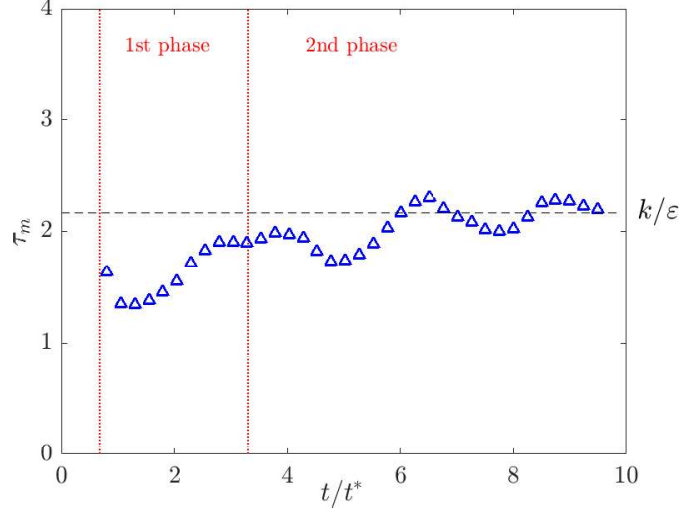


FIG. 5. Mixing timescale  $\tau_m$  vs  $t/t^*$ . In the far field  $\tau_m$  reaches the asymptotic value of  $k/\varepsilon$ .

The above expression can be integrated in order to obtain the temporal evolution of  $\sigma_c^2$ ,

$$\sigma_c^2(t) = \sigma_c^2(0) \exp\left(-2\frac{t}{\tau_m}\right), \quad (18)$$

and, therefore,

$$\sigma_c(t) = \sigma_c(0) \exp\left(-\frac{t}{\tau_m}\right). \quad (19)$$

Since we have  $\bar{c}(t) = \bar{c}(0)$ , we finally obtain that the temporal decay of  $i_c$  evolves as

$$i_c(t) = i_c(0) \exp\left(-\frac{t}{\tau_m}\right), \quad (20)$$

showing that the assumption of the gamma distribution for the concentration PDF implies that the fluctuations intensity is given by a negative exponential, whose decay is governed by a typical mixing timescale.

The mixing timescale  $\tau_m$  can be estimated from our numerical experiments by locally fitting Eq. (20) (i.e., over short intervals) with the DNS results for  $i_c$ , having  $\tau_m$  as a free parameter (evolving in time). Once excluded the initial transient ( $t/t^* < 1$ ), this timescale exhibits a smoothly growing trend in the first phase and oscillates around a constant value in the second phase. At later times, in the second phase of the simulation  $\tau_m$  attains an asymptotic value equal to the dissipative timescale  $\tau \equiv k/\varepsilon$  ( where  $k \equiv \frac{3}{2}\sigma_u^2$  is the turbulent kinetic energy and  $\varepsilon \equiv 2\nu\langle s_{ij}s_{ij} \rangle$  is its dissipation rate ) [28,29] as pointed out in Fig. 5. We highlight that the numerical results show that for large values of  $t/t^*$  the ratio  $\tau/\tau_m \approx 1$ , which is in agreement with the findings of other authors that reported values in the range of 0.3–1.56 for different configurations [22,30–33].

#### IV. ANALOGIES WITH WIND-TUNNEL RESULTS AND CROSS VALIDATION OF THE GAMMA MODEL

In Sec. III we have shown the temporal evolution of the normalized PDF of the passive scalar concentration and pointed out its link with the value of  $i_c$ : The shape of the PDF exhibits an exponential-like form as far as  $i_c > 1$ , and it abruptly changes shape for  $i_c = 1$  and evolves as a Gaussian-like distribution as  $i_c \rightarrow 0$ . This same behavior, observed here adopting statistics over a

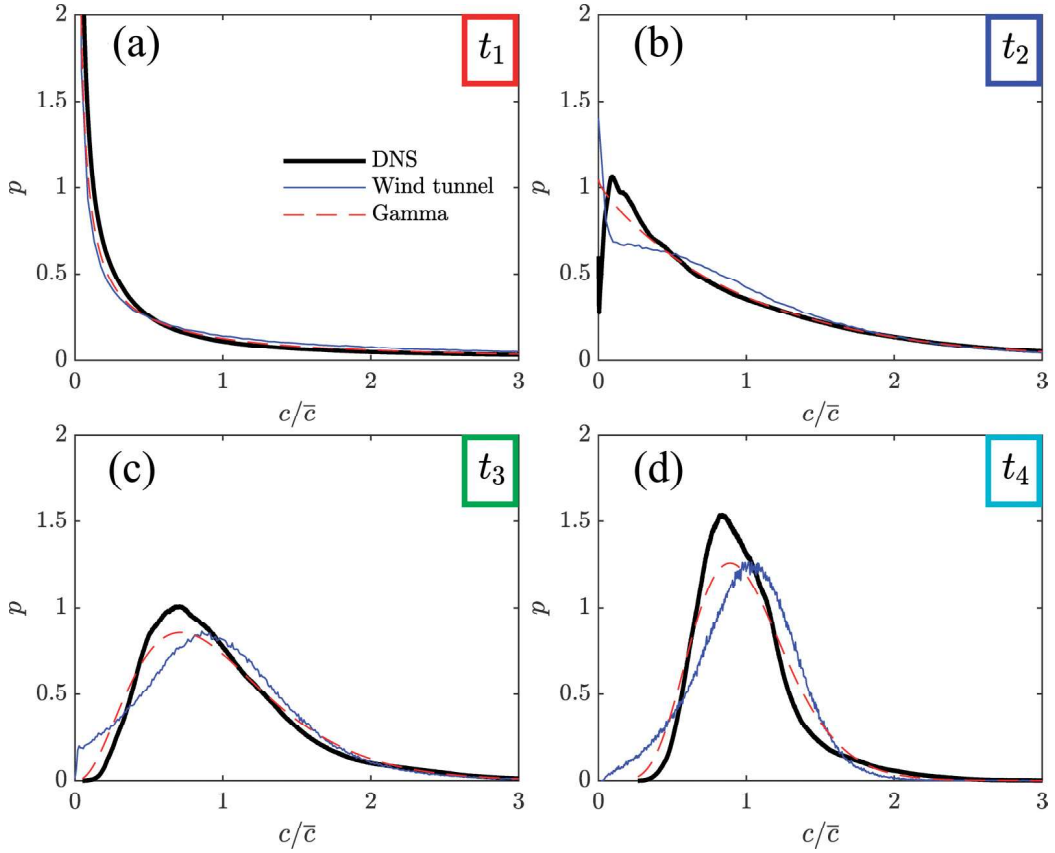


FIG. 6. Comparison between the normalized PDFs of the passive scalar concentration from the DNS, the wind-tunnel measurements by Nironi *et al.* [13], and the gamma distribution of Eq. (3) at decreasing values of  $i_c$ : (a)  $i_c = 2.25$  at  $t_1$ , (b)  $i_c = 1$  at  $t_2$ , (c)  $i_c = 0.53$  at  $t_3$ , and (d)  $i_c = 0.33$  at  $t_4$ .

control fluid volume for each time step, was observed in wind-tunnel experiments when analyzing one-point statistics obtained from concentration time series measured at a fixed location downwind a continuous scalar release in a turbulent boundary layer as described in Ref. [13]. Indeed, wind-tunnel experiments have shown that the statistics of the concentration of a continuous scalar plume in a boundary layer (i.e., a nonisotropic and nonhomogeneous velocity field) can be fully described by a gamma distribution as reported in Eq. (3).

In Fig. 6 we show a comparison between the present DNS results, the one-point wind-tunnel statistics performed by Nironi *et al.* [13] and the gamma distribution [Eq. (3)] for the same values of  $i_c$  (being  $t_1$ ,  $t_2$ ,  $t_3$ , and  $t_4$  the same as in Fig. 3). Here, we can appreciate how the DNS solutions and the wind-tunnel measurements exhibit a similar behavior and that the gamma distribution can be assumed as a suitable model for both numerical and experimental PDFs. To explain this evidence from a phenomenological stand point, we can rely on the depiction in Fig. 7, proposing the analogy between the present DNS simulation of an unsteady decaying puff and the wind-tunnel results of a steady release of a passive scalar in a turbulent wall-bounded flow.

A peculiar aspect of the dispersion of localized atmospheric releases is the appearance of a meandering motion of the plume [12] due to the action of turbulent eddies larger than the plume size. The meandering highly affects the dispersion process in the near field of the source and is gradually attenuated moving away from it as the size of the plume increases under the action of the relative dispersion (due to eddies smaller than the puff size). As the relative dispersion finally induces the

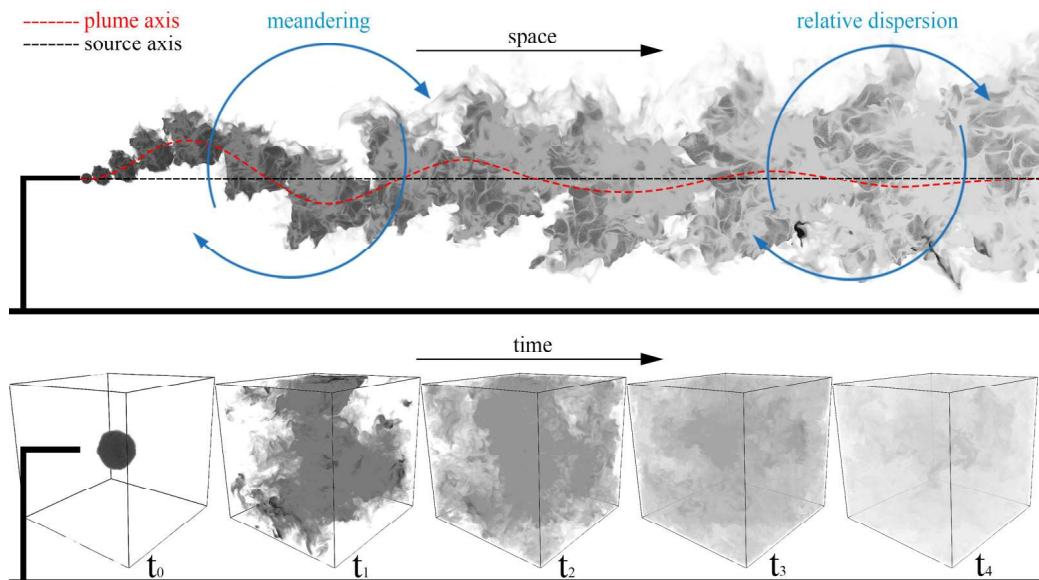


FIG. 7. Top panel: sketch of a plume as made of multiple puffs, the Eulerian approach. Bottom panel: numerical point of view, the Lagrangian approach. We observe the relationship between *space* and *time* in the two different approaches as well as the regions of *meandering* and *relative dispersion*.

plume size to exceed the size of the larger-scale structure of the flow, the plume meandering is suppressed. At first sight, we can consider that the transition between these two regimes occurs as  $i_c$  drops below 1, and the intermittency is suppressed in the core of the plume [13].

In the puff, at each time step, every point of the simulation domain can be considered as a possible realization of the plume along the source axis at a given distance from the source, in the equivalent reference wind-tunnel experiment. In other words, we can consider that the DNS results mimic the evolution of the scalar puffs released in the wind tunnel as they get translated horizontally by the mean flow whereas undergoing turbulent advection. Invoking the ergodicity of both numerical and experimental flows, we could, therefore, compare the spatial statistics computed on the simulation output (Fig. 7, bottom) with the single-point temporal statistics computed in the wind tunnel (Fig. 7, top). Thus, taking a specific instant of the DNS, the spatial statistics of the concentration over the entire simulation box would match the temporal statistics of the concentration signal measured at the corresponding position (always on the plume centreline, i.e., at the source height) in the wind-tunnel experiment. In this framework, the near-source meandering region in the experiments (Fig. 7, top panel) in which one-point statistics exhibit high intermittency, corresponds to the first phase of the DNS simulation (Fig. 7, bottom panel,  $t_1$ ) in which the scalar has not filled the domain yet, and the spatial concentration statistics are affected by the presence of zero values of the concentration in part of it. Similarly, the far-field relative dispersion region in which the intermittency in the one-point statistics is suppressed, corresponds to the second phase of our DNS results (Fig. 7, bottom panel,  $t_3$  and  $t_4$ ) in which the scalar has filled the box and the mixing acts towards a complete homogenization of the concentration.

In the description of the dispersion process made so far, we adopted a jargon familiar to researchers working in the field of the atmospheric pollutant dispersion. Other researcher working reactive and nonreactive scalar mixing in turbulent flows adopt a different terminology to identify different regimes of the time evolution of the tracer distribution. According to this terminology, the second phase of our numerical simulations shows a behavior similar to that of the “confined mixture” regime in which, following Duplat and Villermaux [7], a self-convolution mechanism leads to a sequence of gamma distributions until complete mixing is reached. The dispersion in

the near-source region where the plume meanders in an unbounded environment has been instead referred as “ever dispersion mixture” by Duplat *et al.* [34]. The near-source region investigated by Duplat *et al.* [34] is, however, more similar to the initial transient of our simulations in which the concentration PDFs are not consistent with the gamma model (see Fig. 2 between  $t_0$  and  $t_1$ ), rather than what we referred to as the first phase where the gamma model actually holds. Similar considerations about the lack of accuracy of the gamma distribution as a model for the concentration PDFs very close to the release point were also presented by Sawford and Stapountzis [35] and Ardeshiri *et al.* [14].

## V. CONCLUSIONS

We employed direct numerical simulations to investigate the passive-scalar dispersion and the related mixing processes within turbulent flows in a synergistic approach that involved the use of wind-tunnel measurements for the cross validation (numerical and experimental) of the gamma model for the scalar distribution concentration. In particular, we simulated a single puff in homogeneous isotropic turbulence in a cubic domain with a regular grid and periodic boundary conditions.

Focus of our paper is the analysis of the evolution in time of the spatial statistics of the scalar concentration within a fluid volume as seen in a reference frame following the mean flow. As first step, we tested the capability of different model distributions (the gamma, the lognormal, and the Weibull  $2p$ ) in reproducing the spatial PDF of the concentration showing that the gamma distribution is the most robust and convenient model to describe the whole temporal evolution of the dispersion process. Assuming the gamma distribution as the PDF describing the scalar concentration within a given volume, we developed a simple probabilistic mixing model, that allows us to link the decay rate of the intensity of the concentration fluctuations  $i_c$  to a characteristic mixing timescale.

Finally, drawing an analogy between the present DNS results and the previous experimental data allows us to explain the similarity observed between the spatial statistics in the system considered here and the one-point statistics registered in wind-tunnel experiments. Notably, the first phase of the simulations provides a PDF that can be observed in wind-tunnel experiments by registering the concentration signal close to the source when the meandering of the plume is intense. Instead, in the second phase of the simulation when the scalar has filled the whole domain the concentration PDF corresponds to experimental PDF registered far from the source where the plume meandering is suppressed, and the plume spread is governed by the relative dispersion.

A comparison between DNS and wind-tunnel measurements of stratified turbulence will be the subject of a future investigation along the lines of the present paper. Indeed, unlike the HIT case, in the presence of stratification, sporadic extreme events develop in the vertical component of the velocity and in the temperature affecting mixing and transport properties of turbulent flows as shown in previous works [36–39].

## ACKNOWLEDGMENTS

R.M. acknowledges support from the Project “EVENTFUL” (Grant No. ANR-20-CE30-0011), funded by the French “Agence Nationale de la Recherche”—ANR.

- 
- [1] K. R. Sreenivasan, Turbulent mixing: A perspective, *Proc. Natl. Acad. Sci. USA* **116**, 18175 (2018).
  - [2] E. Villermaux and J. Duplat, Mixing as an Aggregation Process, *Phys. Rev. Lett.* **91**, 184501 (2003).
  - [3] J. Bakosi, P. Franzese, and Z. Boybeyi, Probability density function modeling of scalar mixing from concentrated sources in turbulent channel flow, *Phys. Fluids* **19**, 115106 (2007).
  - [4] Q. Nguyen and D. V. Papavassiliou, A statistical model to predict streamwise turbulent dispersion from the wall at small times, *Phys. Fluids* **28**, 125103 (2016).

- [5] P. R. Van Slooten, Jayesh, and S. B. Pope, Advances in pdf modeling for inhomogeneous turbulent flows, *Phys. Fluids* **10**, 246 (1998).
- [6] E. Yee and A. Skvortsov, Scalar fluctuations from a point source in a turbulent boundary layer, *Phys. Rev. E* **84**, 036306 (2011).
- [7] J. Duplat and E. Villermaux, Mixing by random stirring in confined mixtures, *J. Fluid Mech.* **617**, 51 (2008).
- [8] D. J. Wilson and B. W. Simms, *Exposure time effects on concentration fluctuations in plumes* (Alberta Environment, 1985).
- [9] M. Cassiani, The volumetric particle approach for concentration fluctuations and chemical reactions in Lagrangian particle and particle-grid models, *Boundary-Layer Meteorol.* **146**, 207 (2013).
- [10] M. B. Bertagni, M. Marro, P. Salizzoni, and C. Camporeale, Solution for the statistical moments of scalar turbulence, *Phys. Rev. Fluids* **4**, 124701 (2019).
- [11] M. B. Bertagni, M. Marro, P. Salizzoni, and C. Camporeale, Level-crossing statistics of a passive scalar dispersed in a neutral boundary layer, *Atmos. Environ.* **230**, 117518 (2020).
- [12] M. Cassiani, M. Bertagni, M. Marro, and P. Salizzoni, Concentration fluctuations from localized atmospheric releases, *Boundary-Layer Meteorol.* **177**, 461 (2020).
- [13] C. Nironi, P. Salizzoni, M. Marro, P. Mejean, N. Grosjean, and L. Soulhac, Dispersion of a passive scalar fluctuating plume in a turbulent boundary layer. Part I: Velocity and concentration measurements, *Boundary-Layer Meteorol.* **156**, 415 (2015).
- [14] H. Ardeshiri, M. Cassiani, S. Park, A. Stohl, I. Pizzo, and S. Dinger, On the convergence and capability of large eddy simulation for passive plumes concentration fluctuations in an infinite- $Re$  neutral boundary layer, *Boundary-Layer Meteorol.* **176**, 291 (2020).
- [15] P. D. Mininni, D. Rosenberg, R. Reddy, and A. Pouquet, A hybrid mpi-openmp scheme for scalable parallel pseudospectral computations for fluid turbulence, *Parallel Comput.* **37**, 316 (2011).
- [16] See Supplemental Material at <https://link.aps.org/supplemental/10.1103/PhysRevFluids.6.034502> to suitably capture the connection between the concentration pdf and the concentration fluctuations intensity  $i_c$ .
- [17] S. Kullback and R. A. Leibler, On information and sufficiency, *Ann. Math. Stat.* **22**, 79 (1951).
- [18] *Handbook of Mathematical Functions: With Formulas, Graphs, and Mathematical Tables*, edited by M. Abramowitz and I. A. Stegun, National Bureau of Standards Applied Mathematics Series (National Bureau of Standards, Washington, DC, 1965).
- [19] E. Yee and R. Chan, A simple model for the probability density function of concentration fluctuations in atmospheric plumes, *Atmos. Environ.* **31**, 991 (1997).
- [20] A. Skvortsov and E. Yee, Scaling laws of peripheral mixing of passive scalar in a wall-shear layer, *Phys. Rev. E* **83**, 036303 (2011).
- [21] D. Oetl and E. Ferrero, A simple model to assess odour hours for regulatory purposes, *Atmos. Environ.* **155**, 162 (2017).
- [22] M. Cassiani, P. Franzese, and U. Giostra, A PDF micromixing model of dispersion for atmospheric flow. Part I: development of the model, application to homogeneous turbulence and to neutral boundary layer, *Atmos. Environ.* **39**, 1457 (2005).
- [23] P. G. Moschopoulos, The distribution of the sum of independent gamma random variables, *Ann. Inst. Statist. Math.* **37**, 541 (1985).
- [24] C. H. Sim, Point processes with correlated gamma interarrival times, *Stat. Probabil. Lett.* **15**, 135 (1992).
- [25] A. M. Mathai, Storage capacity of a dam with gamma type inputs, *Ann. Inst. Statist. Math.* **34**, 591 (1982).
- [26] M. Akkouchi, On the convolution of gamma distributions, *Soochow J. Math.* **31**, 205 (2005).
- [27] T. Stewart, L. W. G. Strijbosch, H. Moors, and P. van Batenburg, A simple approximation to the convolution of gamma distributions (CentER Discussion Paper, 2007).
- [28] S. B. Pope, *Turbulent Flows* (Cambridge University Press, Cambridge, UK, 2011).
- [29] M. Cassiani, A. Radicchi, J. Albertson, and U. Giostra, An efficient algorithm for scalar PDF modeling in incompressible turbulent flow; numerical analysis with evaluation of IEM and IECM micro-mixing models, *J. Comput. Phys.* **223**, 519 (2007).



- [30] Z. Warhaft and J. L. Lumley, An experimental study of the decay of temperature fluctuations in grid-generated turbulence, *J. Fluid Mech.* **88**, 659 (1978).
- [31] S. Tavoularis and S. Corrsin, Experiments in nearly homogenous turbulent shear flow with a uniform mean temperature gradient. part 1, *J. Fluid Mech.* **104**, 311 (1981).
- [32] Z. Warhaft, Passive scalars in turbulent flows, *Annu. Rev. Fluid Mech.* **32**, 203 (2000).
- [33] S. Heinz, *Statistical Mechanics of Turbulent Flows* (Springer-Verlag, Berlin, Heidelberg, New York, Tokyo, 2003).
- [34] J. Duplat, C. Innocenti, and E. Villermaux, A nonsequential turbulent mixing process, *Phys. Fluids* **22**, 035104 (2010).
- [35] B. L. Sawford and H. Stapountzis, Concentration fluctuations according to fluctuating plume models in one and two dimensions, *Boundary-Layer Meteorol.* **37**, 89 (1986).
- [36] R. Marino, P. Mininni, D. Rosenberg, and A. Pouquet, Inverse cascades in rotating stratified turbulence: fast growth of large scales, *Europhys. Lett.* **102**, 44006 (2013).
- [37] F. Feraco, R. Marino, A. Pumir, L. Primavera, P. Mininni, A. Pouquet, and D. Rosenberg, Vertical drafts and mixing in stratified turbulence: Sharp transition with froude number, *Europhys. Lett.* **123**, 44002 (2018).
- [38] A. Pouquet, D. Rosenberg, and R. Marino, Linking dissipation, anisotropy and intermittency in rotating stratified turbulence, *Phys. Fluids* **31**, 105116 (2019).
- [39] D. Buaria, A. Pumir, F. Feraco, R. Marino, A. Pouquet, D. Rosenberg, and L. Primavera, Single-particle lagrangian statistics from direct numerical simulations of rotating-stratified turbulence, *Phys. Rev. Fluids* **5**, 064801 (2020).

## Chapter 6

# Conclusions

In this thesis work I developed a framework involving numerical simulations, theoretical modeling, observations and laboratory experiments aimed to characterize the fundamental properties of turbulence in stratified flows of geophysical interest. In particular, the main finding of the thesis concerns the evidence of the presence of large-scale drafts both in the vertical component of the velocity and in the temperature field. Such “large-scale intermittency” has been previously detected in observations of both the atmosphere and the oceans. All the chapters, with the exception of the fifth, aim at providing a characterization of the drafts and how they influence the small scales of the flow, in particular the intermittency at small-scales, the mixing and the dissipation.

In these conclusions, I will briefly summarize the main results of each chapter in view of possible extensions of this thesis work and to suggest possible connections with other fields of investigation, and with other branches of physics which may also offer new outlooks.

After the introductory first chapter in which several details on turbulent flows, the equations and the different tools used are given, the second chapter explains how such large-scale intermittency depends on the Froude number and reveals the importance of this phenomenon for a range of values of the parameters relevant to both the atmosphere and the oceans.

This chapter, not only serves as an introduction to the main finding of the thesis work, that is the presence of the large-scale drafts in fluid flows in presence of both rotation and stratification, but also represents the basis for further possible studies, some of which have been carried out in the subsequent chapters, some others are still ongoing. First, the presence of the large-scale drafts could have deep implications in several physical contexts, like for instance in aerodynamics. It is well known, indeed, that a particularly dangerous phenomenon for the comfort and security of airplane flights is the so called “clear air turbulence” (CAT), in which the presence of large scale velocity shears among air masses moving at different speeds produces sudden pressure forces on the body of the airplane.

An interesting consequence of the findings of this chapter consists in the observed correspondence between the vertical drafts and the regions that are more prone to develop overturning. This intimately connects the presence of the drafts with the enhancement of mixing. In other words, drafts could help in homogenizing the flow in which they develop. These results may have important implications for the dispersion of polluting particles in the atmosphere and deserve further studies, to enlarge the range of parameters and to study in a deeper detail the statistics of two or more particles. Another interesting observation consists in the fact that when the Lagrangian particles encounter the draft, the motion of the particles becomes more chaotic, that is the trajectories of two particles starting in very close positions in the phase space tend to diverge when they meet a draft, while they continue to move together when

they do not. The chaotic behaviour of such a system is still under study and deserves particular attention. Such a problem may have several important implications in different contexts, like in meteorology and climatology, in that it may supply some indications about the origin of the transition to chaos in the atmosphere.

Chapter three, reports the first observation of extreme vertical drafts made through ground-based instruments. The article reported in this section concerns mainly the observational aspects of the investigation. The comparison with the results of the DNSs showed that the structures obtained numerically and the ones observed through radars share some common features. This, however, emphasized the necessity of a deeper investigation, from both the numerical and observational point of view. What could be very important in this kind of study is the correlation between the occurrence of the drafts and the intensity of the shear of the horizontal velocity, also shown in the introduction of the chapter, for the clear connection with CAT cited above.

Although chapter four seems to have a more theoretical aspect, in the attempt to connect intermittency at large-scales with the one at small-scales (internal intermittency), it also has several practical implications for atmospheric studies that deserve further attention. First, a clear connection between the presence of the drafts developing overturning and an enhancement of vorticity, which in turn produces small-scales and internal intermittency is shown. Second, this produced enhancement of vorticity, feeds small-scale turbulence and dissipation. It was shown that for the values of the Froude number at which the peak of kurtosis due to the drafts is observed the sole 10% of the domain volume can account for the 50% of total kinetic energy dissipation. The connection between large scale drafts in inhomogeneous media and enhanced energy dissipation may represent an important theoretical example of a “catastrophe mechanism”, in which large scale shears may produce, through some sort of resonant mechanism (like the one that brings to draft production) small scales in a finite time. In such mechanisms small scales are generated in a time much shorter than that in which the turbulent energy cascade, that brings energy to the smallest scales, is produced by nonlinearities. These mechanisms are usually invoked to explain why, even in presence of an almost vanishing dissipation, the entropy of the system can increase in a relatively short time. Catastrophe mechanisms have been invoked in different contexts as a possible driver for efficient energy dissipation. A typical example is the heating of the solar corona, where the magnetic origin of the high temperature is now a well established paradigm, though a clear connection between the large scale magnetic shears (which represent a source of inhomogeneity and anisotropy for the solar atmosphere, just like stratification does for Earth’s atmosphere), ubiquitous on the Sun, and the mechanism to effectively dissipate them is still unclear.

Further understanding of this mechanism of enhanced dissipation through large scale intermittency, other than being important for the obvious implications it has in the studies of global climate heating and meteorology, in this sense may open new perspectives also in other fields of investigation (like the MagnetoHydroDynamics of the solar atmosphere) which anyway share many similarities with Earth’s atmosphere. Finally, as observed in the conclusions of the articles included in this chapter, establishing a link between large-scale and small-scale intermittency may help to produce more realistic closure models for scholars working, for instance, on Large Eddy Simulations of turbulence, in which the large scales of turbulence are exactly resolved, while the influence of the smallest scales is modeled (see, e.g., the closure models by Smagorinsky [71] and the ones by Germano et al. [23]).

Finally, chapter five deals with the problem of diffusion of passive tracers in turbulent flows and we carried out a comparison between laboratory measurements taken in a wind tunnel and the numerical simulations in a HIT case, by stressing in particular

the very good agreement of the results and the possibility to better investigate what probability function (apparently the Gamma distribution, in our case) yields the best results to describe the concentration of tracers. The importance of studies of this kind in the problem of diffusion of pollutants in the atmosphere cannot be emphasized enough. However, this is a rather preliminary study. The HIT case is not the best model for this kind of studies, since the majority of pollutant is produced in proximity of the Earth's shear layer and, in any case, the effects of rotation and stratification may play an important role in the dispersion and mixing of particles in the atmosphere, as shown in the first chapter. Further investigations about this problem are still in active development.

In conclusion, I hope to have the possibility to continue and expand my research skills by furtherly investigating all the interesting and promising topics explored in the present PhD thesis, with the attitude to think that each finished chapter opens up new scenarios which may bring to a deeper understanding of this marvelous adventure represented by the discovery of the world that surrounds us.



# Bibliography

- [1] S. V. Anisimov et al. “Aeroelectric structures and turbulence in the atmospheric boundary layer”. In: *Nonlinear Processes in Geophysics* 20.5 (2013), pp. 819–824.
- [2] G. K. Batchelor and A. A. Townsend. “The Nature of Turbulent Motion at Large Wave-Numbers”. In: *Proceedings of the Royal Society of London. Series A, Mathematical and Physical Sciences* 199 (1949), pp. 238–255.
- [3] P. Billant and J-M. Chomaz. “Experimental evidence for a new instability of a vertical columnar vortex pair in a strongly stratified fluid”. In: *J. Fluid Mech.* 418 (2000), pp. 167–188.
- [4] R. Bolgiano Jr. “Turbulent spectra in a stably stratified atmosphere”. In: *Journal of Geophysical Research (1896-1977)* 64.12 (1959), pp. 2226–2229.
- [5] G. Brethouwer et al. “Scaling analysis and simulation of strongly stratified turbulent flows”. In: *J. Fluid Mech.* 585 (2007), pp. 343–368.
- [6] S.M. de Bruyn Kops. “Classical scaling and intermittency in strongly stratified Boussinesq turbulence”. In: *J. Fluid Mech.* 775 (2015), pp. 436–463.
- [7] D. Buaria et al. “Single-particle Lagrangian statistics from direct numerical simulations of rotating stratified turbulence”. In: *Phys. Rev. Fluids* 5 (2020), p. 064801.
- [8] M. Cassiani et al. “Concentration Fluctuations from Localized Atmospheric Releases”. In: *Phys. Rev. E* 177 (2020), pp. 461–510.
- [9] S. Chandrasekhar. *Hydrodynamic and Hydromagnetic Stability*. Dover Publications, 1981.
- [10] J. L. Chau et al. “Radar observation of extreme vertical drafts in the polar summer mesosphere”. In: *Geophys. Res. Lett.* 48.16 (2021), e2021GL094918.
- [11] J.L. Chau et al. “Polar mesospheric horizontal divergence and relative vorticity measurements using multiple specular meteor radars”. In: *Radio Science* 52.7 (2017), pp. 811–828.
- [12] E. D’Asaro, R-C. Lien, and F. Henyey. “High-Frequency Internal Waves on the Oregon Continental Shelf”. In: *J. Phys. Oceanogr.* 37 (2007), pp. 1956–1967.
- [13] E. M. Dewan and R. H. Picard. “Mesospheric bores”. In: *Journal of Geophysical Research: Atmospheres* 103.D6 (1998), pp. 6295–6305.
- [14] J Fackrell. “A Flame Ionization Detector for Measuring Fluctuating Concentration”. In: *Journal of Physics E: Scientific Instruments* 13 (1980), pp. 888–893.
- [15] F. Feraco et al. “Connecting Large-Scale Velocity and Temperature Bursts with Small-Scale Intermittency in Stratified Turbulence”. In: *Eur. Phys. Lett.* 135 (2021), p. 14001.
- [16] F. Feraco et al. “Vertical drafts and mixing in stratified turbulence: sharp transition with Froude number”. In: *Eur. Phys. Lett.* 123 (2018), p. 44002.

- [17] J. Finnigan. “A note on wave-turbulence interactions and the possibility of scaling the very stable Planetary Boundary Layer”. In: *Bound. Lay. Met.* 90 (1999), pp. 529–539.
- [18] J. G. Fitzgerald and B.F. Farrell. “Vertically Sheared Horizontal Flow-Forming Instability in Stratified Turbulence: Analytical Linear Stability Analysis of Statistical State Dynamics Equilibria”. In: *Journal of the Atmospheric Sciences* 75 (12) (2018), pp. 4201–4227.
- [19] U. Frisch. *Turbulence: The Legacy of A. N. Kolmogorov*. Cambridge: Cambridge University Press, 1995.
- [20] D. C. Fritts et al. “Mesospheric Bore Evolution and Instability Dynamics Observed in PMC Turbo Imaging and Rayleigh Lidar Profiling Over Northeastern Canada on 13 July 2018”. In: *Journal of Geophysical Research: Atmospheres* 125.14 (2020), e2019JD032037.
- [21] A. C. Naveira Garabato et al. “Widespread Intense Turbulent Mixing in the Southern Ocean”. In: *Science* 303.5655 (2004), pp. 210–213.
- [22] C. Garrett and W. Munk. “Space-time scales of internal waves: A progress report”. In: *Journal of Geophysical Research (1896-1977)* 80.3 (1975), pp. 291–297.
- [23] M. Germano et al. “A dynamic subgrid scale eddy viscosity model”. In: *Phys. Fluids* A3 (1991), pp. 1760–1765.
- [24] H. van Haren and L. Gostiaux. “Where large deep-ocean waves break”. In: *Geophys. Res. Lett.* 42 (2015), pp. 2351–2357.
- [25] J. R. Herring and O. Métais. “Numerical experiments in forced stably stratified turbulence”. In: *J. Fluid Mech.* 202 (1989), pp. 97–115.
- [26] W. K. Hocking, B. Fuller, and B. Vandeppeer. “Real-Time Determination of Meteor-Related Parameters Utilizing Modern Digital Technology”. In: *Journal of Atmospheric and Solar-Terrestrial Physics* 63.2 (2001), pp. 155–169.
- [27] L. N. Howard. “Note on a paper of John W. Miles”. In: *J. Fluid Mech.* 10 (1961), pp. 509–512.
- [28] Y. Hozumi et al. “Geographical and Seasonal Variability of Mesospheric Bores Observed from the International Space Station”. In: *Journal of Geophysical Research: Space Physics* 124.5 (2019), pp. 3775–3785.
- [29] T. Ishihara, T. Gotoh, and Y. Kaneda. “Study of High Reynolds Number Isotropic Turbulence by Direct Numerical Simulation”. In: *Ann. Rev. Fluid Mech.* 41 (2009), pp. 165–180.
- [30] G. Ivey, K. Winters, and J. Koseff. “Density stratification, turbulence but how much mixing?” In: *Ann. Rev. Fluid Mech.* 40 (2008), pp. 169–184.
- [31] J. M. Klymak, R. Pinkel, and L. Rainville. “Direct Breaking of the Internal Tide near Topography: Kaena Ridge, Hawaii”. In: *J. Phys. Oceano.* 38 (2008), pp. 380–399.
- [32] A. N. Kolmogorov. “A refinement of previous hypotheses concerning the local structure of turbulence in a viscous incompressible fluid at high Reynolds number”. In: *Journal of Fluid Mechanics* 13.1 (1962), pp. 82–85.
- [33] A. N. Kolmogorov. “The Local Structure of Turbulence in Incompressible Viscous Fluid for Very Large Reynolds Numbers”. In: *Doklady Akademiia Nauk SSSR* 30 (1941), pp. 301–305.

- [34] R. H. Kraichnan. “Inertial Ranges in Two Dimensional Turbulence”. In: *Physics of Fluids* 10.7 (1967), pp. 1417–1423.
- [35] S. Kullback and R. A. Leibler. “On Information and Sufficiency”. In: *The Annals of Mathematical Statistics* 22.1 (1951), pp. 79–86.
- [36] R. Latteck et al. “MAARSY: The new MST radar on Andøya—System description and first results”. In: *Radio Science* 47.1 (2012).
- [37] Feng Li et al. “Investigation of a “wall” wave event”. In: *Journal of Geophysical Research: Atmospheres* 112.D4 (2007).
- [38] A. Maffioli, G. Brethouwer, and E. Lindborg. “Mixing efficiency in stratified turbulence”. In: *Journal of Fluid Mechanics* 794 (2016), R3.
- [39] L. Mahrt. “Intermittency of Atmospheric Turbulence”. In: *J. Atmos. Sci.* 46.1 (1989), pp. 79–95.
- [40] L. Mahrt and N. Gamage. “Observations of Turbulence in Stratified Flow”. In: *J. Atmos. Sci.* 44 (1987), pp. 1106–1122.
- [41] R. Marino et al. “Inverse cascades in rotating stratified turbulence: Fast growth of large scales”. In: *EuroPhys. Lett.* 102 (2013), p. 44006.
- [42] R. Marino et al. “Turbulence generation by large-scale extreme vertical drafts and the modulation of local energy dissipation in stably stratified geophysical flows”. In: (*PRF, under review*) <https://arxiv.org/abs/2106.15219> (2022).
- [43] A. Mashayek et al. “Efficiency of turbulent mixing in the abyssal ocean circulation”. In: *Geophysical Research Letters* 44.12 (2017), pp. 6296–6306.
- [44] C. Meneveau. “Lagrangian Dynamics and Models of the Velocity Gradient Tensor in Turbulent Flows”. In: *Annual Review of Fluid Mechanics* 43.1 (2011), pp. 219–245.
- [45] O. Métais et al. “Inverse cascade in stably stratified rotating turbulence”. In: *Dynamics of Atmospheres and Oceans* 23.1-4 (1996), pp. 193–203.
- [46] J. W. Miles. “On the stability of heterogeneous shear flows”. In: *J. Fluid Mech.* 10 (1961), pp. 496–508.
- [47] P. D. Mininni et al. “A hybrid MPI-OpenMP scheme for scalable parallel pseudospectral computations for fluid turbulence”. In: *Parallel Computing* 37 (2011), pp. 316–326.
- [48] A. S. Monin and A. M. Yaglom. *Statistical Fluid Mechanics: Mechanics of Turbulence*. MIT Press, Cambridge, vol. 2, 1979.
- [49] M. Nikurashin, G. K. Vallis, and A. Adcroft. “Routes to energy dissipation for geostrophic flows in the Southern Ocean”. In: *Nature Geosci.* 6 (2012), pp. 48–51.
- [50] C. Nironi et al. “Dispersion of a Passive Scalar Fluctuating Plume in a Turbulent Boundary Layer. Part I: Velocity and Concentration Measurements”. In: *Boundary-Layer Meteorology* 156 (2015), pp. 415–446.
- [51] A. M. Obukhov. “Effect of the Archimedean forces on the structure of the temperature field in a turbulent flow”. In: *Dokl. Akad. Nauk SSSR* 125 (1959), pp. 1246–1248.
- [52] A. M. Obukhov. “Spectral energy distribution in a turbulent flow”. In: *Izv. Akad. Nauk. SSSR. Ser. Geogr. i. Geofiz* 5 (1941), pp. 453–466.



- [53] M. Orsi et al. “Scalar mixing in homogeneous isotropic turbulence: A numerical study”. In: *Phys. Rev. Fluids* 6 (3 2021), p. 034502.
- [54] T.R. Osborn. “Estimates of the local rate of vertical diffusion from dissipation measurements”. In: *J. Phys. Oceano.* 10 (1980), pp. 83–89.
- [55] B. Pearson and B. Fox-Kemper. “Lognormal turbulence dissipation in global ocean models”. In: *Phys. Rev. Lett.* 120 (2018), p. 094501.
- [56] A. Pouquet et al. “Scaling laws for mixing and dissipation in unforced rotating stratified turbulence”. In: *J. Fluid Mech.* 844 (2018), pp. 519–545.
- [57] A. Pouquet et al. “Scaling laws for mixing and dissipation in unforced rotating stratified turbulence”. In: *J. Fluid Mech.* 844 (2018), pp. 519–545.
- [58] A. Pumir. “A numerical study of the mixing of a passive scalar in three dimensions in the presence of a mean gradient”. In: *Phys. Fluids* 6 (1994), pp. 2118–2132.
- [59] M. Rapp and F-J. Lübken. “Polar mesosphere summer echoes (PMSE): Review of observations and current understanding”. In: *Atmospheric Chemistry and Physics Discussions* 4.11/12 (2004), pp. 2601–2633.
- [60] O. Reynolds. “On the dynamical theory of incompressible viscous fluids and the determination of the criterion”. In: *Proceedings of the Royal Society of London* 56.336-339 (1894), pp. 40–45.
- [61] L. F. Richardson. “Atmospheric diffusion shown on a distance-neighbour graph”. In: *Proc. Roy. Soc Lond. Series A* 110 (1926), pp. 709–737.
- [62] L. F. Richardson. *Weather Prediction by Numerical Process*. Cambridge University Press, 1922.
- [63] J. Riley and M-P. Lelong. “Fluid Motions in the Presence of Strong Stable Stratification”. In: *Ann. Rev. Fluid Mech.* 32.1 (2000), pp. 613–657.
- [64] J. J. Riley, R. W. Metcalfe, and M.A. Weissman. “Direct numerical simulations of homogeneous turbulence in density-stratified fluids”. In: *AIP Conference Proceedings* 76 (1981), pp. 79–112.
- [65] C. Rorai, P. D. Mininni, and A. Pouquet. “Turbulence comes in bursts in stably stratified flows”. In: *Phys. Rev. E* 89 (2014), p. 043002.
- [66] D. Rosenberg et al. “GPU Parallelization of a Hybrid Pseudospectral Geophysical Turbulence Framework Using CUDA”. In: *Atmosphere* 11.2 (2020).
- [67] H. Salehipour and W. R. Peltier. “Diapycnal diffusivity, turbulent Prandtl number and mixing efficiency in Boussinesq stratified turbulence”. In: *J. Fluid Mech.* 775 (2015), pp. 464–500.
- [68] C. Salem et al. “Solar Wind Magnetohydrodynamics Turbulence: Anomalous Scaling and Role of Intermittency”. In: *The Astrophysical Journal* 702 (2009), pp. 537–553.
- [69] K. Sato et al. “Frequency spectra and vertical profiles of wind fluctuations in the summer Antarctic mesosphere revealed by MST radar observations”. In: *Journal of Geophysical Research: Atmospheres* 122.1 (2017), pp. 3–19.
- [70] L. Seuront et al. “Universal multifractal analysis as a tool to characterize multi-scale intermittent patterns: Example of phytoplankton distribution in turbulent coastal waters”. In: *J. Plankton Res.* 21 (1999), p. 877.
- [71] J. Smagorinsky. “General circulation experiments with the primitive equations: I. The basic experiment”. In: *Mon. Weather Rev.* 22.91 (3) (1963), pp. 99–164.

- [72] G. Stober and J. L. Chau. “A multistatic and multifrequency novel approach for specular meteor radars to improve wind measurements in the MLT region”. In: *Radio Science* 50.5 (2015), pp. 431–442.
- [73] N. E. Sujovolsky and P. D. Mininni. “From waves to convection and back again: The phase space of stably stratified turbulence”. In: *Phys. Rev. F* 5 (2020), p. 064802.
- [74] N. E. Sujovolsky and P. D. Mininni. “Invariant manifolds in stratified turbulence”. In: *Phys. Rev. Fluids* 4 (2019), p. 052402.
- [75] N. E. Sujovolsky, P. D. Mininni, and A. Pouquet. “Generation of turbulence through frontogenesis in sheared stratified flows”. In: *Phys. Fluids* 30 (2018), p. 086601.
- [76] J. Sun et al. “Review of wave turbulence interactions in the stable atmospheric boundary layer”. In: *Rev. Geophys.* 53 (2015), pp. 1–38.
- [77] J. Sun et al. “Turbulence Regimes and Turbulence Intermittency in the Stable Boundary Layer during CASES-99”. In: *Journal of the Atmospheric Sciences* 69 (2011), pp. 338–351.
- [78] J. Sun et al. “Turbulence Regimes and Turbulence Intermittency in the Stable Boundary Layer during CASES-99”. In: *J. Atm. Sci.* 69 (2012), pp. 338–351.
- [79] *Supplemental Material: Movie S1*. <https://agupubs.onlinelibrary.wiley.com/action/downloadSupplement?doi=10.1029%2F2021GL094918&file=2021GL094918-sup-0002-Movie+SI-S01.mp4>.
- [80] *VAPOR*. <https://www.vapor.ucar.edu/>.
- [81] P. Vieillefosse. “Local interaction between vorticity and shear in a perfect incompressible fluid”. In: *Journal de Physique* 43 (1982), pp. 837–842.
- [82] K. B. Winters, P.N. Lombard, and J. J. Riley and E. D’Asaro. “Available potential energy and mixing in density-stratified fluids”. In: *J. Fluid Mech.* 289 (1995), pp. 115–128.
- [83] E. Yee and A. Skvortsov. “Scalar fluctuations from a point source in a turbulent boundary layer”. In: *Phys. Rev. E* 84 (3 2011), p. 036306.